

Effects of Bilayer Asymmetry on Nanotube Formation and Particle Engulfment by Biomembranes and Vesicles

vorgelegt von
Master of Science
Jaime Agudo Canalejo
geboren in Pamplona, Spanien

von der Fakultät II - Mathematik und Naturwissenschaft
der Technischen Universität Berlin
zur Erlangung des akademischen Grades
Doktor der Naturwissenschaften
Dr. rer. nat.

genehmigte Dissertation

Promotionsausschuss:

Vorsitzende: Prof. Dr. Maria Andrea Mroginski

Gutachter: Prof. Dr. Reinhard Lipowsky

Gutachterin: Prof. Dr. Sabine Klapp

Tag der wissenschaftlichen Aussprache: 15. Februar 2016

Berlin 2016

Abstract

Bilayer membranes are an essential component of biological cells, functioning as robust but flexible walls between cellular compartments that can remodel in response to stimuli. Interestingly, many of these remodeling processes can be mimicked in minimal model systems using lipid or polymer vesicles. The goal of this thesis will be to understand two of these processes from a theoretical perspective.

First, we examine the spontaneous formation of nanotubes in giant vesicles as a consequence of bilayer asymmetry. In connection with experimental results, and using numerical energy minimization of a continuum membrane model, we show that the nanotubes appear via a nucleation and growth mechanism that reflects two competing kinetic pathways as the vesicles are osmotically deflated. The first pathway nucleates new isolated buds, whereas the second pathway makes the isolated buds grow into necklace-like tubes. Furthermore, we show that the necklace-like tubes undergo a novel shape transformation into cylindrical tubes once they reach a certain critical tube length, for which we find analytical expressions that are consistent with the experimental results.

Second, we study the engulfment of adhesive nanoparticles by vesicles and biomembranes. We show that the engulfment behavior depends strongly on the asymmetry of the bilayer, as quantitatively described by the membrane spontaneous curvature. We derive analytical expressions for the instabilities of the free and the completely engulfed states of the particle, which depend on the particle size, adhesive strength, bending rigidity and spontaneous curvature. For model membranes with uniform composition, the two instabilities lead to two critical particle sizes that determine four distinct engulfment regimes. Our analytical expressions can be used to extract the membrane spontaneous curvature and the particle–membrane adhesive strength from experimental or simulation studies.

In order to address the process of endocytosis in cells, we then consider adhesion-induced segregation of membrane components. The asymmetric protein coat formed during clathrin-dependent endocytosis is modeled as a bound membrane segment that has a large spontaneous curvature compared to the unbound one. We derive explicit expressions for the engulfment rate and the uptake of nanoparticles by cells, which provide a quantitative fit to experimental data for clathrin-dependent endocytosis of gold nanoparticles.

Finally, we examine the engulfment of nanoparticles by membranes of complex shape, and show that nanoparticles can act as local probes of the membrane curvature. We find that a single vesicle in contact with many nanoparticles can display up to ten distinct engulfment patterns, and describe in detail the morphological transitions between these patterns, which are directly accessible to experiment.

Zusammenfassung

Lipid-Doppelschichten ('lipid bilayers') sind ein essenzieller Bestandteil von biologischen Zellen, sie dienen als robuste, aber gleichzeitig flexible Trennwände zwischen zellulären Kompartimenten, die unter dem Einfluss von äusseren Stimuli umgebaut werden. Interessanterweise können viele dieser Umbauprozesse in relativ einfachen Modellsystemen aus Lipid- oder Polymer-Membranen untersucht werden. In dieser Arbeit geht es um das theoretische Verständnis zweier dieser Umbauprozesse, nämlich der Bildung von Membran-Nanoröhrchen und des Membran-Einschlusses ('engulfment') von festen Nanoteilchen.

Zuerst betrachten wir die spontane Bildung von Nanoröhrchen in Riesenvesikeln ('giant vesicles') als Folge einer relativ großen spontanen Krümmung, die die Asymmetrie zwischen den beiden Monoschichten ('leaflets') der Vesikelmembranen beschreibt. Ausgehend von experimentellen Resultaten, bei denen die Riesenvesikel osmotisch geschrumpft wurden, zeigen wir mittels Energieminimierung, dass Nanoröhrchen durch einen Keimbildungs- und Wachstumsprozess entstehen, der auf zwei kompetitiven kinetischen Pfaden beruht. Der erste Pfad führt zur Bildung von einzelnen neuen Membran-Knospen ('buds'), die dann mittels des zweiten kinetischen Pfades zu Perlenketten verlängert werden. Wenn diese Perlenketten eine kritische Länge erreichen, wandeln sie sich in zylindrische Nanoröhrchen um. Für diese neuartige Form-Transformation wurde eine analytische Theorie entwickelt, die im Einklang mit den bisherigen experimentellen Beobachtungen steht und quantitative Vorhersagen für die kritische Röhrchenlänge liefert.

Anschließend untersuchen wir den Einschluss von adhärennten Nanoteilchen durch Vesikel und biologische Membranen. Wir zeigen, dass das Einschlussverhalten stark von der spontanen Krümmung der Membranen abhängt. Wir leiten analytische Ausdrücke für die Instabilitäten von freien und komplett eingeschlossenen Zuständen der Nanoteilchen ab und bestimmen deren Abhängigkeit von Partikelgröße, Adhäsionsstärke, Biegesteifigkeit und spontaner Krümmung. Für Modellmembranen mit homogener Zusammensetzung erhalten wir zwei kritische Teilchengrößen, aus denen sich vier verschiedenen Parameterbereiche für das Einschlussverhalten ergeben. Die analytischen Ausdrücke können verwendet werden, um die spontane Krümmung und die Adhäsionsstärke aus Experimenten und/oder Simulationen abzuleiten.

Um im Weiteren den Prozess der Endozytose in Zellen zu untersuchen, betrachten wir die durch Adhäsion induzierte Segregation von Membrankomponenten, die auf eine relativ große spontane Krümmung des am Teilchen gebundenen Membransegments führen kann. Wir leiten explizite Ausdrücke für die Einschlussrate und die zelluläre Aufnahme der Nanoteilchen ab. Wenn wir diese theoretischen Ergebnisse mit experimentellen Daten zur Clathrin-abhängigen Endozytose von Gold-Nanoteilchen vergleichen, so erhalten wir eine quantitative Beschreibung der beobachteten Größenabhängigkeit dieses Prozesses.

Abschließend untersuchen wir Membranen und Vesikel von beliebiger Form, die mit vielen Nanoteilchen wechselwirken. Wir zeigen, dass diese Teilchen als Sonde für die lokale Membrankrümmung verwendet werden können. Dabei stellt sich heraus, dass eine Vesikel, die sich in einer Dispersion von identischen Nanoteilchen befindet, bis zu zehn verschiedene Einschlussmuster aufweisen kann. Wir sagen morphologische Übergänge zwischen diesen Mustern voraus, die auch experimentell zugänglich sein sollten.

List of publications and authorship statement

This cumulative thesis is based on the following three publications, which are embedded within the thesis as Chapters 2–4:

- **Chapter 2**

Patterns of Flexible Nanotubes Formed by Liquid-Ordered and Liquid-Disordered Membranes. Y. Liu, J. Agudo-Canalejo, A. Grafmüller, R. Dimova, and R. Lipowsky, *ACS Nano* 10, 463 (2016).

Authorship statement: My contributions focused on sections ‘Nucleation and Growth of Necklace-like Tubes’ and ‘Necklace–Cylinder Coexistence and Critical Tube Length’ of the paper.

- **Chapter 3**

Critical particle sizes for the engulfment of nanoparticles by membranes and vesicles with bilayer asymmetry. J. Agudo-Canalejo and R. Lipowsky, *ACS Nano* 9, 3704 (2015).

Authorship statement: This publication is the result of my own work, with the support of Prof. Reinhard Lipowsky.

- **Chapter 4**

Adhesive Nanoparticles as Local Probes of Membrane Curvature. J. Agudo-Canalejo and R. Lipowsky, *Nano Letters* 15, 7168 (2015).

Authorship statement: This publication is the result of my own work, with the support of Prof. Reinhard Lipowsky.

In addition, during the work for this thesis I also contributed to the following review:

- Wrapping of nanoparticles by membranes. A. H. Bahrami, M. Raatz, J. Agudo-Canalejo, R. Michel, E. M. Curtis, C. K. Hall, M. Gradzielski, R. Lipowsky, and T. R. Weigl, *Advances in Colloid and Interface Science* 208, 214 (2014).

Contents

Abstract	i
List of publications and authorship statement	v
1 Introduction	1
1.1 Motivation	1
1.2 Biomembranes	2
1.2.1 Lipid bilayers	2
1.2.2 The plasma membrane	4
1.3 Elastic theory of membranes	6
1.3.1 General theory	6
1.3.2 Effective constraints on vesicles	9
1.3.3 Shape transformations of vesicles	10
1.3.3.1 Free vesicles	10
1.3.3.2 Vesicles with intramembrane domains	13
1.3.3.3 Vesicles adhering to planar substrates	14
1.4 Membrane nanotubes	15
1.5 Particle–membrane interactions	17
1.5.1 Adsorption, incorporation, translocation and engulfment	17
1.5.2 Engulfment by model membranes	20
1.5.3 Engulfment by cells: endocytosis	23
1.6 Numerical minimization of bending energy	24
1.6.1 Axisymmetric shape equations	24
1.6.2 Application to nanotube formation	26
1.6.3 Application to particle engulfment	27
1.7 References for the Introduction	28
2 Patterns of Flexible Nanotubes Formed by Liquid-Ordered and Liquid-Disordered Membranes	39
2.1 Overview	39
2.2 Abstract	41
2.3 Introduction	41
2.4 Results and Discussion	42
2.5 Conclusions	48
2.6 Methods	50

2.7	References	51
2.8	Supporting Information	53
2.8.1	Critical tube length for VM-A and VM-B morphologies	54
2.8.2	Critical tube length for VM-C morphologies	58
2.8.3	Tube flexibility and persistence length	62
2.8.4	Supporting Figures	63
2.8.5	Supporting Tables	67
2.8.6	Description of Supporting Movies	70
2.8.7	References for the Supporting Information	72
3	Critical Particle Sizes for the Engulfment of Nanoparticles by Membranes and Vesicles with Bilayer Asymmetry	73
3.1	Overview	73
3.2	Abstract	75
3.3	Introduction	75
3.4	Results and Discussion	77
3.5	Receptor-Mediated Adhesion and Engulfment	83
3.6	Conclusions	88
3.7	Methods	89
3.8	References	89
3.9	Supporting Information	92
3.9.1	Free Energy Landscapes for Engulfment Process	92
3.9.2	Exocytic Engulfment of Nanoparticles	99
3.9.3	Kinetics of Membrane Spreading and Engulfment Rate	103
3.9.4	References for the Supporting Information	107
4	Adhesive Nanoparticles as Local Probes of Membrane Curvature	109
4.1	Overview	109
4.2	Abstract	110
4.3	Introduction, Results and Discussion	110
4.4	References	114
5	Summary and Outlook	117
	Acknowledgements	121

1 Introduction

1.1 Motivation

Membranes are present in every living cell, and as such are an essential component of life as we know it.¹ They provide separation between the inside and the outside of cells, as well as intricate compartmentalization within the cell. As a consequence of their role as barriers between distinct compartments with distinct functions, all biological membranes are exposed to an asymmetric environment, a fact that is reflected in a compositional asymmetry between the two leaflets that form the membranes.^{2,3} Thanks to their fluidity, biological membranes are highly dynamic structures that can remodel in response to external and internal cues. Some of these remodeling processes occur on the micrometer scale corresponding to whole-cell deformations, as is the case in cell spreading or cytokinesis.^{4,5} On the other hand, cell membranes can also remodel on the nanometer scale, as occurs in the formation of spherical and tubular membrane protrusions such as blebs or microvilli, which have typical sizes on the order of tens or hundreds of nanometers.⁶

Among these remodeling processes, of particular practical importance are those involved in the entry of nanometer-sized particles into cells. Indeed, nanoparticles are increasingly used for targeted delivery of drugs to biological cells,^{7,8} reaching difficult targets such as tumors^{9,10} or the blood-brain barrier.^{11,12} Novel magnetic nanoparticles are being developed as contrast agents in Magnetic Resonance Imaging,^{13,14} whereas gold nanoparticles are being used in X-Ray imaging and photothermal therapies.^{15,16} Nanoparticles are also more and more common in industrial processes, which has led to concerns about their cytotoxicity. The world production of nanoparticles is projected to increase 25-fold in the period between 2008 and 2020,¹⁷ with nanoparticles being extensively used in cosmetics, food, paints, powders, and surface treatment.¹⁸ Both *in vitro* and *in vivo* studies find that nanoparticles can be cytotoxic in large doses, with toxicity levels depending on nanoparticle size, shape, and surface chemistry.^{17,19,20} A further particularly important class of nanoparticles comprises viruses. Viral capsids typically range in size from 20 to 300 nm, and enter cells *via* the same pathways as artificial nanoparticles.²¹ Insights on these pathways may help in preventing viral infection before replication.

In order to enter a cell, a particle must first cross the cellular membrane. This process is termed *endocytosis*, and starts with the adhesion and engulfment of the particle by the membrane, followed by membrane fission.^{22,23} The particle then ends up inside the cytoplasm, fully enclosed by membrane. Several distinct endocytic pathways used by cells

to take up nanoparticles have been described, depending on the molecular machinery involved.^{22,23} Of these, the most commonly observed is clathrin-mediated endocytosis, which is assisted by the formation of a strongly curved protein coat on the inner side of the membrane.²²

Interestingly, some of these remodeling processes can be mimicked in minimal model systems. First, the formation of nanometer-sized tube-like protrusions has been observed in experiments in which liposomes^{24–28} or Giant Unilamellar Vesicles (GUVs)^{29–31} are exposed to asymmetric concentrations of curvature-generating proteins. Second, engulfment of solid particles by liposomes,^{32,33} GUVs^{34–42} and polymer vesicles⁴³ has also been observed to occur spontaneously in experiments. An understanding of remodeling processes in these biomimetic systems can be very useful, as they allow insight into the fundamental membrane processes underlying their biological counterparts, without the added complexity intrinsic to living cells.

In this work, we set out to understand, from a theoretical perspective, (i) the spontaneous formation of membrane nanotubes in model systems and (ii) the engulfment of particles by biological and biomimetic membranes. In both cases, we will emphasize the key role of membrane asymmetry in the remodeling process.

1.2 Biomembranes

1.2.1 Lipid bilayers

Lipids are among the most important molecules in biology, constituting about 10% of cells by dry weight (data for *E. coli*).⁴⁴ Lipids are amphiphilic molecules, that is, they combine a hydrophilic (water-loving) head and a hydrophobic (water-hating) tail, see Figure 1.1(a).⁴⁵ Typically, the tail is composed of two hydrocarbon chains. At very low concentrations, they are soluble in water. However, as soon as the concentration reaches the so-called critical micelle concentration (CMC), they self-assemble into structures in which only the hydrophilic heads are exposed to the water, thereby shielding the core of hydrophobic tails.⁴⁶ The two most common such structures are micelles and bilayers, see Figures 1.1(b) and 1.1(c). Which structure forms will depend on the concentration and on the shape of the lipids: conical lipids with a single tail or a large head groups form micelles, whereas those with a more cylindrical shape tend to form bilayers.⁴⁶ Free lipid bilayers of finite size in water would have exposed hydrophobic edges, which would involve a large energy cost. For this reason, they typically close into round “bags” called vesicles, which will be described in more detail in Section 1.3.

Lipid bilayers are thin membranes composed of two monolayers of lipids, see Figure 1.1(c). These membranes have the striking property of being just a few nanometers in thickness, while being able to extend to much greater lengths, of the order of tens of micrometers, in the lateral direction. At room or physiological temperatures they are typically in a fluid

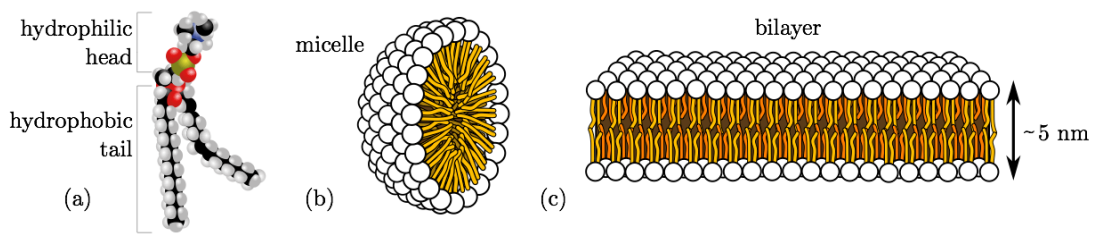


Figure 1.1: Schematic architecture of lipids and lipid structures. (a) Phospholipid (phosphatidylcholine) molecule. (b) Spherical micelle. (c) Flat bilayer. In water, lipids self-assemble in structures such as (b) and (c) above a critical concentration. Adapted from public domain image, Wikimedia Commons.

state, effectively forming a two-dimensional fluid. They offer resistance to stretching and bending but, being fluid, they cannot support shear stresses because the lipid molecules can freely rearrange within each monolayer plane.^{47,48} In contrast to this in-plane mobility, the movement of lipids from one monolayer to the other (known as *flip-flop*) is much more restricted, and happens only in the timescale of hours or days for most lipids.⁴⁹ One important exception to this rule is the biologically-relevant cholesterol, which is known to flip-flop much faster.⁵⁰

At lower temperatures, lipid bilayers are found in a solid state, also known as the gel phase.⁴⁵ In the gel phase, lipids show in-plane crystalline order, which leads to increased bending rigidity, shear resistance and decreased flip-flop rates. The transition from the gel to the fluid phase occurs at a temperature called the melting temperature, which depends on the particular type of lipid that forms the bilayer.⁴⁵ However, it is also possible to form bilayers with a mixture of two or more lipids, leading to a much more complex phase behaviour. In this case, bilayers can display phase coexistence between the fluid and gel phase at intermediate temperatures⁵¹ and, in the presence of cholesterol, there can also be coexistence between two distinct fluid phases.^{52–54} These two phases are called liquid-ordered (Lo) and liquid-disordered (Ld), referring to the order of the lipid chains. It is debated whether binary mixtures of a single phospholipid and cholesterol show fluid-fluid separation,^{53,54} but macroscopic fluid-fluid phase separation is well-documented for ternary mixtures of cholesterol and two other lipids.^{52,54}

A very important characteristic of lipid bilayers is their selective permeability. Hydrophobic molecules can cross lipid membranes with ease, whereas membranes are highly impermeable to ions. In the case of uncharged polar molecules, their permeability depends on size: small molecules (including water) can cross the membrane, while large molecules such as sugars cannot. This fact is of great relevance to the structural stability of biological cells, which actively regulate the passage of ions through the membrane by using specialized proteins called ion channels.⁵⁵

In Figure 1.1(c), a *symmetric* bilayer in which both monolayers are identical is depicted. It is however very common, particularly in biological membranes,^{2,3} to encounter *asymmetric*

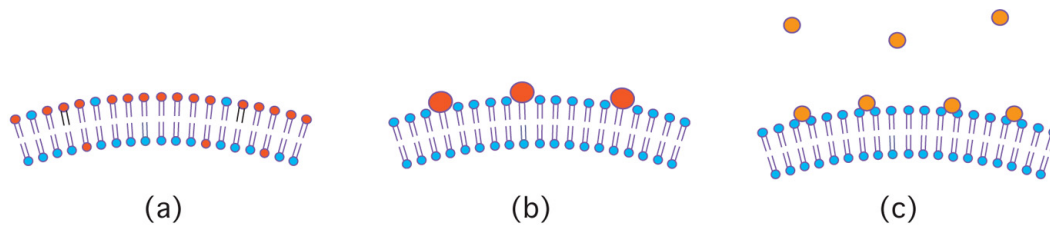


Figure 1.2: Molecular mechanisms for the generation of bilayer asymmetry.

- (a) compositional lipid asymmetry between the two leaflets of the bilayer; (b) asymmetric concentration of membrane-anchored molecules with a bulky headgroup such as glycolipids; and (c) asymmetric adsorption of ions or small molecules.

bilayers in which each monolayer has a different lipid composition from the other, see Figure 1.2(a). Other mechanisms that generate bilayer asymmetry include asymmetric concentration of membrane-anchored molecules with a bulky head group, such as glycolipids, and asymmetric adsorption of ions or small molecules, see Figures 1.2(b) and 1.2(c).³¹ From a mechanistic perspective it is clear that, whereas symmetric bilayers will tend to be flat, asymmetric bilayers will typically prefer to curve towards one of the two sides, acquiring a certain *spontaneous curvature*. In the case of molecules with a bulky headgroup or asymmetric adsorption, membranes will tend to bend away from the side with more bulky or adsorbed molecules. In the case of asymmetric composition of lipids, the preferred curvature will depend mostly on the shape of the lipids involved.⁵⁶

1.2.2 The plasma membrane

Lipid bilayers are the main ingredient of biomembranes, which are the essential structural element of cells, acting as ‘walls’ or separation barriers between cells and their environment, or between different organelles within the cell. Apart from lipids, biomembranes are mainly composed of proteins and a few carbohydrates, see Figure 1.3. In this so-called fluid-mosaic model of cell membranes, first proposed by Singer and Nicolson in 1972,⁵⁷ the cell membrane is viewed as a fluid lipid bilayer in which proteins are embedded and can freely diffuse. As depicted in the figure, biomembranes are strongly asymmetric: the lipid composition is typically different between leaflets, the proteins do not have a symmetric shape, and often the cellular cytoskeleton is coupled to the membrane on one of its sides only.⁵⁶

Biomembranes differ in their composition depending on their particular function, with great differences across cell types and between organelles of the same cell, and more than 1000 different lipid species being present in any eukaryotic cell.¹ Of all biomembranes, perhaps the most studied is the plasma membrane, which separates the interior from the exterior of a cell, protecting the cell from its surroundings. Plasma membranes of animal cells are composed of lipids and proteins in approximately equal weight,⁵⁹ and

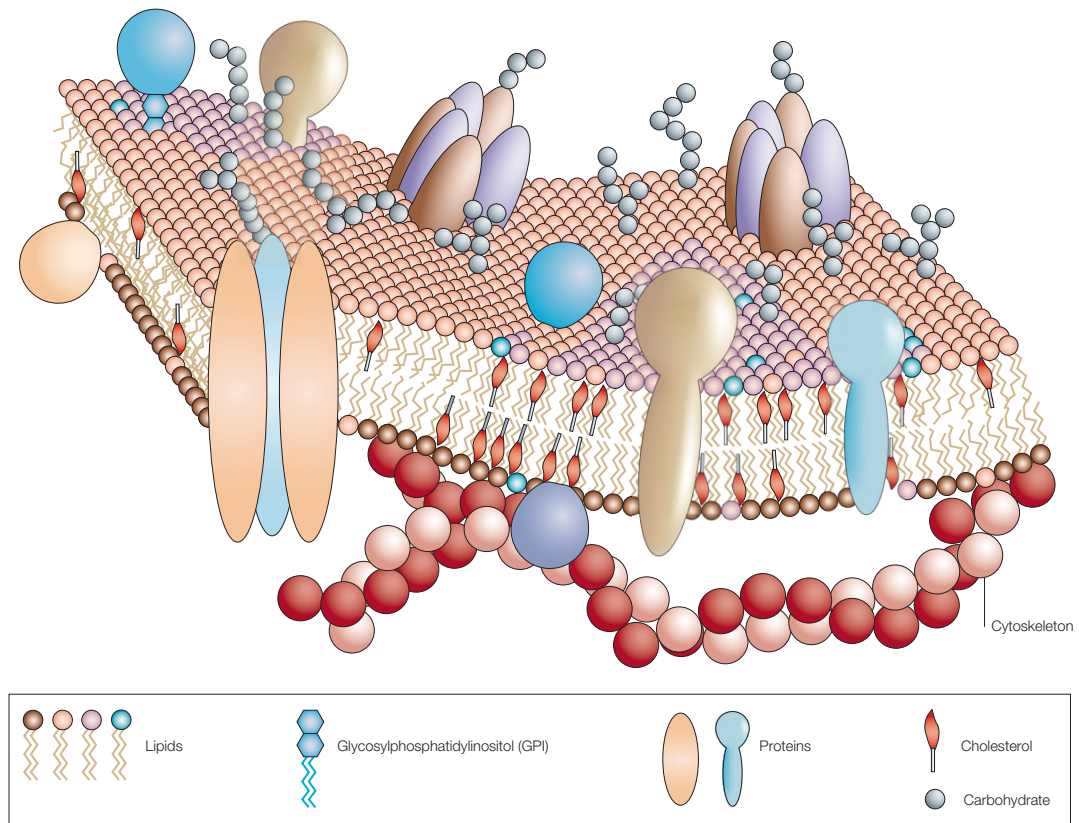


Figure 1.3: Fluid-mosaic model of the plasma membrane. The membrane is viewed as a two-dimensional fluid in which lipids and proteins can diffuse. The outer (upper) and inner (lower) leaflets of the bilayer have different lipid composition. The inner leaflet is coupled to the cytoskeleton or cell cortex. Adapted from Ref 58.

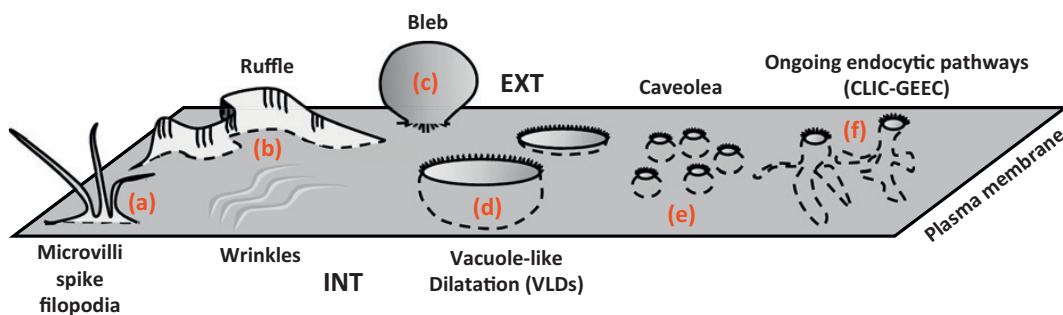


Figure 1.4: Plasma membrane reservoirs in cells. (a) Microvilli and spikes with tubular shape. (b) Membrane ruffles shaped as flat sheets. (c) Membrane blebs with spherical shape. (d) Vacuole-like dilatations with spherical shape. (e) Flask-shaped caveolae. (f) Tubular shapes formed by the clathrin-independent endocytic CLIC/GEEC pathway. Features (a-c) protrude towards the exterior of the cell (EXT), whereas features (d-f) protrude towards the inside (INT). Adapted from Ref 6.

show a strong asymmetry in the lipid compositions of the outer and inner leaflets.^{2,3} In fact, this asymmetry is actively regulated by the cell *via* proteins called flippases and floppases, which respectively bring selected lipids from the outer to the inner leaflet and *vice versa*. Conversely, this asymmetry can be destroyed by proteins called scramblases.^{2,3} Other proteins with important functions present in the plasma membrane include ion transporters, as described in the previous section, and membrane receptors which relay signals between the outside and the inside of cells. Transmembrane proteins often have asymmetric, wedge-like shapes, further contributing to the asymmetry of the membrane.⁵⁶ In addition, the plasma membrane in eukaryotic cells is linked on the inner side to the cellular cortex, which is a dense network of actin filaments and myosin motors that actively regulates the cell shape, see Figure 1.3.⁵⁸

For all these reasons, the plasma membrane of cells is a highly dynamic structure, and typically displays complex shapes, with outwards and inwards protrusions, folds and wrinkles that can act as membrane reservoirs,^{6,60} see Figure 1.4. Membrane reservoirs are particularly important in the case of phagocytic cells, specialized immune cells that have the function of engulfing large solid particles such as bacteria or apoptotic cells. When engulfing a large particle, an initially round phagocytic cell can increase its “apparent” plasma membrane area by up to 5-fold,⁶¹ which implies that up to 80% of the total membrane area is stored in reservoirs. In addition to the area stored in folds and wrinkles, the plasma membrane is subject to constant recycling, with the full content of the plasma membrane being exchanged in the timescale of a few hours.⁶²

1.3 Elastic theory of membranes

1.3.1 General theory

As mentioned in Section 1.2.1, the lateral span of bilayers can be up to three or four orders of magnitude larger than their thickness. Such separation of length scales allows one to describe the membrane as an infinitesimally thin two-dimensional surface embedded in three-dimensional space.⁴⁷ The local shape of the membrane at any given point is characterized by the two principal curvatures $C_1 \equiv 1/R_1$ and $C_2 \equiv 1/R_2$, see Figure 1.5, which are the maximal and minimal curvatures of the membrane along two perpendicular directions on its surface.⁴⁷ More importantly, from these two quantities one can define at each point the *mean curvature*

$$M \equiv (C_1 + C_2)/2 \tag{1.1}$$

and the *Gaussian curvature*

$$K \equiv C_1 C_2 \tag{1.2}$$

which are independent of the choice of coordinates.

It is clear that the local bending energy density of a membrane at any given point should depend on the curvature of the membrane at that point. To a first approximation, one can

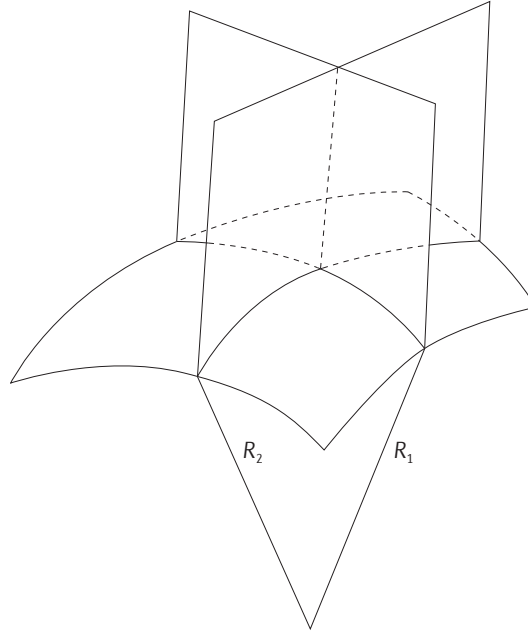


Figure 1.5: Principal radii of curvature R_1 and R_2 of a two-dimensional surface at a given point. The corresponding principal curvatures are defined as $C_1 \equiv 1/R_1$ and $C_2 \equiv 1/R_2$. Adapted from Ref 63.

thus write the bending energy as an expansion in the deviation of the membrane curvature from its optimal value, obtaining^{47,64}

$$E_{\text{be}} = \int dA [2\kappa(M - m)^2 + \kappa_G K] \quad (1.3)$$

to lowest order, where the constants κ and κ_G have units of energy and are known as bending rigidity and Gaussian bending rigidity, respectively. These two bending rigidities are material parameters. The third material parameter is the spontaneous curvature m , which describes the preferred mean curvature of the membrane that results from the existence of bilayer asymmetry. The integral in eq (1.3) runs over the whole surface A of the membrane. The sign of the mean curvature M and the spontaneous curvature m must be defined by convention: in the case of closed vesicles, we will say that curvatures are positive if the membrane bends away from the interior compartment, as in the case of a spherical vesicle, and negative if the membrane bends towards the interior compartment.

A second contribution to the total elastic energy of the membrane comes from area stretching.^{48,65} Indeed, the number of lipids being fixed, the membrane will have a preferred, optimal resting area A_0 . Molecularly, this optimal area can be understood as $A_0 \equiv A_{\text{lip}}(N^+ + N^-)/2$, where A_{lip} is the optimal area per lipid, and N^+ and N^- are the number of lipids in each monolayer. Again, expanding the energy on the deviations from this optimal area, the stretching contribution to the total energy will be given by

$$E_{\text{st}} = \frac{k_A}{2A_0}(A - A_0)^2 \quad (1.4)$$

to lowest order, with k_A being a material parameter known as the area compressibility of the membrane. The tension of the membrane as a response to area stretching or compression can be calculated as the derivative of this stretching energy with respect to the area, obtaining⁴⁸

$$\Sigma = k_A \frac{A - A_0}{A_0} \quad (1.5)$$

and is thus simply proportional to the dimensionless strain of the membrane. By taking into account the bilayer structure of the membrane in a more molecularly detailed theory, one can show that the area compressibility is related to the bending rigidity by $k_A \sim \kappa/d^2$, where d is the bilayer thickness.⁶⁵ Lipid membranes can support little area expansion, rupturing if they are stretched more than a few percent of their optimal area.

As discussed in Section 1.2.1, in the absence of cholesterol the number of lipid molecules on each monolayer is constant in the timescale of hours, as lipid flip-flop from one monolayer to the other is very rare. This fixes the optimal area of each monolayer independently so that the difference in optimal area between monolayers is given by $\Delta A_0 \equiv (N^+ - N^-)A_{\text{lip}}$.⁶⁵ Deviations from this optimal area difference will incur an energy cost, which is given by the area difference elasticity (ADE) model, again to lowest order,⁶⁶

$$E_{\text{ade}} = \frac{\bar{\kappa}\pi}{2Ad^2} (\Delta A - \Delta A_0)^2 \quad (1.6)$$

where $\bar{\kappa}$ is a material parameter called the non-local bending rigidity and d is the bilayer thickness. Taking into account that the typical curvatures of a vesicle are much smaller than the inverse thickness of the bilayer, one can write the area difference ΔA as a function of the membrane shape with

$$\Delta A = 2d \int dAM + O(d^2) \quad (1.7)$$

where again the integral runs over the whole surface A of the membrane.

As previously noted, membranes typically form closed vesicles, which divide the aqueous solution into two compartments, an *interior* one and an *exterior* one. This fact is important because, as discussed before, lipid membranes are impermeable to ions and large uncharged polar molecules. We will call these molecules *osmotically active*, because they exert an osmotic pressure onto the membrane. Assuming an ideal solution of molecules, the difference between the pressures exerted by the molecules in the interior and exterior compartments is⁶⁷

$$\Delta P \equiv P_{\text{int}} - P_{\text{ext}} = k_B T (n/V - \rho_{\text{ext}}) \quad (1.8)$$

where k_B is the Boltzmann constant, T the temperature, n the number of osmotically active molecules inside the vesicle, V the volume enclosed by the vesicle, and ρ_{ext} the number density of osmotically active molecules in the exterior compartment. We can define the optimal volume of the vesicle $V_0 \equiv n/\rho_{\text{ext}}$, at which the osmotic pressure difference is

zero. Deviations from this optimal volume will cost an energy

$$E_{\text{vol}} = \int_{V_0}^V dV' \Delta P(V') = k_B T [n \ln(V/V_0) - \rho_{\text{ext}}(V - V_0)] \approx \frac{k_B T \rho_{\text{ext}}}{2V_0} (V - V_0)^2 \quad (1.9)$$

where the last expression holds for small deviations from the optimal volume $|V/V_0 - 1| \ll 1$.

In principle, the total energy of the system will be given by these four energies of bending (1.3), stretching (1.4), area difference elasticity (1.6) and volume work (1.9), so that

$$E_{\text{tot}} = E_{\text{be}} + E_{\text{st}} + E_{\text{ade}} + E_{\text{vol}} \quad (1.10)$$

Specifying the full system would require eleven parameters: six material parameters defining the membrane, namely the bending rigidity κ , the Gaussian bending rigidity κ_G , the non-local bending rigidity $\bar{\kappa}$, the area compressibility k_A , the bilayer thickness d , and the spontaneous curvature m ; two control parameters, given by the number density of osmotically active molecules in the exterior compartment ρ_{ext} and the temperature T ; and three geometric parameters that define an individual vesicle, namely its optimal area A_0 , optimal volume V_0 and optimal area difference between monolayers ΔA_0 . Exploring such a high-dimensional parameter space would seem like a daunting task. Luckily, as explained in the next subsection, many of these contributions can be simplified or ignored when considered detail.

1.3.2 Effective constraints on vesicles

A first simplification arises from the fact that there is a large separation between the energy scale associated with bending, which is of order κ , and that associated with stretching, which is of order $k_A A_0$. Indeed, the typical value of the bending rigidity for lipid membranes is $\kappa \sim 10^{-19}$ J, whereas the area compressibility is on the order of $k_A \sim 0.2$ J/m².⁶⁸ The energy scale of stretching will be much larger than that of bending as long as $\sqrt{A_0} \gg \sqrt{\kappa/k_A} \sim 0.7$ nm. This is the case for all realistic vesicles, for which $\sqrt{A_0}$ ranges from several tens of nanometers to tens of micrometers. As a consequence, stretching will be negligible and the area of vesicles will not deviate significantly from the optimal area, so that we can set the constraint $A = A_0$

A similar consideration can be done with the volume work. The energy associated with deviations from the optimal volume will be of order $k_B T \rho_{\text{ext}} V_0$, compared to the energy associated with bending κ . Thus, we can consider the enclosed volume to be essentially fixed as long as the number density of osmotically active molecules in the exterior compartment is large enough $\rho_{\text{ext}} \gg \kappa/k_B T V_0$. Using the typical value of κ , and at room temperature, one finds that for small vesicles of size 100 nm the threshold concentration of osmotically active molecules is in the μM range, and goes down to pM range for larger vesicles of size 10 μm . In most experiments, as well as in physiological conditions, the osmolarity of the aqueous solutions is typically above the mM range, and therefore the enclosed volume

of vesicles is constrained to $V = V_0$. However, it is sometimes the case that experiments with vesicles are done in pure water. In such cases, we have $\rho_{\text{ext}} \simeq 0$ and the energetic contribution of volume work can be dropped altogether.

One further simplification arises from the fact that many experiments are done with membranes made from lipid mixtures including cholesterol. As mentioned before, cholesterol can easily flip-flop from one monolayer to the other, therefore uncoupling the monolayers and relaxing the constraint on the area difference between them. This implies that we can formally set $\bar{\kappa} = 0$ in (1.6), that is, neglect the contribution from area difference elasticity.

Finally, we note that the second term in (1.3), the one associated with the Gaussian curvature, does not depend on the specific shape of the vesicle. The Gauss-Bonnet theorem⁶⁹ tells us that the integral of the gaussian curvature over a closed surface is a topological invariant, with $\int dA K = 4\pi(1 - g)$, where g is the genus of the vesicle. For a vesicle of spherical topology $g = 0$, for one of toroidal topology $g = 1$, etc. Therefore, as long as we do not consider changes in the vesicle topology, the Gaussian term of the bending energy only adds a constant term to the total energy and we can formally set $\kappa_G = 0$ in (1.3).

With all these considerations, the total energy that we must consider when describing free vesicles in typical experimental conditions becomes

$$E = \int dA 2\kappa(M - m)^2 \quad (1.11)$$

with only two material parameters, namely the bending rigidity κ and the membrane spontaneous curvature m , and two geometrical constraints on the total area A and volume V that must be explicitly enforced. In practice, one can choose an energy scale, naturally given by κ , and a length scale, such as the vesicle size $R_{\text{ve}} \equiv \sqrt{A/4\pi}$. The equilibrium shapes of free vesicles then depend only on two dimensionless parameters: the reduced spontaneous curvature mR_{ve} and the reduced volume $v \equiv 3V/4\pi R_{\text{ve}}^3$.⁶⁴

1.3.3 Shape transformations of vesicles

1.3.3.1 Free vesicles

A problem of great interest amounts to finding the equilibrium shape of a vesicle for given values of the parameters, that is, finding the shape S that minimizes the energy (1.11) for given mR_{ve} and v . In principle, this is achievable by functional minimization of the energy (1.11). In order to incorporate the area and volume constraints, one minimizes the functional⁷⁰

$$F[S] = E[S] + \Sigma A[S] - \Delta P V[S] \quad (1.12)$$

where Σ and ΔP are Lagrange multipliers. The same symbols Σ and ΔP as for the tension and pressure difference are used, both for historical reasons and because they can be

shown to be identifiable.⁷¹ Functional minimization of F leads⁷⁰ to the so called *shape equation*

$$\Delta P = 2\Sigma M - 2\kappa \{ \nabla^2 M - (M - m) [2(M - m)M - 4M^2 + 2K] \} \quad (1.13)$$

where ∇^2 is the Laplace-Beltrami operator. The shape equation (1.13) is a non-linear fourth order partial differential equation, and is therefore extremely hard to solve analytically. In the limit of zero bending rigidity $\kappa = 0$, it reduces to the Laplace equation for fluid-fluid interfaces as given by $\Delta P = 2\Sigma M$.

A set of solutions that can be obtained by directly inspecting (1.13) is the set of surfaces with constant mean curvature $\nabla^2 M \equiv 0$ that satisfy $\Delta P = 2(\Sigma + 2\kappa m^2)M - 4\kappa m M^2$. Of these, perhaps the most relevant are spheres, for which $M = 1/R$ where R is the radius of the sphere. The sphere is in fact the lowest energy shape for vesicles in the absence of osmotically active molecules $\Delta P = 0$, that is, in the absence of a volume constraint, for small values of the spontaneous curvature. In the presence of a volume constraint, however, spheres can only be the solution for reduced volume $v = 1$, and lower values of the reduced volume necessarily require solutions with non-uniform mean curvature in order to satisfy $0 < v < 1$.⁶⁴

If one wants to find the solutions of (1.13) for given reduced spontaneous curvature mR_{ve} and reduced volume v , one needs to do so numerically. This is still a complicated task, but it becomes particularly simple when considering axisymmetric shapes and, crucially, axisymmetric shapes can be shown to be those of lowest energy for small values of the spontaneous curvature $mR_{ve} = O(1)$.⁶⁴ The two-dimensional phase diagram of lowest energy (stable) shapes in this region of small spontaneous curvatures is shown in Figure 1.6(a). There are four different branches of solutions: prolates, oblate-discocytes, stomatocytes and pear-shaped vesicles. The transitions D between prolates and oblates, D^{sto} between oblates and stomatocytes, and D^{pear} between prolates and pears are discontinuous; whereas the transition C^{pear} between pears and prolates is continuous. At the lines L^{pear} and L^{sto} , limit shapes involving infinitesimally small necks are obtained. The lines SI^{sto} and SI^{ob} delineate regions with self-intersecting, unphysical shapes.

The simplest case that we can consider is that of vesicles without bilayer asymmetry, that is, with no spontaneous curvature $m = 0$, as a function of the reduced volume v . This is indicated by the dotted line in Figure 1.6(a). As one deflates the vesicle from a sphere $v = 1$, one finds stable prolates in the range $1 > v > 0.65$, oblate-discocytes in the range $0.65 > v > 0.59$, and stomatocytes for $0.59 > v > 0$. Example shapes along the deflation trajectory are shown in Figure 1.6(b). As v approaches zero, a limit shape is obtained with two concentric spheres of equal size connected to each other by an infinitesimal neck.

The shape evolution is radically different in the presence of spontaneous curvature. In the upper and lower regions of the phase diagram in Figure 1.6(a) we find *budding*, that is, the formation of a smaller daughter vesicle (bud) connected to the larger mother vesicle as

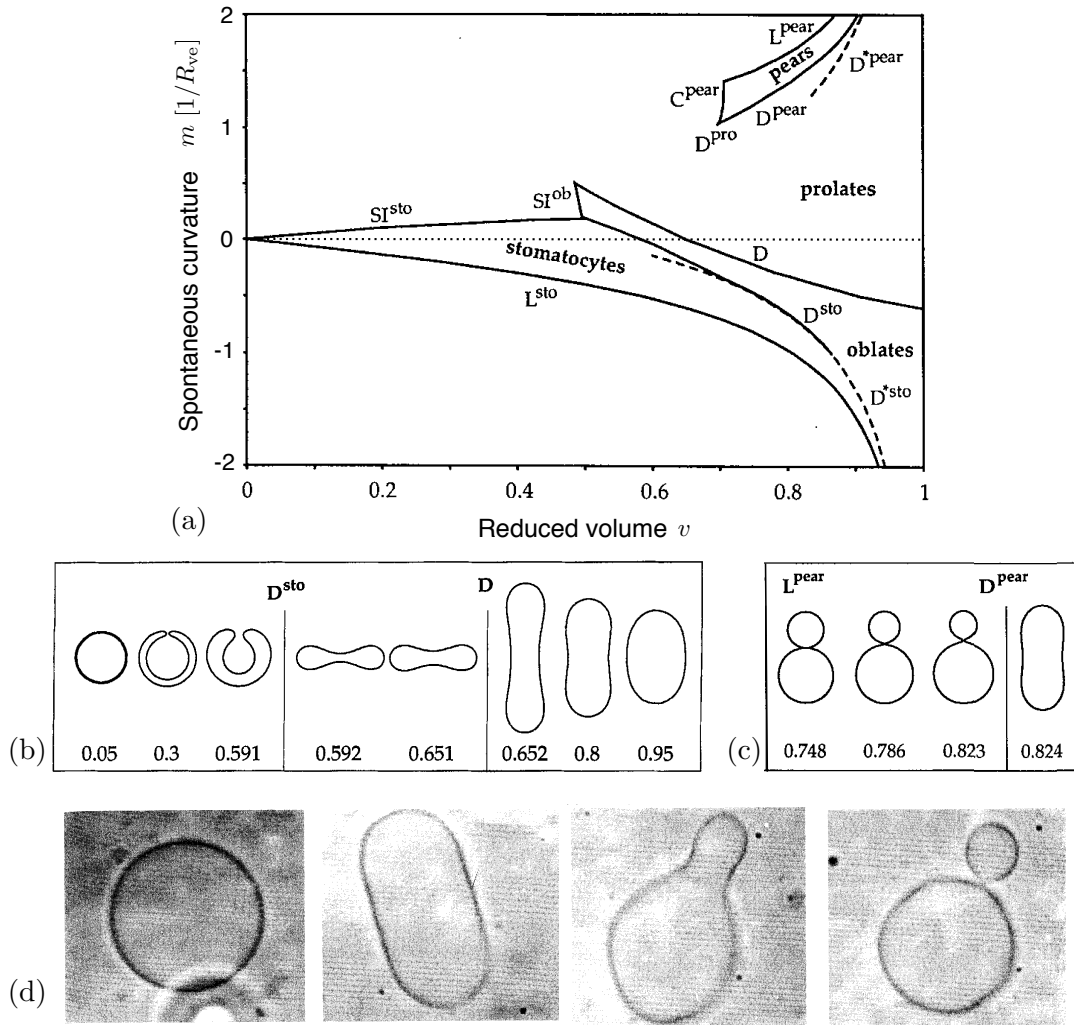


Figure 1.6: The shapes of free vesicles. (a) Phase diagram showing the regions of stability of the different branches of shapes, and the transitions between them as a function of spontaneous curvature and reduced volume, see text. (b–c) Lowest energy shapes as a function of reduced volume v for (b) symmetric membranes with $m = 0$, and (c) asymmetric membranes with $mR_{ve} = +1.5$ which display budding. (d) Experimental observation of a budding transition. Adapted from (a–c) Ref 64 and (d) Ref 72.

the vesicle is deflated. For positive spontaneous curvatures, the budding occurs towards the outside, as shown in Figure 1.6(c) for $mR_{ve} = +1.5$, whereas for negative spontaneous curvatures the budding occurs towards the inside. The budded state has lowest energy to the left of the lines D^{pear} and D^{sto} for positive and negative spontaneous curvatures, respectively. Between the lines D^{pear} and L^{pear} , or D^{sto} and L^{sto} , the bud is connected to the mother vesicle by a small but finite neck. To the left of L^{pear} and L^{sto} , however, the neck becomes infinitesimally small. The stability limit of such infinitesimally small necks is given by the *ideal neck condition*

$$M_{\text{mv}} + M_{\text{bud}} = 2m \quad (1.14)$$

where M_{mv} and M_{bud} are the mean curvature of the mother vesicle and of the bud at the position of the ideal neck, respectively. More generally, it can be shown^{71,73} that out-buds are stable if $M_{\text{mv}} + M_{\text{bud}} < 2m$, whereas in-buds are stable if $M_{\text{mv}} + M_{\text{bud}} > 2m$. The ideal neck condition (1.14) was first found empirically in numerical calculations,⁶⁴ and later proven analytically.⁷³ Such budding transitions have been observed in experiment,⁷² as seen in the micrographs in Figure 1.6(d).

1.3.3.2 Vesicles with intramembrane domains

As mentioned in the Introduction, membranes made from ternary lipid mixtures including cholesterol can phase separate into two distinct fluid macroscopic domains. Suppose a fluid domain of phase β is embedded in a fluid matrix of phase α , see Figure 1.7(a). In general, the phases α and β will have different bending rigidities $\kappa^{(\alpha)}$ and $\kappa^{(\beta)}$, as well as different spontaneous curvatures $m^{(\alpha)}$ and $m^{(\beta)}$. The domain will be bounded by a domain wall or edge with a finite line tension λ , which will contribute a line energy $E_\ell = \lambda \ell_{\alpha\beta}$, where $\ell_{\alpha\beta}$ is the length of the domain edge. Because of the fluid nature of the membrane, it is possible for the domain to reduce this line energy by bending out of plane, that is, by budding.⁷⁴ By balancing the bending contribution with the edge contribution, it is straightforward to see that domains will tend to bud once they become larger than a characteristic size given by $\kappa^{(\beta)}/\lambda$.⁷⁴ Such domain-induced budding has also been observed in experiments, as shown in Figure 1.7(b).

Using numerical energy minimization, the lowest energy shapes of a phase separated vesicle with a fluid domain can be obtained as a function of the relevant parameters.^{76,77} Once again, one finds wide regions of the phase diagrams which display fully-budded states, in which the bud of phase β is connected to the mother vesicle of phase α by an infinitesimally small neck. The stability limit of such states is given by^{76,77}

$$\kappa^{(\alpha)} M_{\text{mv}} + \kappa^{(\beta)} M_{\text{bud}} = \kappa^{(\alpha)} m^{(\alpha)} + \kappa^{(\beta)} m^{(\beta)} \pm \lambda/2 \quad (1.15)$$

where again M_{mv} and M_{bud} are the mean curvature of the mother vesicle and of the bud at the position of the neck, respectively. The plus sign in front of the line tension applies to

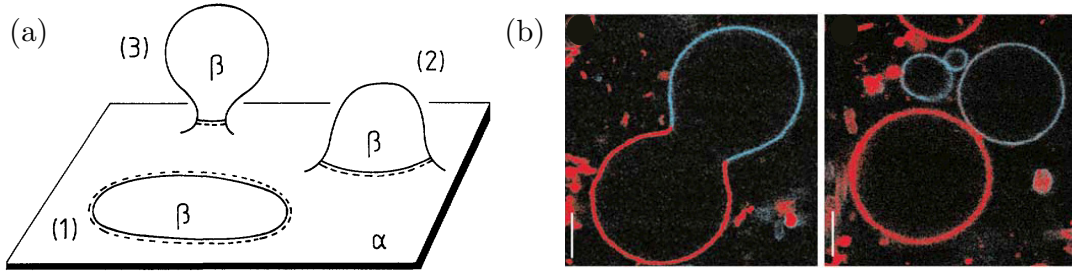


Figure 1.7: Domain-induced budding. (a) Schematic depiction of an initially flat fluid domain (1) that reduces its edge energy by bending out of plane (2) and forming a bud (3). (b) Experimental observation of domain-induced budding, with Lo and Ld phases labeled in blue and red respectively. Scale bars are $5 \mu\text{m}$. Adapted from (a) Ref 74 and (b) Ref 75.

out-buds, whereas the minus sign applies to in-buds. This equation can be understood as a generalization of the ideal neck condition (1.14) to the case of phase separated membranes. Indeed, by setting $\kappa^{(\alpha)} = \kappa^{(\beta)}$, $m^{(\alpha)} = m^{(\beta)}$ and $\lambda = 0$ in (1.15) we directly recover (1.14).

1.3.3.3 Vesicles adhering to planar substrates

Working with free vesicles is experimentally challenging, due to their intrinsic Brownian rotation and translation, that make following a single vesicle with the usual confocal microscope setup difficult. For this reason, experimentalists typically work with vesicles that are bound to a planar substrate either (i) by attractive forces or (ii) through gravitation, by filling the vesicles with a denser solution than the surrounding one. Furthermore, adhesion of membranes to substrates or between each other is a topic of biological relevance, as cells are often cultured in adhesive substrates and membrane-membrane adhesion is always the first step in membrane fusion.⁷⁸

For large vesicles, there is a separation of length scales between the typical range of adhesive forces, such as van der Waals or electrostatic interactions which act on the range of a few nanometers, and the size of the vesicles, which is on the order of micrometers. For this reason, it is possible to use a *contact potential*, in which we replace the microscopic interaction potential by an effective adhesion energy $W < 0$ per unit area of membrane that is bound to the substrate. Thus, if A_{bo} is the membrane area bound to the substrate, the vesicle gains an adhesion energy⁷⁹

$$E_{\text{ad}} = -|W|A_{\text{bo}} \quad (1.16)$$

The presence of the contact potential (1.16) does not affect the shape equation (1.13), but enters into the boundary conditions for the solution. The bound segment and the unbound segment of the vesicle membrane are separated by a contact line. Along this contact line, the principal curvature C_1^* of the membrane parallel to the contact line must

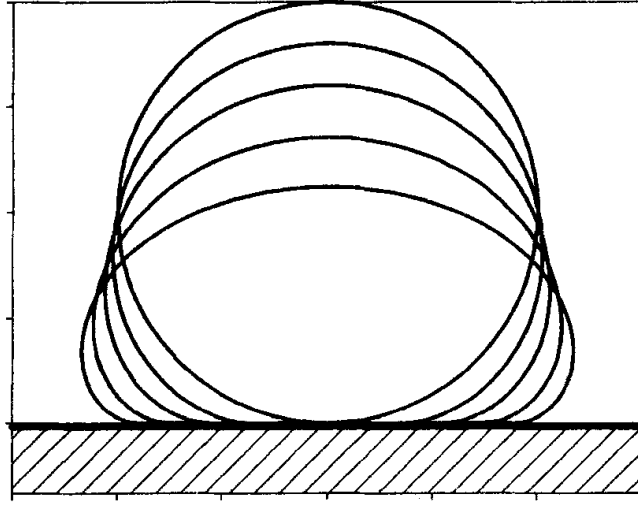


Figure 1.8: Shapes of an adhering vesicle. The vesicle is initially spherical with radius R_{ve} and has no volume constraint. The adhesive strengths used are $|W|R_{ve}^2/\kappa = 2.0, 2.9, 4.1, 6.4$ and 10.2 . Adapted from Ref 79.

be $C_1^* = 0$ because the substrate is planar.⁷⁹ The second principal curvature perpendicular to the contact line follows from mechanical equilibrium along this line, with minimization of the free energy leading to the value $C_2^* = \sqrt{2|W|/\kappa}$.⁷⁹ The *contact mean curvature* is therefore

$$M_{co} = (C_1^* + C_2^*)/2 = \sqrt{|W|/2\kappa} \quad (1.17)$$

In general, one finds that for low adhesion, the vesicles do not bind to the substrate, whereas they do bind for sufficiently large values of the adhesion. The binding transition may be continuous, as is the case for spherical vesicles with no volume constraint, oblates and stomatocytes; or discontinuous in the case of discocytes and prolate vesicles. As the adhesive strength is increased beyond the binding transition, the bound area increases progressively and the shape of the vesicle approaches a spherical cap. Example shapes for the case of a vesicle with no volume constraint for increasing values of the adhesive strength are shown in Figure 1.8. In all cases, the stability limit of the free vesicle state is given by⁶⁵

$$M_{co} = M_{fv} \quad (1.18)$$

where M_{fv} is the mean curvature of the free vesicle at the point of contact with the substrate *before* adhesion. Equation (1.18) can be rewritten as $|W| = 2\kappa M_{fv}^2$, and in particular $|W| = 2\kappa/R_{ve}^2$ in the special case of an initially spherical vesicle.

1.4 Membrane nanotubes

In Section 1.3.3.1, we described the shapes of free vesicles in the case of small spontaneous curvatures, of the order of the vesicle size $m = O(1/R_{ve})$. In practice, however, asymmetric

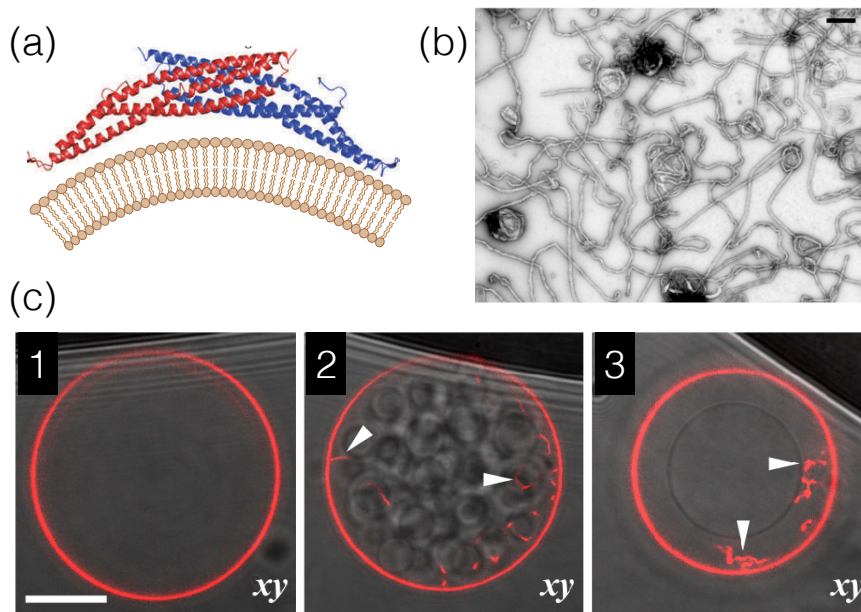


Figure 1.9: Membrane nanotubes in the presence of curvature-inducing proteins. (a) Banana-shaped N-BAR protein amphiphysin induces curvature on a membrane. (b) Tubular shapes observed in liposomes exposed to amphiphysin (scale bar 500 nm). (c) GUV enclosing an aqueous solution of PEG and dextran polymers, (1) before deflation, (2) during deflation and (3) after equilibration. Membrane nanotubes are indicated by arrows (scale bar 15 μm). Adapted from (a) Ref 56, (b) Ref 25 and (c) Ref 29.

protein adsorption to the membrane can induce very high spontaneous curvatures, of up to $|m| = 1/(20 \text{ nm})$ in the case of specialized BAR-domain proteins, see Figure 1.9(a).^{24,56} For a large vesicle of size $R_{\text{ve}} = 20 \mu\text{m}$, this would imply reduced spontaneous curvatures of the order of $|m|R_{\text{ve}} \sim 1000$, far outside the boundaries of the phase diagram of free vesicle shapes in Figure 1.6(a). Indeed, the vesicle morphologies observed in the presence of such large spontaneous curvatures are very different from the ones described in the previous section. In experiments, proteins known to be curvature-inducing in cells, such as N-BAR proteins amphiphysin^{24,25} and endophilin,²⁶ F-BAR protein syndapin,²⁷ as well as endocytosis-related proteins such as epsin,²⁸ have been adsorbed onto liposomes. The adsorption of the curvature-inducing proteins leads to complex shapes consisting of long and thin membrane tubules that spontaneously arise from the liposomes, see Figure 1.9(b).

Spontaneous tubulation has also been observed in model systems consisting of Giant Unilamellar Vesicles that enclose aqueous two-phase solutions of PEG and dextran polymers,^{29,30} see Figure 1.9(c). These systems are very interesting from a biophysical perspective because they can mimic the nanometer-sized membrane area reservoirs present in micrometer-sized living cells, compare Figure 1.4. The nanotubes form spontaneously upon deflation of the vesicle, and can store as much as 20% of the excess area of the vesicle. However, a systematic theory of the formation and shapes of these membrane tubes has been lacking.

Indeed, it was argued²⁹ that the tubes were stabilized by the large negative spontaneous curvatures induced by the asymmetric adsorption or anchoring of the polymers, but what defines the shapes of these tubes was unclear. In principle, the bending energy (1.11) of a vesicle with a strongly negative spontaneous curvature $m \ll -1/R_{ve}$ could be minimized by storing its excess membrane area into either (i) inwards-pointing cylindrical tubes with radius $1/2|m|$; or (ii) inwards-pointing spherical buds with radius $1/|m|$. In both cases, the bending energy would be minimized because the mean curvature of the inwards protrusions would match the spontaneous curvature $M = m$. In addition, it is conceivable that single buds may be isolated from each other, or that they may be strung together into longer necklace-like tubes. The mechanisms that set the shape, number and length of these tubes have not been described so far. Understanding the formation of such nanotubes will be one of the aims of this thesis, see Chapter 2.

1.5 Particle–membrane interactions

1.5.1 Adsorption, incorporation, translocation and engulfment

As explained in the Motivation of this thesis, understanding the interaction between nanoparticles and membranes is of key importance to a number of scientific, medical and industrial fields. ‘Nanoparticle’, however, is an umbrella term that encompasses an astonishing variety of particles, made from different materials and with widely differing characteristics, such as fullerenes,⁸⁰ quantum dots,⁸¹ and silver,⁸² gold⁸³ or silica⁸⁴ nanoparticles. In the context of particle–membrane interactions, we may identify three nanoparticle properties of particular relevance:⁸⁵

- Size: nanoparticles can range from below 1 nm, in the case of spherical fullerenes,⁸⁰ up to a few hundreds of nanometers, in the case of large metallic^{83,86} or silica nanoparticles.⁸⁴ Naturally, nanoparticles that are smaller than the membrane thickness $d \simeq 5$ nm will interact with the membrane in very different ways than those that are of comparable size, or much larger than the membrane.
- Shape: nanoparticles are most commonly spherical; however, they can also show elongated shapes with one dimension larger than the other two, as in the case of carbon nanotubes⁸⁷ or gold nanorods;⁸⁸ as well as flat shapes with two dimensions larger than the third one, as in the case of graphene nanosheets. In this case it will be important whether one, two or all of its dimensions are larger or smaller than the membrane thickness d .
- Surface chemistry: hydrophilicity and hydrophobicity, as well as surface charge, strongly influence the nanoparticle–membrane interactions.⁸⁹ In addition, nanoparticles may be functionalized by coating them with lipids, polymers or specific protein ligands that can bind to receptors on the membrane surface.⁸⁹

Depending on these properties, nanoparticles may either (i) adsorb onto the membrane, (ii) incorporate inside it, (iii) translocate through it or (iv) get engulfed by the membrane.

Particle adsorption onto membranes was already described in Section 1.2.1, see Figure 1.2(c). Particles that adsorb onto membranes are typically hydrophilic, so that they do not tend to penetrate inside the membrane, and small, with sizes comparable to the head group of the lipids.^{90,91} As mentioned, asymmetric adsorption of nanoparticles between the two sides of the bilayer induces spontaneous curvature, with the membrane preferring to bend away from the side with the highest coverage of adsorbates. This was first predicted theoretically⁹² and later confirmed in molecular dynamics simulations.⁹⁰

Hydrophilic particles that are larger, of size comparable to the membrane thickness $d \simeq 5$ nm, and that exhibit an attractive interaction with the lipid headgroups may instead incorporate into the membrane, as found in molecular dynamics simulations, see Figure 1.10(a).^{91,93} In order to maximize the contact with the hydrophilic head groups, the membrane changes its topology and completely surrounds the particle. Incorporation into the membrane also occurs in the case of hydrophobic particles of size comparable to or smaller than the membrane thickness d . Smaller hydrophobic nanoparticles, such as spherical fullerenes, may incorporate into the hydrophobic core of the membrane without altering its structure, see Figure 1.10(b).^{91,94–96} Such nanoparticle incorporation into the bilayer has been widely observed in experiments.^{97–102} Larger hydrophobic particles, on the other hand, will not fit inside the hydrophobic core, and may therefore induce a pore on the membrane that they will span, see Figure 1.10(c).¹⁰³

It is also conceivable that a nanoparticle may directly translocate from one side to the other of the membrane, as shown in Figure 1.10(d). In order to achieve this, a pore must open in the membrane through which the particle can cross to the other side. Very small or elongated nanoparticles, with dimensions around a nanometer, such as uncharged polar molecules, metal nanoclusters, dendrimers and carbon nanotubes have been shown to translocate through membranes with little to no disruption.^{106–110} Larger particles of a few nanometers, on the other hand, can translocate through the membrane only by disrupting its integrity. This occurs in the case of charged particles (such as cationic quantum dots or gold nanoparticles) which induce transient poration of the cell membrane when entering cells, leading to increased cytotoxicity.^{109,111,112}

In all the cases described, the particles were of size comparable or smaller than the membrane thickness d . As soon as particles become larger (in all dimensions) than a few times the membrane thickness, incorporation or translocation become unfavorable and, if the interaction between the hydrophilic surface of the membrane and the particle is attractive, the membrane will instead bend around the particle and engulf it, as in Figure 1.10(e).^{92,113} The engulfment process ends with the particle fully covered by membrane but still connected to the mother membrane by a small neck, as in the rightmost picture of Figure 1.10(e). This neck might then break *via* membrane fission, with the

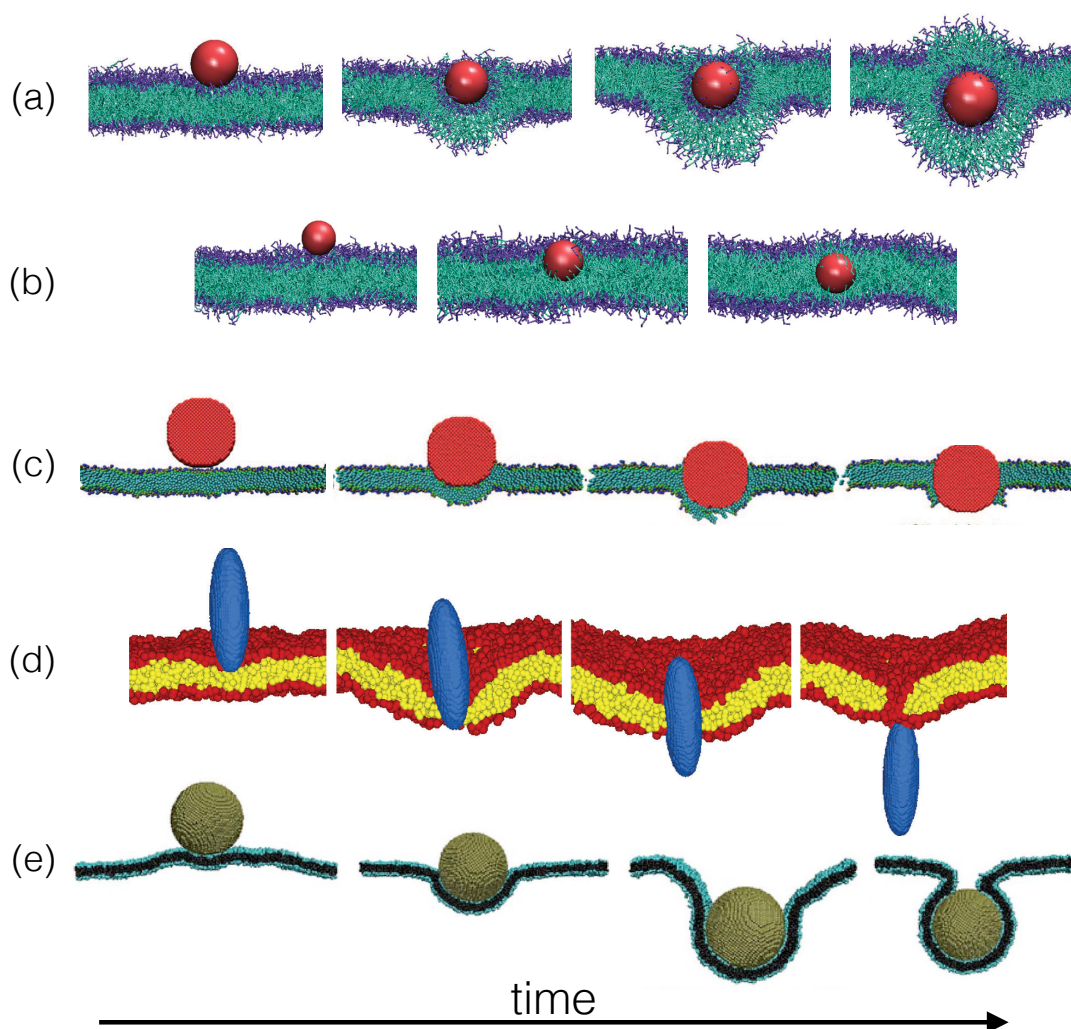


Figure 1.10: Different modes of interaction between particles and membranes. Time-series snapshots (cross-sections) of molecular dynamics simulations of (a–c) incorporation, (d) translocation and (e) engulfment of nanoparticles. The hydrophilic heads of the lipids are dark blue in (a–c), red in (d), and turquoise in (e); the hydrophobic tails of the lipids are turquoise in (a–c), yellow in (d) and black in (e). In (a), the small particle is hydrophilic of radius $R_{\text{pa}} \sim d$ and changes the topology of the bilayer. In (b), the particle is hydrophobic of radius $R_{\text{pa}} < d$ and incorporates into the membrane core. In (c), the hydrophobic particle of radius $R_{\text{pa}} \gtrsim d$ first induces and then spans a pore in the membrane. In (d), an elongated particle of size comparable to d translocates across the membrane by opening a pore. In (e), a hydrophilic particle of radius $R_{\text{pa}} \gg d$ is gradually engulfed by the membrane, remaining connected by a small neck in the end. Adapted from (a–b) Ref 91, (c) Ref 103, (d) Ref 104 and (e) Ref 105.

particle then having been effectively transported from one side of the membrane to the other. In the rest of this section, we will review previous experimental and theoretical work on particle engulfment.

1.5.2 Engulfment by model membranes

The first experiments that mixed vesicles with solid particles were performed nearly 20 years ago, by Dietrich *et al.*³⁴ In those experiments, Giant Unilamellar Vesicles of a few tens of microns in size were made from DMPC or SOPC membranes in the fluid state. Single spherical Latex particles with radii ranging from 1 μm to 10 μm were then brought in contact with a single vesicle using an optical trap. Immediately after the particle made contact with the vesicle membrane, the particle was observed to jump out of the optical trap and into the membrane, that would engulf it. Both complete engulfment and partial engulfment were observed. Occasionally, the particles were observed to induce rupture of the vesicle membrane. Indeed, the vesicles used were initially spherical and semi-tense, and the osmotic conditions were such that the enclosed volume of the vesicle was constrained. As a consequence, in order to engulf the particles the vesicle membrane needs to stretch, leading to rupture if the membrane stretches more than a few percent. Similar experiments with spherical GUVs and single particles manipulated by optical tweezers have been performed later, again finding spontaneous engulfment of the particles by the vesicles.^{35,36}

Other experiments with GUVs and Latex particles have been performed using more deflated, non-spherical vesicles, with enough excess area so that the vesicle can engulf the particles without stretching.³⁷ The vesicles would thus display prolate and oblate-discocyte morphologies, as those described in Section 1.3.3.1. The Latex particles were observed to get partially engulfed at the areas of lowest curvature of the vesicles, such as at the poles of discocyte vesicles or the sides of prolate vesicles, see Figure 1.11(a).

In other experiments, GUVs have been mixed with solutions containing much smaller nanoparticles, in the size range of tens of nanometers. Various types of nanoparticles have been used, such as quantum dots,³⁸ silica,^{39,40} polystyrene⁴¹ or core-shell magnetic nanoparticles.⁴² Depending on the surface properties, in particular surface charge of the particles, as well as the charge of the lipid membranes, nanoparticles were found to localize at the vesicle surface, sometimes leading to deformation and rupture of the membranes. However, the studies used optical microscopy, making it impossible to discern whether the nanoparticles were partially or completely engulfed by the membranes.

Lastly, experiments have been performed in which lipid^{32,33} or polymer⁴³ vesicles of small size, in the range of a few hundred nanometers, were mixed with solutions of silica nanoparticles, with sizes of a few tens of nanometers. In all cases, complete engulfment followed by neck fission and full internalization of the particles by the vesicles was clearly observed using cryo-electron microscopy, see e.g. Figure 1.11(b).

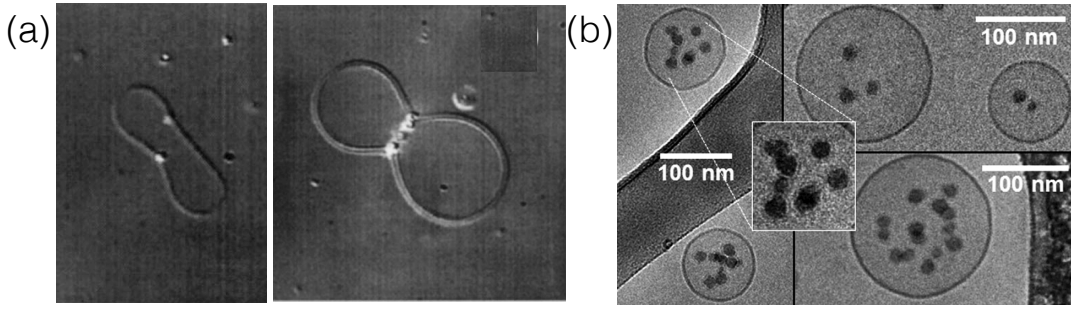


Figure 1.11: Engulfment of particles by vesicles. (a) Partial engulfment of a single Latex particle at the pole of a discocyte GUV (left) and of multiple particles at the side of a prolate GUV. (b) Complete engulfment (followed by neck fission) of silica nanoparticles by a small liposome. Adapted from (a) Ref 37 and (b) Ref 33.

From a theoretical perspective, the engulfment of particles by membranes can be understood as a competition between adhesion and bending energies, as in the case of vesicle adhesion to planar substrates, see Section 1.3.3.3. For particles much larger than the range of the adhesion potential, we can once again consider a contact potential with a given adhesion energy per unit area $W < 0$. The adhesion energy will then be given by $E_{\text{ad}} = -|W|A_{\text{bo}}$, where A_{bo} is the area of membrane that is bound to the particle. The gain in adhesion energy will be opposed by the energetic cost of bending the membrane around the particle.

Such an energy balance was first considered by Lipowsky and Döbereiner,⁹² for the case of a large vesicle (with zero spontaneous curvature) engulfing a small spherical particle. The vesicle is assumed to have enough excess area so that its membrane does not need to stretch in order to accommodate the particle. If the particle has radius R_{pa} , the energy gain from adhesion will amount to $-|W|4\pi R_{\text{pa}}^2$ for a completely engulfed particle, and will therefore increase with particle size. On the other hand, the cost of bending the membrane around the particle amounts to $2\kappa(1/R_{\text{pa}}^2)4\pi R_{\text{pa}}^2 = 8\pi\kappa$, and is therefore independent of particle size. Ignoring the change in bending energy of the unbound part of the membrane due to engulfment, which should be negligible if the particle is much smaller than the vesicle, we find that complete engulfment is energetically favorable if $|W|4\pi R_{\text{pa}}^2 > 8\pi\kappa$ or, equivalently,

$$R_{\text{pa}} > \sqrt{\frac{2\kappa}{|W|}} \quad (1.19)$$

Therefore, engulfment becomes energetically favorable only for large enough particles. If the size of the particle is not negligible compared to the vesicle size, one must consider the energy contribution of the change in shape of the unbound segment of the vesicle after engulfment, $\Delta E_{\text{un}} \equiv E_{\text{un}} - E_{\text{fr}}$, where E_{un} is the energy of the unbound segment after complete engulfment and E_{fr} is the energy of the free vesicle (before engulfment). The condition for energetically favorable engulfment then becomes $|W|4\pi R_{\text{pa}}^2 > 8\pi\kappa + \Delta E_{\text{un}}$.

For vesicles without spontaneous curvature and constrained volume, one finds always $\Delta E_{\text{un}} < 0$, and the threshold radius for engulfment therefore decreases.¹¹⁴ In addition, if the free vesicle is close to a shape transition, such as in the phase boundaries between discocytes/oblates or oblates/prolates as shown in Figure 1.6(b), the engulfment of the particle may induce the shape transition of the vesicle.^{115,116}

A limitation of the approach leading to equation (1.19) is that it simply compares the energy of the free and completely engulfed states, but does not inform us about the stability of each state, that is, about the energy landscape of the engulfment process. Indeed, the transition from the free to the completely engulfed state may in principle occur discontinuously, meaning that there is an energy barrier between the two states, or continuously, *via* partially engulfed states. In order to achieve this, one would need to numerically calculate the energy of the unbound part of the membrane along the engulfment coordinate, that is, for increasing values of the bound area $0 \leq A_{\text{bo}} \leq 4\pi R_{\text{pa}}^2$. This was carried out by Deserno¹¹⁷ in the particular case of a planar membrane with no spontaneous curvature that is connected to a membrane area reservoir with fixed tension.* The condition (1.19) for favorable engulfment was found to be exact in the absence of membrane tension, with the transition being discontinuous, whereas in the presence of tension a continuous transition between free and partially engulfed states as well as a discontinuous transition between partial engulfment and complete engulfment were found. However, a systematic calculation of the energy landscapes of engulfment in the more realistic case of closed vesicles with fixed membrane area (and fixed enclosed volume) has not been attempted in the literature.

More recent theoretical efforts have focused on understanding the engulfment of non-spherical particles, such as ellipsoidal, rod-like or cube-like particles.^{118–123} These particles have the common feature of having non-uniform curvatures, with weakly curved sides coexisting with strongly curved tips or edges. As a consequence, one finds discontinuous orientational changes of the particle during the engulfment process, with engulfment starting from the weakly curved side, but completing at the strongly curved tip.^{118,120,121} Further efforts have been dedicated to the engulfment of soft particles, such as small vesicles^{124,125}, thin elastic shells¹²⁶ or liquid droplets.¹²⁷ In all cases, the softness of the particle enhances partially engulfed states in which the particle and the membrane spread onto each other. Lastly, some efforts have been devoted to understanding the interactions of membranes with multiple spherical particles. If the range of the adhesive potential is non-negligible when compared to the particle size, membrane-mediated interactions can lead to cooperative engulfment of several nanoparticles into membrane tubes.^{128–130}

With a few exceptions,^{115,116,118,128,129} all of these theoretical and simulation studies have dealt with particle engulfment by planar membranes rather than vesicles, and those who did consider vesicles did not explore the parameter space of vesicle sizes and shapes in

*In this case, the tension is neither treated as a mechanical force, as in eq (1.5), nor as a Lagrange multiplier to keep the area constraint, as in eq (1.12), but rather as a chemical potential for the membrane area reservoir.

any detail. In particular, the only two theoretical studies describing engulfment of single spherical particles by vesicles^{115,116} have focused only on engulfment occurring at the poles of axisymmetric vesicles, due to the limitations of the numerical methods used therein. In addition, all of these studies have ignored the (relevant) possibility of bilayer asymmetry, focusing only on membranes with zero spontaneous curvature. Overcoming these limitations will be one of the main goals of this thesis, see Chapters 3 and 4.

1.5.3 Engulfment by cells: endocytosis

Many experiments have been performed in order to understand the endocytic pathways that bring solid nanoparticles into cells. As mentioned in the Introduction, the interaction of nanoparticles and cells is of key importance to the fields of drug delivery, optical imaging, nanotoxicity and virology. Several distinct endocytic pathways used by nanoparticles and viruses to enter cells have been described,^{21–23} depending on the molecular machinery involved in the engulfment process: clathrin-mediated, which involves the formation of protein coats including clathrin triskelions, AP-2 adaptor proteins and membrane receptors; caveolin-mediated, involving membrane rafts enriched in caveolin, cholesterol and glycolipids; macropinocytosis, dependent on actin polymerization; phagocytosis as performed by specialized white blood cells; as well as several less-studied pathways such as Arf6- or flotillin-mediated pathways.

Given the variety of pathways, cell types and nanoparticles involved, it is perhaps too ambitious to try to do a comprehensive review of the existing work on endocytosis. The interested reader can find comprehensive reviews on engulfment of nanoparticles²³ and viruses²¹ elsewhere. It is however worthy to focus our attention on a particular finding with a more physical flavor, namely the study of the dependence of endocytosis on particle size. In several studies, the uptake of gold nanoparticles^{86,131,132} and artificial viral particles^{133,134} by cells has been quantified as a function of the particle size. Intriguingly, the results indicate that there is an optimal particle size for which uptake is maximal: the optimal particle radius is found to be around 25 nm, with cell uptake decreasing both for larger and smaller particles.

This non-monotonic dependence cell uptake with particle size is somewhat puzzling, in light of the theoretical results for engulfment by model membranes discussed in the previous subsection. Indeed, the energetic competition between bending and adhesion there described implied that the larger the particle, the more favorable is engulfment, see eq (1.19). Naively, one would therefore expect cell uptake to increase monotonically with particle size, instead of showing a maximum at a given size.

Attempts to solve this conundrum have so far been based on considering that (i) the particle–membrane adhesion is specific, that is, mediated by ligands on the particle surface that bind to receptors on the membrane, and (ii) the number of receptors on the membrane is limited.^{135–141} In this type of model, particles have to be large enough to overcome the

bending-related threshold given by eq (1.19), but cannot be too large because they will then use up all the available membrane receptors, leading to incomplete engulfment. The competition between these two mechanisms leads to an optimum particle size for maximal cell uptake.

However, the assumptions of these models conflict with several experimental observations. First, not only specific but also non-specific attractive interactions as mediated by surface charge are known to play important roles in endocytosis.^{142–144} Second, it is known that membrane receptors are continuously recycled between the plasma membrane and internal organelles, with constitutive recycling times ranging from a few minutes to half an hour.¹⁴⁵ Finally, the number of receptors bound per nanoparticle is typically just a few.¹⁴⁶ For these reasons, ascribing the decrease in cell uptake for larger particles to depletion of receptors on the membrane does not seem satisfactory. In this thesis, we will explain the size dependence of cell uptake observed in experiments as a consequence of the membrane asymmetry induced by protein coats, without the need of receptor shortage. This is developed in Chapter 3.

1.6 Numerical minimization of bending energy

1.6.1 Axisymmetric shape equations

In order to study the formation of membrane nanotubes and the engulfment of nanoparticles by vesicles, it is necessary to find the shapes of membranes that minimize the bending energy (1.11), subject to the necessary constraints. In the general case of a membrane or vesicle with arbitrary shape, functional minimization of the bending energy leads to the general shape equation (1.13) which, as mentioned previously, is extremely hard to solve. However, the shape equation simplifies greatly when the search of minimum energy shapes is restricted to axisymmetric ones. Luckily, axisymmetry is present when we consider the shape of nanotubes, as well as the engulfment of particles at the poles of vesicles, see Figure 1.12.

Using the parametrization by the arc length s displayed in Figure 1.12, the shape functional (1.12) that includes the bending energy as well as the area and volume constraints by Lagrange multipliers can be written as⁶⁴

$$F = \int_0^{s^*} ds \mathcal{L}(\psi, \dot{\psi}, x, \dot{x}, \gamma) \quad (1.20)$$

where constant terms that do not affect the minimization have been left out, and the ‘Lagrangian’ function is given by

$$\mathcal{L} \equiv \pi \kappa x \left(\dot{\psi} + \frac{\sin \psi}{x} - 2m \right)^2 + 2\pi \Sigma x + \pi \Delta P x^2 \sin \psi + \gamma (\dot{x} - \cos \psi) \quad (1.21)$$

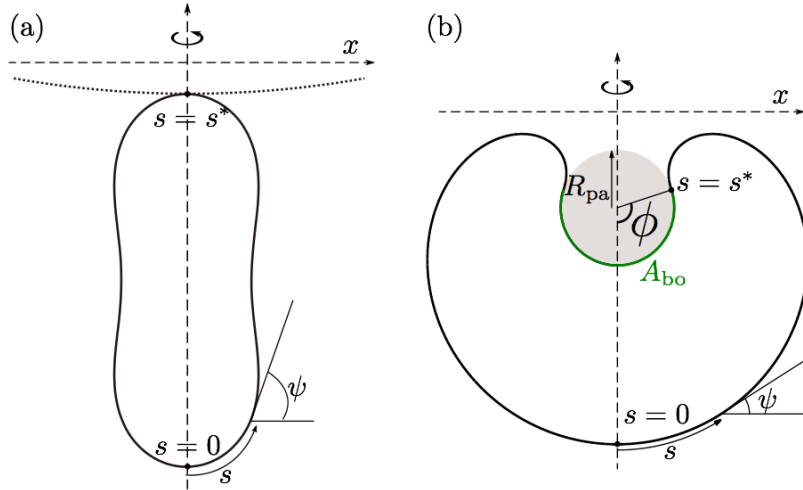


Figure 1.12: Axisymmetric geometry and arc length parametrization. (a) A membrane nanotube that protrudes towards the outside of a spherical vesicle (represented by the dotted segment), to which it connects by an infinitesimally small neck. (b) A vesicle in contact with a spherical particle (grey) that originates from the exterior compartment. The unbound part of the vesicle membrane (black), meets the bound part (green) smoothly at a certain wrapping angle ϕ . The bound part of the membrane has area A_{bo} .

where $\gamma = \gamma(s)$ is a Lagrange multiplier function that serves to impose the geometrical constraint $\dot{x} = \cos \psi$.

We now put the first variation δF in (1.20) equal to zero and obtain the Euler-Lagrange equations of (1.21), which have the form⁶⁴

$$\begin{aligned} \dot{\psi} &= u \\ \dot{u} &= -\frac{u}{x} \cos \psi + \frac{\cos \psi \sin \psi}{x^2} + \frac{\gamma \sin \psi}{2\pi\kappa x} + \frac{\Delta P x \cos \psi}{2\kappa} \\ \dot{\gamma} &= \pi\kappa \left[(u - 2m)^2 - \frac{\sin^2 \psi}{x^2} \right] + 2\pi\Sigma + 2\pi\Delta P x \sin \psi \\ \dot{x} &= \cos \psi \end{aligned} \tag{1.22}$$

where the dot denotes a derivative with respect to the arc length s . These are the axisymmetric shape equations, which form a system of nonlinear ordinary differential equations that can be solved numerically. These equations are subject to the initial conditions

$$\psi(0) = 0, \quad u(0) = u_0, \quad \gamma(0) = 0, \quad x(0) = 0. \tag{1.23}$$

with the initial value u_0 being unknown, which will be used to satisfy the boundary conditions at the end point s^* in a numerical shooting method.

We can augment the system of equations in (1.22) with the equations for the area and

volume as given by

$$\begin{aligned}\dot{A} &= 2\pi x \\ \dot{V} &= \pi x^2 \sin \psi\end{aligned}\tag{1.24}$$

with initial conditions

$$V(0) = 0, \quad A(0) = 0 \quad .\tag{1.25}$$

The shape equations (1.22) and (1.24), as well as the initial conditions (1.23) and (1.25) are identical when considering nanotube formation or particle engulfment. On the other hand, the boundary conditions at the end point s^* are different in each case, as detailed in the following.

1.6.2 Application to nanotube formation

In principle, nanotubes may be connected to the large mother vesicle by an open neck of finite size, or by an infinitesimally small ‘ideal’ neck as shown in Figure 1.12(a). In the latter case, the curvature of the nanotube at the position of the neck must satisfy the inequality associated with the ideal neck condition (1.14), in order for the neck to be stable. Carrying out the calculations, we find (*a posteriori*) that the stability condition for an ideal neck is always satisfied. For this reason, we focus in the following on nanotubes that are connected by an ideal neck to a spherical mother vesicle of radius R_{mv} .

At first sight, the problem has five unknown parameters, namely ΔP , Σ , u_0 , s^* and R_{mv} . These should be used to enforce the boundary conditions at the end point s^* . In order to ensure a smooth matching of the nanotube shape at the north pole, and to satisfy the constraints on the total area A and enclosed volume V , the boundary conditions must be

$$\begin{aligned}\psi(s^*) &= \pm \pi \\ x(s^*) &= 0 \\ A(s^*) &= A - 4\pi R_{\text{mv}}^2 \\ V(s^*) &= V - (4\pi/3)R_{\text{mv}}^3\end{aligned}\tag{1.26}$$

where the plus and minus signs apply to nanotubes that point towards the exterior and the interior of the vesicle, respectively. We would therefore seem to have an underdetermined system with five unknowns and four equations. However, as explained in Section 1.3.3.1, the mother vesicle can have a stable spherical shape of radius R_{mv} only if it satisfies the Laplace-like equation

$$\Delta P = \frac{2(\Sigma + 2\kappa m^2)}{R_{\text{mv}}} - \frac{4\kappa m}{R_{\text{mv}}^2}\tag{1.27}$$

which determines ΔP as a function of Σ and R_{mv} .

We thus have a well-posed boundary problem with four boundary conditions and four unknowns, that can be solved using a non-linear shooting procedure. The numerical

integration of eqs (1.22) and (1.24), with initial conditions in eqs (1.23) and (1.25), is performed using a Runge-Kutta method, while the search for the values of Σ , R_{mv} , u_0 and s^* that satisfy the boundary conditions in (1.26) is carried out using Newton's method. Choosing the vesicle size $R_{ve} \equiv \sqrt{A/4\pi}$ as a length scale and the bending rigidity κ as an energy scale, the shapes of nanotubes can be determined as a function of just two dimensionless parameters: the reduced volume $v \equiv 3V/4\pi R_{ve}^3$ and the reduced spontaneous curvature mR_{ve} .

1.6.3 Application to particle engulfment

In the case of particle engulfment, we want to find the minimum energy shape of the unbound segment of the membrane that matches smoothly with the segment bound to the particle at a wrapping angle ϕ , see Figure 1.12(b). The wrapping angle ϕ acts as a reaction coordinate for the engulfment process, from no engulfment at $\phi = 0$ to complete engulfment at $\phi = \pi$. The bound segment follows the contour of the particle, and thus assumes the shape of a spherical cap. This segment has the area

$$A_{bo} = 2\pi R_{pa}^2(1 - \cos \phi) \quad (1.28)$$

If we cut the spherical particle along the contact line, we obtain two spherical caps. The spherical cap adjacent to the bound membrane segment has the volume

$$V_{bo} = \frac{4\pi}{3} R_{pa}^3 (2 + \cos \phi) \sin^4 \frac{\phi}{2} \quad (1.29)$$

Furthermore, the combined bending and adhesion energy of the bound membrane segment is given by

$$E_{bo} = [4\pi\kappa(1 \pm mR_{pa})^2 - 2\pi|W|R_{pa}^2] (1 - \cos \phi) \quad (1.30)$$

where the plus and minus signs apply to engulfment of particles that originate from the exterior and interior of the vesicle, respectively.

There are in this case four unknown parameters, ΔP , Σ , u_0 and s^* , that are used to satisfy the four boundary conditions that enforce the area and volume constraints as well as the smooth matching,

$$\begin{aligned} \psi(s^*) &= \pi \pm \phi \\ x(s^*) &= R_{pa} \sin \phi \\ A(s^*) &= A - A_{bo} \\ V(s^*) &= V \pm V_{bo} \end{aligned} \quad (1.31)$$

where again the plus and minus signs apply to engulfment of particles that originate from the exterior and interior of the vesicle, respectively. As before, all that remains is to numerically integrate eqs (1.22) and (1.24), with the initial conditions in eqs (1.23) and (1.25), while searching for the values of Σ , ΔP , u_0 and s^* that satisfy the boundary conditions in (1.31).

A given shape will be determined by four dimensionless parameters: the reduced volume v , the reduced spontaneous curvature mR_{ve} , the reduced particle radius R_{pa}/R_{ve} and the wrapping angle ϕ . By repeating this procedure for different values of ϕ in the range $0 \leq \phi \leq \pi$, while keeping the other parameters fixed, we can obtain the bending energy of the unbound segment $E_{un}(\phi)$ along the reaction coordinate of the engulfment process.

Taking the bending energy $E_{un}(\phi)$ of the unbound segment together with the bending and adhesion energies of the bound segment as given by (1.30), we obtain an energy landscape for engulfment $E(\phi) \equiv E_{un}(\phi) + E_{bo}(\phi)$. The energy landscapes for engulfment will thus depend on four dimensionless parameters: the reduced volume v , the reduced spontaneous curvature mR_{ve} , the reduced particle radius R_{pa}/R_{ve} , and the reduced adhesive strength $|W|R_{pa}^2/\kappa$.

1.7 References for the Introduction

- [1] G. van Meer, D. R. Voelker, and G. W. Feigenson, "Membrane lipids: where they are and how they behave," *Nat. Rev. Mol. Cell Biol.*, vol. 9, no. 2, pp. 112–124, 2008.
- [2] M. Ikeda, A. Kihara, and Y. Igarashi, "Lipid asymmetry of the eukaryotic plasma membrane: functions and related enzymes," *Biol. Pharm. Bull.*, vol. 29, no. 8, pp. 1542–1546, 2006.
- [3] B. Fadeel and D. Xue, "The ins and outs of phospholipid asymmetry in the plasma membrane: roles in health and disease," *Crit. Rev. Biochem. Mol. Biol.*, vol. 44, no. 5, pp. 264–77, 2009.
- [4] D. Raucher and M. P. Sheetz, "Cell spreading and lamellipodial extension rate is regulated by membrane tension," *J. Cell Biol.*, vol. 148, pp. 127–136, jan 2000.
- [5] R. A. Green, E. Paluch, and K. Oegema, "Cytokinesis in animal cells," *Annu. Rev. Cell Dev. Biol.*, vol. 28, pp. 29–58, jan 2012.
- [6] N. C. Gauthier, T. A. Masters, and M. P. Sheetz, "Mechanical feedback between membrane tension and dynamics," *Trends Cell Biol.*, vol. 22, pp. 527–35, oct 2012.
- [7] J. Panyam and V. Labhasetwar, "Biodegradable nanoparticles for drug and gene delivery to cells and tissue," *Adv. Drug Deliv. Rev.*, vol. 55, pp. 329–347, feb 2003.
- [8] R. Singh and J. W. Lillard, "Nanoparticle-based targeted drug delivery," *Exp. Mol. Pathol.*, vol. 86, pp. 215–23, jun 2009.
- [9] G. F. Paciotti, L. Myer, D. Weinreich, D. Goia, N. Pavel, R. E. McLaughlin, and L. Tamarkin, "Colloidal gold: a novel nanoparticle vector for tumor directed drug delivery," *Drug Deliv.*, vol. 11, pp. 169–83, jan 2004.

- [10] K. Cho, X. Wang, S. Nie, Z. G. Chen, and D. M. Shin, "Therapeutic nanoparticles for drug delivery in cancer," *Clin. Cancer Res.*, vol. 14, pp. 1310–6, mar 2008.
- [11] J. Kreuter, "Nanoparticulate systems for brain delivery of drugs," *Adv. Drug Deliv. Rev.*, vol. 47, pp. 65–81, mar 2001.
- [12] P. R. Lockman, R. J. Mumper, M. A. Khan, and D. D. Allen, "Nanoparticle technology for drug delivery across the blood-brain barrier," *Drug Dev. Ind. Pharm.*, vol. 28, pp. 1–13, feb 2002.
- [13] J.-H. Lee, Y.-M. Huh, Y.-w. Jun, J.-w. Seo, J.-t. Jang, H.-T. Song, S. Kim, E.-J. Cho, H.-G. Yoon, J.-S. Suh, and J. Cheon, "Artificially engineered magnetic nanoparticles for ultra-sensitive molecular imaging," *Nat. Med.*, vol. 13, pp. 95–9, jan 2007.
- [14] C. Sun, J. S. H. Lee, and M. Zhang, "Magnetic nanoparticles in MR imaging and drug delivery," *Adv. Drug Deliv. Rev.*, vol. 60, pp. 1252–1265, aug 2008.
- [15] X. Huang, I. H. El-Sayed, W. Qian, and M. A. El-Sayed, "Cancer cell imaging and photothermal therapy in the near-infrared region by using gold nanorods," *J. Am. Chem. Soc.*, vol. 128, pp. 2115–20, feb 2006.
- [16] J. F. Hainfeld, D. N. Slatkin, T. M. Focella, and H. M. Smilowitz, "Gold nanoparticles: a new X-ray contrast agent," *Br. J. Radiol.*, vol. 79, pp. 248–253, mar 2006.
- [17] N. Lewinski, V. Colvin, and R. Drezek, "Cytotoxicity of nanoparticles," *Small*, vol. 4, no. 1, pp. 26–49, 2008.
- [18] K. Schmid and M. Riediker, "Use of nanoparticles in swiss industry: a targeted survey," *Environ. Sci. Technol.*, vol. 42, no. 7, pp. 2253–2260, 2008.
- [19] H. C. Fischer and W. C. W. Chan, "Nanotoxicity: the growing need for in vivo study," *Curr. Opin. Biotechnol.*, vol. 18, no. 6, pp. 565–571, 2007.
- [20] Y. Pan, S. Neuss, A. Leifert, M. Fischler, F. Wen, U. Simon, G. Schmid, W. Brandau, and W. Jahnke-Dechent, "Size-dependent cytotoxicity of gold nanoparticles," *Small*, vol. 3, no. 11, pp. 1941–1949, 2007.
- [21] J. Mercer, M. Schelhaas, and A. Helenius, "Virus entry by endocytosis," *Annu. Rev. Biochem.*, vol. 79, pp. 803–33, jan 2010.
- [22] S. Mukherjee, R. N. Ghosh, and F. R. Maxfield, "Endocytosis," *Physiol. Rev.*, vol. 77, no. 3, pp. 759–803, 1997.
- [23] G. Sahay, D. Y. Alakhova, and A. V. Kabanov, "Endocytosis of nanomedicines," *J. Control. Release*, vol. 145, no. 3, pp. 182–195, 2010.
- [24] B. J. Peter, H. M. Kent, I. G. Mills, Y. Vallis, P. J. G. Butler, P. R. Evans, and H. T. McMahon, "BAR domains as sensors of membrane curvature: the amphiphysin BAR structure," *Science*, vol. 303, no. 5657, pp. 495–499, 2004.

- [25] K. Takei, V. I. Slepnev, V. Haucke, and P. De Camilli, “Functional partnership between amphiphysin and dynamin in clathrin-mediated endocytosis,” *Nat. Cell Biol.*, vol. 1, pp. 33–39, 1999.
- [26] K. Farsad, N. Ringstad, K. Takei, S. R. Floyd, K. Rose, and P. De Camilli, “Generation of high curvature membranes mediated by direct endophilin bilayer interactions,” *J. Cell Biol.*, vol. 155, no. 2, pp. 193–200, 2001.
- [27] Q. Wang, M. V. A. S. Navarro, G. Peng, E. Molinelli, S. L. Goh, B. L. Judson, K. R. Rajashankar, and H. Sondermann, “Molecular mechanism of membrane constriction and tubulation mediated by the F-BAR protein Pacsin/Syndapin,” *Proc. Natl. Acad. Sci. U. S. A.*, vol. 106, no. 31, pp. 12700–12705, 2009.
- [28] M. G. J. Ford, I. G. Mills, B. J. Peter, Y. Vallis, G. J. K. Praefcke, P. R. Evans, and H. T. McMahon, “Curvature of clathrin-coated pits driven by epsin,” *Nature*, vol. 419, no. 6905, pp. 361–366, 2002.
- [29] Y. Li, R. Lipowsky, and R. Dimova, “Membrane nanotubes induced by aqueous phase separation and stabilized by spontaneous curvature,” *Proc. Natl. Acad. Sci. U. S. A.*, vol. 108, pp. 4731–6, mar 2011.
- [30] R. Dimova and R. Lipowsky, “Lipid membranes in contact with aqueous phases of polymer solutions,” *Soft Matter*, vol. 8, no. 24, p. 6409, 2012.
- [31] R. Lipowsky, “Spontaneous tubulation of membranes and vesicles reveals membrane tension generated by spontaneous curvature,” *Faraday Discuss.*, vol. 161, pp. 305–331, 2013.
- [32] O. Le Bihan, P. Bonnafous, L. Marak, T. Bickel, S. Trépout, S. Mornet, F. De Haas, H. Talbot, J.-C. Taveau, and O. Lambert, “Cryo-electron tomography of nanoparticle transmigration into liposome,” *J. Struct. Biol.*, vol. 168, pp. 419–25, dec 2009.
- [33] R. Michel, E. Kesselman, T. Plostica, D. Danino, and M. Gradzielski, “Internalization of silica nanoparticles into fluid liposomes: formation of interesting hybrid colloids,” *Angew. Chemie Int. Ed.*, vol. 53, pp. 12441–12445, sep 2014.
- [34] C. Dietrich, M. Angelova, and B. Pouligny, “Adhesion of latex spheres to giant phospholipid vesicles: statics and dynamics,” *J. Phys. II*, vol. 7, pp. 1651–1682, nov 1997.
- [35] A. Fery, S. Moya, P. H. Puech, F. Brochard-Wyart, and H. Mohwald, “Interaction of polyelectrolyte coated beads with phospholipid vesicles,” *C. R. Phys.*, vol. 4, pp. 259–264, mar 2003.
- [36] A. Meinel, B. Tränkle, W. Römer, and A. Rohrbach, “Induced phagocytic particle uptake into a giant unilamellar vesicle,” *Soft Matter*, vol. 10, pp. 3667–78, may 2014.

- [37] I. Koltover, J. O. Rädler, and C. Safinya, “Membrane mediated attraction and ordered aggregation of colloidal particles bound to giant phospholipid vesicles,” *Phys. Rev. Lett.*, vol. 82, pp. 1991–1994, mar 1999.
- [38] C. Luccardini, C. Tribet, F. Vial, V. Marchi-Artzner, and M. Dahan, “Size, charge, and interactions with giant lipid vesicles of quantum dots coated with an amphiphilic macromolecule,” *Langmuir*, vol. 22, no. 5, pp. 2304–2310, 2006.
- [39] F. G. Strobl, F. Seitz, C. Westerhausen, A. Reller, A. A. Torrano, C. Bräuchle, A. Wixforth, and M. F. Schneider, “Intake of silica nanoparticles by Giant Lipid Vesicles: influence of particle size and thermodynamic membrane state,” *Beilstein J. Nanotechnol.*, vol. 5, pp. 2468–2478, 2014.
- [40] X. Wei, W. Jiang, J. Yu, L. Ding, J. Hu, and G. Jiang, “Effects of SiO₂ nanoparticles on phospholipid membrane integrity and fluidity,” *J. Hazard. Mater.*, vol. 287, pp. 217–224, 2015.
- [41] S. Li and N. Malmstadt, “Deformation and poration of lipid bilayer membranes by cationic nanoparticles,” *Soft Matter*, vol. 9, no. 20, p. 4969, 2013.
- [42] M. Laurencin, T. Georgelin, B. Malezieux, J. M. Siaugue, and C. Ménager, “Interactions between giant unilamellar vesicles and charged core-shell magnetic nanoparticles,” *Langmuir*, vol. 26, no. 20, pp. 16025–16030, 2010.
- [43] K. Jaskiewicz, A. Larsen, D. Schaeffel, K. Koynov, I. Lieberwirth, G. Fytas, K. Landfester, and A. Kroeger, “Incorporation of nanoparticles into polymersomes: size and concentration effects,” *ACS Nano*, vol. 6, pp. 7254–7262, aug 2012.
- [44] F. C. Neidhardt, ed., *Escherichia coli and Salmonella: cellular and molecular biology (Vol 1)*. ASM Press, 1 ed., 1996.
- [45] D. Cevc and G. Marsh, *Phospholipid bilayers: physical principles and models*. Wiley-Interscience, 1987.
- [46] J. Israelachvili, *Intermolecular and surface forces*. Academic Press, 3 ed., 2010.
- [47] W. Helfrich, “Elastic properties of lipid bilayers: theory and possible experiments,” *Z. Naturforsch. C.*, vol. 28, no. 11, pp. 693–703, 1973.
- [48] R. Goetz and R. Lipowsky, “Computer simulations of bilayer membranes: self-assembly and interfacial tension,” *J. Chem. Phys.*, vol. 108, no. 17, pp. 7397–7409, 1998.
- [49] R. Homan and H. J. Pownall, “Transbilayer diffusion of phospholipids: dependence on headgroup structure and acyl chain length,” *Biochim. Biophys. Acta*, vol. 938, pp. 155–66, feb 1988.
- [50] J. M. Backer and E. A. Dawidowicz, “Transmembrane movement of cholesterol in small unilamellar vesicles detected by cholesterol oxidase,” *J. Biol. Chem.*, vol. 256, pp. 586–588, jan 1981.

- [51] E. J. Shimshick and H. M. McConnell, “Lateral phase separation in phospholipid membranes,” *Biochemistry*, vol. 12, pp. 2351–2360, jun 1973.
- [52] S. L. Veatch and S. L. Keller, “Separation of liquid phases in giant vesicles of ternary mixtures of phospholipids and cholesterol,” *Biophys. J.*, vol. 85, no. 5, pp. 3074–3083, 2003.
- [53] O. G. Mouritsen, “The liquid-ordered state comes of age,” *Biochim. Biophys. Acta*, vol. 1798, pp. 1286–1288, 2010.
- [54] D. Marsh, “Liquid-ordered phases induced by cholesterol: a compendium of binary phase diagrams,” *Biochemistry*, vol. 1798, no. 3, pp. 688–699, 2010.
- [55] E. Gouaux and R. Mackinnon, “Principles of selective ion transport in channels and pumps,” *Science*, vol. 310, pp. 1461–5, dec 2005.
- [56] H. T. McMahon and J. L. Gallop, “Membrane curvature and mechanisms of dynamic cell membrane remodelling,” *Nature*, vol. 438, pp. 590–6, dec 2005.
- [57] S. J. Singer and G. L. Nicolson, “The fluid mosaic model of the structure of cell membranes,” *Science*, vol. 175, no. 4023, pp. 720–731, 1972.
- [58] J. Pietzsch, “Mind the membrane,” *Nature*, vol. Horizon Sy, pp. 1–4, 2004.
- [59] G. Guidotti, “Membrane proteins,” *Annu. Rev. Biochem.*, vol. 41, pp. 731–752, 1972.
- [60] L. Figard and A. M. Sokac, “A membrane reservoir at the cell surface: unfolding the plasma membrane to fuel cell shape change,” *Bioarchitecture*, vol. 4, no. 2, pp. 39–46, 2014.
- [61] J. Lam, M. Herant, M. Dembo, and V. Heinrich, “Baseline mechanical characterization of J774 macrophages,” *Biophys. J.*, vol. 96, no. 1, pp. 248–254, 2009.
- [62] I. Mellman, R. Fuchs, and A. Helenius, “Acidification of the endocytic and exocytic pathways,” *Annu. Rev. Biochem.*, vol. 55, pp. 663–700, 1986.
- [63] J. Zimmerberg and M. M. Kozlov, “How proteins produce cellular membrane curvature,” *Nat. Rev. Mol. Cell Biol.*, vol. 7, pp. 9–19, jan 2006.
- [64] U. Seifert, K. Berndl, and R. Lipowsky, “Shape transformations of vesicles: phase diagram for spontaneous-curvature and bilayer-coupling models,” *Phys. Rev. A*, vol. 44, no. 2, pp. 1182–1202, 1991.
- [65] U. Seifert and R. Lipowsky, “Morphology of vesicles,” in *Handb. Biol. Phys.* (R. Lipowsky and E. Sackmann, eds.), vol. 1, ch. 8, pp. 403–463, Elsevier Science, 1995.
- [66] L. Miao, U. Seifert, M. Wortis, and H.-G. Döbereiner, “Budding transitions of fluid-bilayer vesicles: the effect of area-difference elasticity,” *Phys. Rev. E*, vol. 49, pp. 5389–5407, jun 1994.

- [67] U. Seifert, “Configurations of fluid membranes and vesicles,” *Adv. Phys.*, vol. 46, pp. 13–137, feb 1997.
- [68] W. Rawicz, K. C. Olbrich, T. McIntosh, D. Needham, and E. Evans, “Effect of chain length and unsaturation on elasticity of lipid bilayers,” *Biophys. J.*, vol. 79, pp. 328–39, jul 2000.
- [69] M. P. do Carmo, *Differential geometry of curves and surfaces*. Prentice-Hall, 1976.
- [70] O.-Y. Zhong-can and W. Helfrich, “Instability and deformation of a spherical vesicle by pressure,” *Phys. Rev. Lett.*, vol. 59, pp. 2486–2488, nov 1987.
- [71] R. Lipowsky, “Coupling of bending and stretching deformations in vesicle membranes,” *Adv. Colloid Interface Sci.*, vol. 208, pp. 14–24, jun 2014.
- [72] J. Käs and E. Sackmann, “Shape transitions and shape stability of giant phospholipid vesicles in pure water induced by area-to-volume changes,” *Biophys. J.*, vol. 60, no. 4, pp. 825–44, 1991.
- [73] B. Fourcade, L. Miao, M. Rao, M. Wortis, and R. Zia, “Scaling analysis of narrow necks in curvature models of fluid lipid-bilayer vesicles,” *Phys. Rev. E*, vol. 49, pp. 5276–86, jun 1994.
- [74] R. Lipowsky, “Budding of membranes induced by intramembrane domains,” *J. Phys. II*, vol. 2, no. 10, pp. 1825–1840, 1992.
- [75] T. Baumgart, S. T. Hess, and W. W. Webb, “Imaging coexisting fluid domains in biomembrane models coupling curvature and line tension,” *Nature*, vol. 425, no. 6960, pp. 821–824, 2003.
- [76] F. Jülicher and R. Lipowsky, “Domain-induced budding of vesicles,” *Phys. Rev. Lett.*, vol. 70, pp. 2964–2967, may 1993.
- [77] F. Jülicher and R. Lipowsky, “Shape transformations of vesicles with intramembrane domains,” *Phys. Rev. E*, vol. 53, pp. 2670–2683, mar 1996.
- [78] J. Zimmerberg, “Molecular mechanisms of membrane fusion: steps during phospholipid and exocytotic membrane fusion,” *Biosci. Rep.*, vol. 7, pp. 251–268, apr 1987.
- [79] U. Seifert and R. Lipowsky, “Adhesion of vesicles,” *Phys. Rev. A*, vol. 42, no. 8, pp. 4768–4771, 1990.
- [80] H. W. Kroto, J. R. Heath, S. C. O’Brien, R. F. Curl, and R. E. Smalley, “C60: Buckminsterfullerene,” *Nature*, vol. 318, pp. 162–163, nov 1985.
- [81] A. P. Alivisatos, “Semiconductor clusters, nanocrystals and quantum dots,” *Science*, vol. 271, no. 5251, pp. 933–937, 1996.
- [82] M. Rai, A. Yadav, and A. Gade, “Silver nanoparticles as a new generation of antimicrobials,” *Biotechnol. Adv.*, vol. 27, pp. 76–83, jan 2009.

- [83] M. C. Daniel and D. Astruc, “Gold nanoparticles: assembly, supramolecular chemistry, quantum-size-related properties, and applications toward biology, catalysis, and nanotechnology,” *Chem. Rev.*, vol. 104, no. 1, pp. 293–346, 2004.
- [84] I. I. Slowing, J. L. Vivero-Escoto, C.-W. Wu, and V. S.-Y. Lin, “Mesoporous silica nanoparticles as controlled release drug delivery and gene transfection carriers,” *Adv. Drug Deliv. Rev.*, vol. 60, pp. 1278–88, aug 2008.
- [85] A. Albanese, P. S. Tang, and W. C. W. Chan, “The effect of nanoparticle size, shape, and surface chemistry on biological systems,” *Annu. Rev. Biomed. Eng.*, vol. 14, no. 1, pp. 1–16, 2012.
- [86] L. A. Dykman and N. G. Khlebtsov, “Uptake of engineered gold nanoparticles into mammalian cells,” *Chem. Rev.*, vol. 114, pp. 1258–88, jan 2014.
- [87] T. W. Odom, J.-L. Huang, P. Kim, and C. M. Lieber, “Atomic structure and electronic properties of single-walled carbon nanotubes,” *Nature*, vol. 391, pp. 62–64, jan 1998.
- [88] N. R. Jana, L. Gearheart, and C. J. Murphy, “Wet chemical synthesis of high aspect ratio cylindrical gold nanorods,” *J. Phys. Chem. B*, vol. 105, pp. 4065–4067, may 2001.
- [89] A. Verma and F. Stellacci, “Effect of surface properties on nanoparticle-cell interactions,” *Small*, vol. 6, pp. 12–21, jan 2010.
- [90] B. Różycki and R. Lipowsky, “Spontaneous curvature of bilayer membranes from molecular simulations: asymmetric lipid densities and asymmetric adsorption,” *J. Chem. Phys.*, vol. 142, p. 054101, feb 2015.
- [91] E. M. Curtis, A. H. Bahrami, T. R. Weigl, and C. K. Hall, “Modeling nanoparticle wrapping or translocation in bilayer membranes,” *Nanoscale*, vol. 7, pp. 14505–14514, 2015.
- [92] R. Lipowsky and H.-G. Döbereiner, “Vesicles in contact with nanoparticles and colloids,” *Europhys. Lett.*, vol. 43, no. 2, pp. 219–225, 1998.
- [93] H. Noguchi and M. Takasu, “Adhesion of nanoparticles to vesicles: a Brownian dynamics simulation,” *Biophys. J.*, vol. 83, pp. 299–308, jul 2002.
- [94] J. Wong-Ekkabut, S. Baoukina, W. Triampo, I.-M. Tang, D. P. Tieleman, and L. Monticelli, “Computer simulation study of fullerene translocation through lipid membranes,” *Nat. Nanotechnol.*, vol. 3, no. 6, pp. 363–368, 2008.
- [95] R. S. G. D’Rozario, C. L. Wee, E. J. Wallace, and M. S. P. Sansom, “The interaction of C60 and its derivatives with a lipid bilayer via molecular dynamics simulations,” *Nanotechnology*, vol. 20, no. 11, p. 115102, 2009.

- [96] M. Schulz, A. Olubummo, and W. H. Binder, “Beyond the lipid-bilayer: interaction of polymers and nanoparticles with membranes,” *Soft Matter*, vol. 8, no. 18, p. 4849, 2012.
- [97] G. Gopalakrishnan, C. Danelon, P. Izewska, M. Prummer, P. Y. Bolinger, I. Geissbühler, D. Demurtas, J. Dubochet, and H. Vogel, “Multifunctional lipid/quantum dot hybrid nanocontainers for controlled targeting of live cells,” *Angew. Chemie Int. Ed.*, vol. 45, no. 33, pp. 5478–5483, 2006.
- [98] G. D. Bothun, “Hydrophobic silver nanoparticles trapped in lipid bilayers: Size distribution, bilayer phase behavior, and optical properties,” *J. Nanobiotechnology*, vol. 6, no. 13, pp. 1–10, 2008.
- [99] M. R. Rasch, E. Rossinyol, J. L. Hueso, B. W. Goodfellow, J. Arbiol, and B. A. Korgel, “Hydrophobic gold nanoparticle self-assembly with phosphatidylcholine lipid: membrane-loaded and Janus vesicles,” *Nano Lett.*, vol. 10, no. 9, pp. 3733–3739, 2010.
- [100] Y. Chen, A. Bose, and G. D. Bothun, “Controlled release from bilayer-decorated magnetoliposomes via electromagnetic heating,” *ACS Nano*, vol. 4, no. 6, pp. 3215–3221, 2010.
- [101] Y. Mai and A. Eisenberg, “Controlled incorporation of particles into the central portion of vesicle walls,” *J. Am. Chem. Soc.*, vol. 132, pp. 10078–84, jul 2010.
- [102] J. Liu, N. Lu, J. Li, Y. Weng, B. Yuan, K. Yang, and Y. Ma, “Influence of surface chemistry on particle internalization into giant unilamellar vesicles,” *Langmuir*, vol. 29, no. 25, pp. 8039–45, 2013.
- [103] Y. Li, X. Chen, and N. Gu, “Computational investigation of interaction between nanoparticles and membranes: hydrophobic/hydrophilic effect,” *J. Phys. Chem. B*, vol. 112, no. 51, pp. 16647–53, 2008.
- [104] K. Yang and Y.-Q. Ma, “Computer simulation of the translocation of nanoparticles with different shapes across a lipid bilayer,” *Nat. Nanotechnol.*, vol. 5, no. 8, pp. 579–583, 2010.
- [105] K. A. Smith, D. Jasnow, and A. C. Balazs, “Designing synthetic vesicles that engulf nanoscopic particles,” *J. Chem. Phys.*, vol. 127, p. 084703, aug 2007.
- [106] J. Yu, S. A. Patel, and R. M. Dickson, “In vitro and intracellular production of peptide-encapsulated fluorescent silver nanoclusters,” *Angew. Chemie Int. Ed.*, vol. 46, no. 12, pp. 2028–2030, 2007.
- [107] P. R. Leroueil, S. Hong, A. Mecke, J. R. Baker, B. G. Orr, and M. M. B. Holl, “Nanoparticle interaction with biological membranes: does nanotechnology present a Janus face?,” *Acc. Chem. Res.*, vol. 40, no. 5, pp. 335–342, 2007.

- [108] K. Kostarelos, L. Lacerda, G. Pastorin, W. Wu, S. Wieckowski, J. Luangsivilay, S. Godefroy, D. Pantarotto, J.-P. Briand, S. Muller, M. Prato, and A. Bianco, “Cellular uptake of functionalized carbon nanotubes is independent of functional group and cell type,” *Nat. Nanotechnol.*, vol. 2, no. 2, pp. 108–113, 2007.
- [109] A. Verma, O. Uzun, Y. Hu, Y. Hu, H.-S. Han, N. Watson, S. Chen, D. J. Irvine, and F. Stellacci, “Surface-structure-regulated cell-membrane penetration by monolayer-protected nanoparticles,” *Nat. Mater.*, vol. 7, no. 7, pp. 588–595, 2008.
- [110] E. J. Wallace and M. S. P. Sansom, “Blocking of carbon nanotube based nanoinjectors by lipids: a simulation study,” *Nano Lett.*, vol. 8, no. 9, pp. 2751–6, 2008.
- [111] J. Lovrić, H. S. Bazzi, Y. Cuie, G. R. A. Fortin, F. M. Winnik, and D. Maysinger, “Differences in subcellular distribution and toxicity of green and red emitting CdTe quantum dots,” *J. Mol. Med.*, vol. 83, no. 5, pp. 377–385, 2005.
- [112] J. Lin, H. Zhang, Z. Chen, and Y. Zheng, “Penetration of lipid membranes by gold nanoparticles: insights into cellular uptake, cytotoxicity, and their relationship,” *ACS Nano*, vol. 4, no. 9, pp. 5421–5429, 2010.
- [113] Y. Roiter, M. Ornatska, A. R. Rammohan, J. Balakrishnan, D. R. Heine, and S. Minko, “Interaction of nanoparticles with lipid membrane.,” *Nano Lett.*, vol. 8, pp. 941–4, mar 2008.
- [114] A. H. Bahrami, M. Raatz, J. Agudo-Canalejo, R. Michel, E. M. Curtis, C. K. Hall, M. Gradzielski, R. Lipowsky, and T. R. Weigl, “Wrapping of nanoparticles by membranes,” *Adv. Colloid Interface Sci.*, vol. 208, pp. 214–224, jun 2014.
- [115] W. T. Gózdź, “Deformations of lipid vesicles induced by attached spherical particles,” *Langmuir*, vol. 23, pp. 5665–5669, may 2007.
- [116] S. Cao, G. Wei, and J. Z. Y. Chen, “Transformation of an oblate-shaped vesicle induced by an adhering spherical particle,” *Phys. Rev. E*, vol. 84, p. 050901, nov 2011.
- [117] M. Deserno, “Elastic deformation of a fluid membrane upon colloid binding,” *Phys. Rev. E*, vol. 69, p. 031903, mar 2004.
- [118] A. H. Bahrami, “Orientational changes and impaired internalization of ellipsoidal nanoparticles by vesicle membranes,” *Soft Matter*, vol. 9, p. 8642, aug 2013.
- [119] S. Dasgupta, T. Auth, and G. Gompper, “Wrapping of ellipsoidal nano-particles by fluid membranes,” *Soft Matter*, vol. 9, p. 5473, may 2013.
- [120] C. Huang, Y. Zhang, H. Yuan, H. Gao, and S. Zhang, “Role of nanoparticle geometry in endocytosis: Laying down to stand up,” *Nano Lett.*, vol. 13, pp. 4546–4550, sep 2013.

- [121] S. Dasgupta, T. Auth, and G. Gompper, “Shape and orientation matter for the cellular uptake of nonspherical particles,” *Nano Lett.*, vol. 14, pp. 687–693, feb 2014.
- [122] S. Dasgupta, T. Auth, N. S. Gov, T. J. Satchwell, E. Hanssen, E. S. Zuccala, D. T. Riglar, A. M. Toye, T. Betz, J. Baum, and G. Gompper, “Membrane-wrapping contributions to malaria parasite invasion of the human erythrocyte,” *Biophys. J.*, vol. 107, pp. 43–54, jul 2014.
- [123] X. Yi, X. Shi, and H. Gao, “A universal law for cell uptake of one-dimensional nanomaterials,” *Nano Lett.*, vol. 14, no. 2, pp. 1049–1055, 2014.
- [124] X. Yi, X. Shi, and H. Gao, “Cellular uptake of elastic nanoparticles,” *Phys. Rev. Lett.*, vol. 107, p. 098101, aug 2011.
- [125] X. Yi and H. Gao, “Phase diagrams and morphological evolution in wrapping of rod-shaped elastic nanoparticles by cell membrane: a two-dimensional study,” *Phys. Rev. E*, vol. 89, p. 062712, jun 2014.
- [126] X. Yi and H. Gao, “Cell membrane wrapping of a spherical thin elastic shell,” *Soft Matter*, vol. 11, no. 6, pp. 1107–1115, 2015.
- [127] H. Kusumaatmaja and R. Lipowsky, “Droplet-induced budding transitions of membranes,” *Soft Matter*, vol. 7, no. 15, pp. 6914–6919, 2011.
- [128] A. H. Bahrami, R. Lipowsky, and T. R. Weigl, “Tubulation and aggregation of spherical nanoparticles adsorbed on vesicles,” *Phys. Rev. Lett.*, vol. 109, p. 188102, oct 2012.
- [129] A. Šarić and A. Cacciuto, “Mechanism of membrane tube formation induced by adhesive nanocomponents,” *Phys. Rev. Lett.*, vol. 109, p. 188101, oct 2012.
- [130] M. Raatz, R. Lipowsky, and T. R. Weigl, “Cooperative wrapping of nanoparticles by membrane tubes,” *Soft Matter*, vol. 10, pp. 3570–7, mar 2014.
- [131] B. D. Chithrani, A. A. Ghazani, and W. C. W. Chan, “Determining the size and shape dependence of gold nanoparticle uptake into mammalian cells,” *Nano Lett.*, vol. 6, pp. 662–8, apr 2006.
- [132] B. D. Chithrani and W. C. W. Chan, “Elucidating the mechanism of cellular uptake and removal of protein-coated gold nanoparticles of different sizes and shapes,” *Nano Lett.*, vol. 7, no. 6, pp. 1542–50, 2007.
- [133] T. Nakai, T. Kanamori, S. Sando, and Y. Aoyama, “Remarkably size-regulated cell invasion by artificial viruses. Saccharide-dependent self-aggregation of glycoviruses and its consequences in glycoviral gene delivery,” *J. Am. Chem. Soc.*, vol. 125, no. 28, pp. 8465–8475, 2003.

- [134] F. Osaki, T. Kanamori, S. Sando, T. Sera, and Y. Aoyama, “A quantum dot conjugated sugar ball and its cellular uptake. On the size effects of endocytosis in the subviral region,” *J. Am. Chem. Soc.*, vol. 126, no. 21, pp. 6520–6521, 2004.
- [135] H. Gao, W. Shi, and L. B. Freund, “Mechanics of receptor-mediated endocytosis,” *Proc. Natl. Acad. Sci. U. S. A.*, vol. 102, pp. 9469–74, jul 2005.
- [136] G. Bao and X. R. Bao, “Shedding light on the dynamics of endocytosis and viral budding,” *Proc. Natl. Acad. Sci. U. S. A.*, vol. 102, pp. 9997–8, jul 2005.
- [137] P. Decuzzi and M. Ferrari, “The role of specific and non-specific interactions in receptor-mediated endocytosis of nanoparticles,” *Biomaterials*, vol. 28, pp. 2915–22, jun 2007.
- [138] S. Zhang, J. Li, G. Lykotrafitis, G. Bao, and S. Suresh, “Size-dependent endocytosis of nanoparticles,” *Adv. Mater.*, vol. 21, pp. 419–424, jan 2009.
- [139] H. Yuan, J. Li, G. Bao, and S. Zhang, “Variable nanoparticle-cell adhesion strength regulates cellular uptake,” *Phys. Rev. Lett.*, vol. 105, p. 138101, sep 2010.
- [140] A. Chaudhuri, G. Battaglia, and R. Golestanian, “The effect of interactions on the cellular uptake of nanoparticles,” *Phys. Biol.*, vol. 8, p. 046002, aug 2011.
- [141] X. Li, “Size and shape effects on receptor-mediated endocytosis of nanoparticles,” *J. Appl. Phys.*, vol. 111, p. 024702, jan 2012.
- [142] C. R. Miller, B. Bondurant, S. D. McLean, K. A. McGovern, and D. F. O’Brien, “Liposome-cell interactions in vitro: effect of liposome surface charge on the binding and endocytosis of conventional and sterically stabilized liposomes,” *Biochemistry*, vol. 37, no. 37, pp. 12875–12883, 1998.
- [143] K. Yin Win and S.-S. Feng, “Effects of particle size and surface coating on cellular uptake of polymeric nanoparticles for oral delivery of anticancer drugs,” *Biomaterials*, vol. 26, no. 15, pp. 2713–2722, 2005.
- [144] J. Wang, D. Mongayt, and V. Torchilin, “Polymeric micelles for delivery of poorly soluble drugs: preparation and anticancer activity in vitro of paclitaxel incorporated into mixed micelles based on poly(ethylene glycol)-lipid conjugate and positively charged lipids,” *J. Drug Target.*, vol. 13, no. 1, pp. 73–80, 2005.
- [145] F. R. Maxfield and T. E. McGraw, “Endocytic recycling,” *Nat. Rev. Mol. Cell Biol.*, vol. 5, pp. 121–32, feb 2004.
- [146] D. K. Cureton, C. E. Harbison, E. Cocucci, C. R. Parrish, and T. Kirchhausen, “Limited transferrin receptor clustering allows rapid diffusion of canine parvovirus into clathrin endocytic structures,” *J. Virol.*, vol. 86, no. 9, pp. 5330–5340, 2012.

2 Patterns of Flexible Nanotubes Formed by Liquid-Ordered and Liquid-Disordered Membranes

2.1 Overview

In this paper, we set out to understand the formation of nanotubes in Giant Unilamellar Vesicles that enclose aqueous two-phase solutions of PEG and dextran polymers, as introduced in Section 1.4 of this thesis. My contributions as a co-author were to

- Elucidate the formation of multiple nanotubes in terms of two competing pathways upon deflation: a pathway of slow lipid flow through membrane necks that leads to the nucleation of new buds *via* an oblate-stomatocyte bifurcation; and a pathway of fast lipid flow through the necks that leads to the growth of pre-existing buds. See ‘Nucleation and Growth of Necklace-like Tubes’ in the main text.
- Study, using numerical energy minimization as described in Section 1.6 of this thesis, the growth of single buds into necklace-like nanotubes, obtaining an energy landscape of tube formation as a function of the reduced volume of the vesicle. See ‘Nucleation and Growth of Necklace-like Tubes’ and Figure 5 in the Main Text.
- Study the pathway of transformation of necklace-like tubes into cylindrical tubes *via* intermediate unduloids, showing that the mean curvature increases monotonically for given tube area and length, or conversely, that tube length increases monotonically for given mean curvature and tube area. See ‘Necklace–Cylinder Coexistence and Critical Tube Length’ and Figure 7 in the Main Text, as well as Figure S5 in the Supporting Information.
- Calculate the critical tube length at which necklace-like tubes transform into cylindrical tubes for VM-C morphologies, by considering the energetics of nanotubes adhering to a liquid-liquid interface. See ‘Necklace–Cylinder Coexistence and Critical Tube Length’ in the Main Text, as well as Section S2 and Figure S4 in the Supporting Information

As a consequence of this work, we have expanded the previously-known theoretical phase diagram of the shapes of free vesicles, see Figure 1.6 in Section 1.3.3.1 of this thesis, to the region of very large spontaneous curvatures. We show that, in a deflation trajectory,

spherical buds form first, later growing into necklace-like tubes that finally transform into cylindrical tubes *via* a novel transition when they reach a certain critical length. The increased theoretical understanding of the nanotube shapes allows us to deduce the spontaneous curvature of the membrane by image analysis of either (i) the tube radius or (ii) the total length and area of the tubes. We also obtain a better understanding of the formation and morphology of area reservoirs in model systems such as lipid or polymer vesicles, that can mimic those present in biological cells.



Patterns of Flexible Nanotubes Formed by Liquid-Ordered and Liquid-Disordered Membranes

Yonggang Liu,^{†,‡} Jaime Agudo-Canalejo,[†] Andrea Grafmüller,[†] Rumiana Dimova,[†] and Reinhard Lipowsky^{*,†}

[†]Theory & Biosystems, Max Planck Institute of Colloids and Interfaces, 14424 Potsdam, Germany

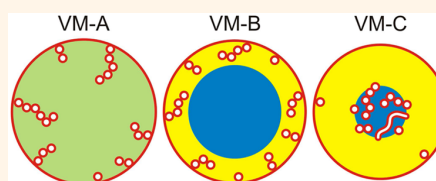
[‡]State Key Laboratory of Polymer Physics and Chemistry, Changchun Institute of Applied Chemistry, Chinese Academy of Sciences, 130022 Changchun, China

S Supporting Information

ABSTRACT: Biological membranes form both intra- and intercellular nanotubes that are used for molecular sorting within single cells and for long-distance connections between different cells. Such nanotubes can also develop from synthetic lipid bilayers in their fluid state. Each nanotube has a large area-to-volume ratio and stably encloses a water channel that is thereby shielded from its surroundings. The tubes are rather flexible and can easily change both their length and their conformation. Here, we study nanotubes formed by liquid-ordered (Lo) and liquid-disordered (Ld)

membranes with three lipid components exposed to aqueous mixtures of two polymers, polyethylene glycol (PEG) and dextran. Both types of membranes form striking patterns of nanotubes when we reduce the volume of giant vesicles by osmotic deflation, thereby exposing the two bilayer leaflets of the membranes to polymer solutions of different composition. With decreasing volume, three different patterns are observed corresponding to three distinct vesicle morphologies that reflect the interplay of spontaneous curvature and aqueous phase separation. We show that tube nucleation and growth is governed by two kinetic pathways and that the tubes undergo a novel shape transformation from necklace-like to cylindrical tubes at a certain critical tube length. We deduce the spontaneous curvature generated by the membrane-polymer interactions from the observed vesicle morphologies using three different and independent methods of image analysis. The spontaneous curvature of the Ld membranes is found to be 4.7 times larger than that of the Lo membranes. We also show that these curvatures are generated by weak PEG adsorption onto the membranes, with a binding affinity of about $1.6 k_B T$ per chain. In this way, our study provides a direct connection between nanoscopic membrane shapes and molecular interactions. Our approach is rather general and can be applied to many other systems of interest such as polymersomes or membrane-bound proteins and peptides.

KEYWORDS: membranes and vesicles, aqueous polymer solutions, membrane nanotubes, tube nucleation and growth, bilayer asymmetry, spontaneous curvature, PEG adsorption



One important function of biological membranes is to partition space into separate compartments. Particularly interesting compartments are provided by membrane nanotubes which represent highly curved membrane structures, have a large area-to-volume ratio, thereby enhancing membrane-dependent processes, and stably enclose thin water channels which are well-separated and shielded from their surroundings. Intracellular nanotubes are ubiquitous structural elements of many membrane-bound organelles such as the endoplasmic reticulum, the Golgi, the endosomal network, and mitochondria.^{1–3} These nanotubes connect distant parts of the cell and are used for molecular sorting, signaling, and transport. Intercellular (or “tunneling”) nanotubes between two or more cells provide long-distance connections for cell–cell communication, intercellular transport, and virus infections.^{4–6}

Synthetic nanotubes formed by lipid or polymer bilayers have been studied in the context of bilayer asymmetry and spontaneous curvature,^{7,8} lipid and protein sorting,^{9,10} cellular delivery of drugs and other chemical agents,¹¹ and as templates for rigid “nanowires”.¹²

Biological and biomimetic nanotubes are formed by fluid membranes which have a stable bilayer structure on the molecular scale but are highly flexible on the nanoscopic scale. The fluidity also allows fast lateral transport of molecules along the membranes, easy changes in tube length and conformation, as well as the formation of intramembrane domains and rafts.

Received: August 27, 2015

Accepted: November 20, 2015

Published: November 20, 2015

Here, we study giant unilamellar vesicles of three-component lipid bilayers. We investigate and compare two different lipid compositions that form a liquid-ordered (Lo) and a liquid-disordered (Ld) phase. The vesicles enclose aqueous polymer mixtures of dextran and polyethylene glycol (PEG), an aqueous two-phase system that has been frequently used in biochemical analysis and biotechnology¹³ to separate and purify biomolecules, cell organelles, and cell membranes. The lipid membranes form striking patterns of nanotubes within the giant vesicles when we deflate these vesicles osmotically, thereby exposing the two bilayer leaflets to polymer solutions of different composition. Three types of nanotube patterns can be distinguished corresponding to three different vesicle morphologies as shown schematically in Figure 1.

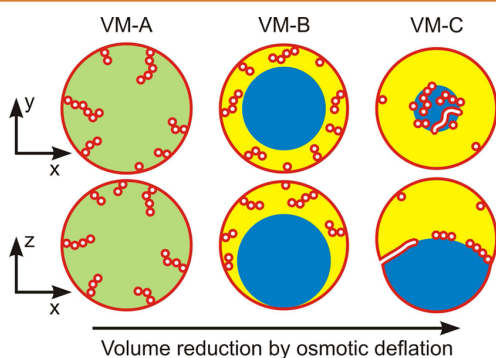


Figure 1. Three nanotube patterns corresponding to the distinct vesicle morphologies VM-A, VM-B, and VM-C observed along the deflation path: Schematic views of horizontal *xy*-scans (top row) and of vertical *xz*-scans (bottom row) across the deflated vesicles. In all cases, the tubes are filled with external medium (white). For the VM-A morphology, the interior polymer solution is uniform (green), whereas it is phase separated (blue-yellow) for the morphologies VM-B and VM-C, with complete and partial wetting, respectively, of the membrane by the PEG-rich aqueous phase (yellow). For the VM-B morphology, the nanotubes explore the whole PEG-rich (yellow) droplet but stay away from the dextran-rich (blue) one. For the VM-C morphology, the nanotubes adhere to the interface between the two aqueous droplets forming a thin and crowded layer along this interface. The different nanotube patterns can be most easily visualized by three-dimensional confocal scans of the vesicles, see [Supporting Movies](#).

The theoretical analysis of these observations reveals that the tubes are nucleated from small buds which subsequently grow into necklace-like tubes. The necklaces are further extended until they transform into cylindrical tubes when their length exceeds a certain critical value. The critical length can be reduced by the adhesion of the nanotubes to interfaces. These morphological features are universal and apply to the deflation-induced formation of membrane nanotubes in general.

The magnitude of the bilayer asymmetry, arising from the exposure of the two leaflets to different polymer concentrations, is quantitatively described by the spontaneous curvature of the membranes. We introduce three different and independent methods of image analysis to deduce this curvature from the observed vesicle morphologies. All three methods give very consistent results. The spontaneous curvature m of the Ld and Lo membranes is found to be $m_{Ld} \approx -1/(125 \text{ nm})$ and $m_{Lo} \approx -1/(600 \text{ nm})$ over a certain range of polymer concentrations. Using atomistic molecular dynamics simulations, we also

elucidate the molecular mechanism for the spontaneous curvatures obtained here and conclude that these curvatures are generated by the weak adsorption of PEG chains onto the membranes, with a binding free energy of about 4 kJ/mol or 1.6 $k_B T$ per chain, and that the curvature ratio $m_{Ld}/m_{Lo} \approx 4.7$ is approximately equal to the ratio κ_{Lo}/κ_{Ld} of the corresponding bending rigidities. Our approach to deduce the spontaneous curvature from the observed tubulation process is quite general and can be extended to other membrane systems of interest. Two examples are provided by polymer bilayers or polymerosomes^{11,14–16} and by the adsorption of proteins^{17,18} or peptides¹⁹ onto lipid membranes. Accurate estimates for the spontaneous curvature are also crucial in order to determine the critical particle sizes for the engulfment of nanoparticles by membranes and vesicles.²⁰

RESULTS AND DISCUSSION

Tubulation of Vesicles Induced by Osmotic Deflation.

Giant unilamellar vesicles were prepared from ternary lipid mixtures of dioleoylphosphatidylcholine (DOPC), dipalmitoylphosphatidylcholine (DPPC), and cholesterol, see [Methods](#). The vesicles were formed in aqueous polymer mixtures of PEG and dextran, which undergo phase separation into two aqueous phases, a PEG-rich and a dextran-rich phase, when the polymer weight fractions exceed a few weight percent^{13,21,22} (Figure 2a,b). Two types of lipid compositions were studied corresponding to a flexible Ld and a more rigid Lo membrane.^{23–25} The Ld membranes were fluorescently labeled by a red dye, the Lo membranes by a green one (Figure 2c,d and [Supporting Information Movies](#)).

Our experiments started with spherical vesicles that enclosed a homogeneous polymer solution (composition 0 in Figure 2b). These vesicles were then deflated osmotically by using exterior solutions that contained fixed weight fractions of the two polymers but an increasing amount of sucrose. The subsequent deflation steps are depicted in Figure 2b and described in more detail in Table S1. After the first deflation step, the interior polymer solution still formed a uniform aqueous phase (composition 1), corresponding to the VM-A morphology in Figure 1. After the second and all subsequent deflation steps, the interior solution underwent phase separation into a PEG-rich and a dextran-rich phase which formed two aqueous droplets within the vesicles. The shapes of these droplets could be directly imaged by differential interference contrast and fluorescence microscopy, see Figure S1. The PEG-rich droplet was always in contact with the membranes, whereas the dextran-rich droplet came into contact with the Ld and Lo membranes only after the third and fourth deflation step, respectively. Therefore, the Ld membranes were completely wetted by the PEG-rich phase for composition 2, while the Lo membranes exhibited the same type of wetting for compositions 2 and 3, corresponding to the VM-B morphology in Figure 1. Subsequent deflation steps led to the VM-C morphology with partial membrane wetting and nonzero contact angles.

Each osmotic deflation step reduces the vesicle volume and, thus, increases the area-to-volume ratio of the vesicle. In the absence of polymers, vesicles undergo smooth shape transformations from spherical toward prolate shapes as studied previously^{26,27} for one-component membranes. In contrast to such conventional shape transformations, the vesicles studied here still assumed a spherical shape after the initial deflation steps, both for the flexible Ld membranes (Figure 2c) and for

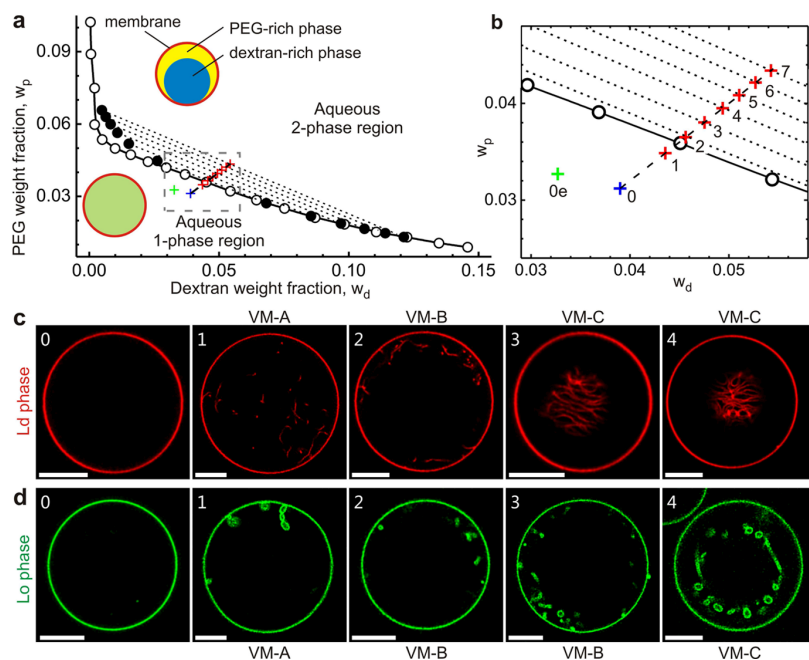


Figure 2. Osmotic deflation and tubulation of vesicles in aqueous PEG–dextran solutions. (a) High-precision phase diagram of aqueous PEG–dextran solution close to its critical demixing point at 24 °C with dotted tie lines and dashed deflation trajectory. (b) Enlarged region of phase diagram around the deflation trajectory which starts from the initial polymer composition 0 (blue cross) within the vesicle and the composition 0e (green cross) of the isotonic external medium. The vesicle is then osmotically deflated in a stepwise manner which leads to the interior compositions 1–7 (red crosses), see Table S1 for more details. (c) Confocal xy -scans of vesicles bounded by an Ld membrane (red) at the deflation steps 0–4. Apart from the initial vesicle 0, all deflated vesicles formed membrane nanotubes pointing into the vesicle interior. The thickness of the Ld tubes was below optical resolution. More detailed views of the three-dimensional morphologies of the vesicles are provided in the [Movies Ld_1](#), [Ld_2](#), and [Ld_4](#). (d) Confocal xy -scans of vesicles bounded by an Lo membrane (green) at the deflation points 0–4. The deflated vesicles in panels 1–4 again form nanotubes; the corresponding three-dimensional scans are shown in the [Movies Lo_1](#), [Lo_2](#), and [Lo_4](#). The thickness of the Lo tubes was above optical resolution. The scale bars are 10 μm in all confocal images. The confocal xz -scans of the vesicles in panels (c) and (d) are displayed in [Figure S2](#).

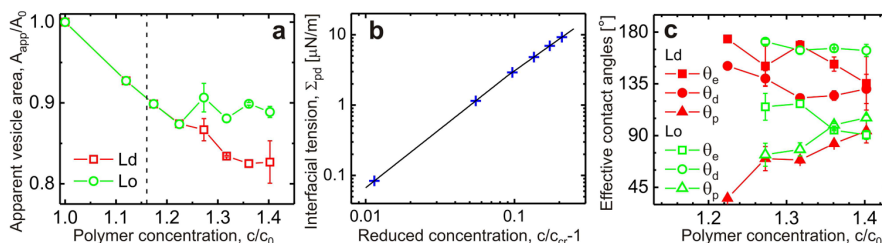


Figure 3. Variation of apparent vesicle area, interfacial tension, and contact angles with osmotic deflation which leads to an increase in the total polymer concentration c within the vesicles. (a) Apparent membrane area of large mother vesicles which decreases monotonically during the first three deflation steps both for the Ld and the Lo membranes. The concentration $c_0 = 0.0714 \text{ g/cm}^3$ represents the initial polymer concentration before deflation; the vertical dashed line corresponds to the critical concentration $c_{cr} = 1.161 c_0$. (b) Interfacial tension Σ_{pd} of the pd interface (p, PEG-rich phase; d, dextran-rich phase) between the PEG-rich and dextran-rich aqueous phases, data (blue crosses) and linear fit (solid black line). The tension vanishes at the critical concentration and increases monotonically for $c > c_{cr}$. (c) Effective contact angles θ_p , θ_d , and θ_e between the pd interface and the two membrane segments as defined in [Figure S3](#). The contact angle θ_p vanishes at the concentration c_{wt} of the complete-to-partial wetting transition with $1.174 < c_{wt}/c_0 < 1.224$ for the Ld membranes (red data) and $1.224 < c_{wt}/c_0 < 1.273$ for the Lo membranes (green data).

the more rigid Lo membranes ([Figure 2d](#)). However, because the vesicle volume was reduced by the deflation, the vesicle shapes had an *apparent* area A_{app} that was smaller than the initial vesicle area A_0 . As shown in [Figure 3a](#), this apparent area decreased by about 7%, 3%, and 2.5% during the first, second, and third deflation step, respectively. The missing membrane area, $A = A_0 - A_{app}$, was stored in nanotubes that protruded into the vesicle interior.

This tube formation was observed for both types of membranes and for all three vesicle morphologies ([Figure 2c,d](#)). For the VM-A and VM-B morphologies, the tubes underwent strong thermally excited undulations and we had to analyze the whole three-dimensional stack of confocal scans in order to estimate the length of the tubes. Examples are provided by the [Movies Ld_1](#) and [Ld_2](#), which display an Ld vesicle after the first and second deflation step, respectively, and

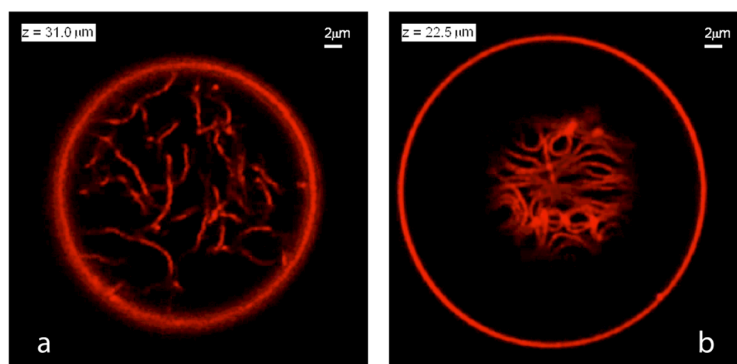


Figure 4. Nanotube patterns within Ld vesicles as observed for the VM-B and VM-C morphologies corresponding to complete and partial wetting of the membranes. (a) Disordered pattern corresponding to an xy scan (with $z = 31 \mu\text{m}$) of the VM-B morphology after the second deflation step. Because the Ld membrane is completely wetted by the PEG-rich phase, the nanotubes explore the whole PEG-rich droplet but stay away from the dextran-rich phase. (b) Layer of densely packed tubes as visible in an xy scan (with $z = 22.5 \mu\text{m}$) of the VM-C morphology after the fourth deflation step. As a result of partial wetting, the nanotubes now adhere to the pd interface between the two aqueous droplets and form a thin layer in which crowding leads to short-range orientational order of the tubes. Note that the tube layer is only partially visible because the pd interface is curved into a spherical cap.

reveal that the Ld tubes were quite long, of the order of $20 \mu\text{m}$. For the VM-C morphologies, longer tube segments can be recognized in a single image because the tubes were then localized close to the pd interface between the PEG-rich and the dextran-rich droplet, see [Movie Ld_4](#). This localization is a direct consequence of partial membrane wetting which favors adhesion of the tubes to the pd interface. Thus, the complete-to-partial wetting transition can be directly deduced from the observed remodelling of the nanotubes which explore the whole PEG-rich droplet for the VM-B but adhere to the pd interface for the VM-C morphology, see [Figure 4](#).

Because the deflation path was close to the critical consolute point, the tension Σ_{pd} of the pd interface was rather low and varied between 0.1 and $10 \mu\text{N/m}$, see [Figure 3b](#). For the VM-C morphology, *i.e.*, for partial wetting of the membranes by the two phases, the pd interface forms a contact line with the membrane and the resulting geometry can be characterized by effective contact angles as defined in [Figure S3](#). The variation of these contact angles with the osmotic deflation is displayed in [Figure 3c](#).

Nucleation and Growth of Necklace-like Tubes. The tubes of the Lo membranes were sufficiently thick to determine their shapes directly from the confocal images. The three-dimensional scans in the [Movies Lo_1](#) and [Lo_2](#) show that each Lo vesicle contains many necklace-like tubes consisting of quasi-spherical membrane beads connected by thin membrane necks. The presence of these tubes can be understood from the competition of two kinetic pathways which are related to two different bifurcations of the vesicle shape. Initial deflation of a spherical vesicle leads, *via* an oblate-stomatocyte bifurcation,²⁶ to the formation of a single spherical bud protruding into the vesicle interior, corresponding to the shape L^{sto} in [Figure 5](#). Upon further volume reduction, the vesicle can follow two alternative pathways depending on the lipid flow through the narrow membrane neck between the bud and the mother vesicle. If this flow is relatively fast, the bud grows in size until it transforms, *via* a sphere-to-prolate bifurcation, into a short necklace of two identical spheres, corresponding to the shape $L^{[2]}$ in [Figure 5](#).

As we continue to deflate the vesicle, the “fast-flow” pathway acts to elongate the necklace-like tube which then passes

through the necklace-like shapes $L^{[n]}$ that consist of an increasing number n of small spheres connected by thin membrane necks, see [Figure 5](#). The energy landscape in [Figure 5a](#) and the tube shapes in [Figure 5b](#) have been obtained by minimizing the bending energy of the membrane, see [Methods](#) and [Section S1](#). On the other hand, if the lipid flow through the neck is relatively slow or blocked, the mother vesicle uses the released excess area to form a second bud. Therefore, the deflation of the vesicle generates new buds *via* the “slow-flow” pathway which are then elongated into necklace-like tubes *via* the “fast-flow” pathway.

Necklace–Cylinder Coexistence and Critical Tube Length. Even though the vast majority of the Lo tubes were necklace-like, we also observed cylindrical tubes for the VM-C morphology of Lo membranes. Somewhat surprisingly, both necklace-like and cylindrical tubes were found to coexist on the same vesicle. One example is provided by the Lo_4 vesicle displayed in [Figure 6](#) and [Movie Lo_4](#). Close inspection of these confocal images reveals the existence of two long cylindrical tubes that spiral around the spherical cap of the pd interface. These observations can be understood from the competition of different energy contributions which favor necklace-like tubes below a certain critical tube length and cylindrical tubes above this length. At the critical tube length, the necklace-like tube transforms into a cylindrical one. Such a transformation can proceed in a continuous manner *via* intermediate unduloids as shown in [Figure 7](#).

For the VM-A and VM-B morphologies, the existence of a critical tube length can be understood intuitively from the following simple argument. A necklace-like tube consisting of small spheres with radius $R_{\text{ss}} = 1/|m|$ as depicted in [Figure 7a](#) has vanishing bending energy. The main body of a cylindrical tube with radius $R_{\text{cy}} = 1/(2|m|)$ as displayed in [Figure 7c](#) also has vanishing bending energy, but the cylinder must be closed by two end-caps which have a finite bending energy. Therefore, the bending energy of the membrane disfavors the cylindrical tube. On the other hand, the necklace-like tube has a larger volume compared to the cylindrical one and the osmotic pressure difference across the membranes acts to compress the tubes when they protrude into the interior solution inside the vesicles.⁸ Therefore, such a tube can lower its energy by

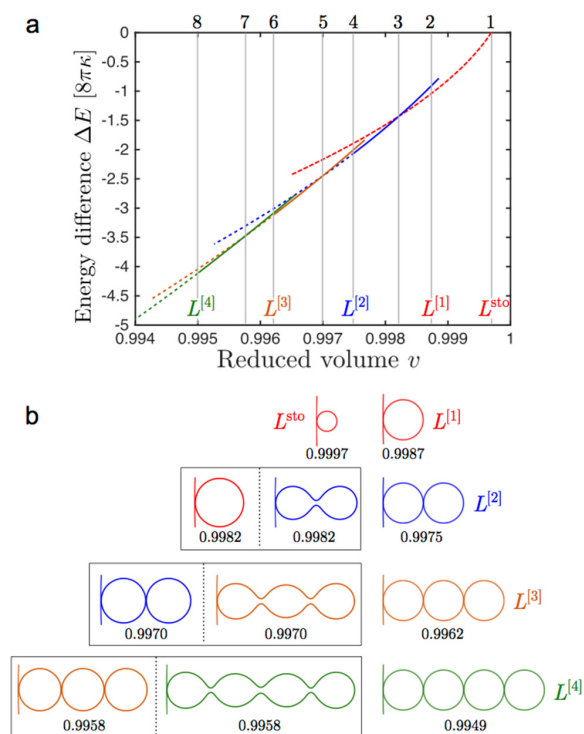


Figure 5. Formation and growth of necklace-like tube. (a) Energy landscape with different branches of equilibrium shapes as a function of the reduced vesicle volume v . The latter volume has the value $v = 1$ for a spherical shape and continuously decreases during deflation, see [Methods](#). The energy difference ΔE describes the deflation-induced reduction in bending energy compared to the initial spherical vesicle. The eight vertical lines labeled from 1 to 8 (top) describe eight discrete deflation steps. (b) Shapes of necklace-like tube corresponding to the eight vertical lines in panel a. The short vertical line on the left end of the tubes corresponds to a short segment of the mother vesicle which is connected to each tube by a thin membrane neck. As we deflate the initial vesicle with $v = 1$, we move along the 1-necklace branch (red) that begins at the limit shape L^{sto} with bead radius $R_{ss} \approx 1/(2|m|)$ and $v = 0.9997$. After passing the shape $L^{[1]}$ with $R_{ss} = 1/|m|$ and $v = 0.9987$, we reach the reduced volume $v = 0.9982$ at which the 1-necklace branch crosses the 2-necklace branch (blue). For the latter v -value, a 1-necklace coexists with an open 2-necklace. Further deflation leads to the 2-necklace $L^{[2]}$ with a closed neck at $v = 0.9975$ and, subsequently, to the 3-necklace branch (orange) and the 4-necklace branch (green). The dashed and solid segments of the free energy landscape in panel a correspond to tubes with closed and open necks, respectively. The parameters used in this example belong to the Lo_{-1} vesicle with size $R_0 = 20.7 \mu\text{m}$ and spontaneous curvature $m = -1.67 \mu\text{m}^{-1}$ as obtained from the area partitioning analysis.

reducing its volume which favors the cylindrical tube. The volume work is proportional to the tube length whereas the bending energy of the end-caps is independent of this length. It then follows from the competition between these two energies that short tubes are necklace-like whereas long tubes are cylindrical.

The same conclusion is obtained from the systematic theory in [Section S1](#) which predicts that an individual necklace-like tube transforms into a cylindrical one when the length of the necklace reaches the critical value L_{tu}^* and that this critical

length lies within the interval $2.84 R_0 < L_{tu}^* < 3R_0$ for the observed VM-A and VM-B morphologies where $R_0 \equiv \sqrt{A_0/(4\pi)}$ represents the radius of the initial vesicle with area A_0 . The upper bound $3R_0$ for the critical tube length is universal and applies to a vesicle with a single tube, whereas the lower bound $2.84R_0$ applies to a vesicle with an arbitrary number of tubes and follows from the observed reduction of the apparent vesicle area during the first two deflation steps. The critical tube area of a single tube is then given by $2\pi L_{tu}^*/|m|$ which is about $6\pi R_0/|m|$. These bounds for the VM-A and VM-B morphologies agree with the observed necklace-like shapes of the Lo tubes which are all shorter than the critical tube length. The Ld tubes are about 5 times longer than the Lo tubes, but they are still shorter than the critical tube length. On the basis of the latter observation and the high flexibility of the Ld tubes, see further below, we conclude that the Ld tubes for the VM-A and VM-B morphologies have a necklace-like shape as well.

For the VM-C morphology, the nanotubes adhere to the pd interface. In this case, the critical tube length is determined by the interplay between (i) the adhesion energy which is proportional to tube length and favors the cylindrical tube and (ii) the bending energy of the end-caps for the cylindrical tube which disfavors the latter tube. The systematic theory in [Section S2](#) now leads to a critical tube length L_{ad}^* that depends on four material parameters, namely the bending rigidity, the spontaneous curvature, the interfacial tension of the pd interface, and the intrinsic contact angle, as described by [eq S47](#) and [Figure S4](#). All of these parameters have been determined experimentally and two of them are found to vary significantly along the deflation path which implies a corresponding variation of the critical tube length L_{ad}^* . The values for the Ld_{-4} and the Lo_{-4} vesicle, for example, are given by 5.6 and $21.4 \mu\text{m}$, respectively ([Figure S4d](#)). The latter value agrees with the length of the cylindrical tubes as observed for the Lo membranes. When we compare the length of individual tubes in [Movie Ld_4](#) with the critical length of $5.6 \mu\text{m}$, we conclude that the Ld tubes have a cylindrical shape for this VM-C morphology.

Spontaneous Curvature from Image Analysis. For the Lo membranes, the spontaneous curvature can be directly estimated from the shape of the tubes. As mentioned, all Lo tubes found for the VM-A and VM-B morphologies were relatively short and necklace-like which implies that the spontaneous curvature can be estimated *via* $m = -1/\langle R_{ss} \rangle$ with the average radius $\langle R_{ss} \rangle$ of the small, quasi-spherical beads. For the Lo_{-1} vesicle after the first deflation step, for example, this direct shape analysis leads to $\langle R_{ss} \rangle = 0.72 \mu\text{m}$ and to the spontaneous curvature $m = -1.4 \mu\text{m}^{-1}$. All m -values obtained in this manner are displayed in [Figure 8a](#) as green stars. These values have an accuracy of about 20%, reflecting the relative standard deviation of the measured bead radius R_{ss} .

The direct shape analysis was also applied to the cylindrical and necklace-like tubes coexisting on the Lo_{-4} vesicle, see [Figure 6](#). The average diameter $\langle 2R_{cy} \rangle$ of the cylindrical tubes as obtained from the confocal scans ([Figure 6d,e](#)) implies the spontaneous curvature $m = -1/(2R_{cy})$ which leads to $m = -1.82 \mu\text{m}^{-1}$ for the cylindrical tubes on the Lo_{-4} vesicle, with an accuracy of about $\pm 13\%$ corresponding to the relative standard deviation of the measured diameter of the cylinders ([Figure 6f](#)). For the latter vesicle, the average bead diameter of the necklace-like tubes leads to $m = -1.56 \mu\text{m}^{-1}$ with an accuracy of about $\pm 19\%$ ([Figure 6g](#)). The good agreement

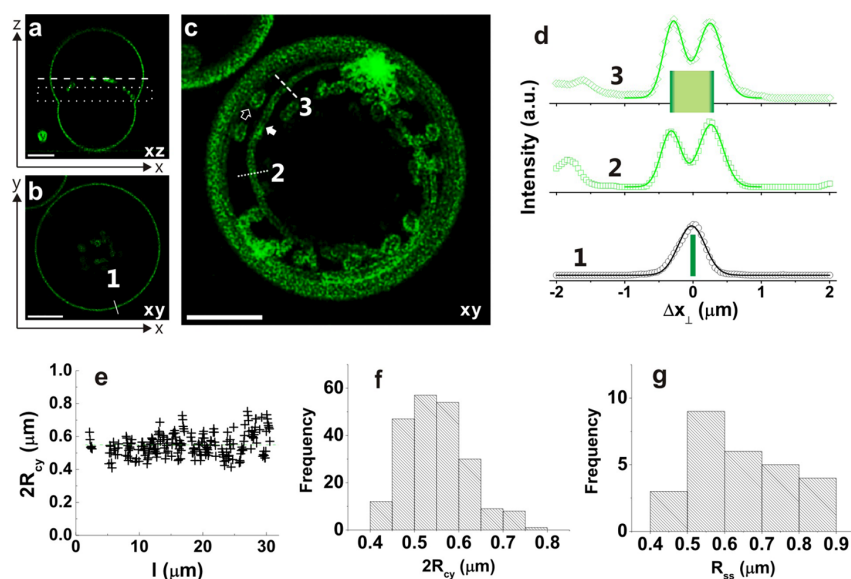


Figure 6. Necklace-cylinder coexistence on Lo₄ vesicle: (a) confocal *xz*-scan; (b) confocal *xy*-scan at $z = 29 \mu\text{m}$ corresponding to the dashed line in panel a; (c) superposition of 6 confocal *xy*-scans at $z = 20, 21, 22, 23, 24,$ and $25 \mu\text{m}$ from [Movie Lo_4](#), corresponding to the dotted rectangle in panel a. This superposition reveals the coexistence of two long cylindrical tubes and several short necklace-like tubes, see also [Movie Lo_4](#). All scale bars are $10 \mu\text{m}$. (d) Fluorescent intensity along the solid white line 1 in panel b perpendicular to the *GUV* contour and along the dotted and dashed white lines 2 and 3 in panel c across a cylindrical tube. The quantity Δx_{\perp} is the coordinate perpendicular to the *GUV* contour or membrane tube. The intensity profiles can be well fitted by Gaussian distributions with a half-peak width of $0.35 \pm 0.05 \mu\text{m}$. The peak–peak separations for the lines 2 and 3 lead to the estimated tube diameters $2R_{\text{cy}} = 0.58$ and $0.54 \mu\text{m}$, respectively. (e) The tube diameter $2R_{\text{cy}}$ as a function of tube position, where l is the distance from the top end of the tube. (f) Cylindrical tubes: histogram of tube diameters $2R_{\text{cy}}$, with average tube diameter $\langle 2R_{\text{cy}} \rangle = 0.55 \mu\text{m}$, standard deviation $\sigma_{\text{cy}} = 0.07 \mu\text{m}$, and relative standard deviation $\sigma_{\text{cy}}/\langle 2R_{\text{cy}} \rangle = 0.13$. (g) Necklace-like tubes: histogram of bead radii R_{ss} with average bead radius $\langle R_{\text{ss}} \rangle = 0.64 \mu\text{m}$, standard deviation $\sigma_{\text{ss}} = 0.12 \mu\text{m}$, and relative standard deviation $\sigma_{\text{ss}}/\langle R_{\text{ss}} \rangle = 0.19$. Therefore, the direct shape analysis of the cylindrical and necklace-like tubes leads to the estimates $m = -1/(2R_{\text{cy}}) = -1.82 \pm 0.24 \mu\text{m}^{-1}$ and $m = -1/R_{\text{ss}} = -1.56 \pm 0.30 \mu\text{m}^{-1}$.

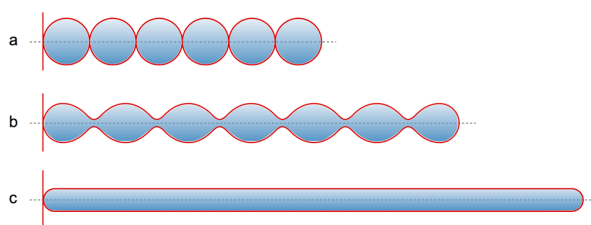


Figure 7. Low energy transformation of a necklace-like tube into a capped cylinder: all three tubes have the same surface area and, apart from the end-caps, the same mean curvature M which is equal to the spontaneous curvature m . (a) Necklace-like tube $L^{[6]}$ with vanishing bending energy consisting of six spherical beads connected by thin membrane necks. The small spheres have radius $R_{\text{ss}} = 1/|m|$ and mean curvature $M = -1/R_{\text{ss}} = m$. (b) Capped unduloid with neck radius R_{ne} , bulge radius R_{bu} , and mean curvature $M = -1/(R_{\text{ne}} + R_{\text{bu}}) = m$. (c) Capped cylinder with radius $R_{\text{cy}} = 1/(2|m|)$ and mean curvature $M = -1/(2R_{\text{cy}}) = m$. The transformation of the sphere-necklace into the cylinder proceeds *via* a continuous family of intermediate unduloids. During this transformation, the tube volume is reduced by a factor $3/4$. Apart from their end-caps, the unduloids and the cylinder have the same bending energy as the sphere-necklace. All curvatures are negative because the tubes protrude into the interior aqueous compartments of the vesicles.

between the m -values obtained from the cylindrical and necklace-like tubes justifies our implicit assumption that the

spontaneous curvature is uniform along the whole membrane of the vesicle.

For the Ld membranes, we could not resolve the shapes of the nanotubes because they had a thickness below optical resolution. However, we could still deduce the spontaneous curvature from two geometric quantities that can be directly determined from the confocal scans: the total tube area $A = A_0 - A_{\text{app}}$ and the total tube length L . The latter length can be directly estimated from the three-dimensional confocal scans, see [Movies Ld_j](#), with an uncertainty of about $\pm 15\%$. Indeed, all tubes with constant mean curvature are then characterized by spontaneous curvatures within the interval $-\pi L/A \leq m \leq -\pi L/A$ ([Figure S5](#)). Furthermore, if a fraction Λ of the total tube length is cylindrical and the remaining fraction $1 - \Lambda$ is necklace-like, we obtain the estimate

$$m = -(2 - \Lambda) \frac{\pi L}{A} = -(2 - \Lambda) \frac{\pi L}{A_0 - A_{\text{app}}} \quad (\text{area partitioning}) \quad (1)$$

For the VM-A and VM-B morphologies of the Lo membranes, all tubes had a necklace-like shape which implies $\Lambda = 0$. After the first deflation step of the Lo vesicle, for example, we measured the excess area $A = 354 \mu\text{m}^2$ and the overall tube length $L = 94 \mu\text{m}$ which leads, *via* [eq 1](#) with $\Lambda = 0$, to the spontaneous curvature $m = -1.67 \mu\text{m}^{-1}$. For the VM-C morphologies, on the other hand, tube adhesion can lead to some cylindrical tubes and nonzero Λ -values ([Table S2](#)). The m -values obtained *via* [eq 1](#) are displayed in [Figure 8a](#) as green

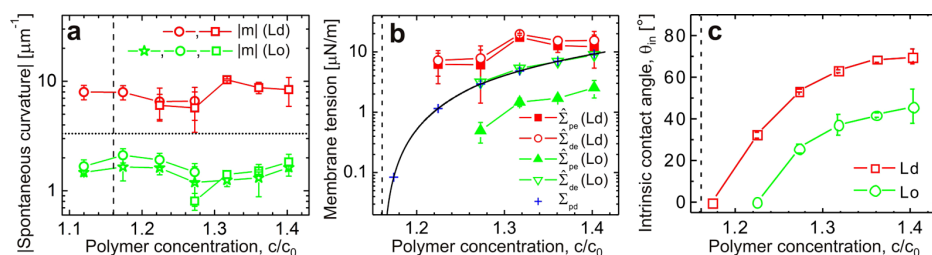


Figure 8. Variation of deduced membrane parameters with osmotic deflation: in all panels, the red and green data correspond to the Ld and Lo membranes, respectively, and the vertical dashed line to the critical concentration c_{cr} . (a) Absolute value of the spontaneous curvature in contact with the uniform aqueous phase (data for $c/c_0 = 1.120$) and with the PEG-rich aqueous phase (data for $c/c_0 \geq 1.174$). The data were obtained by direct shape analysis of the nanotubes (green stars), area partitioning analysis as given by eq 1 (open circles), and force balance analysis described by eq 2 (open squares). The horizontal dotted line corresponds to the optical resolution limit of $1/(300 \text{ nm})$. (b) Membrane tensions Σ_{pe} and Σ_{de} within the pe (p, PEG-rich phase; e, exterior phase) and de (d, dextran-rich phase; e, exterior phase) membrane segments separating the external medium from the PEG-rich and dextran-rich phase within the vesicle as defined in Figure S3b. For comparison, the interfacial tension Σ_{pd} is also included (blue crosses and solid black line). (c) Intrinsic contact angle θ_{in} between the pd interface and the vesicle membrane as defined in Figure S3c. The intrinsic contact angle is obtained from the effective contact angles *via* $\cos(\theta_{in}) = [\sin(\theta_p) - \sin(\theta_d)]/\sin(\theta_e)$.²⁸ Note that the intrinsic contact angle, which represents a material parameter, varies rather smoothly with the polymer concentration, in contrast to the effective contact angles in Figure 3c.

open circles and have an accuracy of $\pm 15\%$, the main uncertainty arising from the measurement of the tube length L .

For the Ld tubes, we could not estimate the fraction Λ from the confocal scans. However, the high flexibility of these tubes as observed for the VM-A and VM-B morphologies provides strong evidence that these tubes were necklace-like as well. The tube flexibility can be characterized by the persistence length for tube bending. Using the parameter values for the Ld membranes, we then find that a cylindrical tube has a persistence length of $15 \mu\text{m}$ (Section S3), whereas the persistence length of the corresponding necklace-like tube should be comparable to the diameter of the small spheres. Inspection of the Movies Ld_1 and Ld_2 reveals that the thermal fluctuations of the Ld tubes lead to hairpin-like conformations with curvature radii of the order of $2 \mu\text{m}$ which implies a persistence length below $2 \mu\text{m}$. Such an upper bound for the persistence length is consistent with a necklace-like but not with a cylindrical tube morphology. As mentioned, the same conclusion is obtained from the observed tube lengths which are shorter than the critical tube lengths for the necklace-cylinder transformation. Therefore, we estimated the spontaneous curvatures for the VM-A and VM-B morphologies of the Ld membranes using eq 1 with $\Lambda = 0$. The spontaneous curvature of the Ld_1 vesicle, for example, is then found to be $m = -1/(125 \text{ nm})$. For the VM-C morphologies of the Ld membranes, we deduced the total tube length L from the density of the tubes at the pd interface and estimated the spontaneous curvature *via* eq 1 using the value $\Lambda = \frac{1}{2} \pm \frac{1}{2}$, thereby taking the whole range $0 \leq \Lambda \leq 1$ of possible Λ -values into account.

For the VM-C morphologies of both the Lo and the Ld membranes, the values of the spontaneous curvature as deduced from the direct shape and the area partitioning analysis could be validated *via* a third, completely different mode of analysis. The latter mode is based on the interfacial tension Σ_{pd} of the pd interface (Figure 3b) as well as on the effective contact angles (Figure 3c). Using these quantities and the force balance along the contact line, we computed the membrane tensions in the two segments (Figure 8b) and the spontaneous curvature *via*

$$m = - \left(\frac{\Sigma_{pd} \sin(\theta_d)}{2\kappa \sin(\theta_e)} \right)^{1/2} \quad (\text{force balance}) \quad (2)$$

With the use of the measured bending rigidities for the Ld and Lo membranes, the expression given by eq 2 leads to m -values that are in good agreement with those obtained *via* the two other modes of analysis, see open squares in Figure 8a.

Spontaneous Curvature Generated by PEG Adsorption. Because vesicle tubulation was only observed in the presence of the polymers, the spontaneous curvature of the vesicle membranes must arise from the polymer-membrane interactions. If these interactions are effectively attractive or repulsive, the polymers form adsorption or depletion layers on the two bilayer leaflets. The membrane then prefers to bulge toward the solutions with the higher and lower concentrations for polymer adsorption and depletion, respectively.²⁹ After the first deflation step, both the PEG and the dextran concentrations in the interior aqueous solution are larger than in the exterior solution (Figure 2a). After the second and all subsequent deflation steps, the PEG concentration in the interior PEG-rich phase is again larger than in the exterior solution, but the dextran concentration in the interior phase is now smaller than in this exterior solution (Figure 2a). Furthermore, all deflation steps lead to a negative spontaneous curvature of the membranes. These observations are only consistent with the theoretical results in ref 29 if the spontaneous curvature is induced by PEG adsorption. The latter conclusion has been confirmed by additional experiments in which we used the same lipid composition but exposed the vesicles to aqueous solutions that contained only PEG and no dextran, see Figure 9. For the latter systems, osmotic deflation of the vesicles again generated membrane nanotubes that protruded into the solution with the higher PEG concentration.

To corroborate these conclusions about PEG adsorption and to obtain direct insight into the conformations of the adsorbed PEG molecules, we performed molecular dynamics simulations of the polymer-lipid systems with atomistic resolution for the experimentally used lipid compositions and chain length of PEG, see Methods. Typical conformations of adsorbed chains are displayed in Figure 10a,b for both Ld and Lo membranes. These conformations indicate that the PEG molecules are only

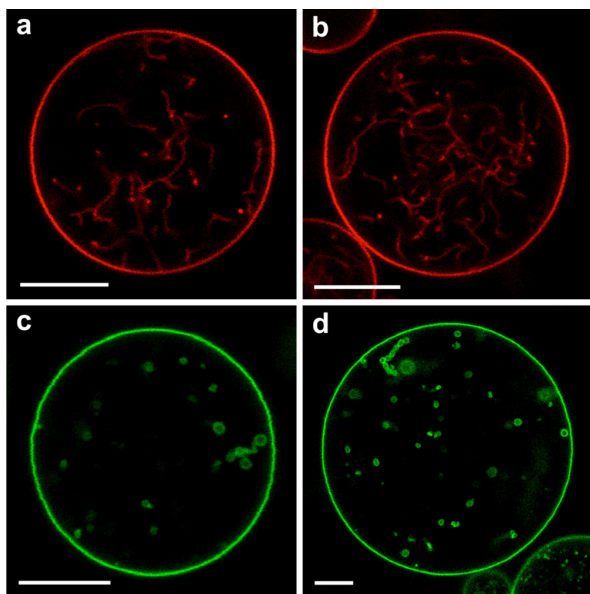


Figure 9. Nanotubes formed in Ld (red) and Lo (green) vesicles exposed to aqueous solutions of PEG and sucrose, *i.e.*, in the absence of dextran. The interior solution contained only PEG and no sucrose with the initial weight fraction $w_p = 0.0443$. The vesicles were deflated by exchanging the external medium by a hypertonic solution with no PEG but an increasing weight fraction w_{su} of sucrose. The vesicles in (a) and (c) are obtained for $w_{su} = 0.0066$, those in (b) and (d) for $w_{su} = 0.01$. The corresponding osmolarity ratios P_e/P_0 are 1.05 and 1.61, respectively. The white scale bars are 10 μm in all panels.

weakly bound, with relatively short contact segments (or “trains”), and relatively long loops in between. The two terminal OH groups of the PEG molecule were frequently bound to the membrane *via* hydrogen bonds. In addition, a small number of contacts was formed between the polymer backbones and the membranes. Combining both types of contacts, the adsorbed polymers formed an average number of 4.5 ± 2.3 and 3.2 ± 2.1 contacts with the Ld and the Lo membranes, respectively. A more quantitative measure for the affinity of the polymers to the membranes is provided by the potentials of mean force displayed in Figure 10c,d. These potentials indicate that the PEG molecules have essentially the same affinity for both types of membranes, with a binding free energy of about 4 kJ/mol or $1.6 k_B T$ per polymer chain.

Discussion of Deduced Spontaneous Curvatures. The spontaneous curvatures displayed in Figure 8a have two remarkable features: (i) they depend only weakly on the total polymer concentration c within the vesicles; and (ii) when exposed to the same asymmetric environment, the spontaneous curvature of the Ld membrane is about 4.7 times larger than that of the Lo membrane. The second feature is relatively easy to explain. Indeed, the spontaneous curvature generated by adsorption is theoretically predicted to be inversely proportional to the bending rigidity of the membrane^{8,29} as recently confirmed for the adsorption of small molecules by molecular dynamics simulations.³⁰ If we assume that the PEG chains have similar affinities to the Ld and Lo membranes as implied by our simulation results (Figure 10c,d), the ratio m_{Ld}/m_{Lo} of the spontaneous curvatures should be equal to the ratio κ_{Lo}/κ_{Ld} of the bending rigidities. The latter rigidity ratio is estimated to be

$\kappa_{Lo}/\kappa_{Ld} \approx 4.5$, based on the experimental results in ref 25, which should be compared with the curvature ratio $m_{Ld}/m_{Lo} \approx 4.7$ in Figure 8a. Because the experimental uncertainty is of the order of 10 to 20% for both ratios, the data are consistent with $m_{Ld}/m_{Lo} \approx \kappa_{Lo}/\kappa_{Ld}$ and, thus, with a comparable amount of adsorbed polymers on both types of membranes, in agreement with our simulation results.

The weak dependence of the spontaneous curvatures on the polymer concentration c within the vesicles is more difficult to understand. Because the polymer weight fractions in the exterior solution were kept constant during all deflation steps, the concentration-dependence of the spontaneous curvatures follows from the concentration-dependence of the PEG coverage on the inner membrane leaflets in contact with the interior polymer solutions. If these leaflets were in contact with dilute PEG solutions, the polymer density within the adsorption layer would be increased by a factor of about $\exp[\Delta F_{ch}/k_B T] \approx 5$ compared to the bulk density, based on the binding free energy $\Delta F_{ch} \approx 1.6 k_B T$ for a single PEG chain (Figure 10c,d). Therefore, as the polymer concentration within the interior solution is increased, the PEG coverage on the interior leaflets of the membranes would also be increased which implied a corresponding increase of the spontaneous curvature.

However, for the deflation path studied here, the PEG–dextran solutions were not dilute but semidilute, with substantial overlaps between the chains, see Table S3, which led to repulsive PEG–dextran interactions in the one-phase region and to repulsive PEG–PEG interactions in the PEG-rich phase. When the PEG chains are adsorbed onto the inner leaflet, the local PEG concentration is increased and the PEG chains must experience even more repulsive PEG–PEG and PEG–dextran interactions than in the bulk solutions. For adsorption onto solid surfaces, repulsive chain–chain interactions typically lead to a saturation of the polymer coverage as observed in many experiments, see, e.g., refs 31–33. In the present context, such a saturation of the PEG coverage is quite plausible after the third deflation step. Furthermore, after the first and the second deflation step, the interior polymer solutions were rather close to the critical consolute point with $\epsilon \equiv |c - c_{cr}|/c_{cr}$ of the order of 10^{-2} (Table S3). In such a situation, the correlation length for compositional fluctuations is expected to be large compared to the size of the PEG chains which implies a thickening of the adsorption layers and a corresponding increase in the PEG coverage on the inner membrane leaflets. Thus, the weak concentration-dependence of this coverage should arise from the antagonistic effects of near-critical fluctuations and repulsive chain–chain interactions along the chosen deflation path.

CONCLUSIONS

In summary, we have shown that both Ld and Lo membranes form nanotubes when their leaflets are exposed to two aqueous polymer solutions that differ in their composition. The total length of the tubes is controlled by the osmotic deflation, while their thickness directly reflects the bilayer asymmetry of the membranes as described by their spontaneous curvature. The vast majority of individual Lo nanotubes had a necklace-like shape (Figure 2 as well as Figure S2 and Movies), but we also observed long cylindrical tubes coexisting with shorter necklace-like tubes on the same vesicle (Figure 6 and Movie Lo_4). The formation of many necklace-like tubes can be understood from the competition of two kinetic pathways. The first pathway nucleates new buds of the mother vesicle whereas

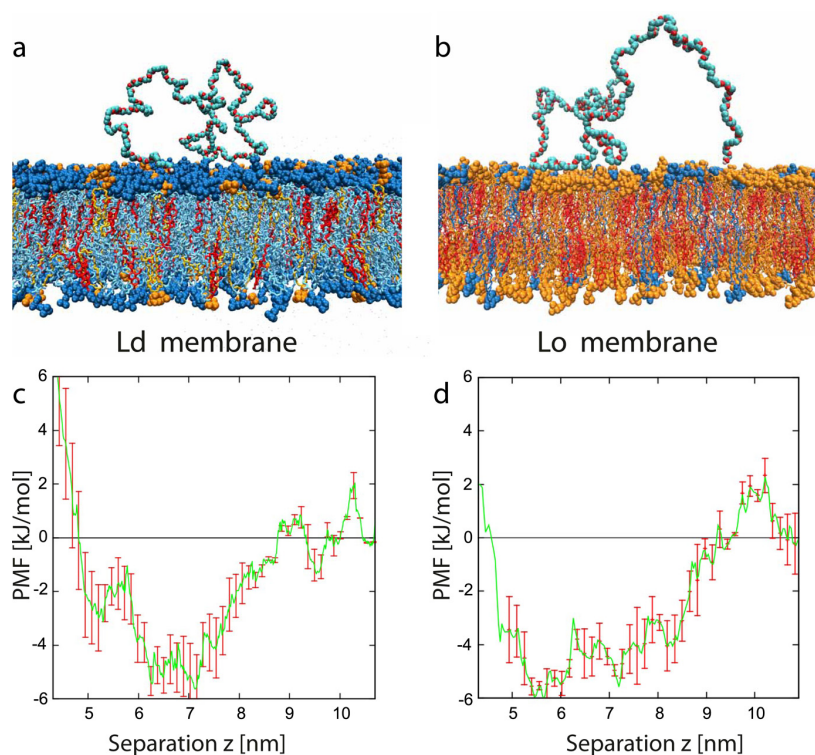


Figure 10. Typical conformation and potential of mean force for adsorbed PEG molecules. (a and b) Simulation snapshots of PEG molecule adsorbed onto Ld and Lo bilayer. The Ld and Lo composition is the same as in Figure 2. The color code for the lipids is blue for DOPC, orange for DPPC, and red for cholesterol. The PEG molecules consist of 180 monomers corresponding to the average molecular weight used in the experiments. Each lipid membrane is immersed in about 27 000 water molecules (not shown). (c and d) Potential of mean force (PMF) for Ld and Lo membranes as a function of the separation z between the polymer's center-of-mass and the bilayer's midplane. The potential wells are relatively broad, with a width of about 4 nm, because the polymer end groups can adsorb even for relatively large z -values. The binding free energy of a single PEG chain is about 4 kJ/mol or $1.6 k_B T$ for both types of membranes.

the second pathway stores additional area in the existing buds and extends these buds into necklace-like tubes (Figure 5b). These necklace-like tubes transform into cylindrical tubes when their length reaches a certain critical length (Sections S1 and S2). It then follows from the magnitude of the critical tube lengths that individual Ld tubes were necklace-like for the VM-A and VM-B morphologies but cylindrical for some of the VM-C morphologies. In the latter case, the tube adhesion led to a reduction of the critical tube length.

To deduce the spontaneous curvature from the observed vesicle morphologies, we used three different and independent methods of image analysis: direct shape analysis (Figure 6), overall partitioning analysis of membrane area (eq 1), and force balance analysis along the contact line of the partially wetted membranes (eq 2). All three analysis methods gave very consistent values for the spontaneous curvature m as summarized in Figure 8a. The spontaneous curvatures of the Ld and Lo membranes were fairly constant over the range of polymer concentrations studied here, with $m_{Ld} \approx -8 \mu\text{m}^{-1}$ and $m_{Lo} \approx -1.7 \mu\text{m}^{-1}$ which implies the curvature ratio $m_{Ld}/m_{Lo} \approx 4.7$.

We also elucidated the molecular mechanism for the generation of the spontaneous curvatures and showed that these curvatures are induced by the weak adsorption of PEG molecules onto the membranes. Indeed, the formation of nanotubes was also observed in the absence of dextran, e.g., when the giant vesicles were exposed to aqueous solutions of

PEG alone (Figure 9). In addition, both the typical conformations of the adsorbed polymers and the associated polymer-membrane affinities were determined by atomistic molecular dynamics simulations (Figure 10). The binding free energies were found to be relatively small and similar in size for Ld and Lo membranes, about 4 kJ/mol or $1.6 k_B T$ per polymer chain. Because of this similarity, the curvature ratio m_{Ld}/m_{Lo} is approximately equal to the rigidity ratio κ_{Lo}/κ_{Ld} .

Our study can be extended in several ways. First, it will be useful to further corroborate our preliminary results for dilute PEG solutions (Figure 9) in order to avoid the added complexity of semidilute polymer mixtures. Second, using other lipid or polymer compositions with different bending rigidities or polymer-membrane affinities, we can easily vary the tube thickness and, in particular, produce thinner and longer nanotubes which should then exhibit a larger fraction of cylinders. Third, using osmotic deflation in combination with micropipette aspiration to shorten the tubes⁷ and/or optical tweezers to extend individual tubes, one should be able to directly probe the dynamics of the necklace-cylinder transformation.

Because our deflation-based approach is both simple and general, it can be applied to other membrane systems of interest. One example is provided by synthetic lipid bilayers with two leaflets that have different compositions as recently produced by a variety of preparation methods.^{34–38} With the use of similar methods, it should also be possible to produce

bilayers of block copolymers with such a compositional asymmetry. Block copolymer bilayers form giant polymerosomes¹⁴ which change their shapes in response to osmotic deflation^{15,16,39} and can form tubular shapes as well.¹¹ Furthermore, our approach can also be used to determine the spontaneous curvature arising from the membrane binding of BAR-domain proteins^{17,18} and amphipathic peptides.¹⁹

In the living cell, the membranes are continuously remodelled by the formation of transport vesicles *via* fission and fusion processes. The magnitude of the spontaneous curvature determines whether these remodelling processes are endergonic or exergonic. If the spontaneous curvature is comparable to the inverse size of the transport vesicle, budding is exergonic and fusion is endergonic. One example for the latter situation is provided by clathrin-dependent endocytosis for which the spontaneous curvature plays a pivotal role.²⁰

METHODS

Materials. Dextran (400–500 kg/mol) and poly(ethylene glycol) (PEG 8000, 8 kg/mol) were purchased from Sigma-Aldrich. The polydispersity, measured with gel permeation chromatography, was 1.11 for PEG and 1.83 for dextran. The binodal of the polymer solution was determined by cloud-point titration.²² The critical consolute (or demixing) point was located at a total polymer concentration of 8.12 wt % with a dextran to PEG weight ratio $w_d/w_p = 1.25$. The interfacial tensions Σ_{pd} between the dextran-rich and PEG-rich phases were measured using a SITE100 spinning drop tensiometer (Krüss) as described in ref 22. Dioleoylphosphatidylcholine (DOPC) and dipalmitoylphosphatidylcholine (DPPC) were purchased from Avanti Polar Lipids and cholesterol from Sigma-Aldrich. Texas Red labeled dihexadecanoyl phosphoethanolamine (DHPE-TR) was purchased from Invitrogen and distearoyl phosphoethanolamine-*N*-[poly(ethylene glycol)2000-*N'*-carboxyfluorescein] (DSPE-PEG-CF) from Avanti Polar Lipids.

Vesicle Preparation and Deflation. Aqueous polymer solutions with initial weight fraction $(w_d, w_p)_0 = (0.0390, 0.0312)$ corresponding to composition 0 (blue cross in Figure 2a,b) were encapsulated within giant vesicles with membranes composed of DOPC, DPPC and cholesterol. The latter vesicles were formed using the electroformation method as described elsewhere.⁷ The Ld membranes with lipid composition DOPC:DPPC:cholesterol = 64:15:21 were labeled by 0.1 mol % DHPE-TR. The Lo membranes with lipid composition DOPC:DPPC:cholesterol = 13:44:43 were labeled with 0.2 mol % DSPE-PEG-CF. For these two lipid compositions, the bending rigidities were previously studied; we used the values $\kappa_{Ld} = 0.82 \times 10^{-19}$ J and $\kappa_{Lo} = 3.69 \times 10^{-19}$ J obtained in ref 25. After preparation, the vesicles were transferred into a chamber filled with an isotonic solution with polymer weight fractions $(w_d, w_p)_{0c} = (0.0327, 0.0327)$, corresponding to the green cross in Figure 2a,b. The deflation was done by exchanging the external medium with a hypertonic solution containing the constant polymer weight fractions $w_d = 0.0327$ and $w_p = 0.0327$ and an increasing weight fraction of sucrose. These conditions ensured that the vesicles sedimented toward the coverslip at the bottom of the chamber and that the symmetry axis was oriented perpendicular to this coverslip; see Figure 2c,d and Figure S2a,b.

Confocal Microscopy. Vesicles were observed by a confocal microscope (Leica TCS SP5) with a 63X water immersion objective (N.A. = 1.20). The images were deconvoluted by Huygens Professional software (version 4.3.1, Scientific Volume Imaging), and analyzed using home-developed software in Matlab to determine the contours of the mother vesicle and the membrane nanotubes. A complete three-dimensional scan of a vesicle consisted of a stack of 37–82 confocal images that were taken at different separations from the coverslip, see the Movies Ld_j and Lo_j which display scans of Ld and Lo vesicles after the first, second, and fourth depletion step. The analysis of these scans is described in more detail in Figure 6 and Table S2.

Computation of Vesicle Shapes via Free Energy Minimization. For the VM-A and VM-B morphologies, the free energy landscapes of the giant vesicles have been determined by minimizing the bending energy of the vesicle membrane for constant membrane area A_0 and deflation-controlled vesicle volume V . The bending energy depends (i) on the shape of the vesicle membrane which is described by its (local) mean curvature M and (ii) on two fluid-elastic parameters, the bending rigidity κ and the spontaneous curvature m .^{26,40} The constraints on area and volume are taken into account by two Lagrange multipliers, Σ and ΔP , and by minimizing the shape functional²⁶

$$\mathcal{E} = \int dA 2\kappa(M - m)^2 + \Sigma A_0 - \Delta P V \quad (3)$$

We used the vesicle size $R_0 \equiv (A_0/4\pi)^{1/2}$ as the basic length scale and the volume-to-area ratio or reduced volume

$$v \equiv V/[(4\pi/3)R_0^3] \leq 1 \quad (4)$$

as the basic control parameter or reaction coordinate, see Sect. S1 for more details. In this way, we obtained the free energy landscape for a giant vesicle with a necklace-like tube as displayed in Figure 5.

For the VM-C morphology, the overall shape of the vesicles can be determined by an appropriate generalization of the shape functional as described in ref 28. The VM-C shape involves the intrinsic contact angle θ_m as an additional material parameter, see Figure S3c. In order to study the adhesion of membrane nanotubes to the pd interface, we ignored the relatively small curvature of the pd interface and calculated the free energies for the adhesion of both necklace-like and cylindrical tubes to a planar pd interface. The results of these calculations are described in Section S2 and summarized in Figure S4.

Molecular Dynamics Simulations of PEG Adsorption. For the atomistic simulations, we used the GROMACS software package 4.5.5 with the Berger force field⁴¹ for the lipids and parameters based on the GROMOS 53A6 force field for the polymers.⁴² For the PEG 8000 polymer chain, this force field leads to a radius of gyration of 3.43 nm in reasonable agreement with the value 3.83 nm for PEG 8000 as obtained by linear extrapolation from the results in ref 43 and the value 4.05 nm as estimated in ref 22 based on the PEO data in ref 44. Lipid bilayers corresponding to the experimentally used compositions for the Ld and Lo membranes were assembled, together with a single polymer chain of PEG 8000, in a cubic simulation box of size $10.3 \times 10.3 \times 14.8$ nm³ with periodic boundary conditions in all three spatial directions for the unrestrained simulations, using the charmm membrane builder.⁴⁵ The Ld membrane contained 256 DOPC, 60 DPPC, and 84 cholesterol molecules, whereas the Lo membrane consisted of 52 DOPC, 176 DPPC, and 172 cholesterol molecules (Figure 10). The PEG 8000 molecules had a length of 180 monomers. Bilayer and polymer were immersed in 27 080 water molecules as described by the SPC water model. Both the Ld and the Lo membranes were simulated for 700 ns. For the computations of the potentials of mean force in Figure 10c,d, we increased the box size perpendicular to the membrane to 20.5 nm corresponding to 51 758 water molecules and used 12 umbrella windows, each of which was simulated for 100 ns.

ASSOCIATED CONTENT

Supporting Information

The Supporting Information is available free of charge on the ACS Publications website at DOI: 10.1021/acsnano.5b05377.

- Additional experimental data (PDF)
- Movie Ld_1 (MPG)
- Movie Ld_2 (MPG)
- Movie Ld_4 (MPG)
- Movie Lo_1 (MPG)
- Movie Lo_2 (MPG)
- Movie Lo_4 (MPG)

AUTHOR INFORMATION

Corresponding Author

*E-mail: lipowsky@mpikg.mpg.de.

Notes

The authors declare no competing financial interest.

ACKNOWLEDGMENTS

We thank Halim Kusumaatmaja for stimulating discussions during the initial phase of this project and acknowledge support by the Partner Group Program of the Max Planck Society and the Chinese Academy of Sciences, the National Natural Science Foundation of China (Grant No. 21274147), the German Science Foundation (DFG) via IRTG 1524, and the Federal Ministry of Education and Research (BMBF) via the consortium MaxSynBio.

REFERENCES

- Marchi, S.; Patergnani, S.; Pinton, P. The Endoplasmic Reticulum-Mitochondria Connection: One Touch, Multiple Functions. *Biochim. Biophys. Acta, Bioenerg.* **2014**, *1837*, 461–469.
- van Weering, J. R. T.; Cullen, P. J. Membrane-Associated Cargo Recycling by Tubule-Based Endosomal Sorting. *Semin. Cell Dev. Biol.* **2014**, *31*, 40–47.
- Westrate, L. M.; Lee, J. E.; Prinz, W. A.; Voeltz, G. K. Form Follows Function: The Importance of Endoplasmic Reticulum Shape. *Annu. Rev. Biochem.* **2015**, *84*, 791–811.
- Wang, X.; Gerdes, H.-H. Transfer of Mitochondria via Tunneling Nnotubes Rescues Apoptotic PC12 Cells. *Cell Death Differ.* **2015**, *22*, 1181–1191.
- He, K.; Luo, W.; Zhang, Y.; Liu, F.; Liu, D.; Xu, L.; Qin, L.; Xiong, C.; Lu, Z.; Fang, X.; Zhang, Y. Intercellular Transportation of Quantum Dots Mediated by Membrane Nanotubes. *ACS Nano* **2010**, *4*, 3015–3022.
- Sowinski, S.; Jolly, C.; Berninghausen, O.; Purbhoo, M. A.; Chauveau, A.; Köhler, K.; Oddos, S.; Eissmann, P.; Brodsky, F. M.; Hopkins, C.; et al. Membrane Nanotubes Physically Connect T Cells over Long Distances Presenting a Novel Route for HIV-1 Transmission. *Nat. Cell Biol.* **2008**, *10*, 211–219.
- Li, Y.; Lipowsky, R.; Dimova, R. Membrane Nanotubes Induced by Aqueous Phase Separation and Stabilized by Spontaneous Curvature. *Proc. Natl. Acad. Sci. U. S. A.* **2011**, *108*, 4731–4736.
- Lipowsky, R. Spontaneous Tubulation of Membranes and Vesicles Reveals Membrane Tension Generated by Spontaneous Curvature. *Faraday Discuss.* **2013**, *161*, 305–331.
- Sorre, B.; Callan-Jones, A.; Manzi, J.; Goud, B.; Prost, J.; Bassereau, P.; Roux, A. Nature of Curvature Coupling of Amphiphysin with Membranes Depends on its Bound Density. *Proc. Natl. Acad. Sci. U. S. A.* **2012**, *109*, 173–178.
- Zhu, C.; Das, S. L.; Baumgart, T. Nonlinear Sorting, Curvature Generation, and Crowding of Endophilin N-Bar on Tubular Membranes. *Biophys. J.* **2012**, *102*, 1837–1845.
- Robertson, J. D.; Yealland, G.; Avila-Olias, M.; Chierico, L.; Bandmann, O.; Renshaw, S. A.; Battaglia, G. pH-Sensitive Tubular Polymersomes: Formation and Applications in Cellular Delivery. *ACS Nano* **2014**, *8*, 4650–4661.
- Tanaka, M.; Critchley, K.; Matsunaga, T.; Evans, S. D.; Staniland, S. S. Fabrication of Lipid Tubules with Embedded Quantum Dots by Membrane Tubulation Protein. *Small* **2012**, *8*, 1590–1595.
- Albertsson, P. A. *Partition of Cell Particles and Macromolecules: Separation and Purification of Biomolecules, Cell Organelles, Membranes, and Cells in Aqueous Polymer Two-Phase Systems and Their Use in Biochemical Analysis and Biotechnology*, 3rd ed.; Wiley, 1986.
- Discher, B. M.; Won, Y.-Y.; Ege, D. S.; Lee, J. C.-M.; Bates, F. S.; Discher, D. E.; Hammer, D. A. Polymersomes: Tough Vesicles Made from Diblock Copolymers. *Science* **1999**, *284*, 1143–1146.
- Salva, R.; Meins, J.-F. L.; Sandre, O.; Brulet, A.; Schmutz, M.; Guenoun, P.; Lecommandoux, S. Polymersome Shape Transformation at the Nanoscale. *ACS Nano* **2013**, *7*, 9298–9311.
- Thiele, J.; Chokkalingam, V.; Ma, S.; Wilson, D. A.; Huck, W. T. S. Vesicle Budding from Polymersomes Templated by Microfluidically Prepared Double Emulsions. *Mater. Horiz.* **2014**, *1*, 96–101.
- McMahon, H. T.; Gallop, J. L. Membrane Curvature and Mechanisms of Dynamic Cell Membrane Remodelling. *Nature* **2005**, *438*, 590–596.
- Rao, Y.; Haucke, V. Membrane Shaping by the Bin/Amphitaphysin/Rvs (BAR) Domain Protein Superfamily. *Cell. Mol. Life Sci.* **2011**, *68*, 3983–3993.
- Arouni, A.; Kiessling, V.; Tamm, L.; Dathe, M.; Blume, A. Morphological Changes Induced by the Action of Antimicrobial Peptides on Supported Lipid Bilayers. *J. Phys. Chem. B* **2011**, *115*, 158–167.
- Agudo-Canalejo, J.; Lipowsky, R. Critical Particle Sizes for the Engulfment of Nanoparticles by Membranes and Vesicles with Bilayer Asymmetry. *ACS Nano* **2015**, *9*, 3704–3720.
- Helfrich, M.; Mangeney-Slavin, L.; Long, M.; Djoko, K.; Keating, C. Aqueous Phase Separation in Giant Vesicles. *J. Am. Chem. Soc.* **2002**, *124*, 13374–13375.
- Liu, Y.; Lipowsky, R.; Dimova, R. Concentration Dependence of the Interfacial Tension for Aqueous Two-Phase Polymer Solutions of Dextran and Polyethylene Glycol. *Langmuir* **2012**, *28*, 3831–3839.
- Veatch, S.; Keller, S. Separation of Liquid Phases in Giant Vesicles of Ternary Mixtures of Phospholipids and Cholesterol. *Biophys. J.* **2003**, *85*, 3074–3083.
- Tian, A.; Capraro, B. R.; Esposito, C.; Baumgart, T. Bending Stiffness Depends on Curvature of Ternary Lipid Mixture Tubular Membranes. *Biophys. J.* **2009**, *97*, 1636–1646.
- Heinrich, M.; Tian, A.; Esposito, C.; Baumgart, T. Dynamic Sorting of Lipids and Proteins in Membrane Tubes with a Moving Phase Boundary. *Proc. Natl. Acad. Sci. U. S. A.* **2010**, *107*, 7208–7213.
- Seifert, U.; Berndl, K.; Lipowsky, R. Shape Transformations of Vesicles: Phase Diagram for Spontaneous Curvature and Bilayer Coupling Model. *Phys. Rev. A: At., Mol., Opt. Phys.* **1991**, *44*, 1182–1202.
- Lipowsky, R. The Conformation of Membranes. *Nature* **1991**, *349*, 475–481.
- Kusumaatmaja, H.; Li, Y.; Dimova, R.; Lipowsky, R. Intrinsic Contact Angle of Aqueous Phases at Membranes and Vesicles. *Phys. Rev. Lett.* **2009**, *103*, 238103.
- Breidenich, M.; Netz, R.; Lipowsky, R. The Influence of Non-Anchored Polymers on the Curvature of Vesicles. *Mol. Phys.* **2005**, *103*, 3169–3183.
- Rózycki, B.; Lipowsky, R. Spontaneous Curvature of Bilayer Membranes from Molecular Simulations: Asymmetric Lipid Densities and Asymmetric Adsorption. *J. Chem. Phys.* **2015**, *142*, 054101.
- Felter, R. E.; Ray, L. N. Polymer Adsorption Studies at the Solid-Liquid Interface Using Gel Permeation Chromatography. *J. Colloid Interface Sci.* **1970**, *32*, 349–360.
- Voronov, A.; Luzinov, I.; Minko, S.; Sidorenko, A. Adsorption of Polymers at the Surface Concentrations in the Diluted to Semidiluted Regimes. *Macromolecules* **1997**, *30*, 6929–6936.
- Liufu, S.; Xiao, H.; Li, Y. Investigation of PEG Adsorption on the Surface of Zinc Oxide Nanoparticles. *Powder Technol.* **2004**, *145*, 20–24.
- Hwang, W. L.; Chen, M.; Cronin, B.; Holden, M.; Bayley, H. Asymmetric Droplet Interface Bilayers. *J. Am. Chem. Soc.* **2008**, *130*, 5878–5879.
- Chiantia, S.; Schwille, P.; Klymchenko, A. S.; London, E. Asymmetric GUVs Prepared by MbCD-Mediated Lipid Exchange: An FCS Study. *Biophys. J.* **2011**, *100*, L01–L03.
- Hu, P. C.; Li, S.; Malmstadt, N. Microfluidic Fabrication of Asymmetric Giant Lipid Vesicles. *ACS Appl. Mater. Interfaces* **2011**, *3*, 1434–40.
- Richmond, D. L.; Schmid, E. M.; Martens, S.; Stachowiak, J. C.; Liska, N.; Fletcher, D. A. Forming Giant Vesicles with Controlled

Membrane Composition, Asymmetry, and Contents. *Proc. Natl. Acad. Sci. U. S. A.* **2011**, *108*, 9431–6.

(38) Matosevic, S.; Paegel, B. M. Layer-by-Layer Cell Membrane Assembly. *Nat. Chem.* **2013**, *5*, 958–63.

(39) Meeuwissen, S. A.; Kim, K. T.; Chen, Y.; Pochan, D. J.; van Hest, J. C. M. Controlled Shape Transformation of Polymersome Stomatocytes. *Angew. Chem., Int. Ed.* **2011**, *50*, 7070–7073.

(40) Helfrich, W. Elastic Properties of Lipid Bilayers: Theory and Possible Experiments. *Z. Naturforsch.* **1973**, *28c*, 693–703.

(41) Berger, O.; Edholm, O.; Jähnig, F. Molecular Dynamics Simulations of a Fluid Bilayer of Dipalmitoylphosphatidylcholine at Full Hydration, Constant Pressure, and Constant Temperature. *Biophys. J.* **1997**, *72*, 2002–2013.

(42) Fuchs, P. F.; Hansen, H. S.; Hünenberger, P. H.; Horta, B. A. C. A GROMOS Parameter Set for Vicinal Diether Functions: Properties of Polyethyleneoxide and Polyethyleneglycol. *J. Chem. Theory Comput.* **2012**, *8*, 3943–3963.

(43) Bhat, R.; Timasheff, S. N. Steric Exclusion is the Principal Source of the Preferential Hydration of Proteins in the Presence of Polyethylene Glycols. *Protein Sci.* **1992**, *1*, 1133–1143.

(44) Devanand, K.; Selser, J. C. Asymptotic Behavior and Long-Range Interactions in Aqueous Solutions of Poly(ethylene oxide). *Macromolecules* **1991**, *24*, 5943–5947.

(45) Wu, E. L.; Cheng, X.; Jo, S.; Rui, H.; Song, K. C.; Davila-Contreras, E. M.; Qi, Y.; Lee, J.; Monje-Galvan, V.; Venable, R. M.; et al. CHARMM-GUI Membrane Builder toward Realistic Biological Membrane Simulations. *J. Comput. Chem.* **2014**, *35*, 1997–2004.

Patterns of Flexible Nanotubes Formed by Liquid-Ordered and Liquid-Disordered Membranes - Supporting Information

Yonggang Liu^{†,‡}, Jaime Agudo-Canalejo[†], Andrea Grafmüller[†], Rumiana Dimova[†]
and Reinhard Lipowsky^{†*}

[†] *Theory and Bio-Systems, Max Planck Institute of Colloids and Interfaces,
Science Park Golm, 14424 Potsdam, Germany*

[‡] *State Key Laboratory of Polymer Physics and Chemistry, Changchun Institute of
Applied Chemistry, Chinese Academy of Sciences, 130022 Changchun, China*

November 20, 2015

This Supporting Information contains the following items:

Supporting Sections:

Sect. S1: Critical tube length for VM-A and VM-B morphologies.

Sect. S2: Critical tube length for VM-C morphologies.

Sect. S3: Tube flexibility and persistence length.

Supporting Figures:

Fig. S1: Shapes of aqueous droplets for different vesicle morphologies.

Fig. S2: Vertical cross sections of the Ld and Lo vesicles in Fig. 2.

Fig. S3: Contact angles for VM-C morphologies.

Fig. S4: Adhesion of membrane nanotubes to the pd interface.

Fig. S5: Different tube shapes with the same membrane area and tube length.

Supporting Tables:

Table S1: Deflation path within the phase diagram of Fig. 2.

Table S2: Geometry of deflated Ld- j and Lo- j vesicles.

Table S3: Overlap of PEG and dextran chains along the deflation path.

Captions for the Movies Ld- j and Lo- j with $j = 1, 2, 4$.

References for Supporting Information

S1 Critical tube length for VM-A and VM-B morphologies

S1.1 Giant vesicle with necklace-like tube

Consider a giant vesicle with a spherical shape of radius R_0 . The vesicle membrane has a large and negative spontaneous curvature m which favors highly curved membrane segments, in contrast to the small curvature $1/R_0$ of the initial vesicle. When the vesicle volume is reduced by osmotic deflation, the membrane can form an ‘ \mathcal{N} -shape’ consisting of a large spherical mother vesicle together with a necklace-like tube that protrudes into the vesicle interior. We have determined the \mathcal{N} -shapes of minimal bending energy as a function of reduced volume

$$v \equiv \frac{V}{V_0} \leq 1 \quad \text{with} \quad V_0 \equiv \frac{4\pi}{3} R_0^3 \quad (\text{S1})$$

where $v = 1$ corresponds to the spherical mother vesicle without a necklace-like tube. The results of the numerical energy minimization, which are based on the shape functional in Eq. 3 of the main text, are displayed in Fig. 5.

The \mathcal{N} -shapes of minimal bending energy contain the shapes $L^{[N]}$ for which the necklace consists of N spherical beads with radius $R_{ss} = 1/|m|$, see Fig. 5. Such a necklace-like tube has constant mean curvature $M = m$ and, thus, vanishing bending energy as follows from Eq. 3 of the main text. Furthermore, the mother vesicle has the radius

$$R_N = R_0 \sqrt{1 - \frac{N}{(|m|R_0)^2}} < R_0 \quad (\text{S2})$$

as obtained from the conservation of membrane area which has the form

$$A_0 = 4\pi R_0^2 = 4\pi R_N^2 + N4\pi|m|^{-2}. \quad (\text{S3})$$

The necklace is anchored to the mother vesicle by an ideal membrane neck. The latter neck is formed as one approaches the limit shape L^{sto} from the branch of stomatocytes. [1] Likewise, the $L^{[N]}$ -shapes with $N \geq 2$ also represent limit shapes which are obtained from necklace-like tubes with open necks, see Fig. 5. The $L^{[1]}$ -shape is special because the necklace consists of a single spherical bead (or bud) which is obtained from the limit shape L^{sto} by increasing the bead radius from $R_{ss} = 1/(2|m|)$ to $R_{ss} = 1/|m|$. The $L^{[N]}$ -shapes with $N \geq 2$ contain two types of ideal necks, the anchor neck between the mother vesicle and the first bead as well as the ss-ss necks between the small spheres of the necklace. Both types of membrane necks are stable provided $R_{ss} \geq 1/|m|$ [2] which includes the limiting case $R_{ss} = 1/|m|$ considered here.

The volume of the $L^{[N]}$ -shapes is given by

$$V_N = \frac{4\pi}{3} R_N^3 - N \frac{4\pi}{3} R_{ss}^3 = V_0 \left(\left[1 - \frac{N}{(|m|R_0)^2} \right]^{3/2} - \frac{N}{(|m|R_0)^3} \right) \quad (\text{S4})$$

which decreases monotonically with increasing number N of the small beads. Therefore, the sequence of $L^{[N]}$ -shapes provides a possible, low-energy pathway for osmotic deflation as depicted in Fig. 5 in the main text.

Because the bending energy of the necklace-like tube with $R_{\text{ss}} = 1/|m|$ vanishes, the bending energy of the $L^{[N]}$ -shapes arises from the mother vesicle alone, *i.e.*,

$$\mathcal{E}_{\text{be}}(L^{[N]}) = 8\pi\kappa (1 - mR_N)^2 \quad (\text{S5})$$

which is equivalent to

$$\mathcal{E}_{\text{be}}(L^{[N]}) = 8\pi\kappa \left[1 + |m|R_0 \sqrt{1 - \frac{N}{(|m|R_0)^2}} \right]^2. \quad (\text{S6})$$

This energy also decreases monotonically with increasing bead number N , compare Fig. 5.

S1.2 Giant vesicle with cylindrical tube

We now transform the $L^{[N]}$ -shapes as considered in the previous section into alternative $C^{[N]}$ -shapes for which the necklace-like tubes are replaced by cylindrical ones. For each value of N , we perform this transformation in such a way that *both the membrane area and the vesicle volume are conserved*.

The cylindrical tubes consist of cylinders that are closed by two spherical caps, where one of these end caps is connected to the mother vesicle by an ideal neck. The body of such a cylinder has length L_{cy} , radius $R_{\text{cy}} = 1/(2|m|)$, and mean curvature $M = m$ which implies that this membrane segment has vanishing bending energy. The radius of the mother vesicle is now denoted by R_{ls} . Because the $C^{[N]}$ -shape is required to have the same membrane area as the $L^{[N]}$ -shape, the length scales L_{cy} and R_{ls} are related *via*

$$R_{\text{ls}}^2 + \frac{1}{4|m|}L_{\text{cy}} + \frac{1}{4m^2} = R_N^2 + \frac{N}{m^2}. \quad (\text{S7})$$

A second relation between these two scales is obtained from the requirement that the $C^{[N]}$ -shape and the $L^{[N]}$ -shape, which both include the mother vesicle, have the same volume which implies

$$R_{\text{ls}}^3 - \frac{3}{16m^2}L_{\text{cy}} - \frac{1}{8|m|^3} = R_N^3 - \frac{N}{|m|^3}. \quad (\text{S8})$$

When we combine the two relations (S7) and (S8) to eliminate L_{cy} , we obtain the implicit equation

$$R_{\text{ls}}^3 \left(1 + \frac{3}{4|m|R_{\text{ls}}} \right) = R_N^3 \left(1 + \frac{3}{4|m|R_N} \right) - \frac{N + 1/4}{4|m|^3} \quad (\text{S9})$$

for the mother vesicle radius R_{ls} of the $C^{[N]}$ -shape where R_N can be expressed in terms of R_0 *via* (S2). The implicit equation (S9) directly implies that $R_{\text{ls}} < R_N$ for all positive values of N . Therefore, the $C^{[N]}$ -shape has a smaller mother vesicle and the membrane area stored in the cylinder exceeds the area stored in the N -necklace. We now define the parameter ϵ *via*

$$R_{\text{ls}} = R_N (1 - \epsilon) \quad (\text{S10})$$

and consider the limit of large $|m|R_0$, in which we obtain the asymptotic equality

$$\epsilon \approx \frac{N + 1/4}{12} \left(\frac{1}{|m|R_0} \right)^3 \quad (\text{large } |m|R_0) \quad (\text{S11})$$

from the implicit equation (S9).

The bending energy of the $C^{[N]}$ -shape is equal to

$$\mathcal{E}_{\text{be}}(C^{[N]}) = 8\pi\kappa(1 - mR_{\text{ls}})^2 + 2\pi\kappa \quad (\text{S12})$$

where the first and the second term represents the energy contributions from the mother vesicle and from the two end caps of the cylinder, respectively.

S1.3 Critical tube length for necklace-cylinder transformation

We now compare the bending energy (S12) of the $C^{[N]}$ -shape with the bending energy (S5) of the $L^{[N]}$ -shape. The mother vesicle of the $C^{[N]}$ -shape has the bending energy $8\pi\kappa(1 - mR_{\text{ls}})^2$ which is smaller than the bending energy $8\pi\kappa(1 - mR_N)^2$ of the $L^{[N]}$ -shape because $R_{\text{ls}} < R_N$ and $|m|R_{\text{ls}} \gg 1$. However, the capped cylinder has the bending energy $2\pi\kappa$ whereas the necklace has vanishing bending energy. Therefore, when we transform the $L^{[N]}$ -shape into the $C^{[N]}$ -shape, we reduce the bending energy of the mother vesicle but increase the bending energy of the tube.

We now define the reduced difference

$$\Delta \equiv \frac{\mathcal{E}_{\text{be}}(C^{[N]}) - \mathcal{E}_{\text{be}}(L^{[N]})}{8\pi\kappa} \quad (\text{S13})$$

between the bending energies of the $C^{[N]}$ - and the $L^{[N]}$ -shape, which has the form

$$\Delta = (1 + |m|R_{\text{ls}})^2 + \frac{1}{4} - (1 + |m|R_N)^2 \quad (\text{S14})$$

or

$$\Delta = |m|(R_{\text{ls}} - R_N) [2 + |m|(R_{\text{ls}} + R_N)] + \frac{1}{4} \quad (\text{S15})$$

Replacing R_{ls} by $R_N(1 - \epsilon)$, the latter relation becomes

$$\Delta = -\epsilon|m|R_N [2 + 2|m|R_N - \epsilon|m|R_N] + \frac{1}{4}. \quad (\text{S16})$$

The $L^{[N]}$ -shape and the $C^{[N]}$ -shape are energetically favored for $\Delta > 0$ and $\Delta < 0$, respectively. The critical bead number N^* and the critical tube length

$$L_{\text{tu}}^* = N^* 2R_{\text{ss}} = N^* 2/|m| \quad (\text{S17})$$

then follow from $\Delta = 0$.

In the limit of large $|m|R_0$ and small $\epsilon \sim (|m|R_0)^{-3}$, see (S11), we obtain the asymptotic equality

$$\Delta \approx -\frac{N + 1/4}{6|m|R_0} + \frac{1}{4} \quad (\text{S18})$$

which implies the critical tube length

$$L_{\text{tu}}^* = N^* 2/|m| \approx 3R_0. \quad (\text{S19})$$

It is interesting to note that exactly the same relation for the critical tube length is obtained if one replaces the bending energy contribution from the mother vesicle by the volume work performed on the tube by the pressure difference ΔP which behaves as $\Delta P \approx 4\kappa m^2/R_{\text{is}}$ for large $|m|R_{\text{is}}$ and acts to compress the necklace-like tube which has a larger volume than the cylindrical one. [3]

S1.4 Critical tube lengths for mother vesicle with many tubes

So far, we have explicitly discussed a mother vesicle with a single tube. However, the above considerations can be easily extended to a mother vesicle with several tubes. Indeed, all we have to do is to select one of the tubes and to redefine the membrane area and the membrane volume in an appropriate manner. Thus, let us label the selected tube by the index s and the remaining tubes by the index $r = 1, 2, \dots$. The selected tube has the area A_s , the remaining tubes have the areas A_r . The redefined membrane area \hat{A}_0 is then given by

$$\hat{A}_0 \equiv A_0 - \sum_r A_r \equiv A_{\text{mv}} + A_s \quad (\text{S20})$$

with the area A_{mv} of the redefined mother vesicle. If we envisage to inflate this mother vesicle to retract the selected tube without changing the remaining tubes, we obtain a spherical vesicle with radius $\hat{R}_0 = [\hat{A}_0/(4\pi)]^{1/2}$ and volume $\hat{V}_0 = \frac{4\pi}{3}\hat{R}_0^3$.

Now, we have to replace the quantities R_0 , V_0 , and A_0 in Eqs. S1 - S3 by \hat{R}_0 , \hat{V}_0 , and \hat{A}_0 and to repeat the whole calculation with the hatted variables. In this way, we study the growth of the selected tube while all the other tubes remain unchanged. As a result, we obtain the critical length $\hat{L}_{\text{tu}}^* \approx 3\hat{R}_0$ for the selected tube. Because the redefined vesicle radius \hat{R}_0 is smaller than R_0 , the critical length \hat{L}_{tu}^* is smaller than L_{tu}^* for a vesicle with a single tube. This difference can, however, be neglected for the VM-A and VM-B morphologies studied here. Indeed, after the first two deflation steps, the total area of all membrane tubes, $A = A_s + \sum_r A_r$, satisfies $A \leq 0.1A_0$, see Fig. 3a in the main text, which implies that $\hat{A}_0 > 0.9A_0$ and $\hat{R}_0 > 0.948R_0$

irrespective of which individual tube we select. Therefore, the critical tube length \hat{L}_{tu}^* of any selected tube lies within the interval $2.84 R_0 < \hat{L}_{\text{tu}}^* \leq 3R_0$ and is always much larger than the individual tube lengths observed for the VM-A and VM-B morphologies.

When a necklace-like tube with length L_{tu}^* is transformed into a cylindrical tube of equal area A_{tu}^* , the tube length becomes twice as large. Therefore, in equilibrium, necklace-like tubes should have a length up to L_{tu}^* whereas cylindrical tubes should have a length exceeding $2L_{\text{tu}}^*$. As a consequence, the length distribution of the tubes is predicted to exhibit a gap defined by the interval $L_{\text{tu}}^* < L_{\text{tu}} < 2L_{\text{tu}}^*$.

S2 Critical tube length for VM-C morphologies

For the VM-C morphologies, the vesicle membrane is partially wetted by the two aqueous phases and the pe membrane segment separating the PEG-rich from the external phase forms the intrinsic contact angle θ_{in} with the pd interface. For the lipid-polymer systems studied here, all intrinsic contact angles were smaller than 90° (Fig. 8c in the main text).

Because of partial wetting, a membrane tube can lower its free energy by adhering to the pd interface. Furthermore, the large separation of length scales between the weakly curved pd interfaces and the strongly curved membrane tubes implies that we can ignore the interfacial curvature and consider the adhesion of the tubes to planar interfaces. In order to obtain explicit expressions for the corresponding adhesion free energies, we also ignore possible deformations of the tube shapes by the adhesion.

S2.1 Adhesion free energy of necklace-like tube

First, consider a necklace-like tube consisting of N spherical beads with radius $R_{\text{ss}} = 1/|m|$ as in Fig. S4a. A single bead will immerse into the dextran-rich phase until the angle between the pd interface and the pe segment of the bead membrane is equal to the intrinsic contact angle θ_{in} . In the following, we will first consider an arbitrary contact angle θ and then require that the adhesion free energy attains its lowest value when this contact angle is equal to the intrinsic contact angle θ_{in} .

When the tube membrane forms the contact angle θ with the pd interface, the total surface area A_{nl} of the necklace-like tube is partitioned into two segments according to

$$A_{\text{nl}} = N 4\pi R_{\text{ss}}^2 = N 4\pi |m|^{-2} = A_{\text{mp}} + A_{\text{md}} \quad (\text{S21})$$

with the contact area

$$A_{\text{mp}} = N 2\pi R_{\text{ss}}^2 (1 + \cos \theta) = N 2\pi |m|^{-2} (1 + \cos \theta) \quad (\text{S22})$$

between the inner leaflet of the membrane and the PEG-rich phase and the contact area

$$A_{\text{md}} = N 2\pi R_{\text{ss}}^2 (1 - \cos \theta) = N 2\pi |m|^{-2} (1 - \cos \theta) \quad (\text{S23})$$

between the inner leaflet of the membrane and the dextran-rich phase. At the same time, the area A_{pd} of the pd interface is reduced by

$$\Delta A_{\text{pd}} = N \pi (R_{\text{ss}} \sin \theta)^2 = N \pi |m|^{-2} \sin^2 \theta \quad (\text{S24})$$

The interfacial free energy of the pd interface and the free, non-adhering necklace fully immersed in the PEG-rich phase has the form

$$\mathcal{F}_{\text{nl,fr}} = \Sigma_{\text{pd}} A_{\text{pd}} + \Sigma_{\text{mp}} A_{\text{nl}} \quad (\text{S25})$$

with the interfacial tension Σ_{mp} of the interface between the inner leaflet of the membrane and the PEG-rich phase. Likewise, the interfacial free energy of the necklace adhering to the pd interface is given by

$$\mathcal{F}_{\text{nl,ad}} = \Sigma_{\text{pd}} (A_{\text{pd}} - \Delta A_{\text{pd}}) + \Sigma_{\text{mp}} (A_{\text{nl}} - A_{\text{md}}) + \Sigma_{\text{md}} A_{\text{md}} \quad (\text{S26})$$

with the interfacial tension Σ_{md} between the inner leaflet of the membrane and the dextran-rich phase. The adhesion free energy of the necklace-like tube is then given by

$$\mathcal{F}_{\text{nl}} \equiv \mathcal{F}_{\text{nl,ad}} - \mathcal{F}_{\text{nl,fr}} = (\Sigma_{\text{md}} - \Sigma_{\text{mp}}) A_{\text{md}} - \Sigma_{\text{pd}} \Delta A_{\text{pd}} \quad (\text{S27})$$

or

$$\mathcal{F}_{\text{nl}} = A_{\text{nl}} \left[\frac{1}{2} (\Sigma_{\text{md}} - \Sigma_{\text{mp}}) (1 - \cos \theta) - \frac{1}{4} \Sigma_{\text{pd}} \sin^2 \theta \right]. \quad (\text{S28})$$

We now require that this free energy attains its equilibrium value when the contact angle θ becomes equal to the intrinsic contact angle θ_{in} corresponding to $\partial \mathcal{F}_{\text{nl}} / \partial \theta = 0$ for $\theta = \theta_{\text{in}}$. This requirement leads to

$$\Sigma_{\text{md}} - \Sigma_{\text{mp}} = \Sigma_{\text{pd}} \cos \theta_{\text{in}} \quad (\text{S29})$$

and to the equilibrium value

$$\mathcal{F}_{\text{nl}}^{\text{eq}} = A_{\text{nl}} \Sigma_{\text{pd}} g_{\text{nl}}(\theta_{\text{in}}) \quad (\text{S30})$$

for the adhesion free energy of the necklace-like tube with the angle-dependent function

$$g_{\text{nl}}(\theta) \equiv \frac{1}{2} \cos \theta (1 - \cos \theta) - \frac{1}{4} \sin^2 \theta = -\frac{1}{4} (1 - \cos \theta)^2. \quad (\text{S31})$$

The second expression for $g_{\text{nl}}(\theta)$ implies that the adhesion free energy $\mathcal{F}_{\text{nl}}^{\text{eq}}$ is negative for nonzero values of the intrinsic contact angle θ_{in} , which shows explicitly that the adhering tube is energetically favored compared to the free tube immersed in the PEG-rich phase. Furthermore, the adhesion free energy density $\mathcal{F}_{\text{nl}}^{\text{eq}} / A_{\text{nl}}$ as obtained from (S30) depends only on two material parameters, the interfacial tension Σ_{pd} of the pd interface and the intrinsic contact angle θ_{in} , both of which can be determined experimentally, see Fig. 3b and Fig. 8c in the main text.

S2.2 Adhesion free energy of cylindrical tube

Next, consider a cylindrical tube with two spherical end caps as in Fig. S4b. The body of the cylinder has length L_{cy} and radius $R_{\text{cy}} = 1/(2|m|)$; the spherical end caps have the same radius as the cylinder. These two membrane segments have the areas

$$A_{\text{cy}}^{\text{bod}} = 2\pi R_{\text{cy}} L_{\text{cy}} = \frac{\pi}{|m|} L_{\text{cy}} \quad \text{and} \quad A_{\text{cy}}^{\text{cap}} = 4\pi R_{\text{cy}}^2 = \frac{\pi}{m^2}. \quad (\text{S32})$$

When the tube membrane forms the contact angle θ with the pd interface, the tube area A_{cy} is partitioned according to

$$A_{\text{cy}} = A_{\text{cy}}^{\text{bod}} + A_{\text{cy}}^{\text{cap}} = A_{\text{mp}} + A_{\text{md}} \quad (\text{S33})$$

with the contact areas

$$A_{\text{mp}} = 2(\pi - \theta) R_{\text{cy}} L_{\text{cy}} + 2\pi R_{\text{cy}}^2 (1 + \cos \theta) \quad (\text{S34})$$

and

$$A_{\text{md}} = 2\theta R_{\text{cy}} L_{\text{cy}} + 2\pi R_{\text{cy}}^2 (1 - \cos \theta). \quad (\text{S35})$$

At the same time, the area A_{pd} of the pd interface is reduced by

$$\Delta A_{\text{pd}} = 2R_{\text{cy}} L_{\text{cy}} \sin \theta + \pi R_{\text{cy}}^2 \sin^2 \theta. \quad (\text{S36})$$

The interfacial free energies $\mathcal{F}_{\text{cy,fr}}$ and $\mathcal{F}_{\text{cy,ad}}$ have the same general form as in (S25) and (S26). It then follows that the adhesion free energy of the cylindrical tube is given by

$$\mathcal{F}_{\text{cy}} = A_{\text{cy}}^{\text{bod}} G_{\text{cy}}^{\text{bod}} + A_{\text{cy}}^{\text{cap}} G_{\text{cy}}^{\text{cap}} \quad (\text{S37})$$

with the body contribution

$$G_{\text{cy}}^{\text{bod}} \equiv (\Sigma_{\text{md}} - \Sigma_{\text{mp}}) \frac{\theta}{\pi} - \Sigma_{\text{pd}} \frac{\sin \theta}{\pi} \quad (\text{S38})$$

and the cap contribution

$$G_{\text{cy}}^{\text{cap}} \equiv (\Sigma_{\text{md}} - \Sigma_{\text{mp}}) \frac{1}{2} (1 - \cos \theta) - \Sigma_{\text{pd}} \frac{1}{4} \sin^2 \theta. \quad (\text{S39})$$

The equilibrium value of the contact angle θ is again imposed by the condition $\partial \mathcal{F}_{\text{cy}} / \partial \theta = 0$ for $\theta = \theta_{\text{in}}$ which leads to the same relation $\Sigma_{\text{md}} - \Sigma_{\text{mp}} = \Sigma_{\text{pd}} \cos \theta_{\text{in}}$ as in (S29). As a consequence, the adhesion free energy of the capped cylindrical tube has the equilibrium form

$$\mathcal{F}_{\text{cy}}^{\text{eq}} = \Sigma_{\text{pd}} A_{\text{cy}}^{\text{bod}} g_{\text{cy}}(\theta_{\text{in}}) + \Sigma_{\text{pd}} A_{\text{cy}}^{\text{cap}} g_{\text{nl}}(\theta_{\text{in}}) \quad (\text{S40})$$

with the function

$$g_{\text{cy}}(\theta) \equiv \frac{\theta}{\pi} \cos \theta - \frac{\sin \theta}{\pi} \quad (\text{S41})$$

and the function $g_{\text{nl}}(\theta)$ as defined in (S31).

S2.3 Critical area and critical length of adhering tubes

We now compare an adhering necklace-like tube with an adhering cylindrical tube of the same tube area A_{tu} which then satisfies

$$A_{\text{tu}} = A_{\text{cy}} = A_{\text{nl}}. \quad (\text{S42})$$

The bending energy of the necklace-like tube vanishes whereas the capped cylinder has the bending energy $2\pi\kappa$ arising from the spherical end caps as in (S12). Therefore, we have to consider the free energy difference

$$\Delta\mathcal{F} = \mathcal{F}_{\text{cy}}^{\text{eq}} + 2\pi\kappa - \mathcal{F}_{\text{nl}}^{\text{eq}} \quad (\text{S43})$$

which can be rewritten in the form

$$\Delta\mathcal{F} = 2\pi\kappa - \Sigma_{\text{pd}}A_{\text{tu}} \left[1 - \frac{\pi}{m^2A_{\text{tu}}} \right] g(\theta_{\text{in}}) \quad (\text{S44})$$

with the function

$$g(\theta) \equiv g_{\text{nl}}(\theta) - g_{\text{cy}}(\theta) = \frac{1}{\pi} (\sin\theta - \theta \cos\theta) - \frac{1}{4} (1 - \cos\theta)^2. \quad (\text{S45})$$

As shown in Fig. S4c, the function $g(\theta)$ is positive for $0 < \theta < \pi$. Therefore, the shape of the adhering tube is determined by the competition between the bending energy $2\pi\kappa$ of the spherical caps, which favors necklace-like tubes, and the adhesion free energy, which favors cylindrical tubes. The spherical cap energy is independent of the tube area whereas the adhesion free energy is proportional to this area. As a consequence, short adhering tubes are necklace-like whereas long adhering tubes are cylindrical. These two regimes are separated by the critical tube area

$$A_{\text{tu}}^* = \frac{2\pi\kappa}{\Sigma_{\text{pd}}g(\theta_{\text{in}})} + \frac{\pi}{m^2} \quad (\text{S46})$$

as follows from $\Delta\mathcal{F} = 0$. The first term directly reflects the interplay between the membrane's bending rigidity κ , the interfacial tension Σ_{pd} , and the intrinsic contact angle θ_{in} for partial wetting. The second term on the right hand side of (S46) represents a correction term arising from the spherical end caps.

In Fig. S4d, we compare the free energies of single necklace-like and cylindrical tubes as a function of tube area A_{tu} for the Ld₄ and the Lo₄ vesicles. The critical tube area is about $4.4 \mu\text{m}^2$ for the Ld₄ vesicle and about $80.7 \mu\text{m}^2$ for the Lo₄ vesicle.

From an experimental point, it is easier to measure the length of individual tubes rather than their area. The critical length $L_{\text{ad}}^* = N_{\text{ad}}^*2/|m|$ of the necklace-like tube with the critical bead number N_{ad}^* is given by

$$L_{\text{ad}}^* = A_{\text{tu}}^* \frac{|m|}{2\pi} = \frac{\kappa|m|}{\Sigma_{\text{pd}}g(\theta_{\text{in}})} + \frac{1}{2|m|}. \quad (\text{S47})$$

When a necklace-like tube with length L_{ad}^* is transformed into a cylindrical tube of equal area A_{tu}^* , the tube length becomes twice as large. Therefore, in equilibrium,

necklace-like tubes should have a length up to L_{ad}^* whereas cylindrical tubes should have a length exceeding $2L_{\text{ad}}^*$. For the example displayed in Fig. S4d corresponding to the fourth deflation step, the critical tube length L_{ad}^* is $5.6 \mu\text{m}$ for the Ld_4 vesicle and $21.4 \mu\text{m}$ for the Lo_4 vesicle.

S3 Tube flexibility and persistence length

The flexibility of membrane nanotubes can be characterized by the persistence length for tube bending. This length scale governs the exponential decay of the two-point correlation function between unit tangent vectors along the tube, in close analogy to semiflexible polymers [4, 5]. A cylindrical tube of radius R_{cy} has the persistence length [6, 7]

$$\xi_p = 2\pi\kappa R_{\text{cy}}/(k_{\text{B}}T). \quad (\text{S48})$$

For $R_{\text{cy}} = 1/(2|m|)$ corresponding to the state of lowest bending energy, this expression becomes

$$\xi_p = \frac{\pi\kappa}{|m|k_{\text{B}}T}. \quad (\text{S49})$$

Using the overall partitioning of the membrane area with total tube area A and total tube length L , a cylindrical tube has the spontaneous curvature $|m| = \pi L/A$ which implies the persistence length

$$\xi_p = \frac{\kappa}{k_{\text{B}}T} \frac{A}{L} \quad (\text{cylindrical tube}). \quad (\text{S50})$$

The persistence length of the necklace-like tube, on the other hand, is comparable to the diameter $2R_{\text{ss}} = 2/|m|$ of the small spheres which implies

$$\xi_p \simeq 2R_{\text{ss}} = \frac{1}{\pi} \frac{A}{L} \quad (\text{necklace-like tube}). \quad (\text{S51})$$

For the Ld membrane studied here, the bending rigidity $\kappa_{\text{Ld}} = 0.82 \times 10^{-19} \text{ J}$ and $\kappa_{\text{Ld}}/(k_{\text{B}}T) = 20$ at room temperature (25°C). For the Ld_1 vesicle, we obtained the total tube area $A = 473 \mu\text{m}^2$ and the total tube length $L = 600 \mu\text{m}$. If the tubes were cylindrical, we would obtain the spontaneous curvature $|m| = 1/(0.251 \mu\text{m})$ and the persistence length $\xi_p = 15.4 \mu\text{m}$. If the tubes were necklace-like, we would obtain the spontaneous curvature $|m| = 1/(0.125 \mu\text{m})$ and the persistence length $\xi_p \simeq 0.25 \mu\text{m}$. Inspection of the Movies Ld_1 and Ld_2 reveals that the thermal fluctuations of the tubes lead to hairpin-like conformations with curvature radii of the order of $2 \mu\text{m}$ which implies a persistence length below $2 \mu\text{m}$. Such an upper bound for the persistence length is consistent with a necklace-like but not with a cylindrical tube morphology.

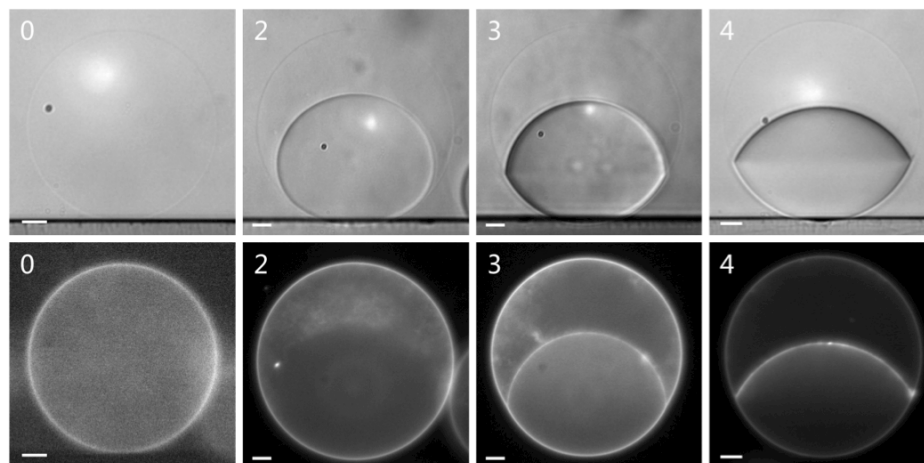


Figure S1: **Shapes of aqueous droplets for different vesicle morphologies:** The images correspond to Ld_j vesicles after the j th deflation step with $j = 0, 2, 3,$ and 4 as observed by differential interference contrast (DIC) microscopy (top row) and fluorescence microscopy (bottom row). The two images with the same j -value display the same vesicle. The white scale bar is $10 \mu\text{m}$ in all panels. The images were obtained by a horizontally aligned inverted microscope (Axiovert 135, Zeiss) equipped with a $40\times$ long distance objective and a mono-color camera.

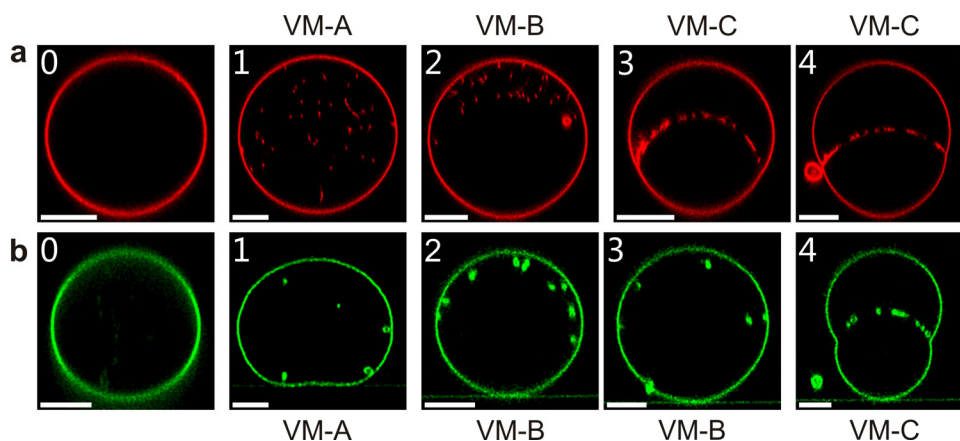


Figure S2: **Vertical cross sections of the Ld and Lo vesicles in Fig. 2:** (a) Confocal xz -scans of the Ld_j vesicles in Fig. 2c; and (b) Confocal xz -scans of the Lo_j vesicles in Fig. 2d. The three vesicle morphologies VM-A, VM-B, and VM-C are explained in Fig. 1.

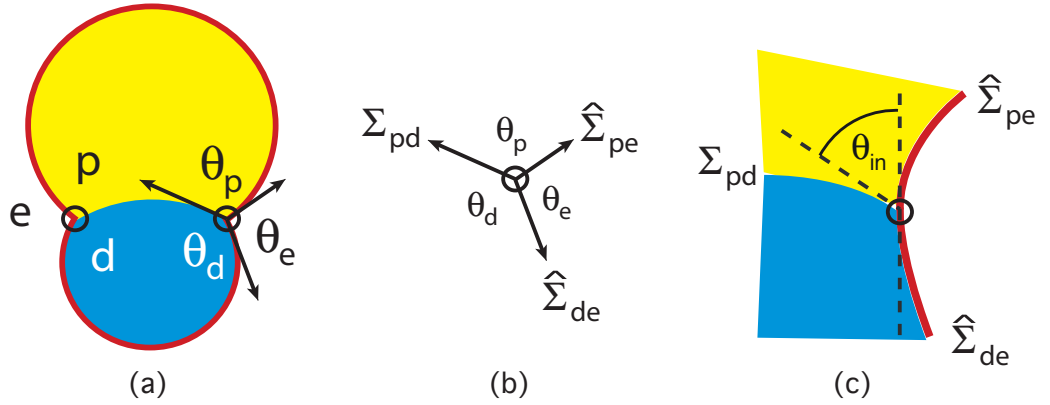


Figure S3: **Contact angles for the VM-C morphology:** The latter morphology involves one droplet of the PEG-rich phase p (yellow) and one droplet of the dextran-rich phase d (blue), both embedded in the exterior phase e (white): **(a)** The pd interface meets the membrane (red) along the contact line (two black circles). The latter line divides the membrane up into two segments, the pe segment between the PEG-rich droplet and the exterior phase as well as the de segment between the dextran-rich droplet and the exterior phase. When viewed with optical resolution, the membrane exhibits a kink at the contact line which defines the effective contact angles θ_p , θ_d , and θ_e ; **(b)** The three arrows represent the interfacial tension Σ_{pd} as well as the two membrane tensions $\hat{\Sigma}_{pe}$ and $\hat{\Sigma}_{de}$ within the pe and de segments of the membrane. Mechanical equilibrium implies that the three tension vectors add up to zero; and **(c)** Enlarged view of the smoothly curved membrane (red) close to the contact line (black circle). The vertical broken line represents the common tangent plane of the two membrane segments. The angle between this common tangent plane and the plane tangential to the pd interface provides the intrinsic contact angle θ_{in} . [8] The membrane nanotubes have been omitted here in order to focus on the shape of the mother vesicle.

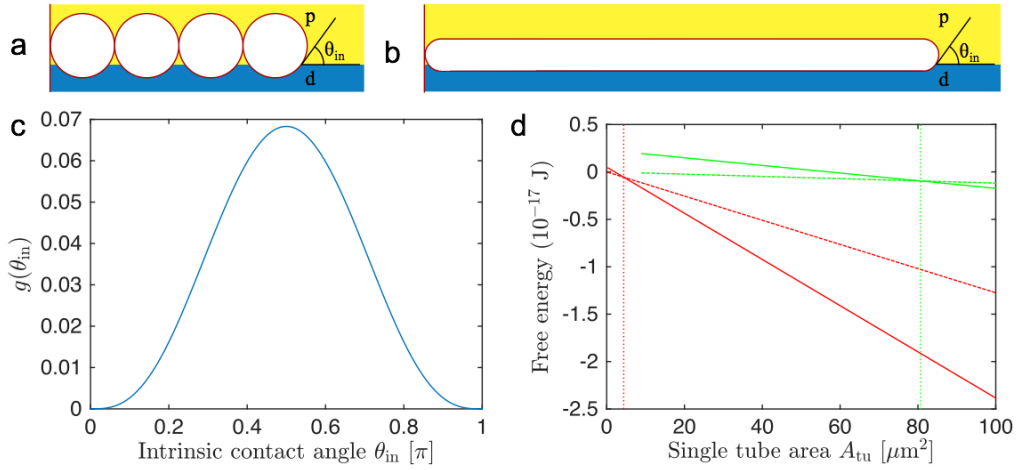


Figure S4: **Adhesion of membrane nanotubes to the pd interface (VM-C morphology):** (a) Necklace-like tube with four spherical beads and (b) Cylindrical tube with the same membrane area. Both tubes adhere to the pd interface which separates the PEG-rich phase p (yellow) from the dextran-rich phase d (blue) and forms the intrinsic contact angle θ_{in} with the tube membranes; (c) Functional dependence of the dimensionless free energy difference g on the intrinsic contact angle θ_{in} as given by equation (S45); and (d) Free energies of single necklace-like (dashed) and cylindrical (solid) tube protruding into the Ld.4 (red) and Lo.4 (green) vesicle as a function of tube area A_{tu} with $A_{tu} \geq 8\pi/m^2$ where the latter area corresponds to the 2-bead necklace $L^{[2]}$. The dashed and solid lines cross at the critical tube area A_{tu}^* which is equal to $4.4 \mu\text{m}^2$ for the Ld.4 vesicle and to $80.7 \mu\text{m}^2$ for the Lo.4 vesicle. The corresponding critical tube lengths are given by $L_{tu}^* = 5.6 \mu\text{m}$ for the Ld.4 and by $L_{tu}^* = 21.4 \mu\text{m}$ for the Lo.4 vesicle. The free energy of the necklace-like tubes is given by \mathcal{F}_{nl}^{eq} as in equation (S30); the free energy of the cylindrical tubes is equal to $\mathcal{F}_{cy}^{eq} + 2\pi\kappa$ with \mathcal{F}_{cy}^{eq} as in equation (S40).

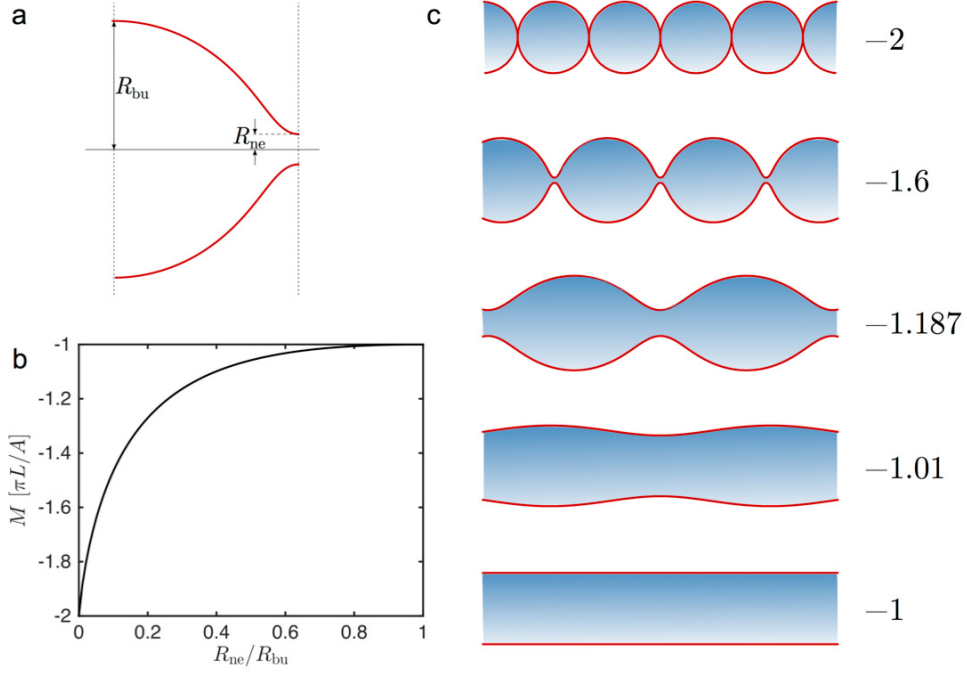


Figure S5: **Different tube shapes with the same membrane area and tube length:** (a) Each unit cell of an unduloid is characterized by its neck radius R_{ne} and its bulge radius R_{bu} . The necklace-like tube corresponds to the ratio $R_{ne}/R_{bu} = 0$, the cylindrical tube to $R_{ne}/R_{bu} = 1$; (b) For given membrane area A and tube length L , the mean curvature M increases monotonically from $M = -2\pi L/A$ for the necklace-like tube to $M = -\pi L/A$ for the cylindrical tube; and (c) Three examples of unduloids for fixed A and L that interpolate between the necklace-like and the cylindrical tube with mean curvature M in units of $\pi L/A$ (right column). As we transform the sphere-necklace into the cylinder, the neck radius R_{ne} of the intermediate unduloid increases monotonically whereas the bulge radius R_{bu} first increases and then decreases again. The latter radius has the value $A/(2\pi L)$ both for the cylindrical tube and for the sphere-necklace and attains its maximum at $M = m = -1.187\pi L/A$ with $\max(R_{bu}) = 0.662A/\pi L$.

Table S1: Deflation path within the phase diagram of Fig. 2: The deflation path in Fig. 2a,b consists of seven deflation steps which lead to seven compositions of the aqueous polymer solution within the vesicle, labeled from $j = 1$ to $j = 7$. The initial compositions in the exterior and interior solution are denoted by 0e and 0. The columns 2 - 7 display the following quantities: Dextran weight fraction w_d , PEG weight fraction w_p , total polymer mass density c_j of the interior solution, as well as concentration ratio c_j/c_0 , osmolarity ratio P_e/P_0 between the exterior and the initial osmolarities, P_e and P_0 . The exterior osmolarity P_e is increased by exchanging the external medium by a hypertonic solution with constant $w_d = w_p = 0.0327$ and an increasing weight fraction of sucrose. For $j \geq 0$, the weight fractions w_d and w_p represent the weight fractions of all dextran and all PEG molecules within the interior solution, irrespective of whether this solution is uniform or phase separated, and are characterized by the constant ratio $w_d/w_p = 1.25$. For comparison, the quantities at the critical point (cr) are also included. ‘APS’ stands for ‘aqueous phase separation’ in the vesicle interior. The last two rows describe the observed vesicle morphologies of the liquid-disordered (Ld) and liquid-ordered (Lo) membranes. The VM-B and VM-C morphologies correspond to phase separation with complete and partial wetting, respectively, of the membranes by the PEG-rich phase.

comp. j	w_d	w_p	c_j [g/cm ³]	c_j/c_0	P_e/P_0	APS	Ld morph.	Lo morph.
0e	0.0327	0.0327	0.0664		1.000	no		
0	0.0390	0.0312	0.0714	1.000	1.000	no		
1	0.0436	0.0349	0.0800	1.120	1.254	no	VM-A	VM-A
cr	0.0451	0.0361	0.0829	1.161	1.350	no		
2	0.0456	0.0365	0.0838	1.174	1.382	yes	VM-B	VM-B
3	0.0475	0.0380	0.0875	1.224	1.511	yes	VM-C	VM-B
4	0.0494	0.0395	0.0909	1.273	1.642	yes	VM-C	VM-C
5	0.0511	0.0408	0.0941	1.317	1.769	yes	VM-C	VM-C
6	0.0527	0.0422	0.0972	1.361	1.901	yes	VM-C	VM-C
7	0.0543	0.0434	0.1002	1.402	2.032	yes	VM-C	VM-C

Table S2: **Geometry of deflated Ld- j and Lo- j vesicles:** The first four rows give the lipid phase, the deflation step number (or polymer composition) j corresponding to the TableS1, the vesicle morphology, and the osmolarity ratio P_e/P_0 . The following rows contain the initial vesicle volume V_0 , the initial area A_0 , and the initial radius R_0 before the first deflation step, the apparent volume V_{app} and the apparent area A_{app} of the mother vesicle after the deflation step j , the total tube area $A = A_0 - A_{\text{app}}$, the total tube length L , and the fraction Λ of the total tube length corresponding to cylindrical tubes.

vesicle	Ld_1	Ld_2	Ld_3	Ld_4	Lo_1	Lo_2	Lo_3	Lo_4
lipid phase	Ld	Ld	Ld	Ld	Lo	Lo	Lo	Lo
defl. step j	1	2	3	4	1	2	3	4
morph.	VM-A	VM-B	VM-C	VM-C	VM-A	VM-B	VM-B	VM-C
P_e/P_0	1.25	1.38	1.51	1.64	1.25	1.38	1.51	1.64
V_0 [μm^3]	49296	30138	10223	30590	37384	14991	35177	37210
A_0 [μm^2]	6500	4683	2278	4730	5407	2940	5192	5390
R_0 [μm]	22.7	19.3	13.5	19.4	20.7	15.3	20.3	20.7
V_{app} [μm^3]	43997	25671	8350	24030	33378	12770	28730	29230
A_{app} [μm^2]	6027	4208	1992	4049	5053	2642	4536	4754
A [μm^2]	473	475	286	681	354	298	656	636
L [μm]	600	600	395	953	94	100	200	195
Λ	0	0	$\frac{1}{2} \pm \frac{1}{2}^a$	$\frac{1}{2} \pm \frac{1}{2}^a$	0	0	0	0.46

^a For the VM-C morphology of the Ld membranes, we used the estimate $\Lambda = \frac{1}{2} \pm \frac{1}{2}$ corresponding to the whole range $0 \leq \Lambda \leq 1$ of possible Λ -values.

Table S3: **Overlap of PEG and dextran chains along the deflation path:** The osmotic deflation steps generate the compositions j with total polymer concentration c_j inside the vesicles, irrespective of whether the interior solution is uniform or phase separated. This concentration determines the reduced polymer concentration $\epsilon = |c_{\text{cr}} - c|/c_{\text{cr}}$ which measures the distance from the critical consolute point with concentration c_{cr} . For the PEG and dextran chains studied here, the radii of gyration have been estimated to be $R_p = 4.05$ nm and $R_d = 21$ nm. [9] The overlap concentrations of PEG and dextran are then given by $1/[(4\pi/3)R_p^3] = 0.00359/\text{nm}^3$ and $1/[(4\pi/3)R_d^3] = 0.0258/(10\text{ nm})^3$ which are equivalent to the overlap weight fractions $w_p^* = 0.0477$ and $w_d^* = 0.0193$. We characterize the degree of overlapping and the associated strength of repulsive chain-chain interactions by the overlap ratios w_p/w_p^* and w_d/w_d^* . Columns 4 and 5 display the overlap ratios of the PEG and dextran chains within the one-phase region. In this region, the large dextran chains overlapped already at the lowest dextran concentration while the smaller PEG chains did not overlap with each other but always overlapped with the dextran chains. The corresponding ratios after phase separation are shown in columns 6 and 7 for the PEG-rich phase as well as in columns 8 and 9 for the dextran-rich phase. In the PEG-rich phase, the overlap of the PEG chains increased with each deflation step whereas the dextran chains became separated after the third step. In the dextran-rich phase, the dextran chains overlapped more and more strongly whereas the PEG chains became more and more dilute but had to overlap with the dextran chains. Thus, all polymer solutions along the deflation path were semi-dilute.

comp.	c_j	ϵ	$\frac{w_p}{w_p^*}$	$\frac{w_d}{w_d^*}$	$\frac{w_p^{\text{PE}}}{w_p^*}$	$\frac{w_d^{\text{PE}}}{w_d^*}$	$\frac{w_p^{\text{DE}}}{w_p^*}$	$\frac{w_d^{\text{DE}}}{w_d^*}$
j	[g/cm ³]							
0e	0.0664		0.69	1.69				
0	0.0714	0.139	0.65	2.02				
1	0.0800	0.035	0.73	2.26				
cr	0.0829	0	0.76	2.34				
2	0.0838	0.011			0.94	1.36	0.57	3.53
3	0.0875	0.055			1.09	0.79	0.46	4.42
4	0.0909	0.097			1.18	0.56	0.39	5.03
7	0.1002	0.209			1.38	0.25	0.28	6.78

Movie Ld_1: Morphology VM-A of Ld membrane

Giant vesicle bounded by an Ld membrane (red) after the first deflation step. The interior aqueous solution had total polymer mass density $c_1 = 1.120 c_0 = 0.965 c_{cr}$ and formed a uniform aqueous phase within the giant vesicle. The movie contains the 3-dimensional scan of the vesicle, provided by a stack of 44 confocal scans corresponding to different separations z from the cover slide, varying from $z = 1 \mu\text{m}$ to $z = 44 \mu\text{m}$ in increments of $1 \mu\text{m}$. The scan reveals many nanotubes that protrude into the vesicle interior. The thickness of these tubes is below optical resolution; the total tube length is $600 \pm 100 \mu\text{m}$.

Movie Ld_2: Morphology VM-B of Ld membrane

Giant vesicle with an Ld membrane (red) after the second deflation step. The interior aqueous solution had total polymer mass density $c_2 = 1.174 c_0 = 1.024 c_{cr}$ and was separated into two aqueous phases forming a PEG-rich and a dextran-rich droplet. The membrane was completely wetted by the PEG-rich phase and, thus, not in contact with the pd interface between the two aqueous droplets. The movie contains the 3-dimensional scan of the vesicle, provided by a stack of 37 confocal scans corresponding to different separations z from the cover slide, varying from $z = 1 \mu\text{m}$ to $z = 37 \mu\text{m}$ in increments of $1 \mu\text{m}$. The Ld membrane has formed many nanotubes that protrude into the vesicle interior but are excluded from the dextran-rich phase which is in touch with the cover slide and thus located at low z -values. The thickness of these tubes is below optical resolution; the total tube length is $600 \pm 100 \mu\text{m}$.

Movie Ld_4: Morphology VM-C of Ld membrane

Giant vesicle with an Ld membrane (red) after the fourth deflation step. The interior aqueous solution had total polymer mass density $c_4 = 1.273 c_0 = 1.097 c_{cr}$ and was phase separated into a PEG-rich and a dextran-rich droplet. The membrane was partially wetted by the PEG-rich phase and formed effective contact angles, θ_p and θ_d , with the pd interface between the two aqueous droplets (Fig. S3a). The movie contains the 3-dimensional scan of the vesicle, provided by a stack of 82 confocal scans corresponding to different separations z from the cover slide, varying from $z = 0.5 \mu\text{m}$ to $z = 41 \mu\text{m}$ in increments of $0.5 \mu\text{m}$. The scan shows many nanotubes that protrude into the vesicle interior and aggregate at the pd interface because of partial wetting. The thickness of these tubes is below optical resolution; the total tube length is $953 \pm 150 \mu\text{m}$.

Movie Lo.1: Morphology VM-A of Lo membrane

Giant vesicle with an Lo membrane (green) after the first deflation step. The interior aqueous solution had total polymer mass density $c_1 = 1.120 c_0 = 0.965 c_{cr}$ and formed a uniform aqueous phase within the vesicle. The movie contains the 3-dimensional scan of the vesicle, provided by a stack of 74 confocal scans corresponding to different separations z from the cover slide, varying from $z = 0.5 \mu\text{m}$ to $z = 37 \mu\text{m}$ in increments of $0.5 \mu\text{m}$. The Lo membrane has formed many nanotubes that protrude into the vesicle interior. The tube morphology can be optically resolved and is provided by short necklace-like tubes; the total tube length is $94 \pm 14 \mu\text{m}$.

Movie Lo.2: Morphology VM-B for Lo membrane

Giant vesicle with an Lo membrane (green) after the second deflation step. The interior aqueous solution had total polymer mass density $c_2 = 1.174 c_0 = 1.024 c_{cr}$ and was phase separated into a PEG-rich and a dextran-rich droplet. The membrane was completely wetted by the PEG-rich phase and, thus, not in contact with the pd interface between the two aqueous droplets. The movie contains the 3-dimensional scan of the vesicle, provided by a stack of 58 confocal scans corresponding to different separations z from the cover slide, varying from $z = 0.5 \mu\text{m}$ to $z = 29 \mu\text{m}$ in increments of $0.5 \mu\text{m}$. The scan reveals many nanotubes protruding into the vesicle interior without entering the dextran-rich phase which is in touch with the cover slide and thus located at low z -values. The tube morphology can be optically resolved and is provided by necklace-like tubes with an average bead radius of $0.63 \pm 0.10 \mu\text{m}$.

Movie Lo.4: Morphology VM-C for Lo membrane

Giant vesicle with an Lo membrane (green) after the fourth deflation step. The interior aqueous solution had total polymer mass density $c_4 = 1.273 c_0 = 1.097 c_{cr}$ and was phase separated into a PEG-rich and a dextran-rich droplet. The membrane was partially wetted by the PEG-rich phase and formed effective contact angles, θ_p and θ_d , with the pd interface between the two aqueous droplets (Fig. S3a). The movie contains the 3-dimensional scan of the vesicle, provided by a stack of 74 confocal scans corresponding to different separations z from the cover slide, varying from $z = 0.5 \mu\text{m}$ to $z = 37 \mu\text{m}$ in increments of $0.5 \mu\text{m}$. The Lo membrane has formed long nanotubes that protrude into the vesicle interior and tend to aggregate at the pd interface because of partial wetting. Detailed analysis of this scan (Fig. 6 in the main text) reveals the coexistence of necklace-like tubes with bead radius $R_{ss} = 0.64 \pm 0.12 \mu\text{m}$ and cylindrical tubes with tube diameter $2R_{cy} = 0.55 \pm 0.07 \mu\text{m}$.

References

- [1] Seifert, U., Berndl, K. & Lipowsky, R. Shape Transformations of Vesicles: Phase Diagram for Spontaneous Curvature and Bilayer Coupling Model. *Phys. Rev. A* **44**, 1182–1202 (1991).
- [2] Lipowsky, R. Coupling of Bending and Stretching Deformations in Vesicle Membranes. *Adv. Colloid Interface Sci.* **208**, 14–24 (2014).
- [3] Lipowsky, R. Spontaneous Tubulation of Membranes and Vesicles Reveals Membrane Tension Generated by Spontaneous Curvature. *Faraday Discuss.* **161**, 305–331 (2013).
- [4] Doi, M. & Edwards, S. *The Theory of Polymer Dynamics* (Clarendon Press, Oxford, 1986).
- [5] Kierfeld, J., Niamploy, O., Sa-yakanit, V. & Lipowsky, R. Stretching of Semi-flexible Polymers with Elastic Bonds. *Eur. Phys. J. E* **14**, 17–34 (2004).
- [6] Helfrich, W. & Harbich, W. Adhesion and Cohesion of Tubular Vesicles. *Chemica Scripta* **25**, 32–36 (1985).
- [7] Baroji, Y. F., Oddershede, L. B., Reihani, S. N. S. & Bendix, P. M. Fluorescent Quantification of Size and Lamellarity of Membrane Nanotubes. *Eur. Biophys. J.* **43**, 595–602 (2014).
- [8] Kusumaatmaja, H., Li, Y., Dimova, R. & Lipowsky, R. Intrinsic Contact Angle of Aqueous Phases at Membranes and Vesicles. *Phys. Rev. Lett.* **103**, 238103 (2009).
- [9] Liu, Y., Lipowsky, R. & Dimova, R. Concentration Dependence of the Interfacial Tension for Aqueous Two-Phase Polymer Solutions of Dextran and Polyethylene Glycol. *Langmuir* **28**, 3831–3839 (2012).

3 Critical Particle Sizes for the Engulfment of Nanoparticles by Membranes and Vesicles with Bilayer Asymmetry

3.1 Overview

In this paper, we study the engulfment of particles by model membranes and vesicles, as well as the endocytosis of nanoparticles by cells, with particular emphasis on the effects of bilayer asymmetry. The bilayer asymmetry is described quantitatively by the spontaneous curvature of the membrane.

First, we study the engulfment of particles by model vesicles using numerical energy minimization, as described in Section 1.6 of this thesis. We describe for the first time the effects of vesicle size on engulfment, and show that even small spontaneous curvatures strongly affect the engulfment behavior. We show that, depending on the values of particle size, vesicle size, adhesive strength and spontaneous curvature, there are four distinct engulfment regimes, with the particle being either free, partially engulfed, completely engulfed, or displaying bistability between the free and completely engulfed states.

We then go on to show that these four engulfment regimes are determined by the instabilities of the free and completely engulfed states, for which we obtain analytical expressions. The instability condition of the free particle state generalizes the condition for vesicle adhesion to planar substrates, see eq (1.18) in Section 1.3.3.3 of this thesis; whereas the instability condition of the completely engulfed state generalizes the ideal neck condition previously known for the budding of homogeneous vesicles, see eq (1.14) in Section 1.3.3.1. The two stability conditions are then used to show that the engulfment of particles by planar or quasi-planar membranes is strongly affected by spontaneous curvature. They also provide a way to measure the spontaneous curvature and particle–membrane adhesive strength from image analysis of experiments or simulations.

Finally, we consider particle-induced segregation of membrane components, leading to a bound membrane segment with different bending rigidity and spontaneous curvature than the unbound segment. We model the case of clathrin-mediated endocytosis in cells by considering bound segments with a large negative spontaneous curvature compared to the unbound segment. We show that the non-monotonic dependence of particle uptake by cells observed in experiments, as introduced in Section 1.5.3 of this thesis, can be explained

as a consequence of the strongly asymmetric clathrin coat. Our analytical expression for the particle uptake provides a fit to existing experimental results on clathrin-mediated endocytosis of gold nanoparticles by HeLa cells.

The paper thus expands the existing literature on engulfment by model membranes as well as by biological cells (see Section 1.5 of this thesis) in a new direction, showing that bilayer asymmetry (in the form of spontaneous curvature) plays a key role in particle engulfment and should not be neglected. The analytical expressions for the instability of the free and completely engulfed states allows one to understand and predict particle engulfment without the need to perform numerical calculations.

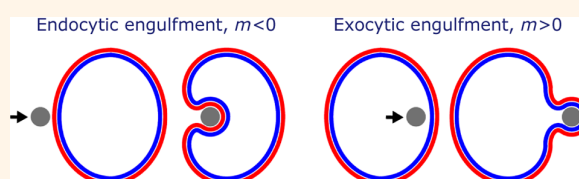


Critical Particle Sizes for the Engulfment of Nanoparticles by Membranes and Vesicles with Bilayer Asymmetry

Jaime Agudo-Canalejo and Reinhard Lipowsky*

Theory & Biosystems, Max Planck Institute of Colloids and Interfaces, 14424 Potsdam, Germany

ABSTRACT The adhesion and engulfment of nanoparticles by biomembranes is essential for many processes such as biomedical imaging, drug delivery, nanotoxicity, and viral infection. Many studies have shown that both surface chemistry, which determines the adhesive strength of the membrane–particle interactions, and particle size represent key parameters for these processes. Here, we show that



the asymmetry between the two leaflets of a bilayer membrane provides another key parameter for the engulfment of nanoparticles. The asymmetric membrane prefers to curve in a certain manner as quantitatively described by its spontaneous curvature. We derive two general relationships between particle size, adhesive strength, and spontaneous curvature that determine the instabilities of (i) the nonadhering or free state and (ii) the completely engulfed state of the particle. For model membranes such as lipid or polymer bilayers with a uniform composition, the two relationships lead to two critical particle sizes that determine four distinct engulfment regimes, both for the endocytic and for the exocytic engulfment process. For strong adhesion, the critical particle sizes are on the order of 10 nm, while they are on the order of 1000 nm for weak or ultraweak adhesion. Our theoretical results are therefore accessible to both experimental studies and computer simulations of model membranes. In order to address the more complex process of receptor-mediated endocytosis, we take the adhesion-induced segregation of membrane components into account and consider bound and unbound membrane segments that differ in their spontaneous curvatures. To model protein coats as formed during clathrin-dependent endocytosis, we focus on the case in which the bound membrane segments have a large spontaneous curvature compared to the unbound ones. We derive explicit expressions for the engulfment rate and the uptake of nanoparticles, which both depend on the particle size in a nonmonotonic manner, and provide a quantitative fit to experimental data for clathrin-dependent endocytosis of gold nanoparticles.

KEYWORDS: nanoparticles · membranes and vesicles · bilayer asymmetry · spontaneous curvature · endo- and exocytic engulfment · adhesion length · clathrin-dependent endocytosis · stability analysis · free energy minimization

The interaction of nanoparticles with biological and biomimetic membranes plays an important role in many different processes such as biomedical imaging, drug delivery, nanotoxicity, and viral infection.^{1–4} Two important steps of these processes are the adhesion of the particles to the membranes and their subsequent engulfment by these membranes, both steps being governed by the interplay of particle adhesion and membrane bending.⁵ Biomimetic model systems consisting of nanoparticles in contact with lipid^{6–10} or polymer¹¹ vesicles have been used to elucidate the particle adhesion and engulfment process experimentally. In addition, several theoretical approaches and computational methods have been applied to these model systems: energy minimization,^{5,12–16} Monte

Carlo simulations,^{17–19} and molecular dynamics simulations.^{20–24} Furthermore, the cellular uptake of nanoparticles, which requires particle engulfment as an important substep, has been intensively studied in the context of receptor-mediated endocytosis, both experimentally^{25,26} and theoretically.^{27–30}

The engulfment process depends on the strength of the attractive membrane–particle interactions, on the bending elasticity of the membranes, on the particle size, and on the geometry of the curved membranes. Experimental studies of several model systems have shown that the adhesive strength between lipid bilayers and inorganic materials can vary between 10^{-5} mN/m for ultraweak adhesion and 1 mN/m for strong adhesion.^{31–33} This range of adhesive

* Address correspondence to lipowsky@mpikg.mpg.de.

Received for review October 27, 2014 and accepted April 3, 2015.

Published online April 03, 2015
10.1021/acsnano.5b01285

© 2015 American Chemical Society

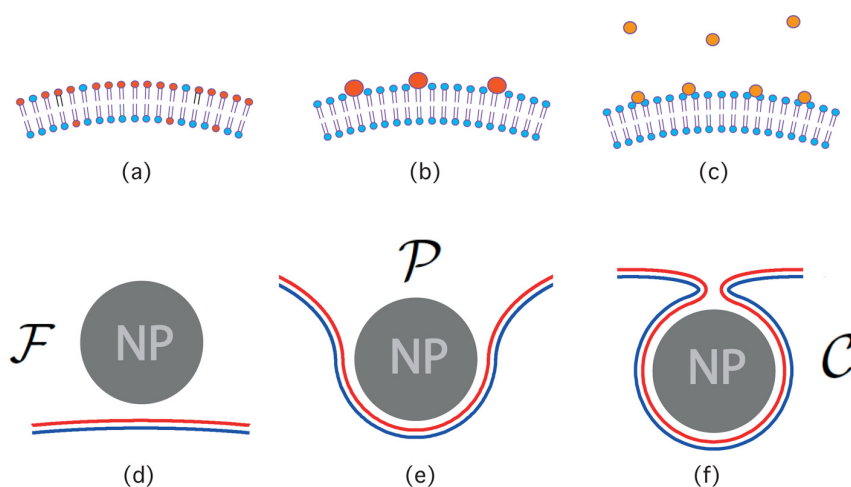


Figure 1. Engulfment of nanoparticles by asymmetric membranes: (a–c) Molecular mechanisms leading to bilayer membranes with two different leaflets: (a) compositional lipid asymmetry between the two leaflets of the bilayer; (b) asymmetric concentration of membrane-anchored molecules with a bulky headgroup such as glycolipids; and (c) asymmetric adsorption of ions or small molecules. (d–f) Different states of a spherical nanoparticle (gray, NP) in contact with an asymmetric bilayer (blue–red): (d) unbound or free state \mathcal{F} ; (e) partially engulfed state \mathcal{P} ; and (f) completely engulfed state \mathcal{C} with a narrow membrane neck that connects the adhering and unbound segments of the membrane. The lipid bilayer has a thickness of about 4 nm in all panels (a)–(f). In panels (d)–(f), the asymmetry of the bilayer is visualized by two different colors (blue and red) for the two leaflets. The nanoparticle has a radius of about 16 nm.

strengths can also be probed *via* specific receptor–ligand bonds by varying the surface density of the ligand molecules on the nanoparticles. An adhesive strength that is large compared to 1 mN/m may lead to membrane rupture. The curvature elasticity of a bilayer membrane depends on its bending rigidity, with a typical magnitude of about 10^{-19} J, and on its spontaneous curvature, which describes the asymmetries between the two leaflets of the bilayer membrane.^{34–36}

Such asymmetries can arise from a variety of molecular mechanisms; see Figure 1. First, all biological membranes have a compositional asymmetry,³⁷ and new experimental protocols have been recently developed^{38–40} by which one can mimic such an asymmetry in lipid and polymer membranes. A special case of compositional asymmetry is provided by membrane-anchored molecules with a bulky headgroup such as the glycolipids schematically shown in Figure 1b. Asymmetric membranes may also arise from the adsorption of small molecules that have different concentrations in the two aqueous phases adjacent to the membranes; see Figure 1c. Very recently, the corresponding spontaneous curvature has been determined by molecular dynamics simulations.⁴¹

In this paper, we first develop a systematic theory for the engulfment of nanoparticles by asymmetric model membranes such as lipid or polymer bilayers. These model membranes are taken to have a laterally uniform composition and, thus, a uniform spontaneous curvature. In addition, we will extend our theory to membranes with intramembrane domains induced by receptor-mediated adhesion and recruitment of coat

proteins. In the latter case, the domains are asymmetrically covered by proteins and then acquire a protein-induced spontaneous curvature. Both for uniform membranes and for membranes with intramembrane domains, we will focus on the dependence of the engulfment process on the particle size, a key parameter for the interaction of nanoparticles with membranes.^{4,25,26}

Even for the relatively simple case of nanoparticles in contact with uniform membranes, our theory predicts two critical particle sizes, R_{fr} and R_{ce} , which separate different size regimes characterized by four distinct engulfment morphologies. When the particle radius R_{pa} exceeds the critical size R_{fr} , the non-adhering or free state (Figure 1d) is unstable and the membrane starts to spread over the particle surface. When the particle radius R_{pa} is smaller than the critical size R_{ce} , the completely engulfed state (Figure 1f) is unstable and the narrow membrane neck starts to open up. In general, the critical size R_{fr} for the instability of the free state may be larger or smaller than the critical size R_{ce} for the instability of the completely engulfed state. Furthermore, we also show that the critical size R_{fr} is independent of the spontaneous curvature of the bilayer membrane, whereas the critical size R_{ce} depends strongly on this curvature, even for rather small bilayer asymmetries. The critical sizes R_{fr} and R_{ce} also depend on the origin of the nanoparticles, *i.e.*, on whether the particles originate from the exterior or interior aqueous solution. In analogy with the corresponding processes for cell membranes, we will use the terms “endocytic” and “exocytic” engulfment for particles that approach the

vesicle membranes from the exterior and interior solution, respectively.

The two critical particle sizes R_{fr} and R_{ce} are predicted to be on the order of 10 nm for strong adhesion and on the order of 1000 nm for weak or ultraweak adhesion between the nanoparticles and the lipid bilayer. This range of sizes is accessible to experimental studies with inorganic nanoparticles such as silica or glass beads as well as with organic nanoparticles based on PLGA⁴² or other polymers. In addition, the strong adhesion regime can be investigated by molecular dynamics simulations,^{20–24} whereas the weak adhesion regime can be studied by Monte Carlo^{17–19} simulations. It is also interesting to note that the typical sizes of viruses lie within the same size range between 10 and 1000 nm.

If the particles are smaller than the lower critical size, they do not adhere to the membrane and remain in their free, nonadhering state. If the particle size exceeds the upper critical size, the particles are completely engulfed by the membrane. The most interesting behavior is found for particles with an intermediate size between the two critical sizes. The intermediate size regime is characterized by partial engulfment (Figure 1e) for $R_{fr} < R_{ce}$, but exhibits bistability for $R_{fr} > R_{ce}$. In the latter case, both the free (Figure 1d) and the completely engulfed (Figure 1f) states represent metastable particle states separated by an energy barrier. For vesicles with a convex shape such as spherical or oblate vesicles, bistability is favored by negative spontaneous curvature and by endocytic engulfment, whereas partial engulfment is favored by positive spontaneous curvature and by exocytic engulfment.

In order to address the more complex process of receptor-mediated endocytosis, we generalize the instability relationships to nonuniform membranes arising from the particle-induced segregation of membrane components. The different compositions of the bound membrane segment in contact with the nanoparticle and the unbound mother membrane will, in general, lead to distinct spontaneous curvatures and bending rigidities for the two types of membrane segments. To model a membrane with a protein coat as in clathrin-dependent endocytosis, we focus on the case in which the spontaneous curvature m_{bo} of the bound segment is large compared to the spontaneous curvature m of the mother membrane. As a result, we find that nanoparticles are completely engulfed if they have an intermediate size R_{pa} with $R_{min} < R_{pa} < R_{max}$.

We also derive an equation of motion for the contact line as it moves from the free to the completely engulfed state. The solution of this equation leads to explicit expressions for the size-dependent engulfment rate and for the uptake of nanoparticles by model membranes. Both the engulfment rate and the particle uptake are nonmonotonic functions of the particle size.

In addition, the expression for the particle uptake provides a quantitative fit to the experimental data of Chithrani *et al.*,^{25,26} who studied the clathrin-dependent endocytosis of gold nanoparticles.

Our paper is organized as follows. First, we explain the basic geometry of endocytic and exocytic engulfment and how these two processes are affected by the sign of the spontaneous curvature. Second, we identify the relevant parameters of vesicle–particle systems and show that real systems can be characterized by a certain adhesion length, which varies in different systems between 10 nm and a couple of micrometers. We then consider endocytic engulfment by spherical and oblate vesicles and study the different engulfment regimes as a function of particle size, vesicle size, and spontaneous curvature. The boundary lines between these different regimes determine the critical particle sizes, which depend both on the overall vesicle size and on the spontaneous curvature of the vesicle membrane. Next, we show that these critical sizes can be obtained, in a rather general and transparent manner, if one studies the stability of the free and completely engulfed states. The corresponding stability analysis leads to two relatively simple relationships between the particle size, the adhesion length, the spontaneous curvature, and the curvatures of the local membrane segments in contact with the free or completely engulfed particles. These two relationships are then used to derive the critical particle sizes for endocytic engulfment. The corresponding results for exocytic engulfment are described in the Supporting Information (SI). We also show how a measurement of the two critical particle sizes can be used to determine the adhesion length and the spontaneous curvature. At the end, we extend our theory to receptor-mediated adhesion and engulfment and compare our results with experimental data on clathrin-dependent endocytosis of gold nanoparticles as well as with previous theoretical studies.

RESULTS AND DISCUSSION

Endocytic and Exocytic Engulfment of Nanoparticles. The strong effect of small bilayer asymmetries on the engulfment of nanoparticles can be understood intuitively if one compares endocytic and exocytic engulfment as depicted in Figure 2. In this figure, we see bilayer membranes of closed vesicles that partition space into two aqueous compartments, an exterior and an interior one. For endocytic engulfment as depicted in Figure 2a, the particle is initially located in the exterior compartment and its engulfment leads to a membrane segment that bulges toward the interior compartment. For exocytic engulfment as in Figure 2b, the particle originates from the interior compartment and leads to an adhering membrane segment that bulges toward the exterior compartment.

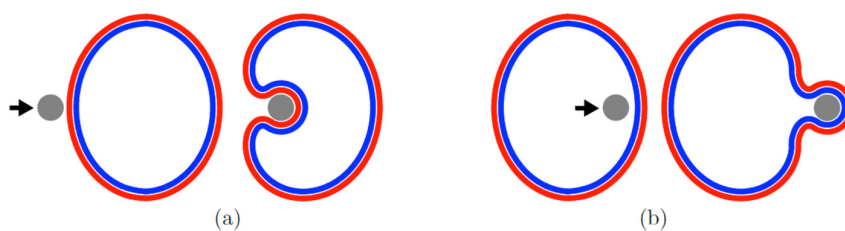


Figure 2. Nanoparticles interacting with lipid vesicles: (a) endocytic and (b) exocytic engulfment of a nanoparticle originating from the exterior and interior aqueous compartment, respectively. In both (a) and (b), the left subfigure displays the initial contact of the nanoparticle with the vesicle membrane. The bilayer membrane consists of two leaflets (blue and red) that can differ in their molecular composition; compare Figure 1. Note that the bound membrane segment around the particle bulges toward the inner (blue) leaflet in (a) and toward the outer (red) leaflet in (b). Therefore, the endocytic and exocytic processes are facilitated by bilayer asymmetries that lead to negative and positive spontaneous curvatures, $m < 0$ and $m > 0$, respectively.

In order to describe these differences in a quantitative manner, we regard the membrane as a smooth surface and consider its mean curvature M as defined by differential geometry. At any point of such a surface, the mean curvature is given by $M \equiv (1/2)(C_1 + C_2)$, where the two principal curvatures C_1 and C_2 represent the smallest and the largest curvatures of all normal surface sections through the chosen point.⁴³ It is important to note that the mean curvature can be positive or negative. The vesicles in Figure 2a and b are both convex before they interact with the nanoparticle. Likewise, after engulfment, all membrane segments of the two vesicles are still convex apart from (i) the segments adhering to the nanoparticle and (ii) the segments that form the narrow membrane necks. Membrane segments of a convex shape have a positive mean curvature $M > 0$. On the other hand, for a nanoparticle of size R_{pa} , the adhering membrane segment around the nanoparticle has the negative mean curvature $M = -1/R_{pa}$ for endocytic engulfment (Figure 2a), whereas the corresponding segment for exocytic engulfment (Figure 2b) has the positive mean curvature $M = +1/R_{pa}$.

A membrane with spontaneous curvature m tries to attain a shape for which the mean curvature M is close to m . Therefore, a *positive* spontaneous curvature supports *exocytic* engulfment as in Figure 2b, for which the adhering membrane segment has positive mean curvature, but suppresses endocytic engulfment as in Figure 2a, for which the adhering membrane segment has negative mean curvature. *Vice versa*, a *negative* spontaneous curvature supports *endocytic* and suppresses exocytic engulfment.

Relevant Parameters of Vesicle–Particle Systems. Our quantitative results are based on the free energy of the vesicle–particle systems as described in the Methods section. This free energy depends on a few geometric and material parameters: particle size, membrane area, vesicle volume, bending rigidity and spontaneous curvature of the vesicle membrane, as well as adhesive strength arising from the molecular interactions between particle and membrane. We use the membrane area A of the vesicle to define the vesicle size,

$$R_{ve} \equiv \sqrt{A/4\pi} \quad (1)$$

and take the bending rigidity κ of the membrane as the basic energy scale. In the absence of nanoparticles, the vesicle shape then depends on only two parameters,³⁵ namely, on (i) the spontaneous curvature m , which describes the asymmetry of the bilayer membrane (see Figure 1), and on (ii) the volume-to-area ratio (or reduced volume) as given by

$$v \equiv 3V/4\pi R_{ve}^3 \quad (2)$$

Note that the dimensionless quantity v satisfies $0 < v \leq 1$, where the maximal value $v = 1$ is obtained for a spherical shape. The volume-to-area ratio is controlled by the osmotic conditions: the vesicle adjusts its volume in such a way that the osmotic pressure within the interior aqueous compartment matches the osmotic pressure in the exterior aqueous compartment, apart from small differences on the order κ/R_{ve}^3 . It is also instructive to consider the special case of small osmotic pressures for which the vesicle can freely adjust its volume. Note that, in the theoretical approach used here, the membrane tension does not represent an independent parameter but plays the role of a Lagrange multiplier that is determined by the geometric and material parameters just described in order to ensure that the membrane has a certain prescribed area A ,^{35,36} see SI Text A.

The vesicle membrane is now exposed to nanoparticles that are taken to be spherical with radius R_{pa} . The intermolecular interactions between the membrane and the particles are described by the adhesive strength $|W|$, which represents the absolute value of the adhesion energy per unit area for the particle bound to the membrane.⁴⁴ A combination of the adhesive strength $|W|$ and the bending rigidity κ defines the adhesion length,

$$R_W \equiv \sqrt{2\kappa/|W|} \quad (3)$$

which we will use instead of the parameter $|W|$. Depending on the lipid composition of the bilayer membrane and on the adhesive material, the adhesion length R_W can vary between about 10 nm for strong adhesion and a few micrometers for ultraweak

TABLE 1. Five Systems Illustrating the Wide Range of Values for the Adhesion Length R_W

adhesion regime	lipid bilayer	adhesive material	κ [10^{-19} J]	$ W $ [mJ/m ²]	R_W [nm]
strong	DMPC	silica	0.8 ^a	0.5–1 ^b	13–18
strong	eggPC	glass	≈ 1	0.15 ^c	26
intermediate	DMPC	receptor–ligand	0.8 ^a	0.03 ^d	73
weak	DOPC/DOPG	coated glass	0.4 ^e	3×10^{-4e}	510
ultraweak	DOPC/DOPG	glass	0.4 ^e	10^{-5e}	2800

^a Ref 46. ^b Ref 33. ^c Ref 31. ^d Ref 45. ^e Ref 32.

adhesion, as illustrated by the examples in Table 1. In this table, we also included one example for adhesion mediated by receptor–ligand bonds as studied in ref 45, even though the surface density of the receptor and ligand molecules has not been measured in these experiments. If the ligands on the nanoparticles have the surface density ρ_{lig} and the receptor–ligand bonds have a binding free energy $|U|$ that is large compared to $k_B T$, the contribution of these bonds to the adhesive strength $|W|$ is given by $|U|\rho_{\text{lig}}$. The binding free energy $|U|$ includes both enthalpic and entropic contributions to the bond formation and, in particular, the losses of configurational entropy suffered by the receptors and ligands during the binding process as well as the entropy gained by the release of “bound” water from the two binding partners.

Thus, apart from the volume-to-area ratio v of the vesicle, the vesicle–particle systems are characterized by four different length scales: the vesicle size R_{ve} , the particle radius R_{pa} , the adhesion length R_W , and the inverse spontaneous curvature $1/m$. The vesicle size and the particle radius represent geometric parameters, whereas the adhesion length and the spontaneous curvature are material parameters. In a typical experiment, the material parameters are more difficult to vary than the geometric parameters. In order to simplify the following discussion, we will typically choose the adhesion length R_W , which is a material parameter, as the basic length scale and then measure the particle size, the vesicle size, and the spontaneous curvature in units of R_W .

As far as the spontaneous curvature is concerned, we will first focus on *small* bilayer asymmetries in the sense that the spontaneous curvature m is small compared to the inverse adhesion length $1/R_W$. As shown below, these relatively small values of the spontaneous curvatures already lead to profound changes in the behavior of the vesicle–particle systems.

Endocytic Engulfment by Spherical and Oblate Vesicles. We now consider endocytic engulfment by vesicles with a convex shape as schematically depicted in Figure 2a and regard the particle size R_{pa} as our basic control parameter. Using a variety of theoretical methods, we studied the parameter regimes for which a nanoparticle in contact with such a vesicle attains a free, partially engulfed, or completely engulfed state. We found that

these parameter regimes can be deduced from the stability of the free particle state \mathcal{F} and the completely engulfed state \mathcal{G} . The corresponding instability lines define four different engulfment regimes denoted by \mathcal{F}_{st} , \mathcal{P}_{st} , \mathcal{G}_{st} , and \mathcal{B}_{st} as shown in Figure 3 and Figure 4 for spherical and oblate vesicles. The bistable regime \mathcal{B}_{st} contains the transition line L_* at which the free and the completely engulfed state have the same free energy. The different engulfment regimes exhibit characteristic free energy landscapes $E(\phi)$ as a function of the wrapping (or spreading) angle ϕ , which determines the fraction of the membrane-covered particle surface and, thus, the contact area between membrane and particle; see Figures S1 and S2 as well as SI Text A.

For particle radii R_{pa} that are small compared to the adhesion length R_W , the nanoparticles are free and do not adhere to the membrane. In the corresponding engulfment regime \mathcal{F}_{st} , the free particle state \mathcal{F} is stable and the completely engulfed state is unstable. For particle radii R_{pa} that are large compared to the adhesion length R_W , the particle is completely engulfed by the membrane and belongs to the engulfment regime \mathcal{G}_{st} , in which the completely engulfed state \mathcal{G} is stable, whereas the free state is unstable. The most interesting behavior is found for intermediate particle radii R_{pa} that are on the order of the adhesion length R_W . For these intermediate sizes, we find two different engulfment regimes, \mathcal{B}_{st} and \mathcal{P}_{st} . The regime \mathcal{B}_{st} is characterized by bistable behavior because both the free and the completely engulfed states are (meta)stable and separated by an energy barrier; see Figure S2d–f. Finally, in the engulfment regime \mathcal{P}_{st} , the states \mathcal{F} and \mathcal{G} are both unstable, which implies that the particle attains a partially engulfed state \mathcal{P} as in Figure 1e. The defining properties of the four engulfment regimes are summarized in Table 2.

The boundaries between the four engulfment regimes are provided by the instability lines L_{fr} and L_{ce} of the free and completely engulfed state, which depend on the vesicle size R_{ve} and on the spontaneous curvature m . Indeed, inspection of Figure 3 and Figure 4 shows that negative spontaneous curvatures lead to the bistable engulfment regime \mathcal{B}_{st} for intermediate particle sizes, whereas positive spontaneous curvatures favor the regime \mathcal{P}_{st} with partially engulfed states. Furthermore, as we increase the vesicle size R_{ve} , the bistable regime \mathcal{B}_{st} shrinks, whereas the partially engulfed regime \mathcal{P}_{st} expands.

Within the latter regime, the contact area between the membrane and the particle changes in a continuous manner as we vary the particle size R_{pa} . Thus, in the regime \mathcal{P}_{st} , the contact area increases continuously from a vanishingly small value at the instability line L_{fr} up to the total surface area of the particle at the instability line L_{ce} . In contrast, when we probe the bistable regime \mathcal{B}_{st} , the contact area changes abruptly or discontinuously as the particle size R_{pa} is varied.

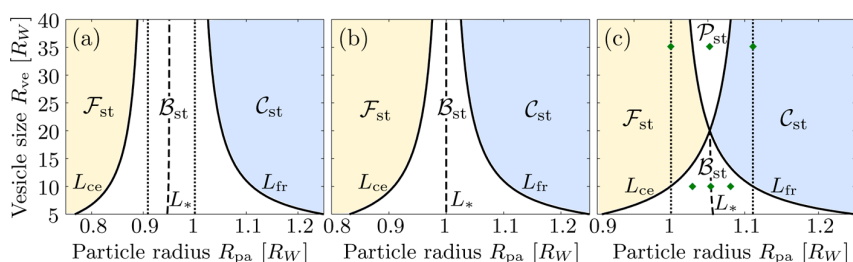


Figure 3. Different engulfment regimes \mathcal{F}_{st} (yellow), \mathcal{C}_{st} (blue), \mathcal{B}_{st} (white), and \mathcal{P}_{st} (white) for the endocytosis of a nanoparticle with radius R_{pa} by a spherical vesicle of size R_{ve} . The vesicle has a fixed membrane area and an adjustable volume. The three panels (a–c) correspond to the three values $m = -0.05/R_W$, 0 , and $+0.05/R_W$ for the spontaneous curvature m . The different regimes are defined by the two instability lines L_{fr} and L_{ce} for the free and the completely engulfed state. The asymptotes of the two instability lines for large R_{ve} are indicated by vertical dotted lines. The bistable regimes \mathcal{B}_{st} contain the transition lines L_* (dashed) at which the free and completely engulfed states coexist. For panel (c) with $m = 0.05/R_W$, the two instability lines L_{fr} and L_{ce} intersect. Close to the intersection point, the system is “multicritical” and reacts sensitively to small changes in both particle and vesicle size. The six diamonds (green) in panel (c) correspond to the free energy landscapes in Figure S2.

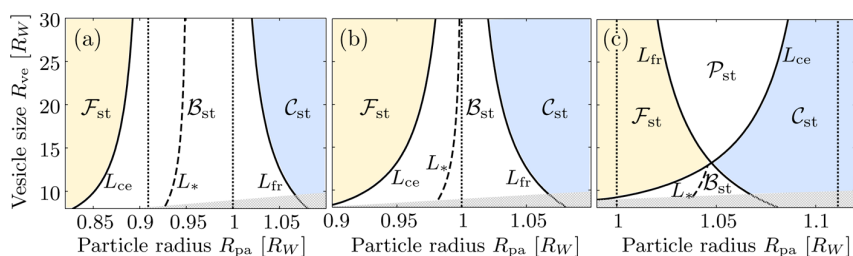


Figure 4. Different engulfment regimes for the endocytosis of a nanoparticle at the pole of an oblate vesicle with volume-to-area ratio $\nu = 0.98$. The three panels (a)–(c) correspond to the three values $m = -0.05/R_W$, 0 , and $+0.05/R_W$ of the spontaneous curvature. The two instability lines L_{fr} and L_{ce} , the transition line L_* , and the four engulfment regimes \mathcal{F}_{st} , \mathcal{P}_{st} , \mathcal{C}_{st} , and \mathcal{B}_{st} have the same meaning as in Figure 3. The vertical dotted lines again indicate the asymptotes of the instability lines for large R_{ve} , with L_{fr} approaching $R_{pa}/R_W = 1$ in all three cases. For panel (c), with $m = 0.05/R_W$, the intersection point of the two instability lines again leads to “multicritical” behavior. The shaded area (grey) close to the x -axis indicates the size regime in which the vesicle becomes too small to accommodate the completely engulfed particle.

TABLE 2. Four Engulfment Regimes \mathcal{F}_{st} , \mathcal{C}_{st} , \mathcal{B}_{st} , and \mathcal{P}_{st} As Defined via the (In)Stability of the Free State \mathcal{F} (Figure 1d) and by the (In)Stability of the Completely Engulfed State \mathcal{C} (Figure 1f)

	\mathcal{F}_{st}	\mathcal{C}_{st}	\mathcal{B}_{st}	\mathcal{P}_{st}
state \mathcal{F}	stable	unstable	(meta)stable	unstable
state \mathcal{C}	unstable	stable	(meta)stable	unstable

Indeed, when we enter the bistable regime \mathcal{B}_{st} from the free regime \mathcal{F}_{st} by crossing the instability line L_{ce} in Figure 3 or Figure 4, the membrane will not spread over the particle surface because the free particle state is stable up to the transition line L_* and remains metastable between the line L_* and the instability line L_{fr} ; see Figure S2d–f. Thus, spreading will occur only when we reach the instability line L_{fr} , at which the free state becomes unstable and the energy barrier between the two states vanishes. Likewise, when we enter the regime \mathcal{B}_{st} from the completely engulfed regime \mathcal{C}_{st} by crossing the instability line L_{fr} , the completely engulfed state is stable up to the transition line L_* and remains metastable until we reach the instability line L_{ce} , where the energy barrier for neck opening vanishes.

For the examples shown in Figure 3 and Figure 4, the engulfment process is discontinuous for all vesicle sizes if the spontaneous curvature $m \leq 0$. For positive values of m , the engulfment process is still discontinuous for small vesicle sizes R_{ve} but continuous for large values of R_{ve} . In the latter case, the two instability lines intersect; see Figure 3c and Figure 4c. Close to the corresponding intersection points, the system exhibits “multicritical” behavior in the sense that it reacts sensitively to small changes in both particle and vesicle size.

The case with zero spontaneous curvature as illustrated in Figure 3b and Figure 4b turns out to be special: as indicated in these panels, both instability lines approach the *same* asymptotic value $R_{pa}/R_W = 1$ as the vesicle size R_{ve} becomes large. The latter behavior can be derived from explicit expressions for the instability lines L_{fr} and L_{ce} as described in the next subsections. In fact, these expressions provide two relatively simple relationships between the parameters of the vesicle–particle systems and two local curvatures of the vesicle membrane. As a consequence, these relationships allow us to explore the parameter space of these systems in a global manner.

Instability of Free State and Onset of Endocytic Engulfment.

In order to determine the instability of the free state \mathcal{F} , we compare the latter state as depicted in Figure 5a to a partially engulfed state with a small contact area as in Figure 5b. The convex membrane segment shown in Figure 5a has a positive mean curvature $M_{ms} > 0$. The latter curvature can be negative but must satisfy $M_{ms} > -1/R_{pa}$ in order to ensure that the membrane does not intersect the particle before contact. The stability limit of the free state is obtained from the requirement that the mean curvature at the attachment point is the same before and after contact, which implies that the mean curvature M_{ms} of the membrane segment before contact is equal to the contact mean curvature $M_{co} = 1/R_W - 1/R_{pa}$; see Methods section. It then follows that the instability line L_{fr} of the free state \mathcal{F} is described by

$$R_{pa} = R_{fr} \equiv \frac{1}{R_W^{-1} - M_{ms}} \quad \text{for} \\ M_{ms} < 1/R_W \quad (L_{fr}, \text{ endocytosis}) \quad (4)$$

and that the membrane segment starts to spread over the particle if

$$R_{pa} > R_{fr} \quad \text{and} \\ M_{ms} < 1/R_W \quad (\text{unstable } \mathcal{F}, \text{ endocytosis}) \quad (5)$$

For strongly curved membrane segments with a positive mean curvature M_{ms} larger than $1/R_W$, the free state \mathcal{F} is stable for all particle sizes; that is, the critical particle size $R_{fr} = \infty$. The latter situation includes the limiting case $R_{pa} = \infty$, for which the adhesive nanoparticle becomes an adhesive planar surface. Therefore, such a surface cannot bind small spherical vesicles with radius $R_{ve} = 1/M_{ms} < R_W$, in agreement with the results of ref 44.

The vesicle with an adjustable volume (Figure 3) has a spherical shape, which implies that the segment curvature M_{ms} has the constant value $M_{ms} = 1/R_{ve}$. For the oblate vesicle with fixed volume-to-area ratio $v = 0.98$ (Figure 4), the segment curvature M_{ms} at the pole depends on the spontaneous curvature m and has to be determined numerically from the shape of the free oblate vesicle, which is calculated by minimizing its free energy as described in the Methods section. The same method has been used to check and validate the instability criterion in eq 5 for a large number of different parameter values.

The onset of adhesion is related to the behavior of the free energy landscape $E(\phi)$ for small values of the wrapping angle ϕ , which is given by $E(\phi) \approx E(0) + (1/2)E''\phi^2$. As shown in the SI Text A, the second derivative E'' of the free energy with respect to ϕ at $\phi = 0$ is given by

$$E'' = 4\pi\kappa \left[-\left(\frac{R_{pa}}{R_W}\right)^2 + (1 + R_{pa} M_{ms})^2 \right] \quad (6)$$

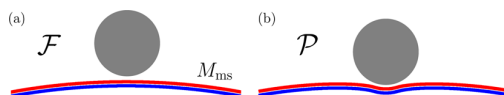


Figure 5. Onset of endocytic engulfment: (a) free state \mathcal{F} of nanoparticle (gray) and asymmetric bilayer (blue–red) compared to (b) partially engulfed state \mathcal{P} with a small contact area. The free state is unstable if the initial spreading of the bilayer membrane onto the particle leads to a gain in adhesion energy that overcompensates the increase in the membrane's bending energy. The corresponding instability criterion in eq 5 involves the mean curvature M_{ms} of the membrane segment before contact. For the convex shape shown here, the segment curvature M_{ms} is positive. In general, this curvature must be larger than $-1/R_{pa}$ to ensure that membrane and particle do not intersect each other.

This expression can be decomposed into two contributions arising from (i) the bound membrane segment in contact with the nanoparticle and (ii) the unbound membrane segment close to the contact line. For $M_{ms} = m$, the contribution from the unbound segment vanishes and E'' becomes equal to the contribution from the bound segment. The free state \mathcal{F} with $\phi = 0$ is stable and unstable if it represents a minimum and maximum of the energy landscape with $E'' > 0$ and $E'' < 0$, respectively; see Figure S2. A bit of algebra shows that the condition $E'' \leq 0$ is equivalent to the relationship $R_{pa} \geq R_{fr}$, as given by eqs 4 and 5, when we take the two constraints $R_{pa} > 0$ and $M_{ms} > -1/R_{pa}$ into account.

Instability of Completely Engulfed State and Neck Opening.

In the completely engulfed state, the nanoparticle is fully covered by the membrane, but still connected to the mother vesicle by a small membrane neck; see Figure 6a. In the coarse-grained description used here, the completely engulfed state corresponds to a limit shape with an ideal neck that is attached to the mother vesicle in a single contact point. At this contact point, the unbound membrane segment of the mother vesicle has the mean curvature M'_{ms} , which must satisfy $M'_{ms} < 1/R_{pa}$ in order to ensure that the membrane does not intersect the particle, whereas the mean curvature of the membrane segment adhering to the particle is equal to the contact mean curvature $M_{co} = 1/R_W - 1/R_{pa}$. For this limit shape, the sum of the two curvatures M_{co} and M'_{ms} is equal to twice the spontaneous curvature; see the Methods section. As a consequence, the instability line L_{ce} for the completely engulfed state \mathcal{G} is described by

$$R_{pa} = R_{ce} \equiv \frac{1}{M'_{ms} - (2m - R_W^{-1})} \quad \text{for} \\ M'_{ms} > 2m - 1/R_W \quad (L_{ce}, \text{ endocytosis}) \quad (7)$$

and the membrane neck starts to open if

$$R_{pa} < R_{ce} \quad \text{and} \\ M'_{ms} > 2m - 1/R_W \quad (\text{unstable } \mathcal{G}, \text{ endocytosis}) \quad (8)$$

If the mean curvature M'_{ms} of the unbound membrane segment is smaller than $2m - 1/R_W$, the completely

engulfed state \mathcal{C} is unstable for all particle sizes, *i.e.*, $R_{ce} = \infty$.

The vesicle with an adjustable volume (Figure 3) still attains a spherical shape after complete engulfment of the nanoparticle, which implies that the local curvature M'_{ms} has the constant value $M'_{ms} = 1/(R_{ve}^2 - R_{pa}^2)^{1/2}$. For the oblate vesicle with $v = 0.98$ (Figure 4), the curvature M'_{ms} of the membrane segment at the pole has to be determined numerically from the shape of the mother vesicle, which is again calculated by minimizing its free energy; see the Methods section. The same method has been used to check and validate the instability criterion as given by eq 8 for a large number of different parameter values.

Critical Particle Sizes for Endocytic Engulfment. As illustrated by the examples in Figure 3 and Figure 4, the critical particle sizes can be deduced from the instability lines L_{fr} and L_{ce} for the free and completely engulfed particle states. These two lines intersect for $m = (1/2)(M_{ms} + M'_{ms})$ as in Figure 3c and Figure 4c because the two instability relations $M_{co} = M_{ms}$ and $M_{co} + M'_{ms} = 2m$ become identical in this case. Therefore, depending on the relative size of the spontaneous curvature m and the segment curvatures M_{ms} and M'_{ms} , the lower and upper critical sizes are equal to the radii R_{fr} and R_{ce} ; see Table 3.

The expressions for the instability lines and the critical particle sizes become particularly transparent in the limit of weakly curved membrane segments with

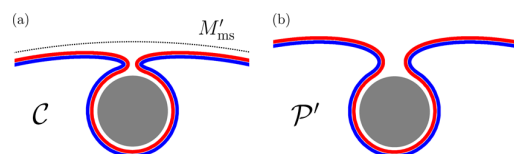


Figure 6. Opening of membrane neck for endocytic engulfment: (a) completely engulfed state \mathcal{C} of nanoparticle (gray) and asymmetric bilayer (blue–red) compared to (b) partially engulfed state \mathcal{P}' , for which the neck has been opened up. The completely engulfed state is unstable if the opening of the neck leads to a decrease in the membrane's bending energy that overcompensates the loss in adhesion energy. The corresponding instability criterion as described by eq 8 involves the mean curvature M'_{ms} of the weakly curved membrane segment (dotted line) of the mother vesicle. For a convex segment as shown here, the segment curvature M'_{ms} is positive. In general, this curvature must be smaller than $1/R_{pa}$ to ensure that the unbound and bound membrane segments do not intersect each other.

TABLE 3. Critical Particle Sizes for Endocytic Engulfment As Obtained from eqs 4–8

range of spontaneous curvature m	intermediate size regime	engulfment process	lower critical size	upper critical size
$m > (1/2)(M_{ms} + M'_{ms})$	partial \mathcal{P}_{st}	continuous	R_{fr}	R_{ce}
$m < (1/2)(M_{ms} + M'_{ms})$	bistable \mathcal{B}_{st}	discontinuous	R_{ce}	R_{fr}

small curvatures M_{ms} and M'_{ms} . More precisely, we will now assume that these segment curvatures are small both compared to the inverse particle size $1/R_{pa}$ and compared to the inverse adhesion length $1/R_W$. These requirements are certainly fulfilled for the shapes of large GUVs and for adhesion lengths R_W between about 10 and 500 nm, which covers the strong and weak adhesion regime; see Table 1. In addition, the limit of small segment curvatures M_{ms} and M'_{ms} also applies to the membrane segments that are typically studied by molecular dynamics simulations with periodic boundary conditions.^{21–23,41}

If we set the segment curvatures M_{ms} and M'_{ms} equal to zero, we obtain the simple expressions $R_{fr} = R_W$ and $R_{ce} = R_W/(1 - 2mR_W)$ for the critical particle sizes. The corresponding engulfment regimes are displayed in Figure 7b. This diagram is universal in the sense that it does not depend on the vesicle shape, which becomes irrelevant in the limit of large R_{ve} . Therefore, as we increase the vesicle size R_{ve} , we approach the engulfment regimes in Figure 7b both for spherical vesicles with adjustable volume (Figure 3) and for oblate vesicles with a certain fixed volume-to-area ratio v (Figure 4). Indeed, comparison of Figure 3a with Figure 4a, which both apply to negative spontaneous curvature $m = -0.05/R_W$, shows that the instability lines L_{ce} and L_{fr} have the same asymptotic values $R_{pa}/R_W = 0.909$ and $R_{pa}/R_W = 1$, corresponding to the vertical dotted lines in these figures. These asymptotic values are indicated in Figure 7b by the two open diamonds for $m = -0.05/R_W$. Likewise, the other open diamonds in Figure 7b correspond to the identical asymptotes in Figure 3b and Figure 4b as well as in Figure 3c and Figure 4c. The open diamond with the coordinates $R_{pa}/R_W = 1$ and $m = 0$ in Figure 7b is special because it represents the “multicritical” intersection point of the two instability lines at which all four engulfment regimes meet.

The engulfment diagram in Figure 7b is obtained for flat membrane segments with $M_{ms} = M'_{ms} = 0$. This diagram undergoes small changes if we consider small but finite values of the local membrane curvatures M_{ms} and M'_{ms} as illustrated in Figure 7a and c. These changes depend primarily on the sign of the curvature sum $M_{ms} + M'_{ms}$, which determines the intersection point for the two instability lines.

Instability Relations and Critical Sizes for Exocytic Engulfment. The instability relations for *exocytic* engulfment differ from those for endocytic engulfment because the expression for the contact mean curvature M_{co} is different; see eq 22 in the Methods section. The modified instability relations lead to changes in the critical particle radii and the engulfment regimes as described in the SI Text B. The Supporting Information also contains (i) Figure S3, which displays the regimes of exocytic engulfment for weakly curved mother

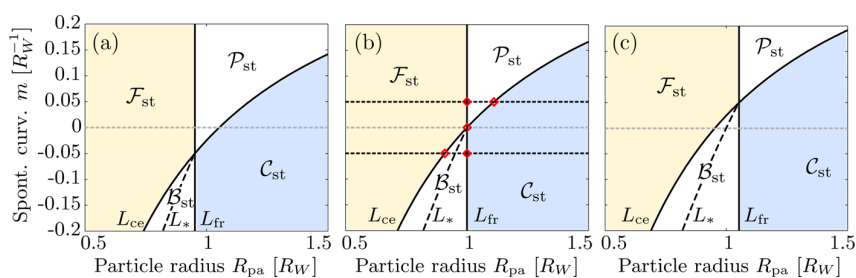


Figure 7. Endocytic engulfment of nanoparticles for weakly curved mother membranes: different engulfment regimes \mathcal{F}_{st} , \mathcal{B}_{st} , \mathcal{C}_{st} , and \mathcal{P}_{st} as a function of particle size R_{pa} and spontaneous curvature m , both measured in units of the adhesion length R_W . (a) Concave membrane segments with negative curvatures $M_{ms} = M'_{ms} = -0.05/R_W$; (b) flat segments with vanishing curvatures $M_{ms} = M'_{ms} = 0$; and (c) convex segments with positive curvatures $M_{ms} = M'_{ms} = +0.05/R_W$. The two instability lines L_{fr} and L_{ce} determine the critical particle sizes R_{fr} and R_{ce} via eqs 4 and 7. The bistable regimes \mathcal{B}_{st} contain the transition lines L_* (dashed), at which the free and completely engulfed states coexist. All four engulfment regimes meet at the “multicritical” intersection points of the two instability lines where $m = (1/2)(M_{ms} + M'_{ms})$. The five open diamonds (red) in panel (b) correspond to the asymptotes of the instability lines L_{fr} and L_{ce} for finite vesicle sizes R_{ver} as indicated by the vertical dotted lines in Figure 3 and Figure 4.

membranes, and (ii) a detailed comparison between the latter figure and Figure 7 for the endocytic process.

Experimental and Computational Studies of Critical Sizes. Inspection of the engulfment diagrams in Figures 3, 4, and 7 as well as Figure S3 shows that the critical particle sizes are always on the order of the adhesion length R_W . More precisely, for the relatively small spontaneous curvatures m studied here, the nanoparticles probe the intermediate engulfment regimes \mathcal{P}_{st} and \mathcal{B}_{st} when the particle size varies in the interval between $0.5R_W$ and $1.5R_W$. For the intermediate engulfment regime \mathcal{P}_{st} , both critical sizes R_{fr} and R_{ce} are accessible to experiment as long as we can distinguish partially from completely engulfed states. For the ultraweak adhesion regime with an adhesion length of a few micrometers (Table 1, fifth row), these different states should be accessible to conventional optical microscopy. For the strong adhesion regime with an adhesion length on the order of 10–30 nm (Table 1, first and second row), the partially and completely engulfed states could be distinguished by cryoelectron microscopy.^{2,9}

The two critical radii are also accessible to computer simulations. Indeed, both Monte Carlo^{17–19} and molecular dynamics^{20–24} simulations have been recently used to study the interactions of nanoparticles with membranes. Nanoparticles with a radius of up to 50 nm can be investigated by coarse-grained molecular dynamics, which can thus be utilized to probe the strong adhesion regime. The weak adhesion regime, on the other hand, can be elucidated *via* Monte Carlo simulations, by which one can study much larger particles. In the simulations, one can even probe the stability of the free and completely engulfed state directly by applying external forces to the particles.

Now, assume that we observed, in experimental studies or computer simulations, the engulfment regime \mathcal{P}_{st} for the *endocytic* process and that we measured the two critical sizes R_{fr} and R_{ce} . From the

microscopy images or the simulation snapshots, we would also be able to obtain the two segment curvatures M_{ms} and M'_{ms} . We can then use the explicit expressions for the instability lines to deduce the adhesion length R_W and the spontaneous curvature m from the critical particle sizes. As a result, we obtain the relationships

$$R_W = \frac{R_{fr}}{1 + R_{fr}M_{ms}} \quad (\text{cont endocytosis}) \quad (9)$$

for the adhesion length R_W and

$$m = \frac{1}{2} \left[\frac{1}{R_{fr}} - \frac{1}{R_{ce}} + M_{ms} + M'_{ms} \right] \quad (\text{cont endocytosis}) \quad (10)$$

for the spontaneous curvature m .

If the intermediate size regime for the endocytic process belongs to the bistable regime \mathcal{B}_{st} , the experimental observation of the two critical sizes is more difficult. Indeed, when we add nanoparticles to the exterior solution, the free state of the particles remains metastable up to the upper critical size and will then undergo an abrupt transition, as a function of particle size, to the completely engulfed state. Thus, for a bistable intermediate regime, we can still measure the upper critical size and, thus, the adhesion length R_W but not the lower critical size, which is necessary to determine the spontaneous curvature. However, if the endocytic process is discontinuous, the exocytic process is continuous as explained in the SI Text B. Therefore, we can then deduce the material parameters from the radii as determined from the exocytic process for the same vesicle–particle system; see eqs S18 and S19.

RECEPTOR-MEDIATED ADHESION AND ENGLUFMENT

Particle-Induced Segregation of Membrane Components. In the previous sections, we considered model membranes with a laterally uniform composition and, thus,

a laterally uniform spontaneous curvature m . If the membrane contains several molecular components, these components will typically experience different interactions with the particle surface. As a consequence, the composition of the bound membrane segment can differ significantly from the composition of the unbound membrane. One example is provided by charged particles and oppositely charged lipid molecules; another example by membrane-anchored receptors or “stickers” that interact with the particle *via* specific receptor–ligand bonds. Both the oppositely charged lipids and the receptors will be enriched (or “recruited”) in the bound segments and depleted in the unbound segments.⁴⁷ The actual concentrations in the two segments are determined by the partitioning of the receptor molecules between the two membrane segments, a partitioning that depends on the affinities or binding free energies of the different components with the particle surface and on the size of the two membrane segments. In equilibrium, these concentrations follow from the requirement that each membrane component has the same chemical potential in the two membrane segments. One major contribution to these chemical potentials comes from the translational entropy of the membrane components. For receptor-mediated endocytosis, these dependencies have been studied in ref 27 using a kinetic model for the diffusing receptors and in ref 30 based on the statistical thermodynamics of many interacting receptors and nanoparticles.

Because of their distinct compositions, the two membrane segments can also differ in their fluid–elastic properties. Thus, we will now consider bound membrane segments that have a spontaneous curvature m_{bo} and a bending rigidity κ_{bo} , while the unbound membrane is still characterized by the spontaneous curvature m and the bending rigidity κ . We will again assume that the spontaneous curvature m is relatively small but will allow large values for the spontaneous membrane curvature m_{bo} of the bound membrane segment in order to model a protein coat as formed in clathrin-dependent endocytosis. Furthermore, the membrane–particle interactions involve, in general, both nonspecific (hydrophobic, van der Waals, or electrostatic) and specific interactions mediated by membrane-anchored receptors.⁴⁸ Both types of molecular interactions will be described by the adhesive strength $|W|$.

The loss of conformational entropy by the receptor–ligand bonds can also be included in $|W|$ *via* the binding free energy U of each bond. If the binding enthalpy of a receptor–ligand bond is $|H|$, the binding free energy of the bond can be estimated by $|U| = |H| - k_B T \ln(\rho_{lig}/\rho_0)$,²⁷ where ρ_{lig} and ρ_0 represent the ligand density on the particle surface and the concentration of receptors on the membrane surface before contact with the particle, respectively. The contribution of the

ligand–receptor bonds to the adhesive strength $|W|$ is then given by $|U|\rho_{lig}$ as mentioned previously.

The combined bending and adhesion free energy of such a nonuniform membrane is equal to the free energy of a uniform membrane with bending rigidity κ and spontaneous curvature m provided we replace the molecular adhesive strength $|W|$ by the effective adhesive strength

$$W_{\text{eff}} = |W| + \frac{2\kappa}{R_{\text{pa}}^2} (1 \pm R_{\text{pa}}m)^2 - \frac{2\kappa_{\text{bo}}}{R_{\text{pa}}^2} (1 \pm R_{\text{pa}}m_{\text{bo}})^2 \quad (11)$$

arising from the difference between the elastic parameters of the unbound and the bound membrane segment where the plus and minus signs apply to endo- and exocytosis, respectively. Because of this parameter mapping, the instability relations for the nonuniform membrane can be directly obtained from the previously discussed relations for uniform membranes. In the following, we will again focus on the endocytic case.

Engulfment Regimes Controlled by Bound Membrane Segment. The instabilities of the free state \mathcal{F} and of the completely engulfed state \mathcal{G} are again described by the relationships $M_{\text{co}} \geq M_{\text{ms}}$ and $M_{\text{co}} + M'_{\text{ms}} \leq 2m$ as before, but the contact mean curvature M_{co} now has the form

$$M_{\text{co}} = \sqrt{\frac{W_{\text{eff}}(R_{\text{pa}})}{2\kappa}} - \frac{1}{R_{\text{pa}}} \quad (\text{endocytosis}) \quad (12)$$

where the notation $W_{\text{eff}}(R_{\text{pa}})$ emphasizes the R_{pa} dependence of the effective adhesive strength W_{eff} as given by eq 11. Because W_{eff} depends quadratically on the particle size R_{pa} , the instability relations $M_{\text{co}} \geq M_{\text{ms}}$ and $M_{\text{co}} + M'_{\text{ms}} \leq 2m$ are no longer linear in R_{pa} . The instability lines L_{fr} and L_{ce} again follow from the instability relations $M_{\text{co}} = M_{\text{ms}}$ and $M_{\text{co}} + M'_{\text{ms}} = 2m$. As in the case of uniform membranes, these two relations are identical for $m = (1/2)(M_{\text{ms}} + M'_{\text{ms}})$, which implies that the two instability lines L_{fr} and L_{ce} are also identical in this case.

We now focus on the case of weakly curved mother membranes for which $|M_{\text{ms}}|$ and $|M'_{\text{ms}}|$ as well as $|m|$ are much smaller than $1/R_{\text{pa}}$. For the limiting case $M_{\text{ms}} = M'_{\text{ms}} = m = 0$, the two instability relations become identical to $M_{\text{co}} = 0$ or

$$\left[\frac{R_{\text{pa}}^2 |W|}{2\kappa} + 1 - \frac{\kappa_{\text{bo}}}{\kappa} (1 + R_{\text{pa}}m_{\text{bo}})^2 \right]^{1/2} = 1 \quad (13)$$

This relation leads to two engulfment regimes, $\mathcal{F}_{\text{st}}^<$ and $\mathcal{F}_{\text{st}}^>$, in which the free state \mathcal{F} is stable and the completely engulfed state \mathcal{G} is unstable; see Figure 8a. As shown in this figure, these two regimes are separated by an intermediate regime \mathcal{G}_{st} in which the free state is unstable and the completely engulfed state is

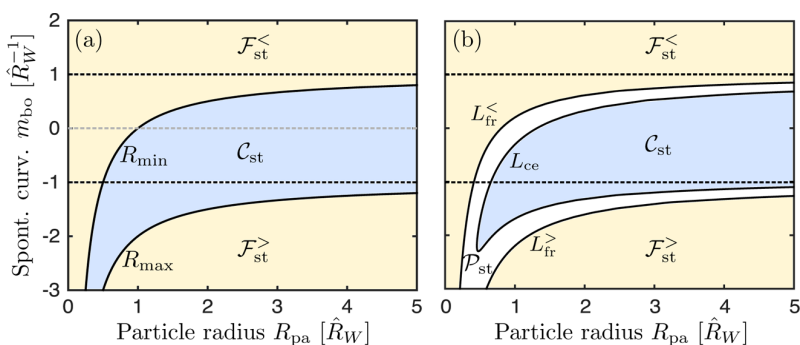


Figure 8. Engulfment regimes for weakly curved mother membranes as a function of particle radius R_{pa} and spontaneous curvature m_{bo} of the bound membrane segment in contact with the nanoparticle. Both quantities are given in units of the modified adhesion length \hat{R}_W defined in eq 16. (a) Engulfment regimes for $M_{ms} = M'_{ms} = m$ that apply to both $m = 0$ and $m \neq 0$: the regime \mathcal{C}_{st} (blue) of completely engulfed particle states is located between the two regimes $\mathcal{F}_{st}^<$ and $\mathcal{F}_{st}^>$ (yellow), both of which exhibit free particle states. For parameter values within the regime \mathcal{C}_{st} , the membrane spreads over the whole particle surface. The two boundary lines $R_{pa} = R_{min}(m_{bo})$ and $R_{pa} = R_{max}(m_{bo})$ are given by eqs 14 and 15; (b) small deviations $M_{ms} - m$ and/or $m - M'_{ms}$ lead to a “broadening” of the boundary lines as illustrated here for $M_{ms} = M'_{ms} = 0$ and $m = 0.2/\hat{R}_W$. The two boundary lines split up into separate instability lines L_{fr} and L_{ce} , which enclose a narrow boundary regime (white) around the regime \mathcal{C}_{st} . In this example, the boundary regime represents a partial engulfment regime \mathcal{P}_{st} .

stable. The boundary lines between the three engulfment regimes are given by

$$R_{pa} = R_{min} \equiv \frac{1}{\hat{R}_W - m_{bo}} \quad \text{for } m_{bo} < +1/\hat{R}_W \quad (14)$$

and

$$R_{pa} = R_{max} \equiv \frac{1}{|m_{bo}| - \hat{R}_W} \quad \text{for } m_{bo} < -1/\hat{R}_W \quad (15)$$

with the modified adhesion length

$$\hat{R}_W \equiv \sqrt{2\kappa_{bo}/|W|} = R_W \sqrt{\kappa_{bo}/\kappa} \quad (16)$$

It turns out that essentially the same solution applies to the more general case with $M_{ms} = M'_{ms} = m \neq 0$, for which the two instability relations become identical to $M_{co} = m$. In the latter case, the two boundary lines are truncated at $m_{bo} = (1/\hat{R}_W) - |m|$ and $m_{bo} = -(1/\hat{R}_W) - |m|$, respectively, reflecting the condition that membrane and particle surface are not allowed to intersect each other but the expressions for R_{min} and R_{max} as given by eqs 14 and 15 remain unchanged.

An expansion of the instability relations $M_{co} = M_{ms}$ and $M_{co} + M'_{ms} = 2m$ around the special case $M_{ms} = M'_{ms} = m$ leads to correction terms that are proportional to $M_{ms} - m$ and $m - M'_{ms}$, respectively. If we take these correction terms into account, the boundary lines $R_{pa} = R_{min}$ and $R_{pa} = R_{max}$ “broaden” and split up into two separate instability lines, L_{fr} and L_{ce} , that enclose a narrow boundary regime around the regime \mathcal{C}_{st} of complete engulfment. This split-up is illustrated in Figure 8b for $M_{ms} = M'_{ms} = 0$ and $m = 0.2/\hat{R}_W$. In general, such a split-up occurs as soon as $M_{ms} + M'_{ms} \neq 2m$, i.e., as soon as the segment curvatures do not match the spontaneous curvature of the mother membrane, and the resulting intermediate size regime may be a partial engulfment regime \mathcal{P}_{st} and/or a bistable regime \mathcal{B}_{st} .

Kinetics of Membrane Spreading and Particle Engulfment.

The spreading of the membrane over the particle surface proceeds *via* the displacement of the contact line. As described in the SI Text C, the contact line experiences two forces, a thermodynamic driving force and a frictional force. The thermodynamic driving force is proportional to the gradient $dE(\phi)/d\phi$ of the free energy landscape $E(\phi)$, where the wrapping angle ϕ varies from $\phi = 0$ for the free particle state to $\phi = \pi$ for the completely engulfed state.

Balancing the thermodynamic driving force with the frictional force, we obtain the equation of motion

$$\sin(\phi) \frac{d\phi}{dt} = \frac{1}{2\pi\eta_{eff}R_{pa}^3} \frac{dE(\phi)}{d\phi} \quad (17)$$

for the wrapping angle ϕ as a function of time t , which involves the effective viscosity η_{eff} . Using this equation of motion with the initial condition $\phi(t = 0) = 0$ corresponding to the free particle state \mathcal{F} , we can determine the engulfment time $t_{\mathcal{F}\mathcal{C}}$ that the membrane needs to spread over the whole particle surface and to attain the completely engulfed state \mathcal{C} within the regime \mathcal{C}_{st} in Figure 8. This time follows from the implicit equation $\phi(t = t_{\mathcal{F}\mathcal{C}}) = \pi$.

As shown in the SI Text C, the gradient $dE(\phi)/d\phi$ becomes particularly simple in the limit of small particle sizes with $R_{pa} \ll R_{ve}$. Indeed, this gradient is then determined by the contribution from the bound membrane segment alone and can be calculated in closed form; see eq S31. As a consequence, the wrapping velocity $d\phi/dt$ becomes constant and the implicit equation $\phi(t = t_{\mathcal{F}\mathcal{C}}) = \pi$ leads to the size-dependent engulfment rate

$$\omega_{\mathcal{F}\mathcal{C}} = \frac{1}{t_{\mathcal{F}\mathcal{C}}} = \frac{f(R_{pa}/\hat{R}_W)}{t_o} \quad \text{in regime } \mathcal{C}_{st} \quad (18)$$

with the time scale $t_o \equiv \pi\eta_{eff}\hat{R}_W^3/(2\kappa_{bo})$ and the dimensionless function

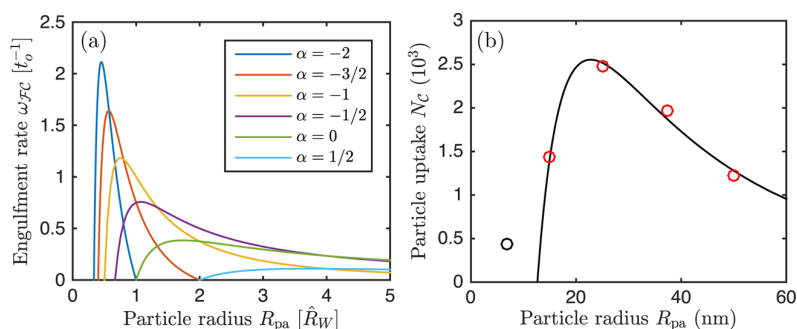


Figure 9. (a) Size dependence of engulfment rate $\omega_{\mathcal{F}c}$ in units of $1/t_0$ as given by eq 18 for different values of the reduced spontaneous curvature $\alpha = \hat{R}_W m_{bo}$ of the bound membrane segment and (b) size dependence of particle uptake as measured by Chithrani *et al.*²⁶ for clathrin-dependent endocytosis of transferrin-coated gold nanoparticles (open circles) fitted by eq 20 with $\hat{R}_W = 48.6$ nm and $m_{bo} = -1/(40.0$ nm). The data point for $R_{pa} = 7$ nm (black open circle) has not been included in the fit because, for this size, the clathrin-coated vesicles were observed²⁶ to engulf more than one nanoparticle. The effective radius of the nanoparticles was increased to $R_{pa} + 9.3$ nm in order to take the size of the transferrin receptor's ectodomain⁵² into account.

$$f(x) \equiv \frac{x^2 - (1 + \alpha x)^2}{x^3} \quad \text{with} \\ x \equiv R_{pa}/\hat{R}_W \quad \text{and} \quad \alpha \equiv \hat{R}_W m_{bo} \quad (19)$$

The function $f(R_{pa}/\hat{R}_W)$ describes the size dependence of the engulfment rate as illustrated in Figure 9a. The numerator $x^2 - (1 + \alpha x)^2$ of $f(x)$ is proportional to $dE/d\phi$.

The effective viscosity η_{eff} depends on the microviscosity of the bilayer and on the molecular interactions between membrane and particle. Typical values for the bilayer's microviscosity lie in the range 0.1–1 Pa s, which corresponds to 10^2 – 10^3 times the viscosity of water.^{49,50} Using $\eta_{\text{eff}} = 1$ Pa s together with $\kappa_{bo} = 10^{-19}$ J, the time scale t_0 is equal to about 1.25 ms for $\hat{R}_W = 20$ nm (strong adhesion) and to about 20 ms for $\hat{R}_W = 50$ nm (intermediate adhesion); compare Table 1. These estimates for the time scale t_0 are consistent with both experimental⁶ and computational⁵¹ studies.

Now, consider a giant vesicle in an aqueous solution without nanoparticles and let us exchange this solution, at time $t = 0$, by an aqueous dispersion of such particles with particle concentration X_{pa} . The vesicle membrane will then start to engulf nanoparticles with the rate $\omega_{\mathcal{F}c}$. The corresponding particle uptake by the vesicle is equal to the number N_C of completely engulfed particles. This number evolves in time according to $dN_C/dt = N_{\mathcal{F}} \omega_{\mathcal{F}c}$, which depends on the number $N_{\mathcal{F}}$ of free particles adjacent to the vesicle membrane. The latter number is determined by the bulk concentration X_{pa} , which will be time independent as long as the number of dispersed particles is much larger than the number of particles attached to the membrane. After a certain observation time Δt , we then obtain the particle uptake

$$N_C(\Delta t) = N_{\mathcal{F}} \Delta t \omega_{\mathcal{F}c} = N_{\mathcal{F}} \frac{\Delta t}{t_0} f(R_{pa}/\hat{R}_W) \quad (20)$$

with the function $f(x)$ as given by eq 19; compare Figure 9a.

Comparison with Clathrin-Dependent Endocytosis. In the previous subsections, we considered receptor-mediated adhesion and engulfment for lipid vesicles with multicomponent membranes containing receptor or “sticker” molecules. The same processes are also involved in the uptake of nanoparticles by eukaryotic cells, which utilize a variety of different endocytic pathways^{53,54} including the much studied pathway of clathrin-dependent endocytosis.^{55–57} The size dependence of the latter process has been elucidated by Chithrani *et al.*,^{25,26} who measured the uptake of gold nanoparticles by HeLa cells for different particle sizes. As a result, the cellular uptake was found to depend on the particle size in a nonmonotonic manner as displayed in Figure 9b for the case of transferrin-coated gold nanoparticles.²⁶

One generic aspect of clathrin-dependent endocytosis is that the clathrin-coated membrane represents a strongly asymmetric membrane domain with receptor–ligand binding on its outer (exoplasmic) face and a thick protein coat consisting of adaptor proteins such as AP-2 and clathrin triskelions on its inner (cytoplasmic) face. The associated spontaneous curvature m_{bo} can be estimated from the dimensions of the clathrin-coated vesicles that are generated by the endocytic process. For native coats from human placenta,⁵⁸ the outer diameter of the coat was found to vary between 75 and 130 nm, while the enclosed vesicle had a radius between 18 and 43 nm. Thus, the spontaneous curvature m_{bo} is expected to have a value between $-1/(18$ nm) and $-1/(43$ nm), where the negative sign reflects the endocytic process; see Figure 2a. That the membrane prefers to curve in this manner can be understood from the dense coverage of the inner (cytoplasmic) face of the cell membrane by bulky adaptor proteins such as AP-2.

As shown in Figure 9b, the size dependence of the experimental data for transferrin-coated nanoparticles²⁶ is well fitted by eq 20 with $m_{bo} = -1/(40.0$ nm),

$\hat{R}_W = 48.6$ nm, and $N_{\mathcal{F}} \Delta t / t_0 = 1.85 \times 10^3$. These values were obtained using the method of least-squares applied to the four data points with $R_{pa} = 15, 25, 37,$ and 50 nm. The data point with $R_{pa} = 7$ nm was excluded from the fit because, for this small size, the clathrin-coated vesicles were observed²⁶ to engulf more than one nanoparticle. The effective radius of the nanoparticles was taken to be $R_{pa} + 9.3$ nm in order to account for the size of the transferrin receptor's ectodomain,⁵² which protrudes from the membrane by 9.3 nm and, thus, increases the local separation between the particle surface and the bilayer membrane by this amount.

The deduced value $m_{bo} = -1/(40.0$ nm) for the coat-induced curvature lies within the range of m_{bo} values as estimated from the observed dimensions of clathrin-coated vesicles. The deduced value $\hat{R}_W = 48.6$ nm for the modified adhesion length together with the bending rigidity $\kappa_{bo} = 1.17 \times 10^{-18}$ J of clathrin-coated vesicles⁵⁹ leads to the adhesive strength $|W| = 2\kappa_{bo}/\hat{R}_W^2 = 0.99$ mN/m $\approx 0.24k_B T/\text{nm}^2$. On one hand, this adhesive strength is on the same order of magnitude as attractive van der Waals interactions between colloidal particles. On the other hand, this $|W|$ value could also arise from the specific receptor–ligand interactions alone. Indeed, the bond between the transferrin receptor and the transferrin molecule has been estimated, based on atomic force microscopy measurements,⁶⁰ to be about $20k_B T \approx 8.2 \times 10^{-20}$ J. Because the lateral size of a single transferrin receptor is about 5×10 nm², a densely packed layer of transferrin receptors with one molecular bond per receptor would lead to the adhesive strength $|W| = 1.64$ mN/m $\approx 0.4k_B T/\text{nm}^2$.

The main difference between clathrin-dependent endocytosis and the engulfment of nanoparticles by lipid membranes is the characteristic time scale t_0 . Indeed, for the simple spreading dynamics described in the previous subsection, this time scale was estimated to be on the order of milliseconds for lipid bilayers. In contrast, it takes between 20 and 80 s to form a clathrin-coated vesicle starting from a nascent clathrin-coated pit.^{56,57} One mechanism for this slowdown of the dynamics is provided by diffusion-limited enrichment of the receptor molecules within the contact area between membrane and nanoparticle as theoretically studied in refs 27–30. For relatively low receptor concentrations and/or for relatively large nanoparticles, it can indeed take tens of seconds for a diffusing receptor to reach the contact area. However, the clathrin-dependent pathway is used by the cells even in the absence of ligands or nanoparticles in order to constitutively internalize and recycle membrane-bound receptors such as the transferrin receptor.^{61,62} Furthermore, a recent fluorescence microscopy study on the uptake of virus capsids by feline cells revealed that the assembly of the protein

coat and the formation of the clathrin-coated vesicle takes between 30 and 70 s regardless of whether it contains a virus capsid or not.⁵⁷ Because these capsids had a diameter of 26 nm and utilized transferrin receptors for their association with the cell membrane, this intrinsic time scale for the coat assembly should also apply to the clathrin-dependent uptake of gold particles as studied by Chithrani *et al.* in refs 25 and 26. After the clathrin-coated vesicle has been formed, it pinches off from the mother membrane by cleavage of the membrane neck *via* the GTPase dynamin. This fission process takes only a few seconds and is, thus, much faster than the vesicle formation step, as revealed by fluorescence microscopy.^{56,57} As a consequence, the observed size dependence of the cellular uptake should be dominated by the size dependence of the engulfment process, which corroborates our estimate based on the engulfment rate $\omega_{\mathcal{F}}$.

Comparison with Previous Theoretical Studies. It is instructive to compare our results with two previous theoretical studies on receptor-mediated endocytosis that also obtained characteristic particle sizes. First, Gao *et al.*²⁷ studied the receptor-mediated engulfment of nanoparticles in the framework of a kinetic model that emphasized the lateral diffusion of the membrane-anchored receptors. Second, Zhang *et al.*³⁰ investigated the statistical thermodynamics of many membrane-anchored receptors interacting with many nanoparticles. Both studies identified two characteristic particle sizes, R_1 and R_2 , that separate three different size regimes. For small particle sizes, $R_{pa} < R_1$, a no-engulfment regime was found in which the bending free energy dominates and prevents the onset of adhesion. For particle sizes $R_{pa} > R_1$, a complete engulfment regime was found. These two regimes were originally identified by Lipowsky and Döbereiner in ref 5 with $R_1 = R_W = (2\kappa/|W|)^{1/2}$. In the present study, these size regimes correspond to the special case of *vanishing* spontaneous curvatures $m = m_{bo} = 0$ and flat mother membranes; see the dashed horizontal lines in Figure 7b and Figure 8a corresponding to $m = 0$ and $m_{bo} = 0$, respectively.

One important result of our study is that, in the presence of even a small bilayer asymmetry generating a small spontaneous curvature $m \neq 0$, the characteristic size $R_1 = R_W$ is replaced by an intermediate size regime in which the particles either are partially engulfed or show bistable behavior; see Figure 7b. These intermediate size regimes are bounded by the two critical particle sizes, R_{fr} and R_{ce} which emerge from the “multicritical” point with $R_{pa} = R_W$ and $m = 0$ in a continuous manner.

For $R_{pa} > R_2$, Gao *et al.*²⁷ and Zhang *et al.*³⁰ considered receptor and ligand concentrations for which complete engulfment is suppressed by a shortage of receptors. Such a constraint has not been included in our theory. As mentioned in the previous subsection,

the transferrin receptors are continuously recycled between the plasma membrane and membrane-bound organelles even in the absence of nanoparticles or ligands.^{61,62} In addition, the number of receptors per nanoparticle can be relatively small, as observed for the uptake of virus capsids by feline cells.⁵⁷ However, we have found that the particle-induced segregation of membrane components can lead to two critical particle sizes, R_{\min} and R_{\max} , even without any receptor shortage provided the bound membrane domain exhibits a large negative spontaneous curvature $m_{\text{bo}} < -1/R_W$, as shown in Figure 8a. Furthermore, as illustrated in Figure 8b, the two critical sizes R_{\min} and R_{\max} are again replaced by intermediate size regimes with partial engulfment or bistable behavior if the sum of the local segment curvatures M_{ms} and M'_{ms} deviates from twice the spontaneous curvature m of the mother membrane.

CONCLUSIONS

In the main part of this paper, we studied nanoparticles in contact with laterally uniform model membranes and showed that the membranes' spontaneous curvature m represents a key parameter of these systems, which leads to two critical radii, R_{fr} and R_{cer} , separating four distinct engulfment regimes. For particle sizes below the lower critical radius, the particle is free and does not bind to the membrane (regime \mathcal{F}_{st}). For particle sizes above the upper critical radius, the particle is completely engulfed by the membrane (regime \mathcal{C}_{st}). For intermediate particle sizes, the particle either is partially engulfed (regime \mathcal{P}_{st}) or exhibits bistable behavior (regime \mathcal{B}_{st}). The corresponding engulfment diagrams have been determined for spherical and oblate vesicles as shown in Figure 3 and Figure 4 as well as for weakly curved membranes corresponding to the limit of large vesicles; see Figure 7 and Figure S3.

The basis length scale for the engulfment processes is provided by the adhesion length $R_W = (2\kappa/|W|)^{1/2}$, which depends on the bending rigidity κ of the lipid bilayer and on the adhesive strength $|W|$ of the attractive membrane–particle interactions. In real systems, the adhesion length can vary between about 10 nm for strong adhesion and a few micrometers for ultraweak adhesion; see Table 1. For the relatively small spontaneous curvatures studied here, the nanoparticles probe the intermediate engulfment regimes \mathcal{P}_{st} and \mathcal{B}_{st} when the particle size varies in the interval between $0.5R_W$ and $1.5R_W$. As a consequence, the two critical sizes are located within the same interval.

The engulfment of silica nanoparticles by DOPC vesicles has been recently studied by cryoelectron microscopy.⁹ Complete engulfment was found for all particle sizes with a radius above 15 nm. Thus, we conclude that this system belongs to the strong adhesion regime with an adhesion length R_W below 15 nm.

This conclusion can be directly corroborated by measuring the adhesive strength $|W|$ between DOPC bilayers and silica.

As explained in the three paragraphs before eq 9, the two critical sizes will be directly accessible to experimental observations and computer simulations if the engulfment process proceeds in a continuous manner *via* partially engulfed states. If the *endocytic* process is discontinuous, corresponding to a bistable intermediate regime, the *exocytic* process will be continuous for the same vesicle–particle system, as follows from the “mirror symmetry” of the instability relations; see SI Text B. Thus, for any vesicle–particle system, either the endocytic or the exocytic engulfment process proceeds continuously *via* partially engulfed particle states.

From the observed values of the critical radii and the local membrane curvatures, one can deduce the adhesion length R_W and the spontaneous curvature m as described by eq 9 and eq 10 for continuous endocytosis and by eq S18 and eq S19 for continuous exocytosis. Therefore, the systematic variation of the size of the nanoparticles provides a possible probe to determine the material parameters of the vesicle–particle system both experimentally and *via* simulations. Using Monte Carlo^{17–19} or molecular dynamics^{20–24} simulations, one can also directly study the bistable regime by applying external forces that push the particle over the energy barrier between the free and the completely engulfed state.

In the last part of the paper, we generalized our theory to receptor-mediated adhesion and engulfment. To model a protein coat on the membrane as assembled during clathrin-dependent endocytosis, we focused on the case in which the spontaneous curvature m_{bo} of the bound membrane segment is large compared to the spontaneous curvature m of the mother membrane. For weakly curved mother membranes, we obtain the engulfment regimes shown in Figure 8. In this case, the complete engulfment regime \mathcal{C}_{st} is “sandwiched” between two regimes $\mathcal{F}_{\text{st}}^<$ and $\mathcal{F}_{\text{st}}^>$ with free particle states and no engulfment. The boundary lines $R_{\text{pa}} = R_{\min}$ and $R_{\text{pa}} = R_{\max}$ in Figure 8a are given by the simple expressions in eqs 14 and 15.

We also derived an equation of motion for the contact line (eq 17), which describes the spreading of the membrane from the free to the completely engulfed state. The solution of this equation leads to explicit expressions for the size-dependent engulfment rate (eq 18) and for the uptake of nanoparticles (eq 20) by model membranes and vesicles. Both the engulfment rate $\omega_{\mathcal{F}_G}$ and the particle uptake $N_G \propto \omega_{\mathcal{F}_G}$ are nonmonotonic functions of the particle size; see Figure 9. In addition, as demonstrated in Figure 9b, the expression in eq 20 for the particle uptake provides a quantitative fit to the experimental data of Chithrani *et al.*,^{25,26} who studied the

size-dependent uptake of gold nanoparticles by clathrin-dependent endocytosis.

For engulfment by model membranes with a uniform spontaneous curvature m , we focused on relatively small m values in order to demonstrate that even small asymmetries between the two leaflets of the lipid bilayer have a strong effect on the engulfment process. Our instability criteria as given by eq 5 and eq 8 for endocytic engulfment as well as by eq S15 and eq S17 for exocytic engulfment are, however, quite general and apply to large values of the spontaneous curvature as well. In the latter case, the vesicles can attain relatively complex shapes with small membrane buds and narrow membrane tubes. For simplicity, we also

focused on the behavior of a single nanoparticle in contact with the membrane. If we expose a vesicle to a solution of nanoparticles and consider the engulfment of many nanoparticles by the vesicle membrane, up to three different engulfment morphologies of the nanoparticles can be simultaneously present on the same vesicle, which then exhibits a characteristic engulfment pattern, as will be described in a subsequent paper. Our approach based on the stability of the free and completely engulfed particle states is rather general and can be extended to nonspherical shapes of the nanoparticles, to deformable particles, to chemically patterned Janus particles, and to membranes with different intramembrane domains or rafts.

METHODS

Free Energy of Vesicle–Particle System. The membrane is treated as a smooth surface with mean curvature M that varies continuously along the surface. For the well-established spontaneous curvature model,^{34–36} the bending free energy of the membrane depends on two material parameters, the bending rigidity κ and the spontaneous curvature m , and has the form

$$E_{be} = \int dA 2\kappa(M - m)^2 \quad (21)$$

where the integral runs over the whole surface area of the membrane or vesicle.

The attractive molecular interactions between membrane and nanoparticle are described by the adhesive strength, $W < 0$, which represents the adhesion free energy per unit area.⁴⁴ The total adhesion free energy is then given by $E_{ad} = -|W|A_{bo}$ where A_{bo} is the area of the membrane segment bound to the particle. The total free energy, $E = E_{be} + E_{ad}$, can be decomposed into a contribution E_{bo} from the bound membrane segment and a second contribution E_{un} from the unbound segment (or mother membrane) as described in the SI Text A. The total free energy was then minimized using the so-called shooting method as described in ref 35. The same minimization procedure was previously used to study the adhesion of vesicles to flat substrate surfaces.⁴⁴

Mean Curvature along the Contact Line. If a vesicle is in contact with a spherical nanoparticle of radius R_{pa} , the bound segment and the unbound segment of the vesicle membrane are separated by a contact line. Along this contact line, the principal curvature C_1^* of the membrane parallel to the contact line is given by $C_1^* = \mp 1/R_{pa}$, where the minus and plus signs apply to endocytic and exocytic engulfment, respectively; compare Figure 2. The second principal curvature perpendicular to the contact line follows from mechanical equilibrium along this line. Minimization of the free energy leads to the value $C_2^* = \pm((2|W|/\kappa)^{1/2} - 1/R_{pa})$, where the plus and minus signs apply to endocytic and exocytic engulfment, respectively. As a consequence, the contact mean curvature has the form

$$\begin{aligned} M_{co} &= \frac{1}{2}(C_1^* + C_2^*) = \pm \left(\sqrt{\frac{|W|}{2\kappa}} - \frac{1}{R_{pa}} \right) \\ &= \pm \left(\frac{1}{R_w} - \frac{1}{R_{pa}} \right) \end{aligned} \quad (22)$$

where the plus and minus signs again apply to endocytic and exocytic engulfment.

Neck Condition for Completely Engulfed Particle. In order to characterize the membrane neck of a completely engulfed particle, we considered vesicle shapes with a finite neck size l and studied the limit of small l . This computational approach has

been previously applied to budding of uniform membranes⁶³ and to budding of intramembrane domains.⁶⁴ In this way, we derived the ideal neck condition

$$M_{co} + M_{ms} = 2m \quad (23)$$

between the contact mean curvature M_{co} , the segment curvature M_{ms} of the mother vesicle (Figure 6a), and the spontaneous curvature m . The same condition can also be obtained, in a somewhat heuristic manner, from the requirement that the free energy density of the membrane as given by $2\kappa(M - m)^2$ (see eq 21) is continuous across the neck. The latter requirement leads to $(M_{co} - m)^2 = (M_{ms} - m)^2$, which is equivalent to eq 23.

Conflict of Interest: The authors declare no competing financial interest.

Acknowledgment. This study was supported by the German Research Foundation (DFG) via the IRTG 1524.

Supporting Information Available: Technical details about (A) free energy landscapes for the engulfment process with Figures S1 and S2; (B) exocytic engulfment of nanoparticles with Figure S3; and (C) spreading dynamics and engulfment rate. Figure S1 depicts the basic geometry of the vesicle–particle system for endocytic engulfment. Figure S2 illustrates the different free energy landscapes for the engulfment process, emphasizing the landscapes for the bistable regime β_{st} . Figure S3 shows the four engulfment regimes for exocytic engulfment by weakly curved membranes as a function of particle size and spontaneous curvature. This material is available free of charge via the Internet at <http://pubs.acs.org>.

REFERENCES AND NOTES

- Rodriguez, P. L.; Harada, T.; Christian, D. A.; Pantano, D. A.; Tsai, R. K.; Discher, D. E. Minimal “Self” Peptides that Inhibit Phagocytic Clearance and Enhance Delivery of Nanoparticles. *Science* **2013**, *339*, 971–975.
- Chen, K. L.; Bothun, G. D. Nanoparticles Meet Cell Membranes: Probing Nonspecific Interactions Using Model Membranes. *Environ. Sci. Technol.* **2014**, *48*, 873–880.
- Björnalm, M.; Yan, Y.; Caruso, F. Engineering and Evaluating Drug Delivery Particles in Microfluidic Devices. *J. Controlled Release* **2014**, *190*, 139–149.
- Mahmoudi, M.; Meng, J.; Xue, X.; Liang, X. J.; Rahmand, M.; Pfeiffer, C.; Hartmann, R.; Gil, P. R.; Pelaz, B.; Parak, W. J.; *et al.* Interaction of Stable Colloidal Nanoparticles with Cellular Membranes. *Biotechnol. Adv.* **2014**, *32*, 679–692.
- Lipowsky, R.; Döbereiner, H.-G. Vesicles in Contact with Nanoparticles and Colloids. *Europhys. Lett.* **1998**, *43*, 219–225.
- Dietrich, C.; Angelova, M.; Pouligny, B. Adhesion of Latex Spheres to Giant Phospholipid Vesicles: Statics and Dynamics. *J. Phys. II Fr.* **1997**, *7*, 1651–1682.

7. Koltover, I.; Rädler, J.; Safinya, C. Membrane Mediated Attraction and Ordered Aggregation of Colloidal Particles Bound to Giant Phospholipid Vesicles. *Phys. Rev. Lett.* **1999**, *82*, 1991–1994.
8. Fery, A.; Moya, S.; Puech, P.-H.; Brochard-Wyart, F.; Möhwald, H. Interaction of Polyelectrolyte Coated Beads with Phospholipid Vesicles. *C. R. Phys.* **2003**, *4*, 259–264.
9. Bihan, O. L.; Bonnafous, P.; Marak, L.; Bickel, T.; Trépout, S.; Mornet, S.; Haas, F. D.; Talbot, H.; Taveau, J.-C.; Lambert, O. Cryo-Electron Tomography of Nanoparticle Transmigration into Liposome. *J. Struct. Biol.* **2009**, *168*, 419–425.
10. Michel, R.; Plostica, T.; Abezgauz, L.; Danino, D.; Gradzielski, M. Control of the Stability and Structure of Liposomes by Means of Nanoparticles. *Soft Matter* **2013**, *9*, 4167.
11. Jaskiewicz, K.; Larsen, A.; Schaeffel, D.; Koynov, K.; Lieberwirth, I.; Fytas, G.; Landfester, K.; Kroeger, A. Incorporation of Nanoparticles into Polymersomes: Size and Concentration Effects. *ACS Nano* **2012**, *6*, 7254–7262.
12. Deserno, M. Elastic Deformation of a Fluid Membrane upon Colloid Binding. *Phys. Rev. E* **2004**, *69*, 031903.
13. Nowak, S. A.; Chou, T. Membrane Lipid Segregation in Endocytosis. *Phys. Rev. E* **2008**, *78*, 021908.
14. Cao, S.; Wei, G.; Chen, J. Z. Y. Transformation of an Oblate-Shaped Vesicle Induced by an Adhering Spherical Particle. *Phys. Rev. E* **2011**, *84*, 050901.
15. Yi, X.; Shi, X.; Gao, H. Cellular Uptake of Elastic Nanoparticles. *Phys. Rev. Lett.* **2011**, *107*, 098101.
16. Gózdź, W. T. Deformations of Lipid Vesicles Induced by Attached Spherical Particles. *Langmuir* **2007**, *23*, 5665–5669.
17. Bahrami, A. H.; Lipowsky, R.; Weikl, T. R. Tubulation and Aggregation of Spherical Nanoparticles Adsorbed on Vesicles. *Phys. Rev. Lett.* **2012**, *109*, 188102.
18. Šarić, A.; Cacciuto, A. Mechanism of Membrane Tube Formation Induced by Adhesive Nanocomponents. *Phys. Rev. Lett.* **2012**, *109*, 188101.
19. Dasgupta, S.; Auth, T.; Gompper, G. Shape and Orientation Matter for the Cellular Uptake of Nonspherical Particles. *Nano Lett.* **2014**, *14*, 687–693.
20. Smith, K. A.; Jasnow, D.; Balazs, A. C. Designing Synthetic Vesicles that Engulf Nanoscopic Particles. *J. Chem. Phys.* **2007**, *127*, 084703.
21. Yue, T.; Zhang, X. Cooperative Effect in Receptor-Mediated Endocytosis of Multiple Nanoparticles. *ACS Nano* **2012**, *6*, 3196–3205.
22. Ding, H.; Ma, Y. Interactions between Janus Particles and Membranes. *Nanoscale* **2012**, *4*, 1116–1122.
23. Guo, R.; Mao, J.; Yan, L.-T. Unique Dynamical Approach of Fully Wrapping Dendrimer-like Soft Nanoparticles by Lipid Bilayer Membrane. *ACS Nano* **2013**, *7*, 10646–10653.
24. Salib, I.; Yong, X.; Crabb, E. J.; Moellers, N. M.; McFarlin, G. T., IV; Kuksenok, O.; Balazs, A. C. Harnessing Fluid-Driven Vesicles to Pick Up and Drop Off Janus Particles. *ACS Nano* **2013**, *7*, 1224–1238.
25. Chithrani, B. D.; Ghazani, A. A.; Chan, W. C. W. Determining the Size and Shape Dependence of Gold Nanoparticle Uptake into Mammalian Cells. *Nano Lett.* **2006**, *6*, 662–668.
26. Chithrani, B. D.; Chan, W. C. W. Elucidating the Mechanism of Cellular Uptake and Removal of Protein-Coated Gold Nanoparticles of Different Sizes and Shapes. *Nano Lett.* **2007**, *7*, 1542–1550.
27. Gao, H.; Shi, W.; Freund, L. B. Mechanics of Receptor-Mediated Endocytosis. *Proc. Natl. Acad. Sci. U.S.A.* **2005**, *102*, 9469–9474.
28. Bao, G.; Bao, X. R. Shedding Light on the Dynamics of Endocytosis and Viral Budding. *Proc. Natl. Acad. Sci. U.S.A.* **2005**, *102*, 9997–9998.
29. Decuzzi, P.; Ferrari, M. The Role of Specific and Non-Specific Interactions in Receptor-Mediated Endocytosis of Nanoparticles. *Biomaterials* **2007**, *28*, 2915–2922.
30. Zhang, S.; Li, J.; Lykotraftis, G.; Bao, G.; Suresh, S. Size-Dependent Endocytosis of Nanoparticles. *Adv. Mater.* **2009**, *21*, 419–424.
31. Schönherr, H.; Johnson, J. M.; Lenz, P.; Frank, C. W.; Boxer, S. G. Vesicle Adsorption and Lipid Bilayer Formation on Glass Studied by Atomic Force Microscopy. *Langmuir* **2004**, *20*, 11600–11606.
32. Gruhn, T.; Franke, T.; Dimova, R.; Lipowsky, R. Novel Method for Measuring the Adhesion Energy of Vesicles. *Langmuir* **2007**, *23*, 5423–5429.
33. Anderson, T. H.; Min, Y.; Weirich, K. L.; Zeng, H.; Fygenson, D.; Israelachvili, J. N. Formation of Supported Bilayers on Silica Substrates. *Langmuir* **2009**, *25*, 6997–7005.
34. Helfrich, W. Elastic Properties of Lipid Bilayers: Theory and Possible Experiments. *Z. Naturforsch., C: J. Biosci.* **1973**, *28*, 693–703.
35. Seifert, U.; Berndl, K.; Lipowsky, R. Shape Transformations of Vesicles: Phase Diagram for Spontaneous Curvature and Bilayer Coupling Model. *Phys. Rev. A* **1991**, *44*, 1182–1202.
36. Lipowsky, R. Coupling of Bending and Stretching Deformations in Vesicle Membranes. *Adv. Colloid Interface Sci.* **2014**, *208*, 14–24.
37. Fadeel, B.; Xue, D. The Ins and Outs of Phospholipid Asymmetry in the Plasma Membrane: Roles in Health and Disease. *Crit. Rev. Biochem. Mol. Biol.* **2009**, *44*, 264–77.
38. Hu, P. C.; Li, S.; Malmstadt, N. Microfluidic Fabrication of Asymmetric Giant Lipid Vesicles. *ACS Appl. Mater. Interfaces* **2011**, *3*, 1434–1440.
39. Richmond, D. L.; Schmid, E. M.; Martens, S.; Stachowiak, J. C.; Liska, N.; Fletcher, D. A. Forming Giant Vesicles with Controlled Membrane Composition, Asymmetry, and Contents. *Proc. Natl. Acad. Sci. U.S.A.* **2011**, *108*, 9431–9436.
40. Matosevic, S.; Paegel, B. M. Layer-by-Layer Cell Membrane Assembly. *Nat. Chem.* **2013**, *5*, 958–963.
41. Rózycki, B.; Lipowsky, R. Spontaneous Curvature of Bilayer Membranes from Molecular Simulations: Asymmetric Lipid Densities and Asymmetric Adsorption. *J. Chem. Phys.* **2015**, *142*, 054101.
42. Danhier, F.; Ansorena, E.; Silva, J. M.; Coco, R.; le Breton, A.; Préat, V. PLGA-Based Nanoparticles: An Overview of Biomedical Applications. *J. Controlled Release* **2012**, *161*, 505–522.
43. do Carmo, M. *Differential Geometry of Curves and Surfaces*; Prentice-Hall: Englewood Cliffs, 1976.
44. Seifert, U.; Lipowsky, R. Adhesion of Vesicles. *Phys. Rev. A* **1990**, *42*, 4768–4771.
45. Moy, V. T.; Jiao, Y.; Hillmann, T.; Lehmann, H.; Sano, T. Adhesion Energy of Receptor-Mediated Interaction Measured by Elastic Deformation. *Biophys. J.* **1999**, *76*, 1632–1638.
46. Brüning, B.-A.; Prévost, S.; Stehle, R.; Steitz, R.; Falus, P.; Farago, B.; Hellweg, T. Bilayer Undulation Dynamics in Unilamellar Phospholipid Vesicles: Effect of Temperature, Cholesterol and Trehalose. *Biochim. Biophys. Acta* **2014**, *1838*, 2412–2419.
47. Weikl, T.; Lipowsky, R. *Membrane Adhesion and Domain Formation*; Advances in Planar Lipid Bilayers and Liposomes; Elsevier, 2007; Vol. 5, pp 64–127.
48. *Structure and Dynamics of Membranes: Generic and Specific Interactions*; Lipowsky, R.; Sackmann, E., Eds.; Handbook of Biological Physics; Elsevier: Amsterdam, 1995; Vol. 1B.
49. *Biomembranes*; Shinitzky, M., Ed.; Balaban Publishers, VCH: Weinheim, 1993.
50. Dimova, R.; Aranda, S.; Bezlyepkina, N.; Nikolov, V.; Riske, K.; Lipowsky, R. A Practical Guide to Giant Vesicles. *J. Phys.: Condens. Matter* **2006**, *18*, S1151–S1176.
51. Rahimi, M.; Arroyo, M. Shape Dynamics, Lipid Hydrodynamics, and the Complex Viscoelasticity of Bilayer Membranes. *Phys. Rev. E* **2012**, *86*, 011932.
52. Fuchs, H.; Lücken, U.; Tauber, R.; Engel, A.; Geßner, R. Structural Model of Phospholipid-Reconstituted Human Transferrin Receptor Derived by Electron Microscopy. *Structure* **1998**, *6*, 1235–1243.
53. Doherty, G. J.; McMahon, H. T. Mechanics of Endocytosis. *Annu. Rev. Biochem.* **2009**, *78*, 857–902.
54. Xu, S.; Olenyuk, B. Z.; Okamoto, C. T.; Hamm-Alvarez, S. F. Targeting Receptor-Mediated Endocytotic Pathways with Nanoparticles: Rationale and Advances. *Adv. Drug Delivery Rev.* **2013**, *65*, 121–138.

55. Pearse, B.; Crowther, R. Structure and Assembly of Coated Vesicles. *Annu. Rev. Biophys. Chem.* **1987**, *16*, 49–68.
56. Loerke, D.; Mettlen, M.; Yarar, D.; Jaqaman, K.; Jaqaman, H.; Danuser, G.; Schmid, S. L. Cargo and Dynamin Regulate Clathrin-Coated Pit Maturation. *PLOS Biol.* **2009**, *7*, e1000057.
57. Cureton, D. K.; Harbison, C. E.; Parrish, C. R.; Kirchhausen, T. Limited Transferrin Receptor Clustering Allows Rapid Diffusion of Canine Parvovirus into Clathrin Endocytic Structures. *J. Virol.* **2012**, *86*, 5330–5340.
58. Vigers, G. P. A.; Crowther, R. A.; Pearse, B. M. F. Location of the 100 kDa-50 kDa Accessory Proteins in Clathrin Coats. *EMBO J.* **1986**, *5*, 2079–2085.
59. Jin, A. J.; Prasad, K.; Smith, P. D.; Lafer, E. M.; Nossal, R. Measuring the Elasticity of Clathrin-Coated Vesicles via Atomic Force Microscopy. *Biophys. J.* **2006**, *90*, 3333–3344.
60. Yersin, A.; Osada, T.; Ikai, A. Exploring Transferrin-Receptor Interactions at the Single-Molecule Level. *Biophys. J.* **2008**, *94*, 230–240.
61. Watts, C. Rapid Endocytosis of the Transferrin Receptor in the Absence of Bound Transferrin. *J. Cell Biol.* **1985**, *100*, 633–637.
62. Hopkins, C. R.; Miller, K.; Beardmore, J. M. Receptor-Mediated Endocytosis of Transferrin and Epidermal Growth Factor Receptors: A Comparison of Constitutive and Ligand-Induced Uptake. *J. Cell Sci. Suppl.* **1985**, *3*, 173–186.
63. Fourcade, B.; Miao, L.; Rao, M.; Wortis, M.; Zia, R. Scaling Analysis of Narrow Necks in Curvature Models of Fluid Lipid-Bilayer Vesicles. *Phys. Rev. E* **1994**, *49*, 5276–5286.
64. Jülicher, F.; Lipowsky, R. Shape Transformations of Inhomogeneous Vesicles with Intramembrane Domains. *Phys. Rev. E* **1996**, *53*, 2670–2683.

Critical Particle Sizes for the Engulfment of Nanoparticles by Membranes and Vesicles with Bilayer Asymmetry – Supporting Information

Jaime Agudo-Canalejo and Reinhard Lipowsky*

*Theory & Biosystems, Max Planck Institute of Colloids and Interfaces,
14424 Potsdam, Germany*

E-mail: lipowsky@mpikg.mpg.de

This Supporting Information contains technical details about

- A. Free energy landscapes for engulfment process, with Figures S1 and S2;
- B. Exocytic engulfment of nanoparticles, with Figure S3; and
- C. Spreading dynamics and engulfment rate.

Figure S1 depicts the basic geometry of the vesicle-particle system for endocytic engulfment. Figure S2 illustrates the different free energy landscapes for the engulfment process, emphasizing the landscapes for the bistable regime \mathcal{B}_{st} . Figure S3 shows the four engulfment regimes for exocytic engulfment by weakly curved membranes as a function of particle size and spontaneous curvature.

A. Free Energy Landscapes for Engulfment Process

Geometry of bound and unbound membrane segments. In order to minimize the free energy of the vesicle-particle system, we decomposed the membrane into a bound seg-

*To whom correspondence should be addressed

ment and an unbound segment as shown in Figure S1 for endocytic engulfment. The bound membrane segment (red in Figure S1) is in contact with the nanoparticle of radius R_{pa} and extends up to the contact line which defines the wrapping angle ϕ . This angle varies from $\phi = 0$ for the free particle state to $\phi = \pi$ for the completely engulfed state and can be regarded as the reaction coordinate for the engulfment process. The total membrane area $A = 4\pi R_{\text{ve}}^2$ is equal to the sum of the area A_{bo} of the bound membrane segment and the area A_{un} of the unbound segment.

The bound segment of the vesicle membrane follows the contour of the particle, and thus assumes the shape of a spherical cap with mean curvature $M = \mp 1/R_{\text{pa}}$ where the minus and plus sign corresponds to the endocytic and exocytic process, respectively (main text, Figure 2). The area of the bound segment is given by

$$A_{\text{bo}} = 2\pi R_{\text{pa}}^2 (1 - \cos \phi). \quad (\text{S1})$$

If we cut the spherical particle along the contact line, we obtain two spherical caps. The spherical cap adjacent to the bound membrane segment has the volume

$$V_{\text{bo}} = \frac{4\pi}{3} R_{\text{pa}}^3 (2 + \cos \phi) [\sin(\phi/2)]^4. \quad (\text{S2})$$

The unbound membrane segment does not experience molecular interactions with the particle and its shape is determined (i) by the location of the contact line, which provides the circular boundary of the unbound membrane segment, (ii) by the area $A_{\text{un}} = A - A_{\text{bo}}$ of the unbound segment, (iii) by the effective volume $V \pm V_{\text{bo}}$, which is enclosed by the unbound membrane segment and the additional planar surface that spans the circular contact line, where the plus and minus sign applies to endo- and exocytosis, respectively; and (iv) by the spontaneous curvature m .

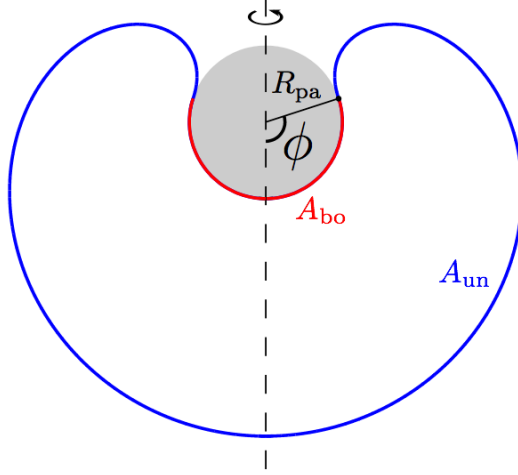


Figure S1: Vesicle membrane (red-blue) in contact with a spherical nanoparticle (gray) of radius R_{pa} . The vesicle shape is axially symmetric with respect to the vertical dashed line. The wrapping (or spreading) angle ϕ denotes the position of the contact line which partitions the membrane into a bound (red) and an unbound (blue) segment. The wrapping angle varies from $\phi = 0$ for the onset of adhesion up to $\phi = \pi$ for the completely engulfed state. The bound and unbound membrane segment have the areas A_{bo} and $A_{\text{un}} = A - A_{\text{bo}}$, respectively.

Decomposition of total free energy. As explained in the *Methods* section, the total free energy E is equal to the sum of the membrane's bending free energy E_{be} (main text, eq 21) and the adhesion free energy $E_{\text{ad}} = -|W| A_{\text{bo}}$. The total free energy can also be decomposed according to

$$E = E_{\text{bo}} + E_{\text{un}} \quad (\text{S3})$$

with the free energy

$$E_{\text{bo}} \equiv [-2\pi|W|R_{\text{pa}}^2 + 4\pi\kappa(1 \pm mR_{\text{pa}})^2] [1 - \cos(\phi)]. \quad (\text{S4})$$

of the bound membrane segment, where the plus and minus sign correspond to endocytic and exocytic engulfment, respectively, and the free energy

$$E_{\text{un}} = \int dA_{\text{un}} 2\kappa(M - m)^2 \quad (\text{S5})$$

of the unbound membrane segment where the integral extends over the area $A_{\text{un}} = A - A_{\text{bo}}$ of the latter segment.

In eq S4, we used the convention that the upper and lower sign of the \pm symbol corresponds to the endocytic and exocytic case, respectively. The same convention will be used below in all equations in which a \pm symbol appears.

Free energy minimization. In order to find the shape of the unbound segment that minimizes E_{un} for a given value of the wrapping angle ϕ and, thus, for a given location of the contact line, we minimize the shape functional

$$F_{\text{un}} \equiv E_{\text{un}} + \Sigma(A - A_{\text{bo}}) - \Delta P(V \pm V_{\text{bo}}) \quad (\text{S6})$$

where Σ and ΔP are Lagrange multipliers which ensure that the membrane area has the prescribed value A and that the unbound and bound membrane together enclose the vesicle volume V . The auxiliary volume $V \pm V_{\text{bo}}$ is enclosed by the unbound membrane segment and the additional planar surface that spans the circular contact line. When we calculate the free energy $E_{\text{un}}(\phi)$ of the unbound membrane segment by minimizing the shape functional F_{un} in eq S6 for many different values of ϕ within the interval $0 < \phi < \pi$, keeping both the area A and the volume V fixed, we obtain the corresponding free energy landscape

$$E(\phi) = [-2\pi|W|R_{\text{pa}}^2 + 4\pi\kappa(1 \pm mR_{\text{pa}})^2] [1 - \cos(\phi)] + E_{\text{un}}(\phi) \quad (\text{S7})$$

where the first term on the right hand side follows from eq S4. Typical free energy landscapes $E(\phi)$ obtained in this way are displayed in Figure S2 corresponding to the parameter values marked with green diamonds in Figure 3c. In general, the free energy landscapes may contain additional minima corresponding to additional intermediate states. For the uniform membranes considered in the main text, these additional states can always be ignored because they represent satellite minima very close to the free or completely engulfed states, from

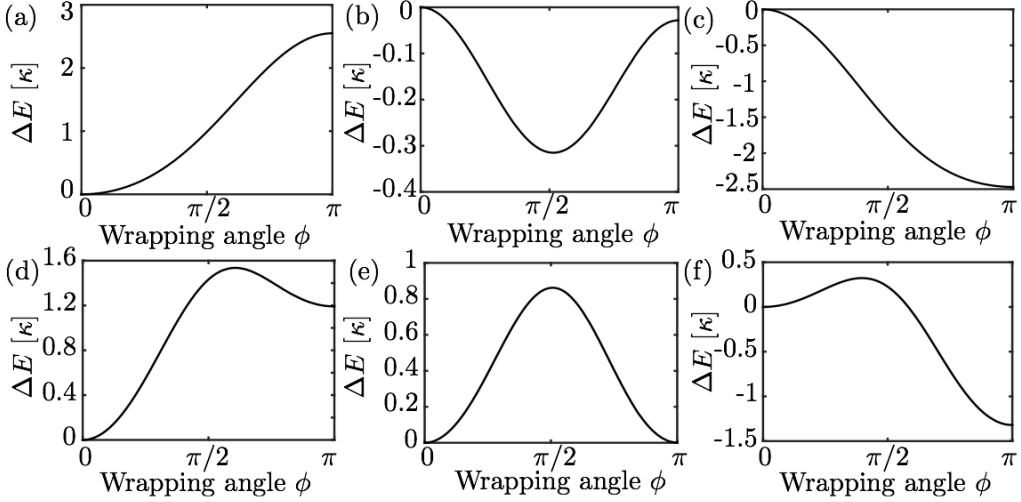


Figure S2: Free energy landscapes $\Delta E(\phi) \equiv E(\phi) - E(0)$ corresponding to the six parameter values marked by green diamonds in Figure 3c: (a) For the free (or non-engulfment) regime \mathcal{F}_{st} , the landscape has a minimum at $\phi = 0$, which corresponds to the free state \mathcal{F} , and a maximum at $\phi = \pi$, which defines the completely engulfed state \mathcal{C} ; (b) For the partial engulfment regime \mathcal{P}_{st} , the landscape has maxima both at $\phi = 0$ and at $\phi = \pi$ and a minimum at an intermediate ϕ -value corresponding to a partially engulfed state; (c) For the complete engulfment regime \mathcal{C}_{st} , the landscape exhibits a minimum at $\phi = \pi$ and a maximum at $\phi = 0$; (d, e, f) Three landscapes within the bistable regime \mathcal{B}_{st} with two local minima at $\phi = 0$ and $\phi = \pi$ separated by a free energy barrier. In panels (d) and (f), the global minima are provided by the states \mathcal{F} and \mathcal{C} , respectively. Panel (e) corresponds to the transition line L_* at which both states \mathcal{F} and \mathcal{C} have the same free energy.

which they are separated by tiny energy barriers that can be easily overcome by thermal fluctuations.

Free energy landscape close to free particle state \mathcal{F} . Close to the free particle state \mathcal{F} with $\phi = 0$, the free energy landscape behaves as

$$E(\phi) \approx E(0) + \frac{1}{2} E'' \phi^2 \quad \text{with} \quad E'' \equiv \left. \frac{d^2 E(\phi)}{d\phi^2} \right|_{\phi=0}. \quad (\text{S8})$$

The free particle state is (meta)stable as long as $E'' > 0$ and unstable for $E'' < 0$, which implies that $E'' = 0$ determines the instability line L_{fr} . Using the decomposition $E = E_{\text{bo}} + E_{\text{un}}$ of the free energy into the contributions from the bound and unbound membrane

segments, as in eqs S3 - S5, we obtain $E'' = E''_{\text{bo}} + E''_{\text{un}}$ with

$$E''_{\text{bo}} = -2\pi R_{\text{pa}}^2 |W| + 4\pi\kappa(1 \pm R_{\text{pa}} m)^2 \quad (\text{S9})$$

with the plus (minus) sign corresponding to endocytosis (exocytosis).

The instability line L_{fr} is now determined by

$$E'' = -2\pi R_{\text{pa}}^2 |W| + 4\pi\kappa(1 \pm R_{\text{pa}} m)^2 + E''_{\text{un}} = 0. \quad (\text{S10})$$

Alternatively, we may also determine L_{fr} from the instability relation

$$M_{\text{co}} = M_{\text{ms}} \quad \text{or} \quad \sqrt{R_{\text{pa}}^2 |W| / (2\kappa)} = 1 \pm R_{\text{pa}} M_{\text{ms}} \quad (\text{S11})$$

where the expression for the contact mean curvature M_{co} in eq 23 of the main text has been used. The two relationships as given by eqs S10 and S11 are only equivalent if the unbound membrane segment makes the contribution

$$E''_{\text{un}} = 4\pi\kappa R_{\text{pa}} [M_{\text{ms}} - m] [\pm 2 + R_{\text{pa}} (M_{\text{ms}} + m)] \quad (\text{S12})$$

to the second derivative E'' . A combination of E''_{bo} in eq S9 and E''_{un} in eq S12 then leads to

$$E'' = E''_{\text{bo}} + E''_{\text{un}} = -2\pi R_{\text{pa}}^2 |W| + 4\pi\kappa(1 \pm R_{\text{pa}} M_{\text{ms}})^2. \quad (\text{S13})$$

For endocytosis (+ sign), this relationship is identical to eq 6 in the main text.

Relation between membrane area and mechanical membrane tension. In the theoretical approach used here, the mechanical tension Σ does not represent an independent parameter but plays the role of a Lagrange multiplier Σ , see eq S6, which is determined in terms of the other parameters in order to ensure that the membrane area has the prescribed

value A .¹⁻³ The minimization procedure typically leads to Lagrange multipliers Σ that correspond to relatively small tensions of the order of κ/R_{ve}^2 , $\kappa m/R_{ve}$, or κm^2 . If we stretched the membrane with such a tension, the change in membrane area arising from the membrane's area compressibility would be rather small which provides a consistency check on the theory. In fact, even in the presence of relatively large tensions of the order of 1 mN/m, the membrane area can only change by a few percent without rupturing. Thus, as long as the membrane does not rupture, its area remains constant to a very good approximation. For giant unilamellar vesicles (GUVs), the membrane area A can be directly measured and it is then possible to corroborate the theory by a systematic comparison of calculated and experimentally observed membrane shapes as has been successfully done for lipid vesicles in the absence of nanoparticles.⁴⁻⁶

An alternative theoretical approach has been used in refs 7 and 8 where the engulfment of nanoparticles was theoretically studied in the presence of a certain prescribed membrane tension Σ' . This tension was treated as an independent control parameter and then represents a 'chemical potential' for membrane area which would govern the exchange of area with a putative area reservoir, in analogy to a grand-canonical ensemble. This approach is motivated by the view that eukaryotic cells control the tension of their plasma membranes, presumably by regulating the osmotic conditions and by remodelling the cytoskeletal forces acting on the cell membrane, which leads to the so-called cortical tension. Because the mechanisms underlying this tension are complex and poorly understood, it is appealing to reduce this complexity to a single tension parameter. One difficulty with this approach is that the measured tension values are quite variable and change during the cell cycle. Indeed, recent experiments provide Σ' -values in the range between 0.05 and 2 mN/m.^{9,10} Another difficulty is that the actin-myosin cortex exerts complex patterns of forces onto the cell membrane which contribute to the membrane tension but, at the same time, directly affect the membrane shape, and it is not obvious that these two effects of the cortical forces may be decomposed and considered separately.

The lipid membranes and vesicles addressed in our study do not involve an area (or lipid) reservoir which implies that the membrane area A rather than the membrane tension should be regarded as the basic control parameter. Furthermore, the instability relations for the free and completely engulfed particle states as derived here depend only on *local* properties of the membrane close to the nanoparticle and can, thus, also be applied to cell membranes. In fact, one can show that the free energy landscapes for particle engulfment remain unaffected by small tensions $\Sigma' \ll \Sigma_o \equiv \kappa/R_{\text{pa}}^2$. For a membrane with a clathrin coat, the bending rigidity is $\kappa = 10^{-18}$ J as measured in ref 11 which leads to crossover tensions $\Sigma_o \geq 0.4$ mN/m for particle sizes $R_{\text{pa}} \leq 50$ nm as studied experimentally in refs 12 and 13.

B. Exocytic Engulfment of Nanoparticles

Instability relations for exocytic engulfment. For exocytic engulfment, the curvature M_{ms} of the membrane segment adjacent to the free particle state \mathcal{F} (main text, Figure 5) must be smaller than $1/R_{\text{pa}}$ in order to ensure that the membrane and the particle do not intersect each other. Furthermore, the contact mean curvature is given by $M_{\text{co}} = -\frac{1}{R_W} + \frac{1}{R_{\text{pa}}}$ as explained in the *Methods* section. As a consequence, the relation $M_{\text{co}} = M_{\text{ms}}$ for the instability line L_{fr} of the free state \mathcal{F} leads to

$$R_{\text{pa}} = R_{\text{fr}} \equiv \frac{1}{M_{\text{ms}} + R_W^{-1}} \quad \text{and} \quad M_{\text{ms}} > -1/R_W \quad (L_{\text{fr}}, \text{exocytosis}). \quad (\text{S14})$$

and the membrane segment starts to spread over the particle if

$$R_{\text{pa}} > R_{\text{fr}} \quad \text{and} \quad M_{\text{ms}} > -1/R_W \quad (\text{unstable } \mathcal{F}, \text{exocytosis}). \quad (\text{S15})$$

For strongly curved membrane segments with a negative mean curvature M_{ms} smaller than $-1/R_W$, the free state \mathcal{F} is stable for all particle sizes, *i.e.*, the critical particle size $R_{\text{fr}} = \infty$.

For exocytic engulfment, the curvature M'_{ms} of the mother membrane adjacent to the

membrane neck of the completely engulfed state \mathcal{C} (main text, Figure 6) must be larger than $-1/R_{\text{pa}}$ in order to ensure that the mother membrane does not intersect the membrane segment bound to the particle. The instability line L_{ce} for the state \mathcal{C} as determined by $M_{\text{co}} + M'_{\text{ms}} = 2m$ now has the form

$$R_{\text{pa}} = R_{\text{ce}} \equiv \frac{1}{2m + R_W^{-1} - M'_{\text{ms}}} \quad \text{for } M'_{\text{ms}} < 2m + 1/R_W \quad (L_{\text{ce}}, \text{ exocytosis}), \quad (\text{S16})$$

and the membrane neck starts to open if

$$R_{\text{pa}} < R_{\text{ce}} \quad \text{and} \quad M'_{\text{ms}} < 2m + 1/R_W \quad (\text{unstable } \mathcal{C}, \text{ exocytosis}). \quad (\text{S17})$$

If the unbound membrane segment has a mean curvature M'_{ms} larger than $2m + \frac{1}{R_W}$, the completely engulfed state \mathcal{C} is unstable for all particle sizes, *i.e.*, $R_{\text{ce}} = \infty$. The physical requirement that the membrane has no self-intersections in state \mathcal{C} leads to the additional condition that M'_{ms} is larger than $-1/R_{\text{pa}}$. Therefore, stable states \mathcal{C} without self-intersections are only possible for $-\frac{1}{R_{\text{pa}}} < M'_{\text{ms}} < 2m + \frac{1}{R_W}$.

These instability lines and instability criteria for exocytic engulfment can be transformed into those for endocytic engulfment, if we change (i) the sign of the spontaneous curvature m as well as (ii) the signs of the curvatures M_{ms} and M'_{ms} of the two membrane segments. This ‘mirror symmetry’ implies that we have a one-to-one correspondence between the engulfment diagrams for exocytic and endocytic engulfment as illustrated further below for the case of weakly curved membranes.

For notational simplicity, we have used the same notation R_W for the adhesion length of both the endocytic and the exocytic process. Note, however, that the two adhesion lengths may have different numerical values because the molecular interactions described by the adhesive strength W may be different on the two sides of the asymmetric bilayer.

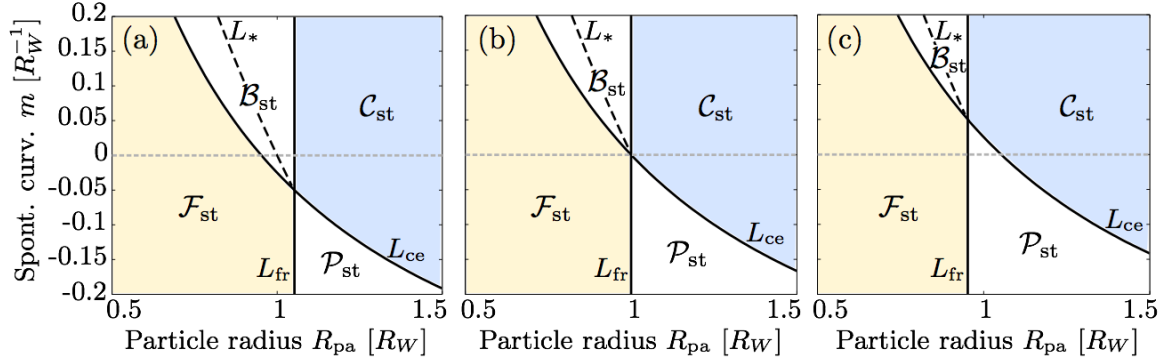


Figure S3: Exocytic engulfment of nanoparticles by weakly curved membranes: Different engulfment regimes \mathcal{F}_{st} , \mathcal{B}_{st} , \mathcal{C}_{st} and \mathcal{P}_{st} as a function of particle size R_{pa} and spontaneous curvature m , both measured in units of the adhesion length R_W . (a) Concave membrane segments with small negative curvatures $M_{\text{ms}} = M'_{\text{ms}} = -0.05/R_W$; (b) Flat membrane segments with vanishing curvatures $M_{\text{ms}} = M'_{\text{ms}} = 0$; and (c) Convex membrane segments with small positive curvatures $M_{\text{ms}} = M'_{\text{ms}} = +0.05/R_W$. The two instability lines L_{fr} and L_{ce} for the free and completely engulfed states are given by eq S14 and eq S16 and define the critical particle sizes R_{fr} and R_{ce} . The bistable regimes \mathcal{B}_{st} contain the transition lines L_* (dashed) at which the free and completely engulfed states coexist. All four engulfment regimes meet at the ‘multicritical’ intersection points of the two instability lines. Compared to endocytic engulfment (main text, Figure 7), the relative locations of the regimes \mathcal{B}_{st} and \mathcal{P}_{st} have been swapped.

Critical particle sizes for exocytic engulfment. The equations of the previous subsection imply that the intersection point of the two instability lines is again located at $m = \frac{1}{2}(M_{\text{ms}} + M'_{\text{ms}})$ but that the relative positions of the intermediate size regimes \mathcal{B}_{st} and \mathcal{P}_{st} are now swapped compared to the endocytic case. Therefore, the engulfment process is continuous for $m < \frac{1}{2}(M_{\text{ms}} + M'_{\text{ms}})$ and discontinuous for $m > \frac{1}{2}(M_{\text{ms}} + M'_{\text{ms}})$, see Table S1. The latter table also contains the two critical particle radii for exocytic engulfment as obtained from the corresponding instability criteria in eqs S15 and S17.

Exocytic engulfment by weakly curved mother membranes. For sufficiently large values of the vesicle size R_{ve} , the two membrane curvatures M_{ms} and M'_{ms} can again be neglected. The corresponding engulfment diagram is depicted in Figure S3b as a function of particle size R_{pa} and spontaneous curvature m , both measured in units of the adhesion length

Table S1: Critical particle sizes for *exocytic* engulfment as derived from eqs S15 and S17.

Range of spontaneous curvature m	Intermediate size regime	Engulfment process	Lower critical size	Upper critical size
$m > \frac{1}{2} (M_{\text{ms}} + M'_{\text{ms}})$	bistable \mathcal{B}_{st}	discontinuous	R_{ce}	R_{fr}
$m < \frac{1}{2} (M_{\text{ms}} + M'_{\text{ms}})$	partial \mathcal{P}_{st}	continuous	R_{fr}	R_{ce}

R_W . Inspection of Figure S3b shows that exocytic engulfment by flat membranes leads to partially engulfed states for negative spontaneous curvature and to bistability for positive spontaneous curvature. This behavior for the exocytic process is exactly the opposite of the behavior for the endocytic process for which partially engulfed states occur for positive spontaneous curvature and bistability is found for negative spontaneous curvatures (main text, Figure 7b). For small but finite values of the segment curvatures M_{ms} and M'_{ms} , the regimes for exocytic engulfment again undergo small changes, primarily determined by the sign of $M_{\text{ms}} + M'_{\text{ms}}$, as illustrated in Figure S3a and Figure S3c.

A detailed comparison of the different regimes for exocytic and endocytic engulfment as displayed in Figure S3 and Figure 7 shows that the exocytic diagrams can be obtained from the endocytic ones if we simultaneously change the sign of the spontaneous curvature m as well as the signs of the segment curvatures M_{ms} and M'_{ms} . In this way, we obtain Figure S3c from Figure 7a and Figure S3a from Figure 7c. This ‘mirror symmetry’ of the engulfment diagrams is a direct consequence of the corresponding ‘mirror symmetry’ of the instability criteria as pointed out after eq S17.

Adhesion length and spontaneous curvature from critical particle sizes. If the exocytic engulfment process is continuous and proceeds *via* partially engulfed states, the two critical particle sizes R_{fr} and $R_{\text{ce}} > R_{\text{fr}}$ are accessible to direct observation, either in experimental or in simulations studies. From the observed critical sizes, we can then

determine the adhesion length *via*

$$R_W = \frac{R_{\text{fr}}}{1 - R_{\text{fr}} M_{\text{ms}}} \quad (\text{cont exocytosis}) \quad (\text{S18})$$

and the spontaneous curvature *via*

$$m = \frac{1}{2} \left[\frac{1}{R_{\text{ce}}} - \frac{1}{R_{\text{fr}}} + M_{\text{ms}} + M'_{\text{ms}} \right] \quad (\text{cont exocytosis}) \quad (\text{S19})$$

as follows from eqs S14 and S16.

C. Kinetics of Membrane Spreading and Engulfment Rate

Force balance at the contact line. The spreading of the membrane over the particle surface is induced by the attractive membrane-particle forces and proceeds *via* the displacement of the contact line. For the engulfment of a spherical particle, the membrane geometry is axially symmetric and the contact line has the total length

$$L_{\text{co}} = 2\pi R_{\text{pa}} \sin(\phi). \quad (\text{S20})$$

The position of the contact line is determined by the contact point of the membrane contour.

The coordinate of this point is taken to be the arc length

$$s \equiv R_{\text{pa}} \phi \quad (\text{S21})$$

of the bound membrane contour measured from the south pole of the particle with $\phi = 0$ as in Figure S1. The displacement of the contact line now corresponds to changes in s .

The contact line at position s experiences two forces: a thermodynamic driving force and a friction force. The thermodynamic driving force F_1 reflects the change in the system's

energy as we displace the contact line. This force has the form

$$F_1 = -\frac{dE_s(s)}{ds} = -\frac{1}{R_{\text{pa}}} \frac{dE(\phi)}{d\phi} \quad (\text{S22})$$

where $E_s(s)$ is the free energy landscape of the system as a function of s , *i.e.*, $E_s(s) = E(\phi(s)) = E(s/R_{\text{pa}})$ with the free energy landscape $E(\phi)$ as discussed before, see Figure S2. The force F_2 , on the other hand, depends on the dissipation mechanism. If the contact line does not move, there will be no friction. Therefore, the friction force F_2 is taken to be proportional to the velocity $v = ds/dt$ of the contact line which is equal to the derivative of arc length s with respect to time t . The friction coefficient for the displacement of the whole contact line should be proportional to the length L_{co} of the contact line which implies $F_2 = \eta_{\text{eff}} L_{\text{co}} ds/dt$ which defines the effective dynamic viscosity η_{eff} . Using eq S20 for the contact length L_{co} and changing variables from arc length s to wrapping angle ϕ *via* $s = R_{\text{pa}} \phi$, we obtain the ϕ -dependent friction force

$$F_2 = 2\pi \eta_{\text{eff}} R_{\text{pa}}^2 \sin(\phi) \frac{d\phi}{dt}. \quad (\text{S23})$$

We now balance the thermodynamic driving force F_1 in eq S22 with the friction force F_2 in eq S23, *i.e.*, we set $F_1 = F_2$ which leads to the equation of motion for the contact line as given by

$$\sin(\phi) \frac{d\phi}{dt} = -\frac{1}{2\pi \eta_{\text{eff}} R_{\text{pa}}^3} \frac{dE(\phi)}{d\phi} \quad (\text{S24})$$

which is identical with eq 17 in the main text.

Size-dependent engulfment rate. The equation of motion for the contact line (eq S24) involves the gradient $dE/d\phi$ of the free energy landscape which can again be decomposed into two contributions from the bound and unbound membrane segment, *i.e.*,

$$\frac{dE(\phi)}{d\phi} = \frac{dE_{\text{bo}}(\phi)}{d\phi} + \frac{dE_{\text{un}}(\phi)}{d\phi} \quad (\text{S25})$$

with

$$\frac{d E_{\text{bo}}(\phi)}{d \phi} = [-2\pi|W|R_{\text{pa}}^2 + 4\pi\kappa_{\text{bo}}(1 \pm m_{\text{bo}} R_{\text{pa}})^2] \sin(\phi) \quad (\text{S26})$$

with the plus sign corresponding to endocytosis.

As far as the gradient $d E_{\text{un}}(\phi)/d \phi$ of the unbound membrane (or mother membrane) is concerned, it is intuitively plausible that $E_{\text{un}}(\phi)$ changes primarily by shape changes of the unbound membrane segment close to the contact line and that these changes are small if this segment can adapt its mean curvature to the spontaneous curvature m . For $m = 0$, for example, this segment can attain a shape close to a catenoid which has vanishing bending energy and, thus, makes no contribution to E_{un} . This expectation can be directly confirmed for the initial spreading close to the free state \mathcal{F} , *i.e.*, for small values of the wrapping angle ϕ because

$$\frac{d E_{\text{un}}(\phi)}{d \phi} \approx E''_{\text{un,fr}} \phi = 4\pi\kappa R_{\text{pa}} [M_{\text{ms}} - m] [\pm 2 + R_{\text{pa}}(M_{\text{ms}} + m)] \phi \quad \text{for small } \phi \quad (\text{S27})$$

as follows from $E_{\text{un}}(\phi) \approx E_{\text{un}}(0) + \frac{1}{2} E''_{\text{un,fr}} \phi^2$ and eq S12 with $E''_{\text{un}} = E''_{\text{un,fr}}$. The latter equation also applies to the present case because the unbound membrane segment (or mother membrane) is characterized by the same fluid-elastic parameters m and κ as in the case of the uniform membrane.

Likewise, for the final spreading process close to the completely engulfed state \mathcal{C} , *i.e.*, for small deviations $\delta\phi \equiv \phi - \pi$, the free energy landscape for the unbound membrane segment behaves as $E_{\text{un}}(\phi) \approx E_{\text{un}}(\pi) + \frac{1}{2} E''_{\text{un,ce}} \delta\phi^2$ with

$$E''_{\text{un,ce}} \equiv \left. \frac{d^2 E_{\text{un}}(\phi)}{d \phi^2} \right|_{\phi=\pi} = 4\pi\kappa R_{\text{pa}} [M'_{\text{ms}} - m] [\pm 2 + R_{\text{pa}}(3m - M'_{\text{ms}})]. \quad (\text{S28})$$

which implies the gradient

$$\frac{d E_{\text{un}}(\phi)}{d \phi} \approx 4\pi\kappa R_{\text{pa}} (M'_{\text{ms}} - m) [\pm 2 + R_{\text{pa}}(3m - M'_{\text{ms}})] \delta\phi \quad \text{for small } \delta\phi. \quad (\text{S29})$$

Inspection of eqs S27 and S29 shows that the gradient $dE_{\text{un}}(\phi)/d\phi$ is proportional to $R_{\text{pa}}(M_{\text{ms}} - m)$ for small ϕ and to $R_{\text{pa}}(M'_{\text{ms}} - m)$ for small $\delta\phi = \phi - \pi$. These dependencies have two implications. First, the gradient $dE_{\text{un}}(\phi)/d\phi$ vanishes for small ϕ and $M_{\text{ms}} = m$ as well as for small $\delta\phi$ and $M'_{\text{ms}} = m$ as expected. Second, this gradient becomes small if both the segment curvatures M_{ms} and M'_{ms} as well as the spontaneous curvature m are small compared to the inverse particle radius $1/R_{\text{pa}}$. The latter property motivates a systematic expansion of the free energy E_{un} in powers of the size ratio $\epsilon \equiv R_{\text{pa}}/R_{\text{ve}}$ with $R_{\text{ve}} = \sqrt{A/4\pi}$ as before. Such an expansion shows (i) that $M'_{\text{ms}} \approx M_{\text{ms}}$ to leading order in ϵ and (ii) that the free energy gradient $dE_{\text{un}}/d\phi$ of the unbound membrane segment behaves as

$$\frac{dE_{\text{un}}(\phi)}{d\phi} = \pm 8\pi\kappa R_{\text{pa}}(M_{\text{ms}} - m) \sin(\phi) \cos(\phi) + \mathcal{O}(\epsilon^2). \quad (\text{S30})$$

For small values of ϕ and $\delta\phi = \phi - \pi$, this expression becomes identical, to first order in $\epsilon = R_{\text{pa}}/R_{\text{ve}}$, with eq S27 and eq S29, respectively. This asymptotic behavior has been confirmed by numerical minimization of the total free energy. Therefore, in the limit of small size ratios $R_{\text{pa}}/R_{\text{ve}}$, the gradient $dE_{\text{un}}(\phi)/d\phi$ is proportional to $R_{\text{pa}}(M_{\text{ms}} - m) \approx R_{\text{pa}}(M'_{\text{ms}} - m)$ for all values of ϕ . As a consequence, this gradient can be neglected if both the segment curvatures M_{ms} and M'_{ms} as well as the spontaneous curvature m are much smaller than the inverse particle radius $1/R_{\text{pa}}$. In the latter case, the gradient of the free energy landscape is determined by the bound membrane segment alone and behaves as

$$\frac{dE(\phi)}{d\phi} \approx \frac{dE_{\text{bo}}(\phi)}{d\phi} = [-2\pi|W|R_{\text{pa}}^2 + 4\pi\kappa_{\text{bo}}(1 \pm m_{\text{bo}}R_{\text{pa}})^2] \sin(\phi) \quad (\text{S31})$$

as follows from eq S26. When we insert this expression for $dE(\phi)/d\phi$ into the equation of motion as given by eq S24 (or eq 17 in the main text), the factors proportional to $\sin(\phi)$ cancel and we obtain the simplified equation of motion

$$\frac{d\phi}{dt} = \frac{|W|R_{\text{pa}}^2 - 2\kappa(1 \pm mR_{\text{pa}})^2}{\eta_{\text{eff}} R_{\text{pa}}^3} \quad (\text{S32})$$

which implies that the wrapping velocity $d\phi/dt$ is constant and that the engulfment time $t_{\mathcal{FC}}$ follows from

$$\pi = \frac{|W|R_{\text{pa}}^2 - 2\kappa(1 \pm mR_{\text{pa}})^2}{\eta_{\text{eff}}R_{\text{pa}}^3} t_{\mathcal{FC}}. \quad (\text{S33})$$

For the plus sign corresponding to endocytosis, eq S33 is equivalent to eq 18 in the main text.

References

- (1) Deuling, H.; Helfrich, W. The Curvature Elasticity of Fluid Membranes: A Catalogue of Vesicle Shapes. *J. Physique* **1976**, *37*, 1335–1345.
- (2) Seifert, U.; Berndl, K.; Lipowsky, R. Shape Transformations of Vesicles: Phase Diagram for Spontaneous Curvature and Bilayer Coupling Model. *Phys. Rev. A* **1991**, *44*, 1182–1202.
- (3) Lipowsky, R. Coupling of Bending and Stretching Deformations in Vesicle Membranes. *Adv. Colloid Interface Sci.* **2014**, *208*, 14–24.
- (4) Berndl, K.; Käs, J.; Lipowsky, R.; Sackmann, E.; Seifert, U. Shape Transformations of Giant Vesicles: Extreme Sensitivity to Bilayer Asymmetry. *Europhys. Lett.* **1990**, *13*, 659–664.
- (5) Lipowsky, R. The Conformation of Membranes. *Nature* **1991**, *349*, 475–481.
- (6) Döbereiner, H.-G.; Evans, E.; Kraus, M.; Seifert, U.; Wortis, M. Mapping Vesicle Shapes into the Phase Diagram: A Comparison of Experiment and Theory. *Phys. Rev. E* **1997**, *55*, 4458 – 4474.
- (7) Deserno, M. Elastic Deformation of a Fluid Membrane upon Colloid Binding. *Phys. Rev. E* **2004**, *69*, 031903.

- (8) Zhang, S.; Li, J.; Lykotrafitis, G.; Bao, G.; Suresh, S. Size-Dependent Endocytosis of Nanoparticles. *Adv. Mater.* **2009**, *21*, 419 – 424.
- (9) Tinevez, J.-Y.; Schulze, U.; Salbreux, G.; Roensch, J.; Joanny, J.-F.; Paluch, E. Role of Cortical Tension in Bleb Growth. *Proc. Nat. Acad. Sci. USA* **2009**, *106*, 18581–18586.
- (10) Fischer-Friedrich, E.; Hyman, A. A.; Jülicher, F.; Müller, D. J.; Helenius, J. Quantification of Surface Tension and Internal Pressure Generated by Single Mitotic Cells. *Scientific Rep.* **2014**, *4*, 6213.
- (11) Jin, A. J.; Prasad, K.; Smith, P. D.; Lafer, E. M.; Nossal, R. Measuring the Elasticity of Clathrin-Coated Vesicles *via* Atomic Force Microscopy. *Biophys. J.* **2006**, *90*, 3333 – 3344.
- (12) Chithrani, B. D.; Ghazani, A. A.; Chan, W. C. W. Determining the Size and Shape Dependence of Gold Nanoparticle Uptake into Mammalian Cells. *Nano Lett.* **2006**, *6*, 662 – 668.
- (13) Chithrani, B. D.; Chan, W. C. W. Elucidating the Mechanism of Cellular Uptake and Removal of Protein-Coated Gold Nanoparticles of Different Sizes and Shapes. *Nano Lett.* **2007**, *7*, 1542 – 1550.

4 Adhesive Nanoparticles as Local Probes of Membrane Curvature

4.1 Overview

Here, we build up on the results of the previous paper in order to study the engulfment of nanoparticles at non-axisymmetric locations of vesicles with complex shape, that is, shapes with non uniform membrane curvature. By using the analytical expressions obtained before for the instability conditions of the free and completely engulfed states we show that, depending on the local curvature of the vesicle at the point of contact with the particle, a particle will either remain free, be partially or completely engulfed, or show bistability between the free and the completely engulfed states.

The four engulfment regimes that we had described previously can therefore coexist on the surface of a single vesicle, forming different engulfment patterns. For a homogeneous vesicle, we show that up to three different engulfment regimes can be simultaneously present on a single vesicle, combining to form a total of ten possible engulfment patterns. These patterns depend strongly on the vesicle shape, as defined by its reduced volume; on the spontaneous curvature; and on the particle size and adhesiveness, which are both encoded into a single parameter, the contact mean curvature. We obtain exact morphology diagrams showing the regions of stability of the different engulfment patterns, as well as the transitions between them.

This paper thus provides for the first time a way to predict engulfment behavior at non-axisymmetric locations of vesicles, expanding the literature on particle engulfment in yet another new direction. This is achieved without the need of carrying out numerical calculations, thanks to the instability conditions obtained before. The importance of bilayer asymmetry to the engulfment process is highlighted once again, and novel engulfment patterns that should be observable in experiment are predicted.



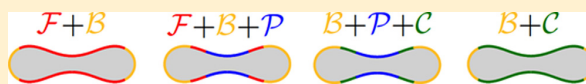
Adhesive Nanoparticles as Local Probes of Membrane Curvature

Jaime Agudo-Canalejo and Reinhard Lipowsky*

Theory and Bio-Systems, Max Planck Institute of Colloids and Interfaces, 14424 Potsdam, Germany

ABSTRACT: Biological and biomimetic membranes display complex shapes with nonuniform curvature. Because the interaction of adhesive nanoparticles with such membranes depends on the local membrane curvature, different segments of the same membrane can differ in their engulfment behavior. For a single vesicle in contact with many nanoparticles, we predict ten distinct engulfment patterns as well as morphological transitions between these patterns, which are directly accessible to experiment.

KEYWORDS: membranes and vesicles, nanoparticle–membrane adhesion, nanoparticle engulfment, bilayer asymmetry, local stability analysis, contact mean curvature, spontaneous curvature



Nanoparticles are widely used to deliver drugs, imaging agents, and toxins to biological cells.^{1,2} The cellular uptake of a nanoparticle requires the engulfment of this particle by the cell membrane, a process that is dominated by the competition between particle adhesion and membrane bending.³ The underlying interactions can be studied experimentally in biomimetic systems consisting of nanoparticles and lipid^{4–8} or polymer⁹ vesicles. Several theoretical and computational methods have also been used to elucidate the engulfment process.^{10–18} However, all of these previous studies of nanoparticle–membrane systems have ignored one important aspect of biological and biomimetic membranes, namely their complex, nontrivial shapes.^{19–22} Cells and cellular organelles display a whole catalogue of shapes, such as the prolate-like shapes of dividing cells or mitochondria; the discocyte, stomatocyte, and echinocyte shapes of red blood cells; the invaginated, stomatocyte-like shapes of nascent autophagosomes; or the recently reported “parking garage” shapes of the endoplasmic reticulum.²³ Interestingly, many of these shapes can be mimicked using lipid¹⁹ or polymer vesicles.²⁴ In particular, prolate, discocyte, and stomatocyte shapes arise naturally as the shapes that minimize the bending energy of closed vesicle membranes with constrained volume²⁰ and will be used as examples of complex membrane shapes in the following. Our results also apply to vesicle shapes that are topologically distinct from a sphere, corresponding to toroidal or higher genus shapes with one or several handles.^{25,26}

Previous theoretical studies of nanoparticle–membrane systems have been subject to certain limitations. Direct computation of minimal energy shapes of membranes is only possible for axisymmetric geometries, and therefore, previous work has been restricted to the engulfment of spherical particles by planar membranes^{10,12} or at the poles of closed axisymmetric vesicles.^{11,13,14} The study of nonaxisymmetric geometries is computationally expensive because it requires the numerical energy minimization of triangulated or spline surfaces,^{15,16} or alternatively molecular dynamics simulations,^{17,18} and efforts have focused mainly on the engulfment of nonspherical particles by planar membranes. In this Letter, we show how

the approach introduced in ref 14, based on local stability analysis of free and completely engulfed particles, can be used to understand the engulfment of spherical particles at nonaxisymmetric locations on the vesicle surface. In this way, we can elucidate the interaction of nanoparticles with membranes of any shape.

In general, attractive interactions between a nanoparticle and a membrane can lead to different states of engulfment. Previous studies have shown that spherical nanoparticles do not bind to membranes for weak attractive interactions but become completely engulfed for sufficiently strong adhesion.^{3,10} Recently, we found¹⁴ that concave membrane segments with negative mean curvature stabilize partially engulfed states, in which the membrane covers only a fraction of the particle surface, whereas convex segments with positive mean curvature favor bistability of unbound and completely engulfed particles. We thus identified four distinct stability regimes for the nanoparticles and the associated membrane segments: free \mathcal{F} segments do not bind the particles at all; \mathcal{C} segments completely engulf the particles, whereas \mathcal{P} segments engulf them only partially; finally, bistable \mathcal{B} segments exhibit an energy barrier between free and completely engulfed particles.

Each type of membrane segment is stable over a certain range of mean curvatures. As a consequence, the different types of segments can coexist on a single vesicle, creating engulfment patterns with many nanoparticles when the vesicle is exposed to a solution of such particles; see Figure 1. We predict that a single vesicle can exhibit ten distinct engulfment patterns: four single-segment patterns, with the whole vesicle membrane being composed of a single \mathcal{F} , \mathcal{P} , \mathcal{C} , or \mathcal{B} segment, four two-segment patterns, namely $\mathcal{F} + \mathcal{B}$, $\mathcal{B} + \mathcal{C}$, $\mathcal{F} + \mathcal{P}$, or $\mathcal{P} + \mathcal{C}$, and two three-segment patterns provided by $\mathcal{F} + \mathcal{B} + \mathcal{P}$ or $\mathcal{B} + \mathcal{P} + \mathcal{C}$. Which pattern is present depends on three parameters: the spontaneous curvature of the membrane, the reduced volume of the vesicle, which controls its overall shape, and the

Received: August 28, 2015

Revised: September 29, 2015

Published: October 2, 2015

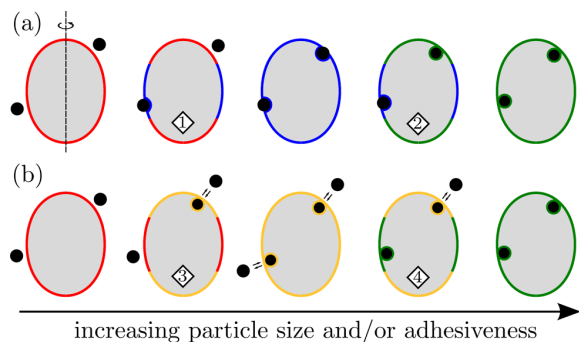


Figure 1. Different engulfment patterns of nanoparticles (black) on a prolate vesicle. The spontaneous curvature of the vesicle membrane is positive in (a) and negative in (b). The patterns involve four types of membrane segments: free segments with no engulfment (red) and bistable segments with activated engulfment and release (yellowish orange) as well as segments decorated by partially engulfed (blue) and completely engulfed (green) particles. A change in particle size or adhesiveness leads to continuous morphological transitions between these patterns. The numbered diamonds refer to Figure 3, below.

contact mean curvature, which encodes the information on the size and adhesiveness of the nanoparticles. All three parameters can be controlled experimentally, and changes in these parameters lead to continuous morphological transitions between the different patterns.

Our Letter is organized as follows. We first focus on endocytic engulfment of particles originating from the *exterior* aqueous compartment and briefly review how the stability of free and completely engulfed particles leads to four stability regimes for a single particle.¹⁴ We then show how, for sufficiently small nanoparticles, these stability regimes depend on only three parameters that also determine the possible engulfment patterns. Next, we extend our theory to exocytic engulfment of particles originating from the *interior* aqueous compartment and argue that membrane-mediated interactions between the particles do not affect the engulfment patterns. Finally, we discuss the engulfment patterns in connection to experiments.

Engulfment can be understood from the interplay between particle adhesion and membrane bending. According to the spontaneous curvature model,^{20,27} the bending energy density of the membrane is given by $\mathcal{E}_{be} = 2\kappa(M - m)^2$, where M is the mean curvature, which typically varies along the vesicle membrane. The relevant material parameters of the membrane are its bending rigidity κ and its spontaneous curvature m . The attractive interaction with the particle is described by the adhesive strength, $|W|$, which represents the absolute value of the adhesive free energy per unit area.²⁸ We first focus on endocytic engulfment of rigid spherical particles with radius R_{pa} by a vesicle with total membrane area A and enclosed volume V . These three geometrical parameters, together with the three material parameters κ , m , and $|W|$, determine the particle-vesicle morphologies. It will be useful to define the *contact mean curvature*

$$M_{co} \equiv \frac{1}{R_{pa}} \left(\sqrt{\frac{|W|R_{pa}^2}{2\kappa}} - 1 \right) \quad (1)$$

which encodes the competition between adhesion and bending into a single length scale, and represents¹⁴ the equilibrium

mean curvature of the membrane along the contact line with the adhering particle. It is important to note that the contact mean curvature increases both with increasing particle size and with increasing adhesive strength.

Let us consider a small segment of the vesicle membrane with mean curvature M_{ms} . The stability limit L_{fr} of a free particle coming into contact with this segment is given by the relation

$$M_{co} = M_{ms} \quad (2)$$

between the contact mean curvature M_{co} and the mean curvature M_{ms} of the unperturbed membrane segment. The free state is stable for large segment curvatures with $M_{ms} > M_{co}$ but is unstable for small segment curvatures with $M_{ms} < M_{co}$.

In the completely engulfed state, the particle is fully covered by the membrane but is still connected to the mother vesicle by a narrow membrane neck. In the continuum approach used here, the completely engulfed state represents a limit shape with an ideal neck that is attached to the mother vesicle at a single contact point. If the mean curvature of the mother vesicle at this contact point is denoted by M'_{ms} , the stability limit L_{ce} of the completely engulfed particle is given by

$$M_{co} + M'_{ms} = 2m \quad (3)$$

The completely engulfed state is stable if the mother segment curvature is large and satisfies $M'_{ms} > 2m - M_{co}$ but unstable if it is small with $M'_{ms} < 2m - M_{co}$.

Equations 2 and 3 were validated in ref 14 via extensive numerical calculations and detailed theoretical considerations. We also found that, in the case of particles much smaller than the vesicle, a partially engulfed state can only be stable if both the free and the completely engulfed state are unstable. The two relations in eqs 2 and 3 then define the boundaries of four stability regimes for the nanoparticles and the associated membrane segments: (i) For $M_{ms} > M_{co}$ and $M'_{ms} < 2m - M_{co}$, the free state is stable and the completely engulfed state is unstable, which defines a stable \mathcal{F} segment; (ii) for $M_{ms} > M_{co}$ and $M'_{ms} > 2m - M_{co}$, both the free and the completely engulfed state are stable and the segment belongs to a bistable \mathcal{B} segment; (iii) for $M_{ms} < M_{co}$ and $M'_{ms} > 2m - M_{co}$, the free state is unstable and the completely engulfed state is stable, which implies a stable \mathcal{C} segment; and (iv) for $M_{ms} < M_{co}$ and $M'_{ms} < 2m - M_{co}$, both the free and the completely engulfed state are unstable, and the particle should be partially engulfed by the membrane segment, which then belongs to a stable \mathcal{P} segment.

Vesicle membranes divide the aqueous phase into an interior and exterior compartment. When both compartments contain osmotically active agents, the vesicle adapts its volume in such a way that the osmotic pressure in the interior compartment balances the exterior osmotic pressure. The equilibrium shapes of such a vesicle with volume V , membrane area A , and vesicle size $R_{ve} \equiv \sqrt{A/4\pi}$ are then determined, in the absence of nanoparticles, by the reduced volume $\nu \equiv 3V/4\pi R_{ve}^3$ and the spontaneous curvature m .²⁰ In general, these equilibrium shapes form several stable branches such as the prolate and oblate branches for $0.65 \lesssim \nu < 1$ and $m = 0$. When a vesicle with area A and volume V completely engulfs N_{pa} nanoparticles, its overall shape is determined by the decreased area $A - 4\pi R_{pa}^2 N_{pa}$ and the increased volume $V + (4\pi/3)R_{pa}^3 N_{pa}$. Therefore, the reduced overall volume is increased from ν to

$$v' = \frac{v + N_{pa}(R_{pa}/R_{ve})^3}{[1 - N_{pa}(R_{pa}/R_{ve})^2]^{3/2}} \approx v \left[1 + \frac{3N_{pa}}{2} \left(\frac{R_{pa}}{R_{ve}} \right)^2 \right] \quad (4)$$

where the asymptotic equality holds for small particle radii $R_{pa} \ll R_{ve}/\sqrt{N_{pa}}$. As an example, a giant unilamellar vesicle of size $10 \mu\text{m}$ could engulf 100 nanoparticles of radius 100 nm, and its reduced volume would increase by less than 2%. Thus, for sufficiently small nanoparticles, we can ignore the tiny changes in the overall vesicle shape and identify the mean curvature M_{ms}^i in eq 3 with the mean curvature M_{ms} in eq 2. This approximation is justified as long as the overall vesicle shape stays on the same branch of equilibrium shapes as the reduced volume is increased from v to v' , that is, unless the vesicle undergoes a shape transition (see Figure 4 below). Furthermore, the relevant properties of the nanoparticles are encoded in the contact mean curvature M_{co} as defined by eq 1). Therefore, the nanoparticle-vesicle morphologies are now determined by only three parameters, namely v , m , and M_{co} (measured in units of $1/R_{ve}$).

Now, consider a certain vesicle shape as determined by v and m . Unless the vesicle is perfectly spherical, which corresponds to the limit case $v = 1$, the mean curvature M_{ms} will vary along the vesicle membrane in a continuous fashion. As a consequence, such a vesicle will display all membrane curvatures in the closed interval $M_{v,m}^{\min} \leq M_{ms} \leq M_{v,m}^{\max}$, where $M_{v,m}^{\min}$ and $M_{v,m}^{\max}$ are the minimal and maximal membrane curvatures of the vesicle. Using the inequalities described above that define the different stability regimes, it is now straightforward to determine which types of membrane segments will be present on a given vesicle. The general procedure is illustrated in Figure 2. A given vesicle can be

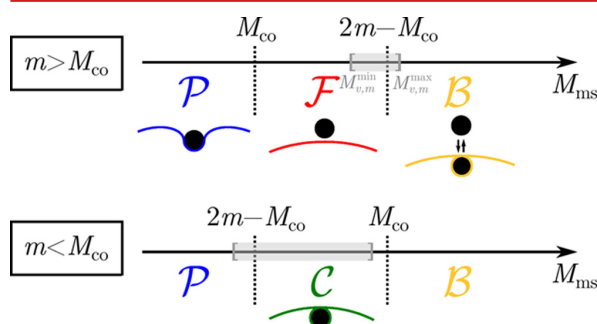


Figure 2. Engulfment regimes \mathcal{P} , \mathcal{B} , \mathcal{F} , or \mathcal{C} as a function of membrane segment curvature M_{ms} . The possible regimes depend on whether the spontaneous curvature m exceeds the contact mean curvature M_{co} (top row) or vice versa (bottom row). The boundaries between the different regimes follow from the stability limits $M_{ms} = M_{co}$ and $M_{ms} = 2m - M_{co}$. For a given shape of the vesicle, all segment curvatures are located within a closed interval $M_{v,m}^{\min} \leq M_{ms} \leq M_{v,m}^{\max}$, as illustrated by the two shaded rectangles. For $m = 0$, these shaded intervals correspond to a prolate (top) and a stomatocyte (bottom), see Figure 4.

represented by the closed interval $M_{v,m}^{\min} \leq M_{ms} \leq M_{v,m}^{\max}$. The M_{ms} -axis is divided up into three nonoverlapping intervals by the two stability limits $M_{ms} = M_{co}$ and $M_{ms} = 2m - M_{co}$. It then follows that not all combinations of different engulfment regimes or engulfment patterns can be found on the same vesicle. For the case $m > M_{co}$, we find six possible patterns:

three single-segment patterns with the whole vesicle being composed of a \mathcal{P} , \mathcal{F} , or \mathcal{B} segment, two two-segment patterns with coexistence of $\mathcal{F} + \mathcal{P}$ or $\mathcal{F} + \mathcal{B}$ segments, and one three-segment pattern of coexisting $\mathcal{F} + \mathcal{B} + \mathcal{P}$ segments. For the case $m < M_{co}$, we find again the single-segment \mathcal{P} and \mathcal{B} patterns, plus four new possible patterns: a single-segment \mathcal{C} pattern, two two-segment patterns $\mathcal{P} + \mathcal{C}$ and $\mathcal{B} + \mathcal{C}$, and one three-segment pattern $\mathcal{B} + \mathcal{P} + \mathcal{C}$. Thus, in contrast to the naive expectation that the four different types of membrane segments might form $2^4 - 1 = 15$ different engulfment patterns, which represents the number of nonempty subsets of a set with four elements, we find that a vesicle can exhibit only ten such patterns: four single-segment patterns, four two-segment patterns, and two three-segment patterns. Furthermore, we can exclude the $\mathcal{P} + \mathcal{B}$ two-segment pattern (apart from the exceptional case $M_{co} = m$) and all patterns that contain both an \mathcal{F} and a \mathcal{C} segment, compare Figure 2.

We can now use this type of reasoning to quantitatively describe the engulfment patterns present on the equilibrium shapes of free vesicles, as a function of the three free parameters v , m , and M_{co} . In Figure 3, we illustrate the engulfment patterns

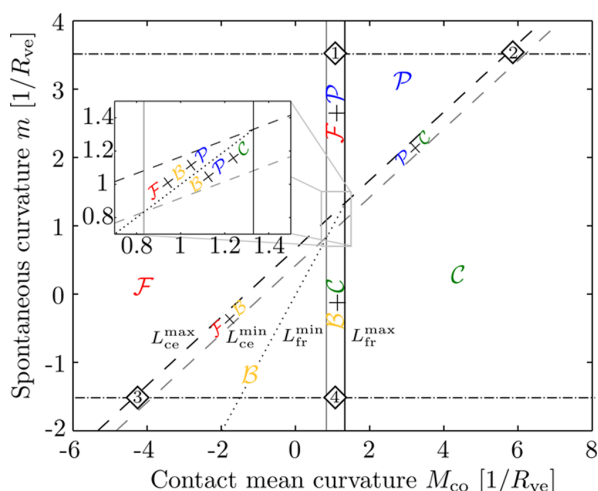


Figure 3. Engulfment patterns as a function of contact mean curvature M_{co} and spontaneous curvature m for a prolate vesicle with reduced volume $v = 0.98$. The solid vertical lines and the dashed tilted lines are given by the stability limits L_{fr}^{\min} , L_{fr}^{\max} , L_{ce}^{\min} , and L_{ce}^{\max} ; see text. These four lines partition the (M_{co}, m) plane into the four extended regions \mathcal{F} , \mathcal{B} , \mathcal{C} , and \mathcal{P} , characterized by single-segment patterns, the four stripes $\mathcal{F} + \mathcal{B}$, $\mathcal{B} + \mathcal{C}$, $\mathcal{P} + \mathcal{C}$, and $\mathcal{F} + \mathcal{P}$, corresponding to two-segment patterns, and the intersection region of the stripes. The latter region contains the two three-segment patterns $\mathcal{F} + \mathcal{B} + \mathcal{P}$ and $\mathcal{B} + \mathcal{P} + \mathcal{C}$, which are separated by the dotted line with $m = M_{co}$; see inset. The dotted line also provides a very good approximation to the transition line at which the free and completely engulfed states switch metastability in the bistable \mathcal{B} region. The horizontal dotted-dashed lines and the numbered diamonds refer to Figure 1.

as a function of spontaneous curvature m and contact mean curvature M_{co} for a prolate vesicle with reduced volume $v = 0.98$. The different engulfment patterns are separated from each other by the four lines L_{fr}^{\min} , L_{fr}^{\max} , L_{ce}^{\min} , and L_{ce}^{\max} , corresponding to the stability limits L_{fr} and L_{ce} , as given by eqs 2 and 3, for the membrane segments of minimal and maximal curvature of the vesicle $M_{ms} = M_{v,m}^{\min}$ and $M_{v,m}^{\max}$. In this case, the four lines appear essentially straight because the overall shape of the vesicle

hardly changes as we vary the spontaneous curvature m over the range displayed in Figure 3. In addition, the line $M_{co} = m$ separates the two three-segment patterns $\mathcal{F} + \mathcal{B} + \mathcal{P}$ and $\mathcal{B} + \mathcal{P} + \mathcal{C}$, and provides a very good approximation to the transition line at which the free and completely engulfed states of the particle switch their metastability in the bistable \mathcal{B} region. Large positive values of m lead to single-segment patterns with partially engulfed states. In contrast, negative values of m increase the stability of completely engulfed states and enhance the bistability of the system, which may be used to reversibly load and release the nanoparticles in response to external forces. The horizontal dotted–dashed lines and the numbered diamonds refer to Figure 1, and represent the evolution of the engulfment patterns as a function of increasing particle size or adhesiveness. As seen in Figure 1a, partial engulfment is more persistent at the weakly curved equator of the prolate vesicle. As the contact curvature increases and we cross the vertical line L_{fr}^{min} in Figure 3, a \mathcal{P} segment starts to grow continuously from the equator until it covers the whole vesicle when we reach the L_{fr}^{max} line. The \mathcal{P} segment only starts to shrink once we cross the L_{ce}^{max} line, and disappears at the equator when we cross the line L_{ce}^{min} , the vesicle being now covered by a single \mathcal{C} segment. In contrast, bistable behavior is favored at the strongly curved poles of the vesicle, from which the \mathcal{B} segments start to grow and then shrink; see Figure 1b.

In Figure 3, which applies to reduced volume $\nu = 0.98$, the parameter regions with stable two- or three-segment patterns are relatively small and, thus, require fine-tuning of the parameters M_{co} and m . Multisegment patterns, on the other hand, become more and more frequent as we decrease the reduced volume ν and, thus, increase the difference between M_{vm}^{min} and M_{vm}^{max} . This tendency is illustrated in Figure 4, which displays the engulfment patterns as a function of reduced volume ν and contact mean curvature M_{co} for vesicles with spontaneous curvature $m = 0$. As the reduced volume ν is decreased by osmotic deflation, the vesicle undergoes two morphological transitions, from prolates to discocytes and from

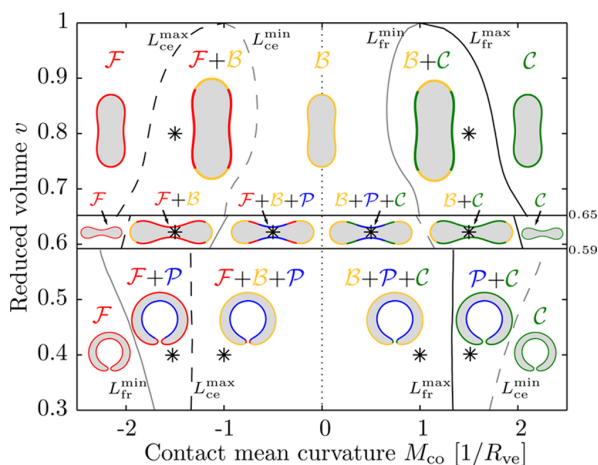


Figure 4. Engulfment patterns as a function of contact mean curvature M_{co} and reduced volume ν for spontaneous curvature $m = 0$. The four lines L_{fr}^{min} , L_{fr}^{max} , L_{ce}^{min} , and L_{ce}^{max} are now highly curved, compare to Figure 3, and are discontinuous along the two solid horizontal lines, which represent shape transitions of the free vesicle. The asterisks indicate the precise positions of the displayed 2-segment and 3-segment patterns.

discocytes to stomatocytes,²⁰ corresponding to the two horizontal lines in Figure 4. For the prolate branch, the two-segment regions rapidly expand as the vesicle is deflated from a sphere. For the discocyte and stomatocyte branches, one finds large regions of the parameter space with stable three-segment patterns. In these regions, partial engulfment is again favored at the segments of lowest membrane curvature, such as at the poles of the discocyte and at the central invagination of the stomatocyte, whereas bistability occurs in the segments of highest membrane curvature. Moving vertically along this engulfment pattern diagram can be easily accomplished experimentally, by simply changing the reduced volume via osmotic deflation and inflation.

In order to obtain the stability regimes for nanoparticles originating from the interior aqueous compartment, we must replace R_{pa} by $-R_{pa}$ in the expression 1 for the contact mean curvature M_{co} , which now decreases for increasing particle size R_{pa} or adhesive strength $|W|$. The inequalities that define the different segment types then change sign, which implies that the stability regimes in Figures 2, 3, and 4 are swapped according to $\mathcal{F} \leftrightarrow \mathcal{C}$ and $\mathcal{B} \leftrightarrow \mathcal{P}$. In contrast to the endocytic case, positive spontaneous curvatures and small segment curvatures now enhance bistability, whereas negative spontaneous curvatures and large segment curvatures promote partial engulfment.

In this Letter, we focused on the membrane–particle interactions and ignored possible particle–particle interactions mediated by the membrane. The latter interactions are obviously absent for the \mathcal{F} segments but should also play no role for \mathcal{B} and \mathcal{C} segments because, in the completely engulfed state, the membrane experiences only a local, point-like deformation at the position of the neck, which costs no energy. Thus, completely engulfed particles are unable to “feel” each other and are expected to diffuse freely on the \mathcal{B} and \mathcal{C} segments. On the other hand, if a completely engulfed particle diffuses from a \mathcal{B} or \mathcal{C} segment into an \mathcal{F} or \mathcal{P} segment, it will unbind or partially unwrap from the membrane. The partially engulfed particles within \mathcal{P} segments may “feel” local curvature gradients and can then aggregate into particle clusters.^{5,29,30} However, such a clustering process does not affect the distinction between the \mathcal{F} , \mathcal{B} , \mathcal{C} , and \mathcal{P} segments and, thus, does not change the engulfment patterns described above.

The engulfment patterns described here should be directly observable in the optical microscope using fluorescently labeled particles. For a membrane with known bending rigidity, the mean contact curvature can be tuned by using nanoparticles of an appropriate material and size. As an example, the adhesive strength between DMPC bilayers and silica was measured³¹ to be on the order of $|W| \approx 0.5$ mJ/m². Using eq 1 and the measured value³² of the bending rigidity $\kappa \approx 18 k_B T$ for DMPC bilayers, we see that the contact mean curvature can be varied from $M_{co} \approx -1/(75$ nm) to $+1/(79$ nm) as we increase the nanoparticle size from $R_{pa} = 14$ to 22 nm. In addition, the adhesive strength and thus the contact mean curvature may be tuned in a continuous manner by changing the salt concentration of the aqueous solution.⁸ Furthermore, the spontaneous curvature of the membrane can be varied over a wide range from $|m| \sim 1/(100$ μ m) to $1/(20$ nm) via asymmetric adsorption of ions, small molecules or larger polymers and proteins,^{33,34} as well as through the controlled formation of bilayers with compositional asymmetry.^{35–37} Finally, the reduced volume and therefore the vesicle shape can be controlled using osmotic deflation and inflation.

We have shown that the nonaxisymmetric configurations of nanoparticles and membranes can be studied by local stability analysis, as embodied in the two stability relations (eqs 2 and eq 3). These relations depend on two material parameters: the contact mean curvature M_{co} as given by eq 1, and the spontaneous curvature m , and imply four distinct types of stable membrane segments. As a consequence, a nanoparticle will be either free, partially engulfed, completely engulfed, or show bistability between partially and completely engulfed states, depending on the local curvature of the membrane. For small particle radii, the stability relations can be used to predict ten distinct engulfment patterns on complex membrane shapes as provided, for example, by prolate, discocyte, or stomatocyte vesicles as well as morphological transitions between these patterns, see Figures 1–4. These patterns should be directly observable in the optical microscope using fluorescently labeled particles.

The stability relations (eqs 2 and 3) have been derived for the spontaneous curvature model in ref 14 but should have the same form in the area-difference-elasticity model.³⁸ The latter model describes bilayer membranes for which one can ignore molecular flip-flops between the two leaflets of the bilayers and, thus, assume that each leaflet has a fixed number of molecules irrespective of the membrane shape. For this model, the stability relations (eqs 2 and 3) should again hold provided one replaces the spontaneous curvature m by the effective spontaneous curvature $m_{eff} \equiv m - \zeta/(4R_{ve})$ with $\zeta \sim R_{pa}/R_{ve}$. [The dimensionless quantity ζ is equal to $(\bar{\kappa}/\kappa)(q - q_0)$ where $\bar{\kappa}$ is the second bending rigidity of the area-difference-elasticity model³⁸ with $\bar{\kappa}/\kappa \simeq 1$ and q denotes the integrated mean curvature $q \equiv \int dAM/R_{ve}$, which attains the value q_0 for the relaxed vesicle shape with an optimal packing of the molecules in both leaflets. When the latter shape is quasispherical, one finds $q - q_0 \approx \pm 4\pi R_{pa}/R_{ve}$ for small size ratios R_{pa}/R_{ve} where the plus and minus sign apply to exo- and endocytosis, respectively. Note that $q - q_0$ has a fixed value for a given vesicle shape.] For the systems considered here, the size R_{pa} of the nanoparticles was taken to be much smaller than the size R_{ve} of the vesicles which implies that the effective spontaneous curvature m_{eff} is approximately equal to the spontaneous curvature m even in the absence of flip-flops between the bilayer leaflets.

In the present study, we focused on the engulfment patterns of free vesicles exposed to a single species of nanoparticles in order to demonstrate the far-reaching consequences of the stability relations (eqs 2 and 3). Because of their local nature, these relations can be generalized to more complex membrane systems. Relatively simple examples are provided by (i) binary mixtures of two nanoparticles with different sizes and (ii) vesicle membranes with coexisting membrane domains formed by liquid-ordered and liquid-disordered phases. In case (i), the two particle sizes lead to two different engulfment patterns which are superimposed on the vesicles. In case (ii), the different fluid–elastic parameters of the two membrane phases lead to coexisting engulfment patterns that are confined to the two types of membrane domains. Furthermore, we may consider vesicles that experience external forces or constraints arising, for example, from adhesive surfaces, micropipettes, or optical tweezers. In the latter cases, the stability relations (eqs 2 and 3) remain valid for the “unperturbed” membrane segments, that is, for those membrane segments that are neither in contact with other surfaces nor directly exposed to localized external

forces. For the “perturbed” segments, on the other hand, we can derive generalized stability relations as will be shown in a subsequent paper. Finally, it will be rather interesting to study the engulfment patterns of cellular membranes. The shape of these membranes is often strikingly similar to the shape of vesicles but the particle engulfment usually involves additional processes such as the formation of protein coats in receptor-mediated endocytosis¹⁴ or localized forces arising from the coupling to the cytoskeleton.

■ AUTHOR INFORMATION

Corresponding Author

*E-mail: lipowsky@mpikg.mpg.de.

Notes

The authors declare no competing financial interest.

■ ACKNOWLEDGMENTS

This study was supported by the German Research Foundation (DFG) via the IRTG 1524.

■ REFERENCES

- (1) Petros, R. A.; DeSimone, J. M. *Nat. Rev. Drug Discovery* **2010**, *9*, 615–627.
- (2) Rodriguez, P. L.; Harada, T.; Christian, D. A.; Pantano, D. A.; Tsai, R. K.; Discher, D. E. *Science* **2013**, *339*, 971–975.
- (3) Lipowsky, R.; Döbereiner, H.-G. *Europhys. Lett.* **1998**, *43*, 219–225.
- (4) Dietrich, C.; Angelova, M.; Pouligny, B. *J. Phys. II* **1997**, *7*, 1651–1682.
- (5) Koltover, I.; Rädler, J.; Safinya, C. *Phys. Rev. Lett.* **1999**, *82*, 1991–1994.
- (6) Fery, A.; Moya, S.; Puech, P. H.; Brochard-Wyart, F.; Mohwald, H. *C. R. Phys.* **2003**, *4*, 259–264.
- (7) Michel, R.; Kesselman, E.; Plostica, T.; Danino, D.; Gradzielski, M. *Angew. Chem., Int. Ed.* **2014**, *53*, 12441–12445.
- (8) Strobl, F. G.; Seitz, F.; Westerhausen, C.; Reller, A.; Torrano, A. A.; Bräuchle, C.; Wixforth, A.; Schneider, M. F. *Beilstein J. Nanotechnol.* **2014**, *5*, 2468–2478.
- (9) Jaskiewicz, K.; Larsen, A.; Schaeffel, D.; Koynov, K.; Lieberwirth, I.; Fytas, G.; Landfester, K.; Kroeger, A. *ACS Nano* **2012**, *6*, 7254–7262.
- (10) Deserno, M. *Phys. Rev. E* **2004**, *69*, 031903.
- (11) Gózdź, W. T. *Langmuir* **2007**, *23*, 5665–5669.
- (12) Nowak, S. A.; Chou, T. *Phys. Rev. E* **2008**, *78*, 021908.
- (13) Cao, S.; Wei, G.; Chen, J. Z. Y. *Phys. Rev. E* **2011**, *84*, 050901.
- (14) Agudo-Canalejo, J.; Lipowsky, R. *ACS Nano* **2015**, *9*, 3704–3720.
- (15) Yi, X.; Shi, X.; Gao, H. *Nano Lett.* **2014**, *14*, 1049–1055.
- (16) Dasgupta, S.; Auth, T.; Gompper, G. *Nano Lett.* **2014**, *14*, 687–693.
- (17) Vácha, R.; Martinez-Veracoechea, F. J.; Frenkel, D. *Nano Lett.* **2011**, *11*, 5391–5395.
- (18) Huang, C.; Zhang, Y.; Yuan, H.; Gao, H.; Zhang, S. *Nano Lett.* **2013**, *13*, 4546–4550.
- (19) Lipowsky, R. *Nature* **1991**, *349*, 475–481.
- (20) Seifert, U.; Berndl, K.; Lipowsky, R. *Phys. Rev. A: At, Mol, Opt. Phys.* **1991**, *44*, 1182–1202.
- (21) Voeltz, G. K.; Prinz, W. A. *Nat. Rev. Mol. Cell Biol.* **2007**, *8*, 258–264.
- (22) Shibata, Y.; Hu, J.; Kozlov, M. M.; Rapoport, T. A. *Annu. Rev. Cell Dev. Biol.* **2009**, *25*, 329–354.
- (23) Terasaki, M.; Shemesh, T.; Kasthuri, N.; Klemm, R. W.; Schalek, R.; Hayworth, K. J.; Hand, A. R.; Yankova, M.; Huber, G.; Lichtman, J. W.; Rapoport, T. A.; Kozlov, M. M. *Cell* **2013**, *154*, 285–296.

- (24) Kim, K. T.; Zhu, J.; Meeuwissen, S. A.; Cornelissen, J. J. L. M.; Pochan, D. J.; Nolte, R. J. M.; Van Hest, J. C. M. *J. Am. Chem. Soc.* **2010**, *132*, 12522–12524.
- (25) Jülicher, F.; Seifert, U.; Lipowsky, R. *Phys. Rev. Lett.* **1993**, *71*, 452–455.
- (26) Michalet, X.; Bensimon, D. *Science* **1995**, *269*, 666–668.
- (27) Helfrich, W. *Z. Naturforsch. C* **1973**, *28*, 693–703.
- (28) Seifert, U.; Lipowsky, R. *Phys. Rev. A: At., Mol., Opt. Phys.* **1990**, *42*, 4768–4771.
- (29) Bahrami, A. H.; Lipowsky, R.; Weikl, T. R. *Phys. Rev. Lett.* **2012**, *109*, 188102.
- (30) Šarić, A.; Cacciuto, A. *Phys. Rev. Lett.* **2012**, *109*, 188101.
- (31) Anderson, T. H.; Min, Y.; Weirich, K. L.; Zeng, H.; Fygenson, D.; Israelachvili, J. N. *Langmuir* **2009**, *25*, 6997–7005.
- (32) Brüning, B. A.; Prévost, S.; Stehle, R.; Steitz, R.; Falus, P.; Farago, B.; Hellweg, T. *Biochim. Biophys. Acta, Biomembr.* **2014**, *1838*, 2412–2419.
- (33) Lipowsky, R. *Faraday Discuss.* **2013**, *161*, 305–331.
- (34) Różycki, B.; Lipowsky, R. *J. Chem. Phys.* **2015**, *142*, 054101.
- (35) Hu, P. C.; Li, S.; Malmstadt, N. *ACS Appl. Mater. Interfaces* **2011**, *3*, 1434–1440.
- (36) Richmond, D. L.; Schmid, E. M.; Martens, S.; Stachowiak, J. C.; Liska, N.; Fletcher, D. A. *Proc. Natl. Acad. Sci. U. S. A.* **2011**, *108*, 9431–9436.
- (37) Matosevic, S.; Paegel, B. M. *Nat. Chem.* **2013**, *5*, 958–963.
- (38) Miao, L.; Seifert, U.; Wortis, M.; Döbereiner, H.-G. *Phys. Rev. E: Stat. Phys., Plasmas, Fluids, Relat. Interdiscip. Top.* **1994**, *49*, 5389–5407.

5 Summary and Outlook

In this thesis, we have shown that membrane remodeling processes that occur in model systems as well as in biological cells can be understood from a theoretical perspective, in particular, using the continuum elastic theory of membranes. We have emphasized the importance of including the effects of bilayer asymmetry, as quantified by the membrane spontaneous curvature, on the membrane description. Indeed, the formation of nanotubes in giant vesicles cannot be explained in the absence of spontaneous curvature, as shown in Chapter 2. Furthermore, in Chapters 3 and 4 we have shown that spontaneous curvature strongly affects the engulfment of particles by model membranes; and we have provided a satisfactory explanation for the observed size-dependence of clathrin-mediated endocytosis of nanoparticles by cells based on the strong membrane asymmetry induced by the clathrin coat, see Chapter 3.

In Chapter 2, using numerical energy minimization, we expanded the previously known phase diagram of free vesicle shapes to the regions of very large spontaneous curvature $|m|R_{ve} \gg 1$, where R_{ve} is the vesicle size. In this case, osmotic deflation of a spherical vesicle initially leads, *via* an oblate-stomatocyte transition, to the formation of a spherical bud. Upon further deflation, there are two competing kinetic pathways: the first pathway leads to the creation of new buds, whereas the second pathway makes existing buds grow into necklace-like nanotubes. Furthermore, we describe for the first time a transition between necklace-like and cylindrical tubes that occurs once the tubes reach a certain critical length. This increased understanding of nanotube shapes allows one to deduce the spontaneous curvature of the membrane by optical imaging of the nanotubes.

Membrane nanotubes connected to vesicles are an interesting model system for the membrane area reservoirs present in cells, see Figure 1.4. These area reservoirs equip cells with increased versatility and robustness, as in the case of phagocytic cells, which can increase their apparent surface area by up to 400%, implying that up to 80% of their membrane area is stored in hidden reservoirs, see Section 1.2.2. In the experiments described in Chapter 2, up to 20% of the total membrane area was stored in the tubes, but there is in principle no reason why this number should be an upper limit. Indeed, further deflation should lead to more area stored in nanotubes. The added complexity caused by the presence of aqueous phase-separation within the vesicle in the experiments of Chapter 2 can be avoided by using solutions of only PEG and sucrose.

It will be interesting to see if vesicles with nanotubes show increased robustness, as in the case of biological cells. Indeed, as explained in Section 1.5.2, the interaction of initially

spherical vesicles (in the absence of nanotubes) with large strongly adhesive particles leads to vesicle rupture. This can be easily understood, as lipid membranes can only stretch by typically 4% before rupturing. The engulfment of a particle of radius R_{pa} requires a spherical vesicle of radius R_{ve} to stretch by a factor $R_{\text{pa}}^2/R_{\text{ve}}^2$. This implies that a vesicle will rupture when brought in contact with strongly adhesive particles if the particle radius is larger than $\sqrt{0.04}R_{\text{ve}} = R_{\text{ve}}/5$. In contrast, a spherical vesicle with apparent radius R_{ve} and 20% of its area stored in nanotubes could in principle engulf of the order of $0.2R_{\text{ve}}^2/R_{\text{pa}}^2$ particles of radius R_{pa} before starting to stretch. The same argument for added robustness in the presence of nanotubes should apply to vesicles squeezing through pores, or vesicles containing active matter such as a reconstituted actin cortex.

In the first part of Chapter 3, we examined in detail the effects of membrane asymmetry as well as vesicle size on particle engulfment, which were previously unexplored. Using extensive numerical energy minimization, as well as theoretical considerations, we obtained two analytical conditions for the stability of the free and completely engulfed states of a particle. These two instability conditions completely determine the engulfment behavior. The instability of the free state was found to be independent of the membrane spontaneous curvature, whereas the instability of the completely engulfed state is dependent on the spontaneous curvature.

We proposed an experimental method by which the membrane spontaneous curvature and the adhesive strength of the particle–membrane interactions can be deduced from image analysis of experiments or simulations in which membranes are put in contact with particles of different sizes. Whereas the analysis of nanotube shapes is useful in measuring very large spontaneous curvatures $|m|R_{\text{ve}} \gg 1$, where R_{ve} is the vesicle size, analysis of particle engulfment gives access to small spontaneous curvatures of the order of the vesicle size $|m|R_{\text{ve}} \sim 1$, which are typically more elusive. It will be exciting to see if this method can be applied in experiments.

In the second part of Chapter 3, we examined the case of adhesion-induced segregation of membrane components by the adhering particle. The theory that we developed is in principle applicable to any multi-component membrane in which some lipid species or membrane-anchored molecules have a higher affinity for the particle than the others. This would be the case, for example, if a charged particle interacts with a membrane made of a mixture of charged lipids of opposite charges, or of a charged lipid with a neutral lipid. In general, the membrane segment bound to the particle will have different composition and thus different elastic properties than the unbound membrane segment.

Of most interest is the limit case in which the bound segment has a much larger spontaneous curvature than the unbound segment, as is the case in the strongly asymmetric protein coats occurring during clathrin-mediated endocytosis by cells. We showed that, in this case, only intermediate-sized particles that are between a lower and an upper threshold can be engulfed. We obtained analytical expressions for the engulfment rate and total uptake of particles by cells, that can explain the experimentally observed size-distribution of gold

nanoparticle uptake by HeLa cells. When compared to previous models, our theory does not depend on the depletion of receptors from the cell membrane, which is a problematic assumption, see Section 1.5.3.

In Chapter 4, we used the analytical conditions of the free and completely engulf states to examine engulfment on nanoparticles at non-axisymmetric locations of vesicles. This would be extremely difficult to do using direct energy minimization, see Section 1.6. We found that the fate of a particle is strongly dependent on the local curvature of the vesicle at the point of contact with the particle. As a consequence, vesicles with a complex shape of non-uniform curvature will display membrane segments in which particles remain free, others in which particles may be partially or completely engulfed, as well as segments where particles show bistability between the free and the completely engulfed states.

We showed that, when exposed to many nanoparticles, a homogeneous vesicle can simultaneously display up to three such different segments on their surface, thereby forming distinct engulfment patterns. We found that there are only ten possible engulfment patterns, and described in detail the transitions between them as a function of the vesicle shape and spontaneous curvature, as well as particle size and adhesiveness. These patterns should be observable under optical microscope by using fluorescently labeled particles. Given the generality of our approach based on the two instability conditions, our results can be directly extended to more complex cases such as phase-separated membranes, or vesicles in contact with mixtures of particles made from different materials or sizes.

To conclude, we hope to have shown that membrane remodeling processes are strongly affected by the asymmetry of the bilayer, which is too often neglected in theoretical treatments. We have provided new analytical tools for researchers to quantify this bilayer asymmetry in experiments or simulations. In addition, our analytical instability conditions for the engulfment of particles by membranes allow for a very thorough understanding of engulfment processes without the need to perform numerical calculations.

Acknowledgements

I would first like to thank my supervisor, Prof. Reinhard Lipowsky, for his invaluable guidance during my work on this thesis. I enjoyed very much all of our discussions during these past few years, both the scientific and the non-scientific ones.

I am also grateful to the rest of the Theory Department at the Max Planck Institute of Colloids and Interfaces; in particular to Susann Weber, for being always helpful, as well as to Dr. Rumiana Dimova and Jan Steinkühler for very interesting discussions and collaborations.

I would also like to thank Prof. Dennis Discher for hosting me at the University of Pennsylvania in Philadelphia. It was a busy period and I hope that our collaboration will soon see the light of day. I am also very thankful to the rest of the Discher Lab for making my stay there great.

I had very good times at the IRTG 1524 meetings, which would not have been possible without the hard organizational work of Prof. Martin Schoen, Dr. Daniela Fliegner, Petra Erdmann and Beatrix Thiele. Thank you.

I want to thank all my friends in Berlin, for making these years something special.

Julia, thank you for always making me happy, and for bearing with me in the last stressful times of wrapping up this thesis.

Finally, I want give the most special thanks to my parents and my two brothers. Thank you for always supporting me. This thesis is dedicated to you.